MINISTRY OF EDUCATION
FEDERAL UNIVERSITY OF RIO GRANDE DO SUL
School of Engineering

Graduate Program in Mining, Metallurgy and Materials

PPGE3M

# MEASURING THE EFFECT OF CATHODIC PROTECTION ON THE PERFORMANCE OF THERMALLY SPRAYED ALUMINIUM COATINGS AT ELEVATED TEMPERATURE

**Nataly Araujo Cé**

Thesis submitted for the degree of Doctor of Philosophy in Engineering.

Porto Alegre
2017

MINISTRY OF EDUCATION
FEDERAL UNIVERSITY OF RIO GRANDE DO SUL
School of Engineering

Graduate Program in Mining, Metallurgy and Materials

PPGE3M

# MEASURING THE EFFECT OF CATHODIC PROTECTION ON THE PERFORMANCE OF THERMALLY SPRAYED ALUMINIUM COATINGS AT ELEVATED TEMPERATURE

NATALY ARAUJO CÉ
Metallurgical Engineer

Study conducted at the Department of Metallurgy from School of Engineering of UFRGS within the Graduate Program in Mining, Metallurgy and Materials - PPGE3M as part of the requirements for obtaining the title of Doctor of Philosophy in Engineering.

Concentration Area: Materials Science and Technology

Porto Alegre
2017

MINISTÉRIO DA EDUCAÇÃO
UNIVERSIDADE FEDERAL DO RIO GRANDE DO SUL
Escola de Engenharia

Programa de Pós-Graduação em Minas, Metalurgia e Materiais

PPGE3M

# AVALIAÇÃO DO EFEITO DA PROTEÇÃO CATÓDICA NO DESEMPENHO DO REVESTIMENTO DE ALUMÍNIO PULVERIZADO TERMICAMENTE SUBMETIDO A ALTAS TEMPERATURAS

NATALY ARAUJO CÉ
Engenheira Metalúrgica

Estudo conduzido no Departamento de Metalurgia da Escola de Engenharia da UFRGS através do Programa de Pós-Graduação em Minas, Metalurgia e Materiais - PPGE3M-como parte dos requerimentos para obtenção do título de Doutor em Engenharia.

Área de Concentração: Ciência e Tecnologia dos Materiais

Porto Alegre
2017

This thesis was judged adequate for obtaining a Doctor of Philosophy degree, concentration area in Materials Science and Technology and approved in its final form by the supervisor and by the Examination Board of the Graduate Program.


Supervisor: Prof. Dr. Afonso Reguly


Examination Board:

Dr. Marcelo T. Piza Paes, PETROBRAS
Dr. Walmar Baptista, PETROBRAS
Prof. Dr. Tiago Falcade, DEQUI/UFRGS


Prof. Dr. Carlos Perez Bergman
Coordinator of PPGE3M

# ACKNOWLEDGEMENTS

SUMMARY

LIST OF FIGURES

# LIST OF TABLES

# LIST OF EQUATIONS

# LIST OF ABBREVIATIONS AND SYMBOLS

| | |
|---|---|
| AE | Auxiliary Electrode |
| CP | Cathodic Protection |
| CR | Corrosion rate |
| DC | Direct Current |
| EDX | Energy Dispersive X-Ray |
| ICCP | Impressed Current Cathodic Protection |
| $K_{sp}$ | Solubility Product Constant |
| LPR | Linear Polarisation Resistance |
| MMO | Mixed Metal Oxides |
| SPS | Subsea Production System |
| TC | Thermocouple |
| TSA | Thermally Sprayed Aluminium |
| TSA - Al | TSA coating composed of 99.5% Al |
| TSA - AlMg | TSA coating composed of Al- 5%Mg |
| TWAS | Twin Wire Arc Spray System |
| XRD | X-Ray Diffraction |

ABSTRACT

Thermally Sprayed Aluminium (TSA) is widely used in offshore facilities as sacrificial anode coating for carbon-steel risers and pipelines. Transportation and installation of those components can lead to small damages in the coating, which can expose the steel surface to the seawater. It is known that calcareous deposit is formed on the cathodically polarised steel surface. Thus, this research evaluated the TSA applied by twin wire arc spray system (TWAS) on S355J2+N carbon-steel when damage (holidays) is present in order to study the calcareous deposit formation on steel and acquire data regarding the TSA performance at high temperatures. Application of different conditions was also considered: presence of sealing; coating alloy (99.5%Al and Al-5%Mg) and buried/unburied conditions. Generally, two types of experiment were conducted – i) tests at free potential at steady temperatures (30, 60 and 90°C) and different holiday sizes (exposing 5, 10 and 20% of the steel surface) and ii) tests under thermal gradient where oil at ~125°C was added in polymeric tower and external water at ~10°C was in contact with the samples surface (both free potential and polarisation of -950 mV$_{Ag/AgCl}$ were applied). Methodology of analyses included visual inspection, scanning electron microscope and X-ray Diffraction. From the tests at steady temperatures, the TSA reached a very good protective potential (-800 to -900 mV$_{Ag/AgCl}$) and little difference in results due to difference in TSA composition and holiday size was observed. Corrosion rates were kept between 0.02 and 0.01 mm/year. From the thermal gradient test under free potential, the coating loss and corrosion rates were 0.4 to 0.002 mm/year. Also, the potential achieved was in a lower range than previously obtained (-745 to -835 mV$_{Ag/AgCl}$). However, when TSA was combined with external cathodic protection and thermal gradient, the thickness of the TSA was satisfactory and corrosion rates obtained were below 0.076 mm/year. The calcareous deposit formed within the holiday protected the steel substrate against corrosion and its growth mechanism based in this research was built.

**Keywords**: TSA, Sacrificial anode, Calcareous deposit, Cathodic Protection.

# RESUMO

Alumínio Pulverizado Termicamente (TSA) é amplamente utilizado em instalações offshore como revestimento de ânodo de sacrifício em tubulações de aço carbono. O transporte e a instalação desses componentes podem levar a pequenos danos no revestimento, o que pode expor a superfície do aço à água do mar. Sabe-se que o depósito calcário é formado na superfície do aço polarizado catodicamente. Assim, esta pesquisa avaliou o TSA aplicado por sistema de pulverização de arco duplo (TWAS) no aço ao carbono S355J2 + N quando ocorrem danos (*holidays*) para estudar a formação de depósitos calcários no aço e adquirir dados sobre o desempenho do TSA sob altas temperaturas. A aplicação de diferentes condições também foi considerada: presença de selantes; liga do revestimento (99,5% de Al e Al-5% de Mg) e condições enterradas/não enterradas. Dois tipos de experimentos foram realizados: i) testes em potencial livre sob temperaturas constantes (30, 60 e 90°C) e diferentes tamanhos de *holidays* (expondo 5, 10 e 20% da superfície do aço) e ii) testes sob gradient térmico onde óleo a ~125°C foi adicionado em uma torre polimérica e água externa a ~10°C ficou em contato com a superfície das amostras (tanto potencial livre como polarização de -950 $mV_{Ag/AgCl}$ foram aplicados). Análises incluíram inspeção visual, microscópio eletrônico de varredura e difração de Raio-X. A partir dos testes em temperaturas constante, o TSA atingiu um bom potencial de proteção (-800 a -900 $mV_{Ag/AgCl}$) e pouca diferença nos resultados devido à diferença na composição doTSA e no tamanho do *holiday* foi observada. As taxas de corrosão foram mantidas entre 0,02 e 0,01 mm/ano. No ensaio sob gradiente térmico e potencial livre, a perda de revestimento e as taxas de corrosão foram de 0,4 a 0,002 mm/ano. Além disso, o potencial alcançado foi de uma faixa menor do que a obtida anteriormente (-745 a -835 $mV_{Ag/AgCl}$). No entanto, quando o TSA foi combinado com proteção catódica externa e gradiente térmico, a espessura do TSA foi satisfatório e as taxas de corrosão obtidas foram inferiores a 0,076 mm/ano. O depósito calcário formado no *holiday* protegeu o aço contra a corrosão e seu mecanismo de crescimento baseado nesta pesquisa foi construído.

**Keywords**: TSA, Sacrificial anode, Calcareous deposit, Cathodic Protection.

# 1        INTRODUCTION

Corrosion problems in the oil and gas field leads to several problems, since small damages on structures may lead to catastrophes that can result in large-scale environment mess. Losses related to corrosion problems in the oil and gas sector in USA are estimated to be $1.4 billion/year, according report released by U.S. Federal Highway Administration in 2002. The total is shared into $0.6 billion in surface pipeline and facility costs, $0.5 billion in downhole tubing expenses, and another $0.3 billion in capital expenditure related to corrosion. In order to reduce expenses in this area, anti-corrosion techniques are applied on components reducing its corrosion rate (mm/year) thus increasing its life cycle (FHWA 2002, HEIDERSBACH, 2011, NACE, POPOOLA 2013).

Corrosion process happens whenever cathodic and anodic areas appears on a metallic surface, making electrons flow from anode to cathode areas as long as it has a electrolyte to allow the process. To eliminate the process, cathodic protection (CP) is applied on structures, what is an artificial way to make the material to acquire cathodic behaviour.  It happens to stop the flow of current from anode to cathode direction what ends up the corrosion (GENTIL 1996). High strength materials are the most used material for pipelines and risers construction but its high reactivity into seawater requires corrosion control methods to be taken such as combination of coatings and external CP on external surfaces (HARTT 2005, HEIDERSBACH 2011).

As aluminium is anodic to carbon steel, thermally sprayed aluminium (TSA) coating has been increasingly used to protect subsea components as a long-term corrosion protection of onshore and offshore structures providing corrosion rate as low as <10 µm/year (PAUL 2015). This protection works as a sacrificial coating and results in formation of a thin layer of calcareous deposits over the exposed carbon steel due to changes on local pH. These deposits have a favourable function regarding the corrosion protection since it acts as an inorganic barrier, restricting the oxygen diffusion towards the steel surface and therefore decreasing the corrosion rate (NEVILLE 2002, BARCHICHE 2003, PAUL 2015, CE 2016).

Although there are several publications regarding the behaviour of TSA on submerged carbon steel in the offshore industry, few cover its performance considering hot environment and when damage takes place. Literature reports that several hot risers have severely corroded in the 70's for inadequate design of current demand and pipelines had to be taken from service due premature failure of sacrificial anodes operating hot (PALMER 2008). Moreover, limited data is available on the interaction of TSA coatings combined with CP at high temperatures.

# 2        OBJECTIVES

The general objective of this study is to show the performance of TSA when damage (holiday) is present. This will include the selection of environmental conditions (low to high temperature and thermal gradient), range of potential (free potential and external polarisation), use of different coating composition (99.5%Al and Al-5%Mg) and use of sealant (sealed and non-sealed). This study is based in two main parts: samples exposed to steady temperatures (30, 60 and 90°C) and samples exposed to thermal gradient. The specific objectives is to generate corrosion data regarding the CP of damaged TSA-coated carbon steel subjected to heat and it also aims to better understand the mechanism involved in calcareous deposition on cathodically polarised steel surface at high temperature, as available studies cover this matter considering temperatures up to 30°C (BARCHICHE 2004, NEVILLE 2002, MOLLER 2006, BARCHICHE 2003, BARCHICHE 2009, BERNER 1975).

## 3        LITERATURE REVIEW

3.1      Risers

The fossil fuels comprise oil, natural gas and coal among which ~80% is oil and gas what plays an important role in the world's energy supply (BAI 2012).

The concept of subsea production system (SPS) came up in the 70's and completions are divided in shallow-water (less than 305 m depths) and deep-water completions (greater than 305 m) (BAI 2012). In the last 40 years the engineering advances allowed the extraction of petroleum to move to depths of at least 2,000 m. The SPS can be associated with an existing production platform or an onshore facility. A movable rig drills the oil well and the extracted oil or natural gas is transported by pipeline under the sea to the risers an then to a processing facility (BAI 2012, KUIPER 2008, SPEIGHT 2014). During transportation of crude oil from a subsea well, the high temperature fluid, typically between 100°C and 200°C, cools along the pipeline by conduction, but still arrives at the platform at an elevated temperature (PALMER 2008).

Risers are a type of pipeline that provides the vertical transportation of crude oil and natural gas from the wellhead to the production platform being critical components due the services loads they are submitted (KUIPER 2008, SPEIGHT 2014). Those components are also susceptible to corrosion due to the exposure to seawater or marine sediments and cathodic protection is necessary (DNV-RP-B401 2010). The standard NORSOK M-001 recommends C-Mn steel for pipeline system that will process oil and gas and its manufacturing must be in accordance with DNV-OS-F101 standard.

Seawater is a very corrosive solution with 3.5% salt content containing high concentration of sodium chloride combined with high electrical conductivity and alkaline pH (pH ~8.2). Its corrosion rate is mainly controlled by the chloride content, oxygen availability and temperature (GHALI 2010, TALBOT 2007). However, the dissolved oxygen content in seawater can be high as 12 ppm (depending on the temperature and salinity) and is the factor that most influences the corrosion on materials acting as the principal depolarizer of anodic reactions in seawater (SHIFLER 2005, TALBOT 2007).

Soil is not very corrosive media and the corrosion on buried pipelines develops by contact with water and oxygen diffusion likewise, however localised corrosion is more probable to happen due the nonhomogeneous contact of the pipeline surface and the surrounding soil. Therefore, factors that promote the corrosivity of a soil are porosity, resistivity, dissolved salts, moisture and pH (REVIE 2011).

Oil and gas infrastructure requires high investment and risk with corrosion and further structure replacement is highly undesirable. In United States there are more than 119,000 km of crude oil transportation and gathering pipelines. The total investment of gas pipeline companies in 1998 was estimated in $63.1 billion. The average cost related to corrosion in the country is estimate at $7 billion being 10% related to failures (FHWA 2002).

3.2     Cathodic Protection

Cathodic protection (CP) is an electrochemical method to reduce corrosion over metallic structures exposed to soil and waters and it is a method to reduce the corrosion rate of a metal by turning it the cathode of an electrochemical cell (JAVAHERDASHTI 2013).

Corrosion on offshore steels can be prevented by combination of external coating and cathodic protection (CP) which will supply sufficient electrical current to the pipeline and prevent corrosion in case of a failure of the coating. The use of CP for protection of the whole bare steel is possible, but cost is a limitation to be considered. Therefore, coating is followed by CP as protection for coating defects, damage and degradation (BAI 2005, PALMER 2008, ISO 15589-2).

The corrosion potential ($E_{corr}$) of a metal is defined as the tendency of the metal surface to release electrons when in contact with an electrolyte and can be defined when measured against a reference electrode (YANG 2008). The CP is an electrochemical protection that will decrease the potential of the metal significantly to below of its corrosion potential and therefore, no corrosion will take place. That process to provide electrons for cathodic reactions in order to replace electrons generated by normal corrosion is known as cathodic polarisation and the number of electrons must be equal the electrons removed by the cathodic reactions as oxygen reduction or hydrogen reduction (DNV-RP-B401, BAI 2005). Seawater is a strong electrolyte and electronic reactions will occur in the external surface of the pipeline, not affecting the inside, although high strength steels may

be susceptible to hydrogen induced stress cracking and coating detachment can occur (PALMER 2008, DNV-RP-B401).

The types of CP system are used in offshore industry are: galvanic anode (external coatings) and impressed current (external power supply) (BAI 2005, ISO 15599-2). It prevents localised corrosion and uniform corrosion as well as blocks galvanic corrosion in case two materials with electrochemical differences are combined (DNV-RP-B401 2010).

It is important to highlight that CP can provide certain drawback effects as hydrogen embrittlement on some high-strength alloys where coating detachment can occur (DNV-RP-B401).

### 3.2.1 Cathodic Protection Design

The CP design comprises several parameters to consider in order to set a CP system and depends on the surrounding environment which varies with geographical location and depth (DNV-RP-B401, PALMER 2008, BAI 2005, ISO 15589-2). The main parameters for design a CP system are described below.

*Cathodic Protection Potential*

The system's protective potential must be determined so that the current demand can be estimated. For C-steel the recommended is $-800$ mV for aerobic environment and $-900$ mV for anaerobic environment, against silver/silver chloride/seawater (Ag/AgCl/seawater) electrode and it is applied for saline mud and normal seawater composition (i.e. salinity $3,2 - 3,8\%$) with resistivity of 30 $\Omega$.cm. The resistivity can change with temperature and salinity of the seawater as shown in Table 3.1. For high strength steel, if there is a risk of hydrogen embrittlement, then potentials more negative than -800 mV should be avoided (DNV-RP-B401, ISO 15589-2, PALMER 2008).

The Ag/AgCl/KCl is similar to Ag/AgCl/seawater, but the difference is that the former is immersed in a saturated solution of potassium chloride and the potential is not affected by the salinity/resistivity from the seawater, being more suitable for laboratory applications (ISO 15589-2).

Table 3.1:    Seawater resistivity for different environments (PALMER 2008).

| Environment | Resistivity ($\Omega$.cm) |
|---|---|
| Seawater (t < 10°C) | 30 |
| Seawater (10 – 20°C) | 25 |
| Seawater (t > 20°C) | 20 |
| Sand | 110 –160 |
| Soft clay and mud | 60 –75 |
| Stiff clay | 75 – 110 |

### *Current Densities*

The current densities are dependent on seawater temperature, oxygen dissolved, seawater flow and the capacity of forming calcareous deposit on exposed steel surface. In water depth less than 500 m the design of current is dependent only on seawater temperature (ISO 15589-2).

Current density ($mA/m^2$) is the current that will be in demand for the cathodic protection per unit of exposed steel area of the pipeline. An initial and final current density must be estimated. The initial current density is the one required to initially polarise a surface and is higher than the final current. The final current density is referred to the surface after the formation of calcareous film and must also consider an extra current demand in case of repolarisation is needed due coating damage (coating breakdown percentage) (DNV-RP-B401, BAI 2005). Mean current density is the achieved current when the protective potential is found steady (DNV-RP-B401).

Recommended initial, final and mean design current densities taking in consideration climatic regions and depth are showed in Table 3.2 and 3.3. Those data are considering a bare metal surface exposed to the seawater where the formation of calcareous deposit is expected to form in certain seawater temperature and certain dissolved oxygen content (DNV-RP-B401). Table 3.4 gives the oxygen content in equilibrium with atmospheric oxygen pressure for different temperatures up to 25°C (TALBOT 2007). For fully buried pipelines a design current density (mean and final) of 20 $mA/m^2$ must be used regardless seawater temperature or depth (ISO 15589-2).

According the standard ISO 15589-2, pipelines operating in temperatures >30ºC must have the design current density reconsidered adding 1 $mA/m^2$ for each degree Celsius over 30ºC since oxygen content is reduced as well as the corrosion rate increases. It is

noted that when >80ºC is applied, current densities should then be reconsidered through new assessments, however no specification is cited.

For components coated with aluminium, a designed current density of 10 mA/m$^2$ is recommended for initial/final as well as mean values. For internally heated components, the design current density shall be increased by 0.2 mA/m$^2$ for each degree rise that the metal/ seawater are assumed to exceed from 25°C (DNV-RP-B401).

The standard DNV RP-F103 gives minimum mean design currents densities applicable for C-Mn steel buried and unburied according the internal fluid temperature. Such values are given in Table 3.5 and are not depended on geographic location and operation depth.

Table 3.2:    Suggested initial and final current densities (A/m$^2$) considering bare pipeline operating in different operation depth and climatic region (DNV-RP-B401).

| Depth (m) | Tropical (>20ºC) | | Sub-tropical (12-20ºC) | | Temperate (7-11ºC) | | Arctic (<7ºC) | |
|---|---|---|---|---|---|---|---|---|
| | initial | final | initial | final | initial | final | initial | final |
| 0-30 | 150 | 100 | 170 | 110 | 200 | 130 | 250 | 170 |
| >30-100 | 120 | 80 | 140 | 90 | 170 | 110 | 200 | 130 |
| >100-300 | 140 | 90 | 160 | 110 | 190 | 140 | 220 | 170 |
| >300 | 180 | 130 | 200 | 150 | 220 | 170 | 220 | 170 |

Table 3.3:    Suggested mean design current densities (mA/m$^2$) considering bare pipeline operating different operation depth and climatic region (DNV-RP-B401).

| Depth (m) | Tropical (>20ºC) | Sub-tropical (12-20ºC) | Temperate (7-11ºC) | Arctic (<7ºC) |
|---|---|---|---|---|
| 0-30 | 70 | 80 | 100 | 120 |
| >30-100 | 60 | 70 | 80 | 100 |
| >100-300 | 70 | 80 | 90 | 110 |
| >300 | 90 | 100 | 110 | 110 |

Table 3.4:    Oxygen content in seawater in equilibrium with air under atmospheric pressure (TALBOT 2007).

| Temperature (°C) | -2 | 0 | 5 | 10 | 15 | 20 | 25 |
|---|---|---|---|---|---|---|---|
| Volume fraction of $O_{2(aq)}$ | 0.0085 | 0.0081 | 0.0072 | 0.0064 | 0.0059 | 0.0054 | 0.0049 |

Table 3.5:    Minimum mean design current densities (mA/m2) for pipelines carrying internal fluids with different temperatures (DNV RP-F103).

| Condition | Internal Fluid Temperature (°C) | | | |
|---|---|---|---|---|
| | ≤50 | >50-80 | >80-120 | >120 |
| Non-buried | 0.050 | 0.060 | 0.070 | 0.100 |
| Buried | 0.020 | 0.025 | 0.030 | 0.040 |

*Coating Breakdown Factor*

It must be considered that coated pipelines have the current demand increased along the time due its deterioration and possible exposition of the steel surface to the environment (ISO 15589-2, DNV-RP-B401 PALMER 2008). The coating breakdown factor describes the extent of current density reduction due to the application of coating and is a function of coating properties, operational parameters and time (BAI 2012).

## 3.3 Impressed Current Cathodic Protection System (ICCP)

Two main reactions happen on metal surface during corrosion (PALMER 2008):

i) anodic areas lose mass and produce electrons;
ii) cathodic areas consume those electrons.

The rate of corrosion is determined mainly by the ratio anode/cathode area, concentration of cathodic reactant and resistivity of the electrolyte (PALMER 2008).

On carbon-steel the corrosion process is basically the loss of iron ions to the seawater (Equation 2.1) which react to form oxides and hydroxides. Due the exchange of electrons to the cathode area the corrosion is allowed as the oxygen reduction (Equation 2.2 and hydrogen evolution (Equation 2.3) happen due the alkaline pH of seawater (pH=8.2). The main reactions will happen (PALMER 2008):

a) Anodic:

$$Fe \rightarrow Fe^{2+} + 2e^- \tag{2.1}$$

b) Cathodic:

$$O_2 + 4H_2O + 4e^- \rightarrow 4OH^- \tag{2.2}$$

$$2H + 2e^- \rightarrow H_2 \tag{2.3}$$
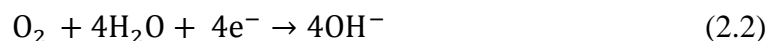
Where $Fe^{2+}$ is abundant, the following overall reaction given in Equation 2.4 will happen (GHALI 2010):

$$Fe^{2+} + 2OH^- \rightarrow Fe(OH)_2 \tag{2.4}$$
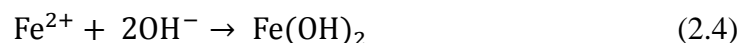
and when $Fe(OH)_2$ is saturated, the oxygenation to $Fe(OH)_3$ will take place as showed in Equation 2.5 (GHALI 2010):

$$2Fe(OH)_2 + H_2O + \frac{1}{2}O_2 \rightarrow Fe_2O_3.nH_2O \tag{2.5}$$
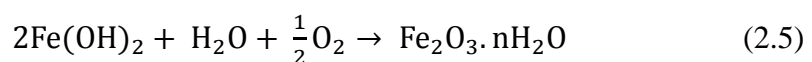
The ICCP system is based on supply current from an external power where a alternating current (AC) is converted in direct current (DC) through a rectifier which will

discharges cathodic current from anodes through the electrolyte arriving on the surface to be protected. The current then returns to the rectifier through the pipeline. The corrosion is ceased when the applied cathodic current is equals the corrosion current (JAVAHERDASHTI 2013, PALMER 2008).

Standard ISO 15589-2 mentions that anode materials should be mixed metal oxides (MMO) or platinum on substrate of titanium, niobium or tantalum. However, depending on the application, alternative materials can be applied as long as its properties were previously reported.

Figure 3.1 shows the anodic and cathodic reactions that occur on a steel surface without CP in contact with seawater causing rusting precipitation. Figure 3.2 shows an ICCP system protecting a steel surface exposed to seawater (JAVAHERDASHTI 2013, PALMER 2008, SHREIR 1994).
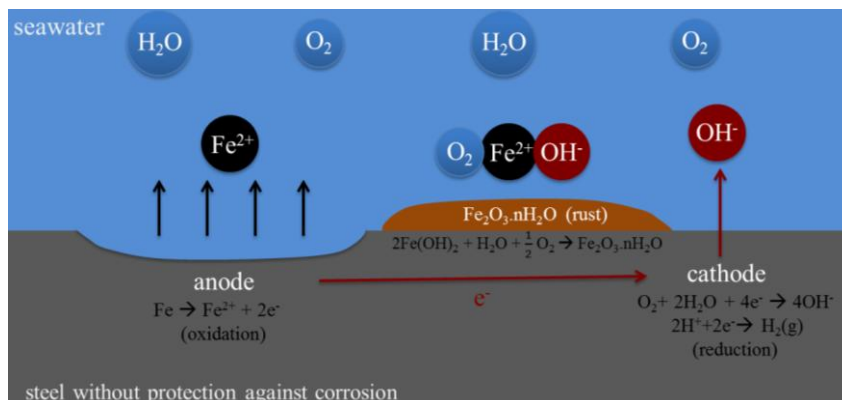


Figure 3.1:    Scheme of rusting on a steel surface without protection.
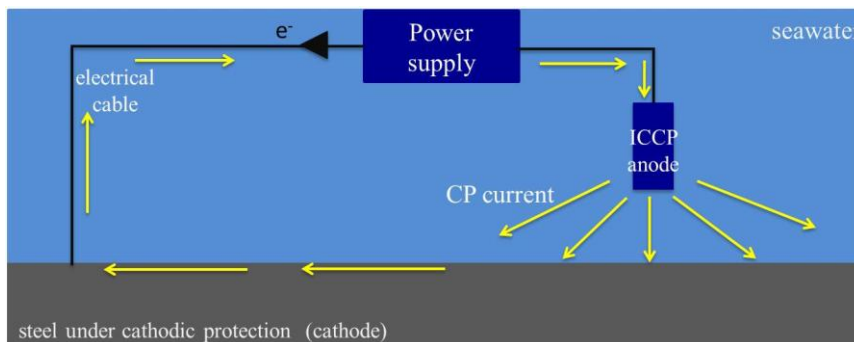


Figure 3.2:    ICCP system acting on steel exposed to seawater (adapted from SHREIR 1994).

A potential of -800 mV against Ag/AgCl reference electrode is advised as CP potential for carbon steels (DNV-RP-B401). However, as mentioned previously, along the time depending on degradation of the coating, the current demand increases and more potential is needed to be applied and some areas may need to be overprotected, but it must

be considered that overprotection can damage the coating (SHREIR 1994). Table 3.6 relates a range of potentials with its impact on a steel pipeline (PALMER 2008).

Table 3.6:    Status of different potentials in steel pipeline (PALMER 2008).

| Steel Potential ($mV_{Ag/AgCl}$) | Cathodic Protection Status |
|---|---|
| -550 | Intense corrosion |
| -551 to -650 | Corrosion |
| -651 to -750 | Some protection |
| -751 to -950 | Zone of cathodic protection |
| -951 to -1050 | Slight over protection |
| -1051 to -1200 | Increased overprotection |
| more than -1200 | Blistering of paint and embrittlement of high strength steels |

The main drawbacks of overprotection are waste of electric power and excessive consumption of anodes. Moreover, the negative potential from -1.05 $V_{Ag/AgCl}$ are not recommended since it can result in a second cathodic reaction showed in Equation 2.6, that can damage the coating and generate hydrogen embrittlement following the equation below (BAI 2005, SCHWEITZER 1983).

$$H_2O + e^- \rightarrow H + OH^- \qquad (2.6)$$

The CP system may not show the best cost-effective corrosion control for very components designed for very long life, becoming impractical unless if applied together with coatings (DNV-RP-B401).

3.4    Sacrificial Anodes

External protection must be used on carbon steel against corrosion (NORSOK M-001). Sacrificial anode is a method to provide electrons to the metal surface as corrosion protection, however it differs from the ICCP system, as an external current source is not required (CHANDLER 1985). Instead, a metal (anode, less noble) is connected with the metal to be protected (cathode, more noble) in order to provide electrical contact producing a galvanic cell. As the anode corrodes, it loses mass and must be periodically repaired/replaced (CHANDLER 1985). The galvanic corrosion happens due the difference of potential between two metals in contact as long as an electrolyte is present, in this case considered to be seawater. The anode supplies ions to the electrolyte and electrons to the cathode, which will become negatively polarised and protected against corrosion. This concept is important when it comes to the building of the steel-galvanic anode system (BAI 2005).

The nobility of metals is specified in ASTM G82-98 and a more compact table is showed in Table 3.7, where the potential is shown according observed in neutral soils and water (GARVERICK 1994). It can be seen that Mg, Zn and Al lead the top of the table as least active material compared to carbon steel. Zinc and aluminium based alloys are the most used anodes on pipelines (ISO 15589-2, BS EN ISO 2063:2005, AWS C2.18-93). Although magnesium is in the top of the galvanic series and provides a higher cell voltage output, it is not usually used for marine structure components due to its shorter life service as it corrodes fast in seawater and only about 50% of its electric current is provided for CP (PALMER 2008).

Table 3.7:    Compact galvanic series of metals and alloys and their potential in neutral soils and water (ASTM G82, GARVERICK 1994, CHANDLER 1985).

| Metal or Alloy | Potential (V) |
|---|---|
| Mg (commercially pure) | -1.75 |
| Magnesium alloys | -1.16 |
| Zinc | -1.1 |
| Aluminium alloy (5% Zn) | -1.05 |
| Al (commercially pure) | -0.8 |
| Carbon steel | -0.5 to -0.8 |
| Cast iron | -0.5 |
| Lead | -0.5 |
| Copper, brass, bronze | -0.2 |
| Carbon, graphite | +0.3 |

There are different types of installation of sacrificial anodes including:

• Bracelet anode: the anodes are attached to the steel equally spaced from each other. The size (mass) and spacing is depending on the current demand desired and other parameters such as environment resistivity (DNV-RP-F103, NORSOK M-503, CHANDLER 1985);

• Stand-off anode: the anode is connected to the steel through electrical cables and a minimum distance of 300 mm is usually recommended. The number of anodes can be mathematically determined based on environment resistivity, anode spacing, anode length, etc. (DNV-RP-F103, NORSOK M-503, CHANDLER 1985, AWWA 2004);

• Coatings: paint and metallic coatings are extensively used by the offshore industry on submerged components. Paint, however, can have its effectiveness affected by ions from three sources - i) electrolytes underneath the film ii) ionogenic elements from the film and iii) electrolytes from water and other exposure sources. Moreover, epoxy paint

is only suitable for submerged steel at $\leq$ 50°C. For high temperatures, the TSA is recommended and will be discussed in item 2.5 (SHREIR 1994, NORSOK M-501).

3.5     Metallic Coatings

Metallic coatings are used in oil and gas industry to isolate the pipeline from the environment such as soil and seawater as well as to provide a resistance path between anodic and cathodic areas (BAI 2005, PALMER 2008, SHREIR 1994).

3.5.1     Thermally Sprayed Coatings (TSC)

Although the high initial cost, the Thermally Sprayed Coating (TSC) was recognised in the early 1980s by its long-term benefits offered for protection of marine and land-base structures as sacrificial coating. TSCs are used for long term protection being expected to last for more than 20 - 40 years for aluminium and zinc TSCs under different exposure environment, and are expect to have a superior performance compared to paint coatings. The type of coating to be applied will depend on the versatility required, however, these coatings can be neutral, cathodic (noble) or anodic (active or sacrificial) and are described below (PAUL 2013, BHATIA 2010, AWS-C2.18-93):

• Neutral*: these coatings (such as alumina, chromium or sprayed polymers) work just as a barrier between steel and environment thus no porosity or scratches are acceptable.

• Cathodic or noble: those (such as nickel alloys, chromium-nickel steels and cooper) work as a barrier for the environment, however the presence of scratches or porosity will accelerate dissolution of the underlying steel through a difference of potential that will be developed (galvanic corrosion).

• Anodic or sacrificial: those coatings - such as cadmium, zinc or aluminium - are less noble metal compared to the steel and are preferably consumed when a galvanic couple is stabilised, offering cathodic protection to steel. In this case, the direction of the current is reversed, causing dissolution of the coating and not the steel substrate.

Defects in coatings detectable by eyes, exposing the steel surface to the environment, are technically named *holidays* and have typically very small cathode-to-anode area ratio (PALMER 2008). The NORSOK M-501 standard defines holiday as a discontinuity in a coating that presents electrical conductivity under specific voltage.

According Gartland[GARTLAND 1990], several properties apart from costs and other must be considered when selecting the TSC to be used in subsea, as follow:

❖ Corrosion potential: desired more electronegative than -800 $mV_{Ag/AgCl}$;

❖ Cathodic current demand at high potentials: in combination with CP, the current flowing through the coating is important to be considered, the lower the better;

❖ Corrosion rate at less negative potentials: ideally must be low enough to keep the component working for at least 30 years;

❖ Corrosion rate at more negative potentials: at high potentials, that overcome the free corrosion potential of the coating, the corrosion rate will increase;

❖ Adhesion strength: if a coating presents poor adhesion to the substrate it will impact on the electrochemical properties in a negative way.

*Thermally Sprayed Aluminium (TSA)*

Aluminum thermal spray system is recommended for seawater immersion such as offshore immersed facilities as well as splash zones platform components (SHREIR 1994, BHATIA 1999).

Thermal sprayed aluminium process is used as anodic coating working as a sacrificial protection for the steel substrate and are widely used as protection for subsea components due the better performance of aluminium in seawater environment compared to zinc as it provides more electricity per unit weight than zinc plus the fact it is less expensive. Moreover, zinc anodes may not be suitable at elevated temperatures in saline mud, where intergranular decohesion at 70°C has been reported (SHREIR 1994). On the other hand, the TSA is suitable for structures submitted to temperatures over 120°C where a minimum of 200 μm coating thickness should be applied (HEIDERSBACH 2011, PAUL 2013, SHRESTHA 2005, PALMER 2008, NORSOK M501).

Three major advantages of thermal spray processes are described below (TUCKER 2013):

\* Versatility: any material that melts without decomposing is acceptable for most of spray devices;

\* Repairing: easy recoating in damaged areas without changing properties or dimensions;

\* Substrate properties: no change in the substrate properties or heating occurs.

The disadvantage of the process is that small or deep cavities are impossible to be

coated as the coating is established only where the gun can clearly aim to (TUCKER 2013).

There are different processes of thermal coating and principle consists on the projection of molten metal on a surface differing on properties and techniques. Processes include: electric arc spray, flame spray, plasma spray, high-velocity oxyfuel, detonation gun deposition and cold spray. When applying metals with low melting temperature like aluminium, the flame spraying or electric arc spraying are the most viable techniques due their cost and application methods (CRAWNER 2013, PAREDES 2006). Proper spray technique and parameters selection is critical for the metallic coating success as poor techniques can lead to coating failure due to lack of adhesion or cohesion, excessive coating porosity or high oxygen content as well as generate an irregular coating thickness along the surface (U.S. ARMY CORPS OF ENGINEERS).

Among the TSA application processes, the arc spray is usually the most economical technique for applying certain types of metal coating including aluminium (BHATIA 2010). Shrestha and Sturgeon estimated the cost of different spray processes considering consumable, labour and power costs relating with application rate and deposition of 1 $m^2$ of coating to a of 250 μm. They concluded that electric arc spray cost is lower compared to other techniques holding a coating cost of 13.52 £.$m^{-2}$ (SHRESTHA 2005).

The process used on samples in this study was the electric arc spray and basically work with two wires being fed together by wires guides in a gun head (scheme is given in Figure 3.3). An electric arc melts the two wires and compressed air atomizes the material accelerating and propelling the molten drops towards the substrate, in a combination of thermal and kinetic energy. The voltage is in the range of 18 – 40 V and DC power supply is used, where one wire is used as cathode and another as anode (BHATIA 1999, CRAWNER 2013).

Some requirements must be matched in order to guarantee the proper adhesion (adhesion requirements will be further discussed in section 2.5.3) and quality of TSA over the steel protection, as (PALMER 2008, SSP-CS 23.00/AWS C2.23M/NACE N$^o$12):

- Surface cleanliness;
- Surface profile;

- Coating adhesion;
- Coating thickness.
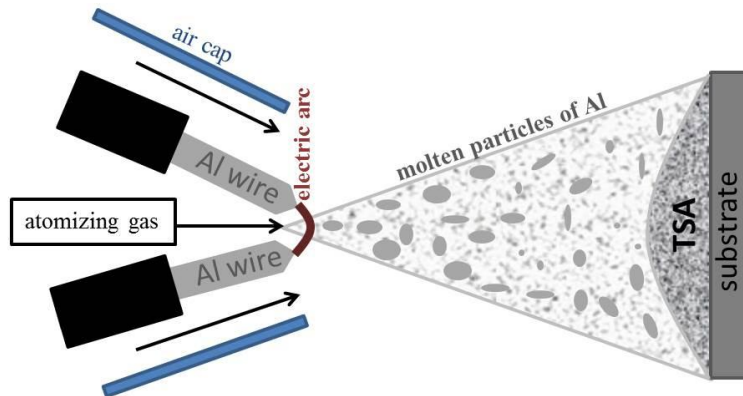


Figure 3.3:    Schematic of electric wire-arc spray gun (adapted from CRAWNER 2013).

Both Al and AlMg alloy show good performance as sacrificial anode under CP (GARTLAND 1990). The standard NORSOK M-501 cites acceptable consumable materials for thermally sprayed metallic coating as aluminium, aluminium alloy with 5% Mg and zinc or alloys of zinc. Table 3.8 shows the composition of Al and Al-Mg consumables in accordance with BS EN ISO 14919 standard. Moreover, Gartland[GARTLAND 1990] highlights that Al-based coatings under CP will not reach a corrosion rate as zero, only stabilizing at a minimum value instead.

Gartland[GARTLAND 1990] carried out tests with different TSA alloys (Al and AlMg) and TSA processes under natural seawater at ~8°C. It was concluded that the 99.6% Al and Al-5% Mg alloy coating performed better over the 85% Zn-15% Al regarding the corrosion rate of samples when exposed for 18 months in free potential and indicated a lifetime over 30 years for a 150 μm of coating thickness. When polarised from approximately -1030 to near -670 mV$_{Ag/AgCl}$ the Al-based coatings also had the best performance showing low corrosion rate until -870 mV$_{Ag/AgCl}$, however corroding fast at -670 mV$_{Ag/AgCl.}$

Table 3.8: Composition for aluminium and aluminium-magnesium alloy for thermal spraying (BS EN ISO 14919).

| Type | Alloying elements mass fraction (%) | | Other elements mass fraction (%) | |
|---|---|---|---|---|
| Al99.5 | Al | ≥ 99.5 | Si | ≤ 0.25 |
| | | | Fe | ≤ 0.40 |
| | | | Ti | ≤ 0.02 |
| | | | Cu | ≤ 0.02 |
| | | | Zn | ≤ 0.07 |
| | | | Mn | ≤ 0.02 |
| | | | other | ≤ 0.03 |
| AlMg5 | Mg | 4.5 to 5.6 | Si | ≤ 0.30 |
| | Mn | 0.05 to 0.2 | Fe | ≤ 0.40 |
| | Cr | 0.05 to 0.2 | Cu | ≤ 0.10 |
| | Ti | 0.06 to 0.2 | Zn | ≤ 0.10 |
| | Al | balance | other | ≤ 0.15 |

### 3.5.2 Sealants

Aluminium coatings applied by arc-spray can present porosity between 4 -14%. Sealer is recommended on TSA to fill porosities and prevent penetration of corrosive substance within the coating. It has been reported that TSA coatings can perform better when sealed with organic or semi-organic silicon sealers; however it will increase the cost of the coating process (NORSOK M-501, FAUCHAIS 2012). It has already been reported that inappropriate sealing and inappropriate TSA thickness can result in blisters and failures of the coating when under certain circumstances (THOMASON 2004).

Sealant must be a penetrating material (viscosity ≤ 3 poise) in order to fill the pores and are usually applied by spraying, brushing, or dipping and are either air cured or cured at elevated temperature (KNAPP 2013, PAUL 2013). According to AWS C2.18-93, a heat-resistant aluminium paint or equivalent is recommended for components operating in temperatures above 80ºC, while NORSOK M-501 mentions that aluminium-silicone may be applied on TSA in carbon steel surfaces submitted to T >120ºC. However NACE standard practice defines sealer as an optional part of the process (NACE 12/AWS C2.23M/SSPC CS-23). Moreover, it must be ideally applied no longer than 24 h after spraying to avoid contamination. The sealant thickness varies from few to several tens of micrometres and thicker than 40 μm is not recommended for submarine applications since the sealant can then contain defects such as pores and also retain moistures decreasing the system shelf life (PAUL 2013, BHATIA 2010, NACE 12/AWS C2.23M/SSPC CS-23).

Gartland[(GARTLAND 1990)] compared the effect of silicon sealer on different TSA composition (including Al and AlMg) and process for eleven months. It was found that between 4 to 6 months, the sealing decreases the current demand of the system at free potential, being reduced to a factor of 2-3 compared with unsealed specimen. However, under high potentials (from -1100 to -700 mV$_{,Ag/AgCl}$), small difference on coating performance with the presence of sealant could be observed. Bhatia[(BHATIA 1999)] mentions that TSA may perform better in seawater environment when no organic sealing is applied and also that thermal spray coatings are self-sealing as, over the time, the corrosion products involved in corrosion process will fill the coating porous.

### 3.5.3  Adherence

The success of the thermal spray coating relies on its adhesion (U.S. ARMY CORPS OF ENGINEERS).  Lack of good adherence between the coating and the submerged pipeline leading to external corrosion and leaking of crude oil has already been reported (HEIDERSBACH 2011). Poor adhesion between steel surface and coating may also lead to completely or partly detachment of the coating during storage (DNV-OS-F101). The adherence of the spray deposit to the substrate is named *bond* and it may be either mechanical or metallurgical, or a combination of both (UNITED STATES NAVY):

- Mechanical bond: the thermally sprayed particles adhere to the rough surface by particle interlocking;

- Metallurgical bond: the adherence of the thermally sprayed particles happens by diffusion of atoms across the interface.

Adhesion deficiency can be result of bad spray parameters selection such as standoff distance and spray angle. Adhesion depends on the kinetics energy of the coating particles; therefore an excessive distance between the gun and the surface to be coated may reduce the coating adhesion to the substrate (U.S. ARMY CORPS OF ENGINEERS).

Areas of non-effective adherence can appear as blister, loose particles, cracks or chips. Surface cleaning and abrasive blasting plays an important role to provide a proper surface to receive the sprayed coating, resulting in possible premature failure if applied over rust, dirt, grease or oil (UNITED STATES NAVY, U.S. ARMY CORPS OF ENGINEERS).

Thermal spray coatings have been reported as materials with good adherence characteristics (ILIESCU 2008). Wire-arc spray adherence on steel is usually over 20 MPa and very little heating is transferred to the substrate (FAUCHAIS 2012).

3.6     Corrosion Behaviour of Aluminium

Aluminium presents high corrosion resistance in different environments as fresh waters, seawater and soils having a wide range of applications due the formation of a protective film that provides passivity (DAVIS 1999).

In contact with water the aluminium develops the anodic reaction showed in Equation 2.7. The cathodic reaction follows the already mentioned Equation 2.2 (oxygen reduction) and $2H + 2e^- \rightarrow H_2$                    (2.3) (hydrogen evolution) (SUKIMAN 2012).

Anodic:

$$Al \rightarrow Al^{3+} + 3e^- \tag{2.7}$$

Aluminium is high reactive metal following beryllium and magnesium and its corrosion behaviour is dependent of the temperature. When the aluminium surface is in contact with air or water, an adherent surface film of aluminium oxide is promptly formed (GHALI 2010). Low temperatures ($< 4°C$) will corrode aluminium slowly compared to room temperature.  However, temperatures between 70 and 80°C will corrode more severally than temperatures of 20 or 100°C. At 200°C pure aluminium in pure water is completely converted into aluminium oxide in few days. Usually, at ~230°C the barrier layer cannot be repaired allowing the aluminium to be converted into oxide in a fast reaction (GHALI 2010, DAVIS 1999).

The $Al_2O_3$ (alumina) is formed when the surface in in contact with air at ambient temperature is very thin (2 to 4 nm) and has high oxidation resistance with the slowest transport rates for metal and oxygen ions (REVIE 2011, DAVIS 1999). Such layer is strongly adherent to the surface and has the ability to re-form when broken. Under some conditions such as the presence of chloride ions this repair will be retarded or even not possible allowing corrosion to occur (DAVIS 1999, REINHART 1976).

The oxide barrier is usually composed of two layers: an inner dense amorphous layer adjacent to the aluminium surface which thickness will vary with the temperature and the external layer is a thicker and porous layer of hydrate oxide, as showed in Figure 3.4 (DAVIS 1999).
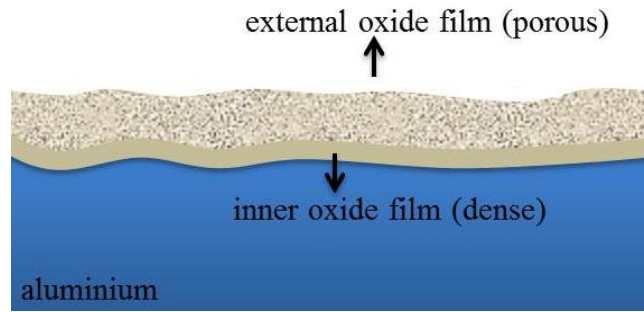
Figure 3.4:   Scheme of morphology of the natural oxide layer formed on aluminium surface (adapted from DAVIS 1999).

Two opposite forces acting on the metal surface: the one willing to form the protective film against the one willing to break it. If destructive forces are not present, like in exposition to air, the film will be present. If destructive forces are present, the oxide layer will be hydrated faster than it can grow, and small film will remain. In cases where the equilibrium is reached, a reasonable thick film will take place (20 to 200 nm or 200 to 2000 Å) (DAVIS 1999, LORKING 1961).

The aluminium oxide ($Al_2O_3$) is amphoteric, i.e. corrodes in both alkaline and acidic environment as shown in Equations 2.8 and 2.9 respectively (DAVIS 1999, GHALI 2010):

$$2Al + 6H_2O + 2OH^- = 2AlOH_4^- + 3H_2 \qquad (2.8)$$

$$2Al + 6H^+ = 2Al^{3+} + 3H_2 \qquad (2.9)$$
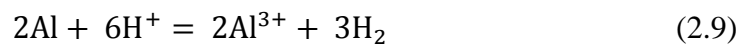
The aluminium thermodynamic stability of the oxide film is found in Pourbaix diagram (Figure 3.5). When the oxide barrier provides protection, it is expressed by passivity area, what happens in pH 4 to 8.5. However, this limitation are given at 25°C and will vary with temperature and also with the specific oxide barrier formed as well as the presence of substances that can form soluble or insoluble salts with aluminium. Above that range the aluminium is supposed to suffer corrosion because its oxides are soluble in some acids (where it produces $Al^{3+}$ ions) and alkalis (where its produces $AlO_2^-$ ions). However, beyond the passive area the corrosion may not occur as long as the oxide layer formed is insoluble or if it is continuously oxidized by the solution. Thus, the corrosion cannot be predicted only by the pH as other elements interact with the metal in the same time. Although E-pH diagrams seem a straightforward prediction of corrosion process, the reactions that lead to metal corrosion depend on more factors apart from pH like i) alloying elements in the metal ii) ions present in the solution such as chloride iii) temperature and iv) type of corrosion and v) rate of reaction (DAVIS 1999, SUKIMAN 2012).

In the passive zone the aluminium is protected by oxides or hydroxides. When in contact with water, the $Al_2O_3$ film hydrolyses and produces hydrate oxide, which are not stable and suffer a process called ageing. Below 70°C the form $Al_2O_3.3H_2O$ (bayerite) or $Al(OH)_3$ (gibbsite or hydrargillite) will appear while above 100°C the $Al_2O_3.H_2O$ or AlOOH (boehmite) can happen (GHALI 2010, DAVID 1999). Four conditions are needed to be fulfilled in order to breakdown of passivity happen (REVIE 2011):

✓ Critical potential: critical potential must be exceeded ($E_{bd}$);

✓ Damaging species: presence of chloride or certain halides for example;

✓ Time: time for initiation of the breakdown process and localized corrosion density to increase;

✓ Local sites: highly localized sites are needed for the breakdown occur.
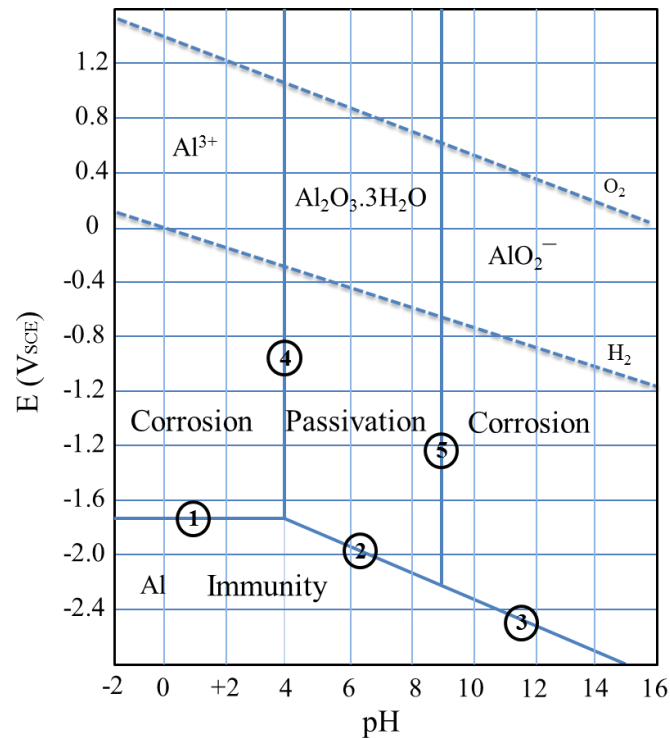


Figure 3.5:  Pourbaix diagram for aluminium exposed to water at 25°C, predicting protection by oxide layer of bayerite (adapted from DAVIS 1999 and GHALI 2010).

The numbered lines limiting areas in Figure 3.5 represent the following reactions respectively showed in Equations 2.10 to 2.14 (GHALI 2010):

$$\textbf{(1)} \qquad Al^{3+} + 3e^- \rightarrow Al \qquad\qquad (2.10)$$

$$\textbf{(2)} \quad Al(OH)_3 + 3H^+ + 3e^- = Al + 3H_2O \qquad\qquad (2.11)$$

$$\textbf{(3)} \qquad Al(OH)_4^- + 3e^- = Al + 4OH^- \qquad\qquad (2.12)$$

$$(\textbf{4}) \quad Al(OH)_3 + 3H^+ = Al^{3+} + 3H_2O \hspace{3cm} (2.13)$$

$$(\textbf{5}) \quad Al(OH)_3 + OH^- = Al(OH)_4^- \hspace{3cm} (2.14)$$
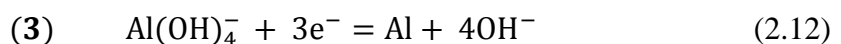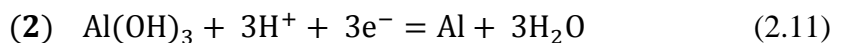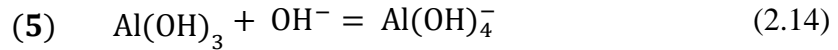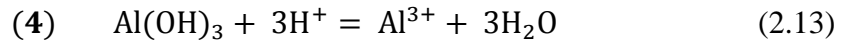
In seawater, aluminium alloys usually present rates of pitting between 3 - 6 µm/year in the first year, decreasing to 0.8 - 1.5 µm/year in 10 years period and this behaviour is due the fact that older pits become inactive along the time and in deep seawater the behaviour do not tend to change compared to the surface. The pity density of aluminium increases with water temperature while the depth of the pits decreases with temperature (REVIE 2011, REINHART 1976). The Al-Mg alloys hold high corrosion resistance to seawater and its use is common in marine applications (GHALI 2010).

In soil environment the corrosion rate of aluminium alloys vary depending on the soil composition and climatic changes. In dry sandy soil the corrosion is negligible while in wet and acid/alkaline, it tends to be severe. However, past corrosion studies showed that some aluminium alloys exposed to well-drained soil was still mild after 5 years while other was severely attacked but still not much as steel (REVIE 2011).

## 3.7    Calcareous Deposit

Calcareous deposit is a thin film formed on the steel surface when CP is applied in seawater environment. It reduces the demand of current density necessary to maintain the protective potential as well as improve its distribution along the metal surface (ISO 15589-2).  In cold seawater, the scales will form slowly and need high current density to develop while in warmer environment it is formed promptly (PALMER 2008).  Coatings are favourable for the formation of calcareous deposit since the initial current density is higher when defects take place. The deposit might not form under cold waters, as the solubility of those elements is temperature is dependent, unless higher initial current are provided (ISO 15589-2, PALMER 2008). The film may be damaged by storm action for example, increasing the current density demand temporarily, but soon the layer is restored allowing lower current demand (SHREIR 1994).

Although cathodic deposits are termed "calcareous deposit", it is wrong to assume that it is only composed by calcium. It is generally accepted that it is formed by an inner layer of magnesium compost, in particular as $Mg(OH)_2$ named brucite, and an outer layer of calcium compound, usually $CaCO_3$ in form of calcite and aragonite (HARTT 1984, BARCHICHE 2003, SHREIR 1994, NEVILLE 2002, YAN 2015).

The steel polarisation develops two main scenarios: the increase on concentration of hydroxyl ions on the interface metal surface/seawater previously mentioned, and the change in calco-carbonate system. The former allows the precipitation of magnesium hydroxide as long as the pH reaches the minimum 9.5 when in room temperature, following Equation 2.15 (BARCHICHE 2004, DESLOUIS 1997, PALMER 2008, SALGAVO 2003, NEVILLE 2002, SHREIR 1994). The high pH is required since seawater is usually unsaturated of $Mg(OH)_2$ (MOLLER 2006). Therefore, the presence of this compost is related either with high current densities or poor seawater renewal (SHREIR 1994).

$$Mg^{2+} + 2OH^- \rightarrow Mg(OH)_2 \qquad (2.15)$$
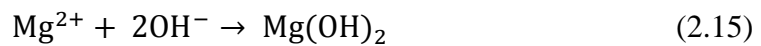
The calco-carbonate equilibrium (Equation 2.16) is also affected by the increasing on $OH^-$ concentration as it will dislocate the equilibrium to the right where the formation of carbonate is favoured where the formation of $CaCO_3$ is likely to happen (following Equation 2.17) when the minimum pH 7.5 is reached (HARTT 1984, PALMER 2008, SHREIR 1994, SALGAVO 2003, NEVILLE 2002, BARCHICHE 2003, AKAMINE 2002). The lower pH is enough for its precipitation because calcium carbonate is supersaturated in seawater under near surface conditions (MOLLER 2006).

$$OH^- + HCO_3^- \rightarrow H_2O + CO_3^{2-} \qquad (2.16)$$

$$Ca^{2+} + CO_3^{2-} \rightleftharpoons CaCO_3 \qquad (2.17)$$
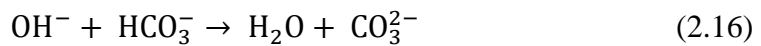
The pH profile surrounding the steel surface is represented in Figure 3.6. The pH is related to the ($OH^-$) production at the interface metal/electrolyte and its extraction via diffusion and/or convection to the solution (HARTT 1984).

Those pH values given at room temperature, however, are mainly acquired through calculations such as modelling approaches, having few experimental data available in literature so far, especially over 30°C.

Dexter and Lin[DEXTER 1992] studied the local pH of a cathodically polarised steel in $NaCl/NaHCO_3$ solution containing the same ionic strength and buffering capacity as the seawater. Values obtained from modelling and experimental procedures were compared against each other. The experiment consisted of collecting the data through microelectrode technique and applying currents of 0,20 and 100 $\mu A/cm^2$. The modelling gave a local pH high as 9.9, while the test value was ~10.2 under the highest current density. This

difference, according to the authors, is related to the distance of the micro-pH electrode from the steel surface, estimated in 50 and 100 μm while the modelling gave values right at the steel surface. Moreover, the modelling did not consider the hydrogen evolution, only the oxygen reduction as cathodic reaction. Salgavo et. al.[SALGAVO 2003] run a test using a sample of 600 (UNS N06600) cathodically polarised to -0.8 to -1.2V (Ag/AgCl) in natural seawater at temperatures between 13 and 27°C. Here the probe was 1 mm distant from the metal surface and the localised pH reached a maximum value of 10.7 at -1.2V (Ag/AgCl). Lewandowski et. al.[LEWANDOWSKI 1989] studied the local pH on a 304 stainless steel (AISI 304SS) surface in synthetic seawater at room temperature and the maximum pH value was 9.5. The distance between the pH microelectrode and the stainless steel surface was not mentioned.

Thus, the above comparison indicates that the interfacial pH steel-seawater varies with the cathodic polarisation, leading to the formation of the calcareous deposit.
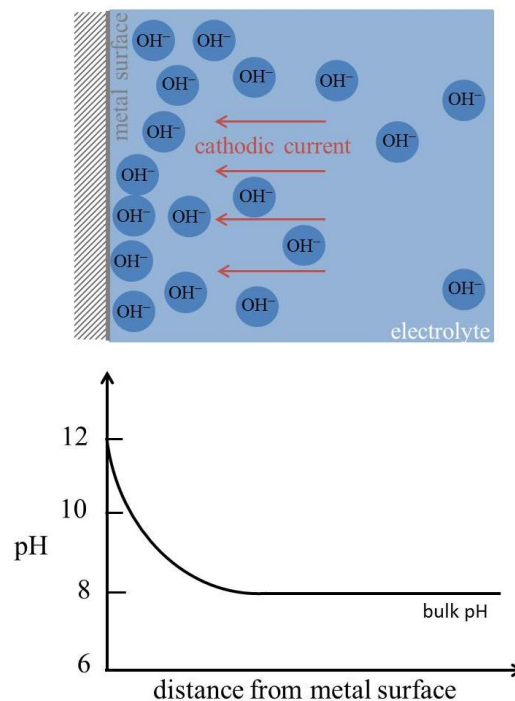


Figure 3.6:  Scheme of change in pH outward a cathodic protected metal surface (adapted from HARTT 1984).

The presence of aragonite rather than calcite is more common due the fact calcite has its precipitation and crystal growth easily inhibited by the presence of magnesium in solution, what also retards the precipitation of aragonite, however once aragonite nucleates magnesium does not affect it growth (HARTT 1984, NEVILLE 2002). Both aragonite and calcite are supersaturated in deep water as higher pressure and lower pH favours its

solubility and the Ca:Mg ratios depends on the ratio of those anions in seawater (HARTT 1984).

Calcareous deposits will precipitate when the solubility of calcium and magnesium compounds exceeds its solubility product (SHIFLER 2004, NEVILLE 2002). Solubility product ($K_{sp}$) is the equilibrium constant of a slightly soluble compound dissolved in a saturated solution, calculated from the product of the concentration of the anions involved raised to the power of their stoichiometric coefficients (PERRY 1997).

Table 3.9 compares solubility values of the main calcareous composts in water at lower and higher temperatures (temperatures are those approximate to the ones used in this study due to lack of data at 30, 60 and 90°C). It can be noticed that the solubility of $Mg(OH)_2$ decreases until ~75°C but it is increased at 100°C. The values given show that until ~75°C the $Mg(OH)_2$ is more favourable to precipitate due its lower solubility and at 100°C the $CaCO_3$ has the preference. The $CaCO_3$ presents a behaviour called *retrograde solubility* since its solubility is higher at low temperatures (LIBES 2009). Table 3.10 shows the respective $K_{sp}$ at 25°C. However, as mentioned previously, the deposition process is complex and another factors acting together must be considered and deeper studied. Interaction of other ions such as $SO_4^{2-}$ is believed to hinder the deposition of $CaCO_3$ under low temperature facilitating the precipitation of Mg-containing layer by a mechanism not well understood (BARCHICHE 2004, BARCHICHE 2009). Also, for the precipitation of a compound to occur, the ionic product of the ions involved must exceed its $K_{sp}$, where the compost will be then saturated (TAN 2011).

Table 3.9:  Solubility of $CaCO_3$ and $Mg(OH)_2$ at different temperatures (WEST 1995, PERRY 1997).

| Compound | Temperature (°C) | Solubility (g per 100 ml) |
|---|---|---|
| CaCO₃ | 25°C | 0.0153 |
| | 75°C | 0.0019 |
| | 100 °C | 0.0020 |
| Mg(OH)₂ | 35°C | 0.00098 |
| | 72°C | 0.00069 |
| | 100 °C | 0.0040 |

Table 3.10: Solubility product of $CaCO_3$ and $Mg(OH)_2$ at 25°C (DODD 1990, LIDE 2006, MYERSON 2001).

| Compound | $K_{ps,25°C}$ |
|---|---|
| $CaCO_3$ (aragonite) | $6.0 \times 10^{-9}$ |
| $CaCO_3$ (calcite) | $3.36 \times 10^{-9}$ |
| $Mg(OH)_2$ | $5.61 \times 10^{-12}$ |

Summarizing, deposition of calcareous deposit evolves when three main steps take place (NEVILLE 2002):

- Increase in interfacial pH by formation of hydroxyl ions;

- Increase in carbonate ion concentration;

- Precipitation of compound that exceeds its solubility product ($CaCO_3$ and $Mg(OH)_2$).

The level of saturation of carbonate and hydroxides in seawater depends on several factors such as temperature, pressure, salinity and pH and it is already known that scales form faster under higher temperatures (PALMER 2008, HARTT 1984). However, most of studies so far do not comprise data regarding calcareous deposit formation over 60°C seawater. Therefore, there is a lack in literature regarding pipelines exposed to high temperatures that is important to address, as it influences diffusion, reaction kinetics, solubility, among others (HARTT 1984, BARCHICHE 2004, BARCHICHE 2003, AKAMINE 2003, DESLOUIS 1997, MOLLER 2006, BERNER 1975, ROUSSEAU 2010).

### 3.7.1 Morphology of Calcareous Deposit

It is reported in literature that brucite provides a much less effective protection compared to aragonite or calcite due its porous aspect which facilitates the oxygen diffusion towards the steel surface (PALMER 2008, CHENGJIE 2014), however this matter will be further questioned in this study. A deeper insight in calcareous deposit morphology is necessary to understand its effects over cathodically protected steel under different parameters as various factors such as temperature, pH, applied potential, among others, influence on its morphology and therefore its protective properties (NEVILLE 2002, MOLLER 2006).

Barchiche et. al.[BARCHICHE 2003] verified the influence of different potentials and presence of $Mg^{2+}$ in artificial seawater at 20°C and monitored by chronoamperometric

technique. The $CaCO_3$ was formed in both aragonite and calcite structures between -900 to -1100 $mV_{SCE}$. Aragonite was seen as caulifower form (or needles) and calcite as cubic crystals. At more negative potential (-1300 $mV_{SCE}$) only an homogeneous brucite layer was deposited. Both $Mg(OH)_2$ and $CaCO_3$ under -1200 $mV_{SCE}$. When the solution was enriched with $Mg^{2+}$, no calcite was observed. In further study carried out by Barchiche et. al[BARCHICHE 2004] where it was reported the influence of different parameters on calcareous deposit growth including temperature. It was observed presence of aragonite (needles shape) at 10°C and 30°C under -1000 $mV_{SCE}$. When under more negative potential (-1200 $mV_{SCE}$) at 20°C brucite was observed as a compact layer, similar to his previous work, after a bit more than 100 h of exposure. In both studies, the protective status of the deposits were confirmed by the decreasing in current demand over the specimens. Same morphologies of $CaCO_3$ (calcite and aragonite) were registered by Deslouis[DESLOUIS 1997] when samples were tested under artificial seawater but lacking $MgCl_2$ and potential range of -800 to -1200 $mV_{SCE}$. Again, when magnesium was not present, calcite growth was favourable. Same characteristics were found in Neville et. al[NEVILLE 2002]'s study where the growth of calcareous deposit on steel surface under cathodic protection of -1000 mV in artificial seawater was monitored. After 3 days, needle aragonite and cubic calcite were observed.

Chengje et. al.[CHENGJIE 2014] found brucite as needle structure when studying the calcareous deposits formed on the steel surface when under cathodic protection at 25°C under free potential, which was possible to be observed due to the breaking of the external protective layer ($CaCO_3$) exposing its internal brucite layer.

## 3.8    General Effect of Temperature

Temperature influences the corrosion rate of the metal and deposition of calcareous deposit: at higher temperatures the calcareous deposit will mainly consist of $Mg(OH)_2$ and at low temperature it consists of both $CaCO_3$ and $Mg(OH)_2$. It alters gases diffusion and reactions kinetics as well as the physicochemical properties at the metal interface. It is accepted that each 10°C rise in solution temperature double the corrosion rate and increase ions diffusion on steel surface. Moreover, the rate of oxidation and the type of oxide scales will depend on the steel alloy, temperature and oxygen pressure (GHALI 2010, PALMER 2008).

The temperature range of seawater at the surface varies between -2 to 35°C and although it is expected the rise in temperature to increase corrosion, this may not always

happen. Thus, steel immersed in tropical seawater not necessarily will present corrosion rate greater than if in temperate environment. In this case, other factors have influence, for example the difference in oxygen content and less marine growth in colder waters. In general, along the seawater temperature range, a reasonable linear relation of doubling the corrosion rate for a rise around 10°C is applied as mentioned previously, however in practice that may be not true (SCHWEITZER 1983, CHANDLER 1985).

Barchiche et. al.[BARCHICHE 2004] obtained corrosion rate curves from steel exposed to seawater at 10, 20 and 30°C under -1000 mV. It was found that the corrosion rate reached almost zero at 20 and 30°C what did not happen at 0 to 10°C, although low corrosion was presented. Also, it was observed that the formation of calcareous deposit was strongly slowed down at 10°C, coming up that the effect of temperature was more effective below 20°C, however this conclusion is referent to this study conducted with specific conditions applied.

On aluminium, the increasing in temperature usually leads to higher corrosion rates in the most of environments including alkaline solutions. The temperature also affects the galvanic corrosion, as the corrosion potential for some alloys will change (DAVIS 1999).

In the case thermal cycling is occurring, it will stress the coating, however thermal sprayed metal coatings are proved to have coefficients of expansion similar to the substrate (carbon steel) and thus no failure tends to happen (BHATIA 1999). The same may not happen with the scales layers, which can suffer cracking and flaking either by stresses due to differential expansion of scale and underlying metal, or by dimensional changes associated with the phase changes in the metal or in the scale. If that is the case, higher corrosion rate will happen (SHREIR 1994).

In addition, literature also reports that the exploitation of oil and gas in deeper seas will results in crude oil in wells at temperatures up to 200 - 300°C and, according to studies, the relationship between the operating temperature on steel surface and the required current density for cathodic protection in seawater is still lacking, and thus more study in this area needs to be developed (GARVERICK 1994, PALMER 2008).

# 4        EXPERIMENTAL PROCEDURE

## 4.1      Experimental

The tests consisted of two main experiments i) expose samples to synthetic seawater at different steady temperatures and ii) expose samples (in buried and unburied conditions) under a thermal gradient.

## 4.2      Exposure Samples Preparation

Steel samples were prepared for the exposure tests as described from item 3.2.1 to 3.2.5.

## 4.2.1      Substrate

Corrosion tests were carried out in carbon-manganese steel (S355J2+N) samples (40x40x7 mm, composition given in Table 4.1) coated with TSA. Previously to the coating process, the samples had their surfaces degreased in order to avoid contaminants and abrasive-blasted at 80 psi with NK36 alumina to provide better adherence.

Table 4.1:     Composition of S355J2+N steel.

| (% m/m) | | | | | | | | | | | | | | |
|------|------|------|------|------|------|------|------|------|------|------|------|------|------|------|
| Fe | Ni | Cr | Mo | Cu | Ti | Mn | Si | Al | Nb | C | P | S | V | N |
| Bal | 0.018 | 0.052 | 0.003 | 0.035 | 0.001 | 1.40 | 0.289 | 0.031 | 0.001 | 0.14 | 0.024 | 0.018 | 0.043 | 0.003 |

## 4.2.2      Coating

Twin wire arc spray system (TWAS) was used for deposition of the aluminium. Two types of TSA-coating composition were used: 99,5% Al (commercially pure aluminium) and Al-5%Mg, which were applied on steel substrate through a twin wire arc spray gun. Chemical composition of the Al-wires and process parameters are shown in Table 4.2 and Table 4.3 respectively. In order to simplify, the composition will be further indicated as Al and AlMg in this thesis. Figure 4.1 shows a micrograph in cross section of a sample after the TSA coating process with a nominal thickness of 300 µm.

Table 4.2:    Chemical composition of Al and AlMg wires used for coating (% m/m).

|      | Si   | Fe   | Cu    | Mg   | Mn    | Ni    | Cr   | Ti   | Pb   | Sn   | Zn   | Zr    | Al   |
|------|------|------|-------|------|-------|-------|------|------|------|------|------|-------|------|
| Al   | 0.07 | 0.21 | <0.01 | -    | <0.01 | -     | -    | -    | -    | -    | -    | -     | bal. |
| AlMg | 0.11 | 0.13 | <0.01 | 4.94 | 0.12  | <0.01 | 0.11 | 0.08 | 0.01 | 0.02 | 0.16 | <0.01 | bal. |

Table 4.3:    TSA coating parameters.

| Element | Parameter |
|---------|-----------|
| Equipment | Metallisation - Arc 528 |
| Wire size | 2.3 nm |
| Wire feed rate | 98.7 g/min |
| Spray distance | 95 mm |
| Thickness range | 250 – 300 µm |
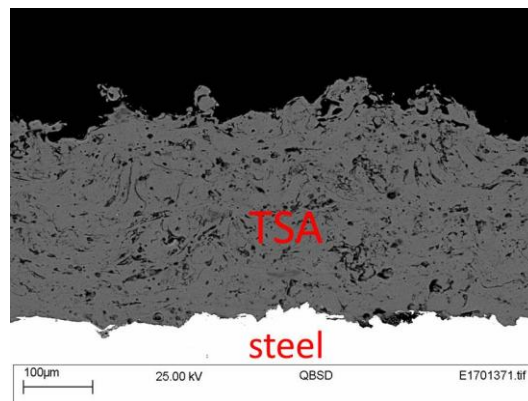


Figure 4.1:    Cross-section of a sample TSA-coated with a nominal thickness of 300 µm.

4.2.3    Sealing

Aluminium-silicon sealing was applied in eight samples for the thermal gradient test following specifications of NACE No. 12/AWS C2.23M/SSPC CS-23 Standard Practice. The layer was applied by brushing technique and sealers were cured for approximately 24 h at room temperature. Figure 4.2 shows a cross section micrography of a sealed TSA-coated sample. The sealing was measured as 30 - 50 µm.
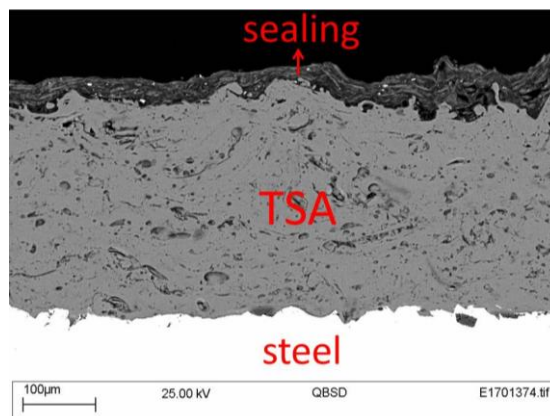


Figure 4.2:    Cross-section of a sample TSA-coated with a nominal thickness of 300 µm with aluminium-silicon sealer applied.

### 4.2.4    Holiday

Holidays were made with different diameter drillers in order to expose the steel substrate. The coating was machined about 0.8 mm depth exposing 5, 10 or 20% of the front surface area of the carbon steel substrate.

### 4.2.5    Specimens Previous to Exposure

The back and edges of the samples were covered with belzona 1591 resin in order to isolate the part of the sample not TSA sprayed, avoiding its influence on the measurements. A M4 hole was tapped in one of the side faces of each sample in order to introduce the stainless steel rod that would be further connected to electrochemical wires. Belzona 1591 resin covered the interface along the steel and the rod to avoid crevice corrosion and a polymeric cap covered the whole extension of the rod to prevent its influence in the results. Figure 4.3 shows unsealed TSA-coated samples with holiday before exposure tests at 30, 60 and 90ºC.



|  |  |  |
|:---:|:---:|:---:|
| a) | b) | c) |
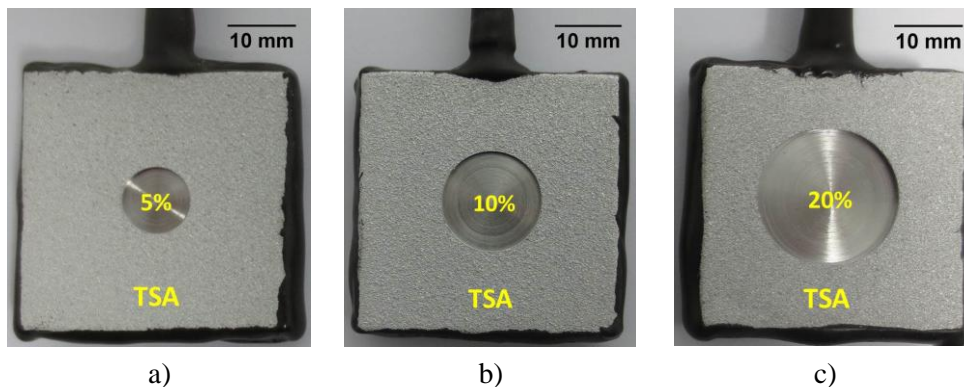
Figure 4.3:    Coated metallic samples prior to the exposure: a) sample with 5% holiday, b) sample with 10% holiday and c) sample with 20% holiday.

Figure 4.4a shows one of the samples prepared for the thermal gradient experiment where in total sixteen samples (Ø25 x 16 mm) TSA-coated (unsealed and sealed) with 5% holiday were used. Two samples (T1 and T2) were specifically used only for the temperature measurement and connected with two thermocouples (TC) as showed in Figure 4.4b where one buried and one unburied sample was monitored.

|  | a) | | b) |
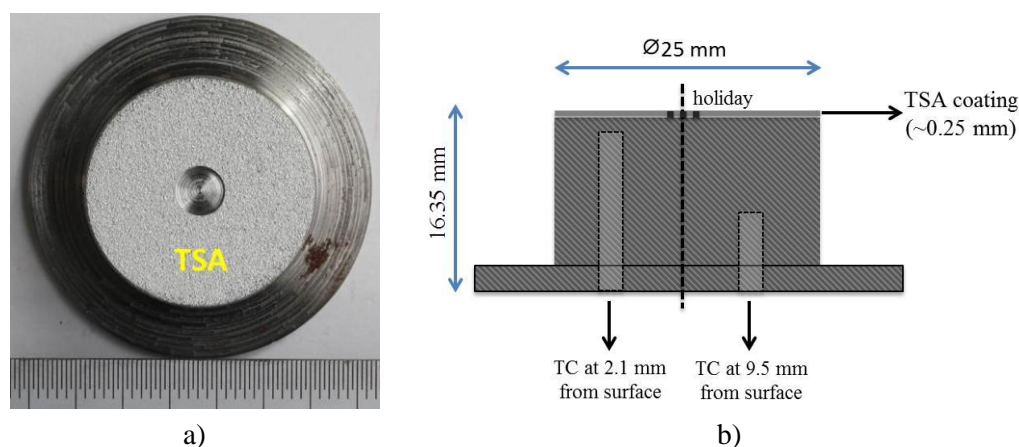
Figure 4.4:    Sample used in the part II experiments: a) steel substrate TSA coated with 5% holiday; b) scheme showing samples dimensions and the thermocouple holes made in T1 and T2 samples.

## 4.3    Exposure Test Arrangements

Exposure tests were performed at steady temperatures of 30, 60 and 90°C and under thermal gradient. Description of the arrangement and monitoring techniques are given in items 4.3.1 and 4.3.2.

### 4.3.1    Steady Temperature Tests

The solution used in corrosion tests was synthetic seawater (ASTM D1141) which composition is given in Table 4.4 and three separated tests were run under different temperature: 30, 60 and 90°C. In total 18 samples were used, where 6 samples were introduced together in each electrochemical cell (see scheme in Figure 4.5). The synthetic seawater is initially filled in a previous tank apart from the electrochemical cell. A level was set up in order to control the loss of solution by evaporation and pumpers controlled the water flow.

Table 4.4:    Synthetic seawater composition (ASTM D1141).

| Compound | NaCl | $MgCl_2$ | $Na_2SO_4$ | $CaCl_2$ | KCl | $NaHCO_3$ | KBr | $H_3BO_3$ | $SrCl_2$ | NaF |
|---|---|---|---|---|---|---|---|---|---|---|
| Concentration (g/L) | 24.53 | 5.20 | 4.09 | 1.16 | 0.695 | 0.201 | 0.101 | 0.027 | 0.025 | 0.003 |
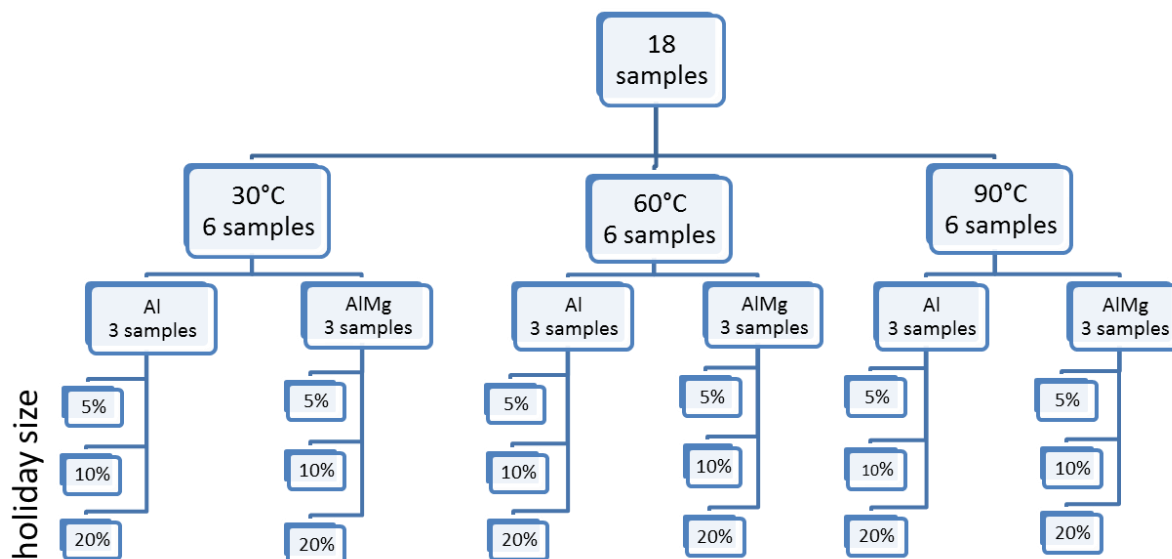
Figure 4.5: Flowchart of the division of samples among experiments at steady temperatures.

The water temperature control was made through one inside heater the cell connected to two thermocouples: one for the heater and another one for the water temperature control, which were displayed in a heater instrument.

The tests were run in free potential ($E_{corr}$) for up to 145 days under atmospheric pressure. Figure 4.6 show the arrangement of samples inside the electrochemical cell. The measurements were collected simultaneously from each sample and silver/ silver chloride (Ag/AgCl, KCl saturated) reference electrodes were used, which were calibrated previous to the experiment and kept outside the electrochemical cell connected to the synthetic seawater through salt bridge. Platinised titanium (PtTi) wire electrode was used as auxiliary electrode (AE), which was positioned close to each sample (one per sample).
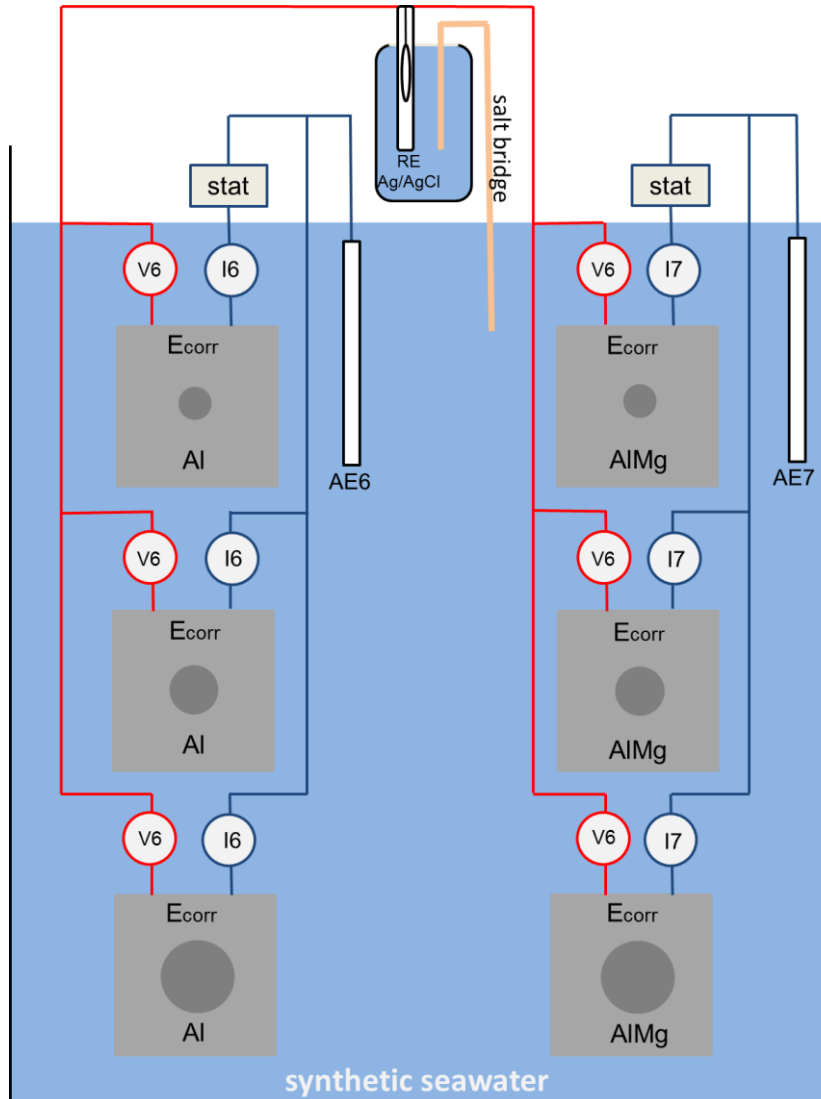
Figure 4.6: Arrangement of metallic samples connected with auxiliary electrodes (AE) and silver chloride electrode (Ag/AgCl) for free potential tests. The V6 and I7 correspond to the voltage and current paths respectively.

## 4.3.2 Thermal Gradient Test

In the thermal gradient experiment an internal high temperature was combined with an external low temperature. It consisted in a polymeric tower centred inside a tank which was filled with hot oil at ~125°C.  The specimens were attached at the walls of the tower by screws and polymeric resin (belzona 1591), having their surfaces exposed to the external environment: either synthetic seawater (Table 4.4) at ~10°C or synthetic sand. The latter is mainly composed by silica matter (higher than 97%) having water content lower than 0.1% (typical composition is specified in Table 4.5), following the requirements from ASTM C778-06 standard. The test was conducted under atmospheric pressure. The pH of the seawater was 8.2 previous to the test starting. Figure 4.7 shows the

arrangements of the experiment in the oil tower and Figure 4.8 shows the experiment tank external to the oil tower.

Table 4.5:    Typical composition of synthetic sand (AGSO).

| Element | Content |
|---|---|
| Silica ($SiO_2$) | 99.80% |
| Aluminium Oxide ($Al2O_3$) | 0.04% |
| Iron Oxide ($Fe_2O_3$) | 0.03% |
| Titanium Dioxide ($TiO_2$) | 0.005% |
| Calcium Oxide (CaO) | 0.01% |
| Magnesium Oxide (MgO) | 0.006% |
| Potassium Oxide ($K_2O$) | 0.01% |
| Sodium Oxide ($Na_2O$) | 0.004% |

Eight samples were kept under free potential and monitored by LPR technique as described in item 4.4 while eight of them had potential applied. Reference electrodes (Ag/AgCl, KCl saturated) were kept outside the tank connected to the solution through salt bridge. The other half was submitted to the Potentiostatic Polarisation technique. Samples were duplicated.

Samples were distributed within the test with four different conditions: potential applied, surrounding environment and presence of sealant (Table 4.6). Only 99.5%Al coating was applied. The duration of the experiment was ~120 days.

Table 4.6: Division of samples among different conditions of the thermal gradient experiments.

| Sample | Potential | Environment | Sealant | Composition |
|--------|-----------|-------------|---------|-------------|
| E1 | $E_{corr}$ | buried | unsealed | Al |
| E2 | $E_{corr}$ | buried | unsealed | Al |
| E3 | $E_{corr}$ | buried | sealed | Al |
| E4 | $E_{corr}$ | buried | sealed | Al |
| E5 | $E_{corr}$ | unburied | unsealed | Al |
| E6 | $E_{corr}$ | unburied | unsealed | Al |
| E7 | $E_{corr}$ | unburied | sealed | Al |
| E8 | $E_{corr}$ | unburied | sealed | Al |
| CP1 | -950 mV$_{Ag/AgCl}$ | buried | unsealed | Al |
| CP2 | -950 mV$_{Ag/AgCl}$ | buried | unsealed | Al |
| CP3 | -950 mV$_{Ag/AgCl}$ | buried | sealed | Al |
| CP4 | -950 mV$_{Ag/AgCl}$ | buried | sealed | Al |
| CP5 | -950 mV$_{Ag/AgCl}$ | unburied | unsealed | Al |
| CP6 | -950 mV$_{Ag/AgCl}$ | unburied | unsealed | Al |
| CP7 | -950 mV$_{Ag/AgCl}$ | unburied | sealed | Al |
| CP8 | -950 mV$_{Ag/AgCl}$ | unburied | sealed | Al |
| T1 | - | buried | unsealed | Al |
| T2 | - | unburied | unsealed | Al |
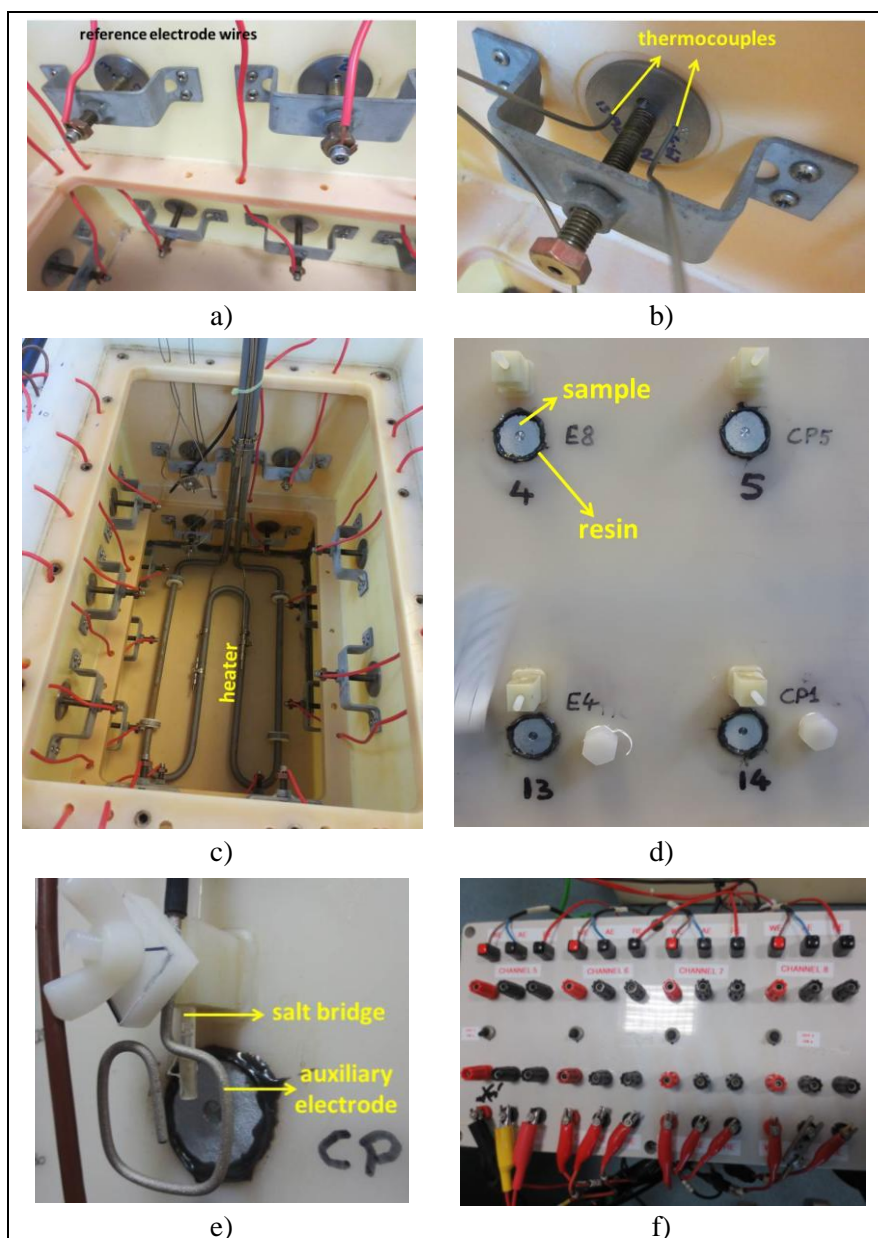
Figure 4.7: Oil tower apparatus: a) inside of the tower showing the back of the samples and connection with the reference electrode; b) thermocouples connected to the sample T2, c) heater located in the bottom of the oil tower, d) some of the samples attached to the oil tower with the surface exposed to its outside, e) positioning of the salt bridge and auxiliary electrode at the sample, f) some of the electrodes (WE, AE and RE) connections in the multichannel potentiostatic equipment.
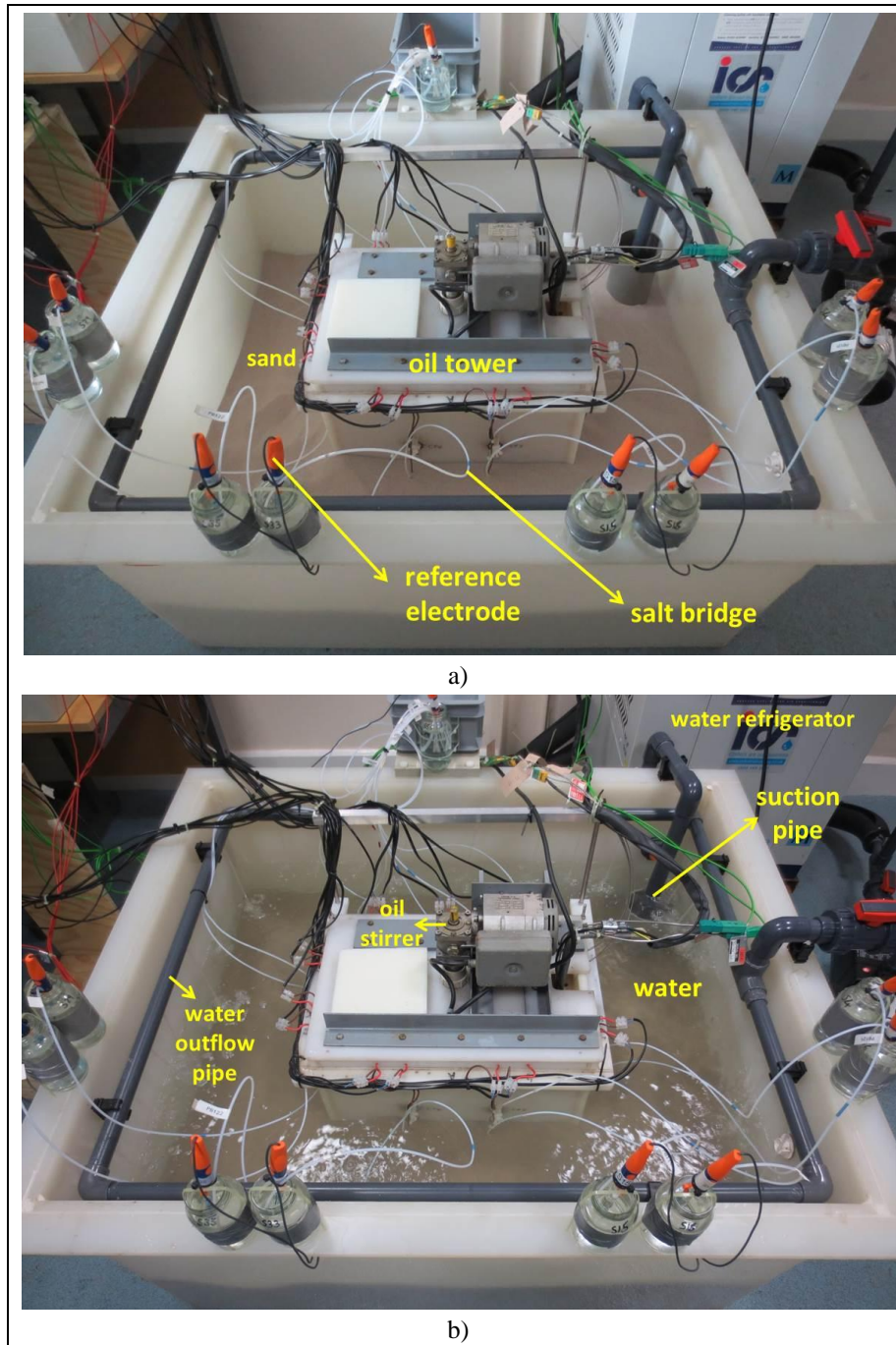
Figure 4.8:   Images of the test tank: a) previous to the start of the test, showing the synthetic sand in the tank covering the samples at the bottom of the oil tower wall; b) during the test, with synthetic water added to the tank, covering the samples at the upper part of the oil tower wall.

## 4.4      Linear Polarisation Resistance Technique (LPR)

The ACM instrument was used for Linear Polarisation Resistance (LPR) monitoring method, which allows corrosion rates to be measured almost in real time using the principle that if the potential of the corroding metal is displaced slightly from the corrosion potential ($E_{corr}$) then the new potential E is a linear function of the current

density. The slope of the linear polarisation is the polarisation resistance. The LPR technique is able to work in a microscopy scale and measures the corrosion current flowing between anodic and cathodic sites applying a small voltage on the specimen and measuring the resultant current flow.

A small sweep from ± 10 mV at a scan rate of 10 mV/min[-1] around the free potential was performed to adjust the slope so that the current and voltage show a straight line which is inversely proportional to the corrosion rate. The polarisation resistance itself is the ratio of the applied potential and the resulting current response: if the electrodes are corroding at a high rate, the small potential will provide a high current and therefore a low polarisation resistance. The Figure 4.9 shows how the LPR technique basically works.



| voltage step | current response | voltage sweep | current response |
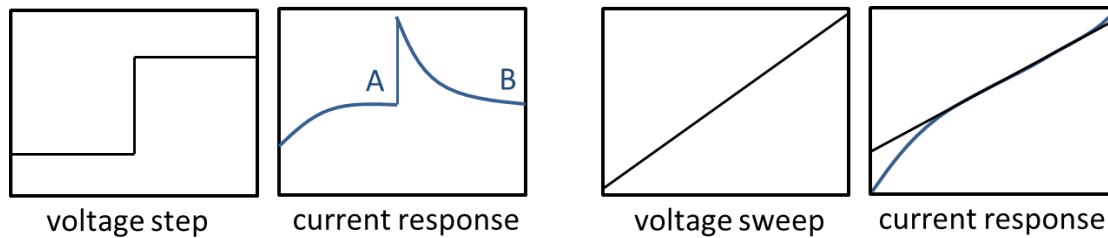
Figure 4.9:   LPR steps generated by ACM instrument. The two left images show a free potential and its current response respectively (the current is measured at points A and B once the initial current surge has steadied). The voltage sweep results in a best fit straight line given the charge transfer resistance (right) (ACM Instruments manual).

The raw data acquisition was obtained through ACM Analysis V4 software which is able to derivate the data in corrosion rate and potential versus time. The corrosion rate is calculated through the Stern Geary equation, where the current density ($i_{corr}$) relationship is given by Equation 3.1 (BABOIAN 2002, SANKARA 2013):

$$i_{corr} = \frac{B}{R_p} \tag{3.1}$$

where B is the Stern-Geary coefficient which is 18 mV for the Al in seawater and 25 mV for the carbon steel in seawater and is related to the anodic and cathodic Tafel slopes ($\beta_a$ and $\beta_c$) as follow in Equation 3.2 (BABOIAN 2002, SANKARA 2013). However for the calculations in this study, the Al coefficient was applied, as the potential provided by the galvanic pair is mainly from the most anodic material.

$$B = \frac{\beta_a \cdot \beta_c}{2,303(\beta_a + \beta_c)} \tag{3.2}$$

while $R_p$ (polarization resistance) is determined by Equation 3.3, where $\Delta E$ is the variation of the applied potential around the corrosion potential and $\Delta i$ is the resulting polarization current (BABOIAN 2002, SANKARA 2013).

$$R_p = \frac{2.\Delta E}{\Delta i} \qquad (3.3)$$

The corrosion rate (CR) is then determined by derivation of the Faraday's Law as showed in Equation 3.4 (SANKARA 2013):

$$CR = \frac{K.i_{corr}.EW}{\rho} \qquad (3.4)$$

where CR is given in mm/y; $i_{corr}$ in $\mu A/cm^2$ and K is a constant of value $3.27 \times 10^{-3}$ in mm.g/$\mu$A.cm.y. The EW is the equivalent weight of the corroding species and $\rho$ is the density of the corroding species, which in those calculations was taken to be the aluminium (SANKARA 2013).

A direct conversion from a current density value in $mA/cm^2$ to corrosion rate in mm/year can be done which can be estimated as follow (ROBERGE 2007):

$$1\,mA.\,cm^{-2} = \frac{3.28.M}{n.d}\,mm.\,year^{-1} \qquad (3.5)$$

where *M* is the atomic mass, n is the number of electrons freed by the corrosion reaction and *d* is the density in $g/cm^3$. Therefore, considering only Al as the metal being corroded it gives that

$$1\,mA.cm^{-2} = 10.93\,mm.year^{-1} \qquad (3.6)$$

Error in LPR test include the uncertainty in the parameter B in Equation 3.2, choice of the scan rate what can neglect the solution resistance and non-linearity which is only a small percentage of the result (ACM Instruments).

The LPR in this study is considering the mixed system steel-aluminium, although the steel measurement will be mainly affect the results in the first day(s) of tests due to the formation of calcareous deposit on the exposed steel.

## 4.5    Potentiostatic Polarisation

Potentiostatic polarisation is usually used when polarisation is time-dependant and data regarding the galvanic corrosion performance is desired. The technique involves the exposure of samples under a potential until its stabilisation is reached (BABOIAN

2005). This is achieved by keeping a desired potential between the WE and RE constant what results in a current flow (MARCUS 2006).

In this test the interest was to obtain the current demand. The consumption of material is related to the electric current $i$ (A) by Faraday's Law as shown in Equation 3.7, where m (g) is the amount of material consumed, M (g.mol$^{-1}$) is the molar weight, F (96487 A.s.mol$^{-1}$) is the Faraday number, t (s) is the time and z is the charge number (MARCUS 2006):

$$m = \frac{M.i.t}{z.F}$$ (3.7)

When differentiation is applied as $t$ function o produce the rate of material consumption, the Equation 3.8 takes place (MARCUS 2006):

$$\frac{dm}{dt} = \frac{M.i}{z.F}$$ (3.8)

Thus, the rate $dm/dt$ is proportional to $i$, which if divided by the area relates the corrosion rate to the corrosion current density (MARCUS 2006).

The polarisation tests were monitored through the multichannel Bio-logic VMP 300 instrument. This potentiostatic equipment is able to measure extreme low corrosion rates and uses DC power transmission and is supposed to accurately control the potential between the RE against the sample. Samples were driven to an individual cathodic potential of -950 mV$_{Ag/AgCl}$ and the required current was continuously monitored through the three-electrode cell configuration. The instantaneous current of each potential step was recorded every 300 s. No current limits were set for the steps. The potential range was set as ±2 V and a fast bandwith (8) was used. The instrument worked with the Ec-Lab V10.38 software and can derivate the acquired data in current density (mA/cm$^2$) x time.

## 4.6 Post-Exposure Test Analysis

After exposure tests, samples were analysed as described in items 4.6.1 to 4.6.3.

## 4.6.1 Visual Inspection

After the experiments the specimens were dried and photographed. The visual inspection gives a general view of the samples in order to observe presence of deposit formed on the surface area as well as presence of cracks or blisters in the coating.

### 4.6.2 Microstructural Characterization

Scanning Electron Microscope (SEM) was carried out in backscattered mode on metallic samples in top and cross section view in order to identify the morphology and characteristics of the deposits' layers. Prior to the analysis, the specimens were sputter coated with Au. Energy Dispersive X-ray (EDX) was performed on all specimens using an accelerating voltage of 25 kV in order to perform qualitative chemical analysis. Both analysis were carried out in the equipment model ZEISS 1455EP. The cutting and view schemes of the samples are showed in Figure 4.10. The preparation of samples included cutting with SiC disc, grinding with SiC paper and polishing with ethanol.
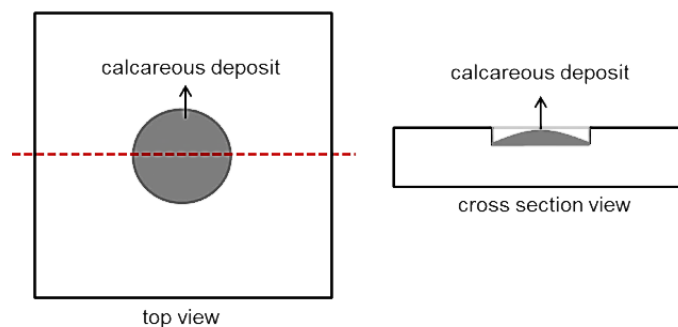


Figure 4.10: Scheme showing top view (left) and cross-section view (right).

### 4.6.3 Crystalline Phases Identification

The XRD was carried out on the calcareous deposit extracted from specimens with the aim of identify its crystalline phases. The deposit samples were spread on a silicon sample holder with a greasy mass, however those elements do not affect the results. The equipment used was a Bruker D8 Advanced where the θ-2θ system is applied.

The principle of the XRD is to emit electrons across a high voltage (20-50 kV) from a heated cathode (tungsten filament) to an anode material (Cupper) producing radiation (X-ray). X-ray diffraction is then produced in a process where X-rays impinging on a crystalline material are reflected by the atoms, which are arranged in ordered arrays. The resulting X-ray diffraction patterns (set of peaks of a given phase) is characteristic of the material and are the function between the scattered X-ray intensities and 2Theta which is the diffraction angle (see Figure 4.11).
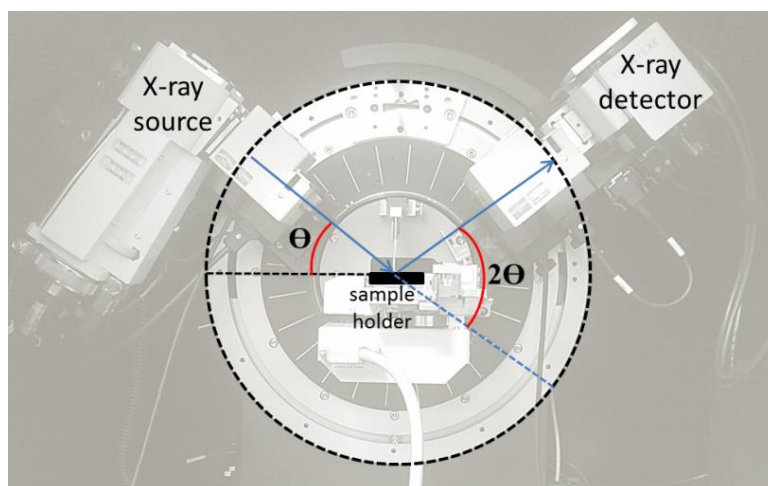
Figure 4.11: XRD's operating scheme. The X-ray aims the rotating sample at an incident angle Ө and the detector interprets its intensity which is 2Ө away from its diffraction.

The measurements were made from 5 to 80° with a step size of 0.01°. The radiation from the CuKα source used a 40 kV energy and 40 mA of current. The wavelength generated was 1.54°.

The analysis of patterns was made through Diffrac.Suite software. As calcareous deposit can have a very low level of crystallinity, an amorphous background is expected to be associated with the peaks, what can make the pattern analysis more difficult. Due to that, the background was reduced, what can give the impression of high crystallinity. An example of this treatment is showed in Figure 4.12 where same analysis appears with background and without background.
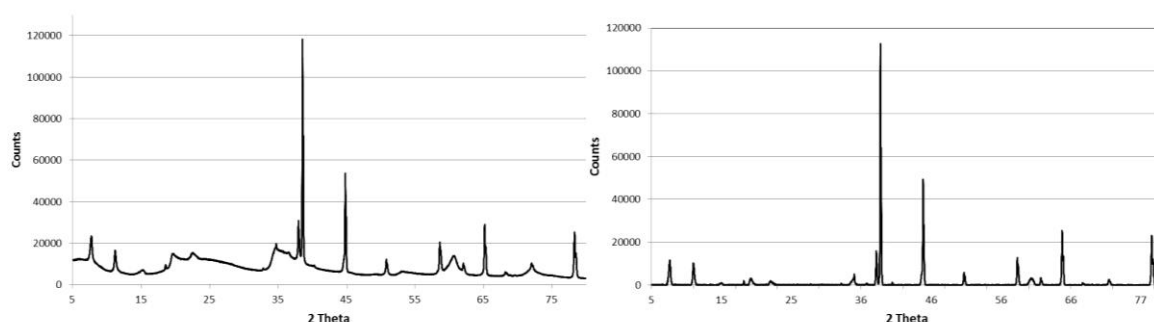


Figure 4.12: Example of X-ray diffraction patterns as measured (left) and with the background reduced (right) (images obtained by the author).

4.7     Additional Tests

In order to complement data or to better understand some phenomena from the study, some additional tests were carried out as specified in items 4.7.1 to 4.7.4.

4.7.1     Adhesion Test

Adhesion tests were performed in order to compare the data between Al and AlMg TSA coating sprayed through TWAS technique. The test was carried out in accordance with ASTM D4541- Method E. Generally, the test consists in dollies being pulled with load increasing until one of the events happens i) the material is detached or ii) specific value is reached. Thus, the test can determine whether the surface remains intact at a specific force (pass/fail).

Two S355J2+N steel (Table 4.1) plates (150 x 100 x 6 mm) TSA- coated through TWAS with Al and AlMg alloys as described in item 3.2.2. The wire thickness used was 2.3 mm for the Al and 1.6 mm for the AlMg alloy. The surface was cleaned with solvent. Dollies with Ø14 mm were bonded with Araldite V AV170 glue and left curing for 1 h at 143ºC. Eight dollies on each plate were prepared, where five from each plate were pulled and three were left as spare samples. A cut was made surrounding the dollies surface in order to provide the appropriate test area. A scheme of the test is showed in Figure 4.13.

An automatic PosiTest AT-A equipment was used, where an automatic hydraulic pumper is coupled. The self-aligning loading fixture head is attached to the dolly to apply normal tension to the coating surface and the force indicator is set as zero. The dollies were pulled at a loading rate of 0.7 MPa.s$^{-1}$. The failure is classified according three failure types:

- Glue failure: detachment happens between glue and coating;
- Adhesive failure: detachment happens between coating and substrate;
- Cohesive failure: detachment happens between particles within the coating.

A comparative graph containing the coating strength was also plotted. The industry accepts adhesion value as $\geq$ 7 MPa for arc spray application (NACE NO. 12/AWS C2.23M/SSPC CS-23).
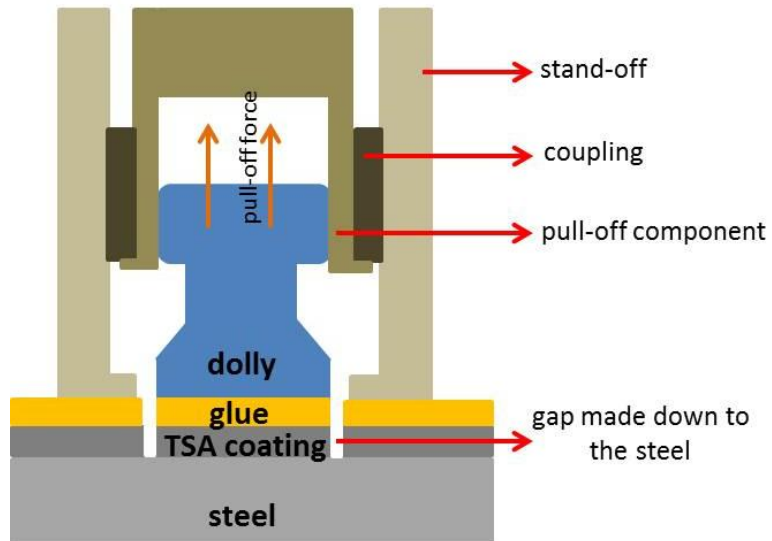
Figure 4.13: Schematic of the adhesion test on TSA coating.

4.7.2     TSA Corrosion Tests

Corrosion tests were performed on glass rods TSA-coated in order to obtain the corrosion rate and potential data provided only by the coating, suppressing the possibility of effect from the steel substrate or exposed steel substrate. The tests were carried out under three temperatures: 30, 60 and 90ºC. Tests were run at free potential (as described in item 3.3.1) in synthetic seawater (composition given in Table 4.4) for up to 145 days. Figure 4.14 shows a glass rod TSA-coated previous to exposure with Ø10 mm and were sprayed along 300 mm length. In total, six glass rod were used, two for each set of temperature. Samples were identified according the coating alloy such as TSA-Al or TSA-AlMg. The potential was measured against silver/silver chloride (Ag/AgCl) reference electrode and platinised titanium (PtTi) wire electrode was used as auxiliary electrode (AE). Previous to the start of the test, the pH of the solution was measured as 8.1. Figure 4.15 shows the schematic of the test arrangement. The XRD analysis (item 3.6.3) in the deposits formed on the glass rods surface was performed.

Figure 4.14: Glass rod TSA-coated previous to the exposure test in synthetic seawater.
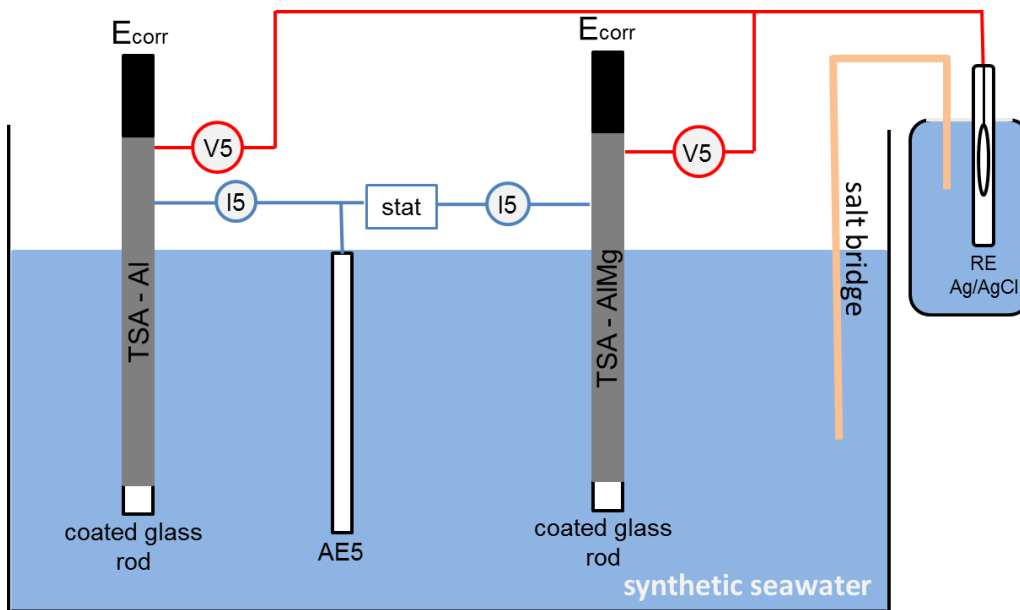


Figure 4.15: Arrangement of glass rods linked with auxiliary electrode (AE) and silver chloride electrode (Ag/AgCl) for free potential tests.

### 4.7.3    Carbon Steel Corrosion Tests

Samples of S355J2+N steel (Table 4.1) were prepared for exposure to the synthetic seawater (Table 4.4) at 30, 60 and 90ºC under free potential. Dimensions were approximately 40 x 40 x 6.5 mm and the surfaces were grinded until 600 grit SiC paper. A M4 hole was tapped in one of the side faces of each sample in order to introduce the stainless steel rod that were connected to electrochemical wires. Belzona 1591 resin covered the interface along the steel and the rod to avoid crevice corrosion and a polymeric cap covered the whole extension of the rod to prevent its influence in the results. The potential was measured against silver/silver chloride (Ag/AgCl) reference electrode and platinised titanium (PtTi) wire electrode was used AE. Salt bridge connected the reference electrode to the synthetic seawater and was positioned next to the sample and the AE. The pH of the synthetic seawater was measured as 8.09 before to the test starting. Figure 4.16

shows the samples previous to the exposure tests. The XRD analysis (item 3.6.3) in the corrosion product was performed.
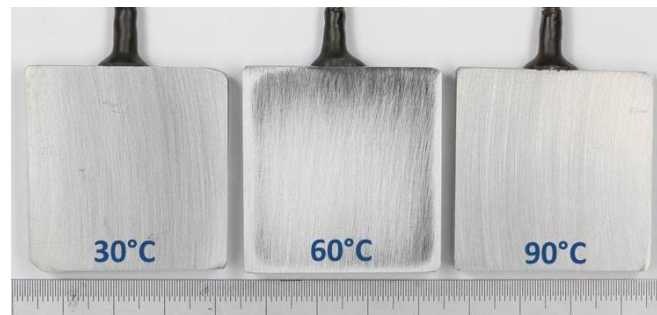


Figure 4.16: S355J2+N steel previous to the corrosion test in synthetic seawater at 30, 60 and 90ºC.

4.7.4    Local pH Test

Favourable precipitation pH of brucite and aragonite are well known in literature at room temperature, however it lacks data at higher temperature. Therefore, in order to better understand the mechanism of the calcareous deposit formation on cathodically polarized steel surface at 30 and 60°C, the local pH test was performed. The study comprises measurement of interfacial pH of TSA coated steel samples 20% holiday (Figure 4.3c) exposed to the seawater (Table 4.4) at those temperatures. Tests were conducted at corrosion potential for up to 350 h. It was not possible to reproduce the test at 90°C due to the temperature range of the pH probe which is up to 60°C.

A flat tip pH electrode was centred in the holiday region, touching the steel surface (Figure 4.17). A pH-meter was used for data acquisition and a temperature compensator was also employed. The temperature was set in the analogical bath heater and the evaporative loss was replenished by adding deionized water. The tests were monitored until reasonably stable pH values were reached, which took up to 350 h. The pH of the bulk seawater (away from the sample surface) was recorded daily. Prior to each experiment, the pH electrode was calibrated in buffer solutions of pH 7 and 10. Finally, the pH profile from the samples and from the bulk seawater were plotted and analysed.

Figure 4.17: Photograph showing the specimen with 20% holiday exposed to the seawater showing the pH probe centred within the holiday.

# 5        RESULTS AND DISCUSSION

## 5.1      Steady Temperature Tests

The results of the experiments conducted at 30, 60 and 90°C will be presented in sections 5.1.1 to 5.1.4.

## 5.1.1    Visual Inspection

Figure 5.1 to 5.3 show the samples TSA-coated with different holiday sizes after the exposure to the seawater at 30, 60 and 90ºC. The first observation was the white deposit covering the steel surfaces, however it was noticed that for the 90ºC samples the deposit had a rougher appearance, differing from the others. One can think that this porous aspect can lead to a lack of protection to the steel surface as it also seems to be easily detached. Moreover, a rust colour deposit was observed coming out from samples AlMg 10 and 20% holiday samples at 60ºC, suggesting a corrosion in the steel happened previous to the calcareous deposit formation. Regarding the TSA coating, no detachment, blister or cracks was observed and corrosion product seemed to have developed on it as well.

| | 5% holiday | 10% holiday | 20% holiday |
|---|---|---|---|
| **Al** | | | |
| **AlMg** | | | |
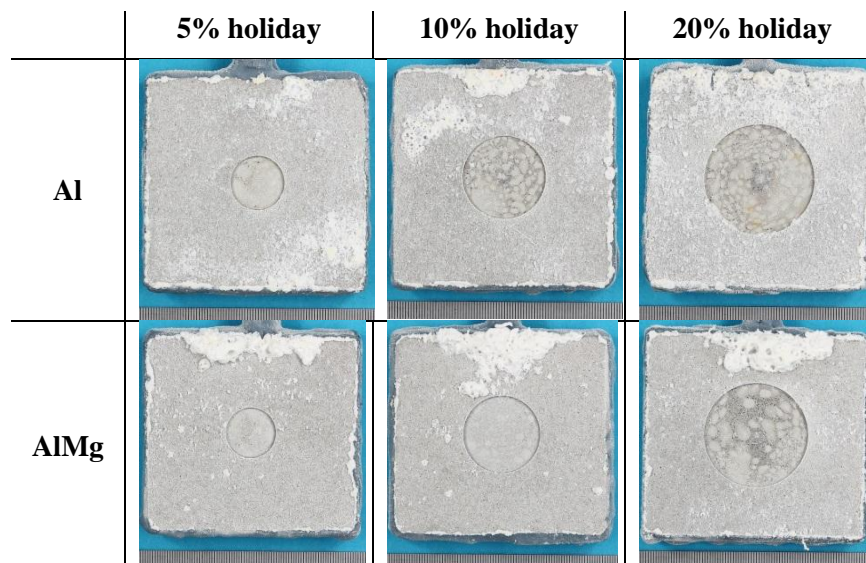
Figure 5.1:    Samples after exposure in synthetic seawater at 30ºC under free potential.

|  | **5% holiday** | **10% holiday** | **20% holiday** |
|---|---|---|---|
| **Al** | | | |
| **AlMg** | | | |
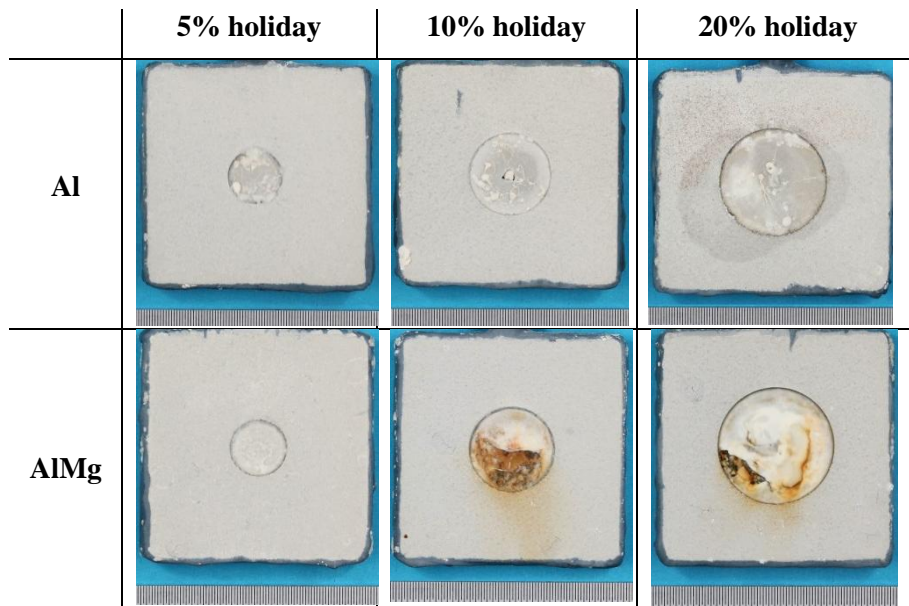
Figure 5.2:   Samples after exposure in synthetic seawater at 60ºC under free potential.

|  | **5% holiday** | **10% holiday** | **20% holiday** |
|---|---|---|---|
| **Al** | | | |
| **AlMg** | | | |
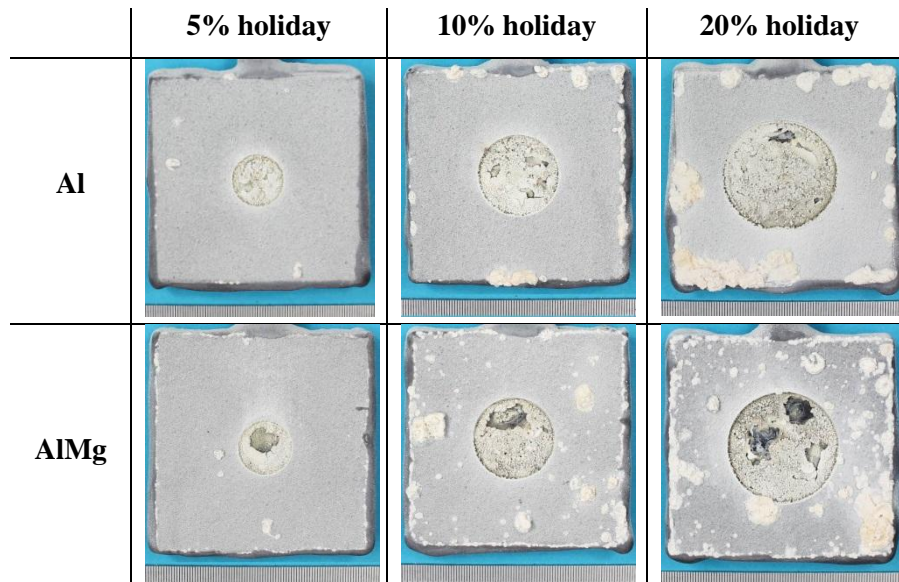
Figure 5.3:   Samples after exposure in synthetic seawater at 90ºC under free potential.

### 5.1.2   <u>Microstructural Characterization</u>

Microstructural characterisation was performed in top view and cross section. The latter had the aim to analyse the holiday area, the interface holiday-TSA and the TSA itself.

*Top View*

Top-view analysis in SEM revealed similar microstructure of the deposit from 30 and 60ºC samples.  That was the typical needles structure (Figure 5.4a) from aragonite form of $CaCO_3$ and it is well known from literature as earlier described in item 2.7.1. The EDX (Figure 5.4b) showed strong peak of Ca followed by C and O, also suggesting the deposit to be $CaCO_3$. A different morphology was observed from samples at 90ºC (Figure

5.5) where a flower-shape structure was formed, which the EDX analysis identified as Mg-O compound. Apart from the main peaks, seawater elements (Na, Cl, S) and contaminants (Si) were also detected. The different composition of the deposits explains the different appearance observed in the visual inspection previously. Only one image of each case, representing all the samples will be shown since the results were similar. The images corresponding to each sample can be seen in APPENDIX A.



a)                                b)
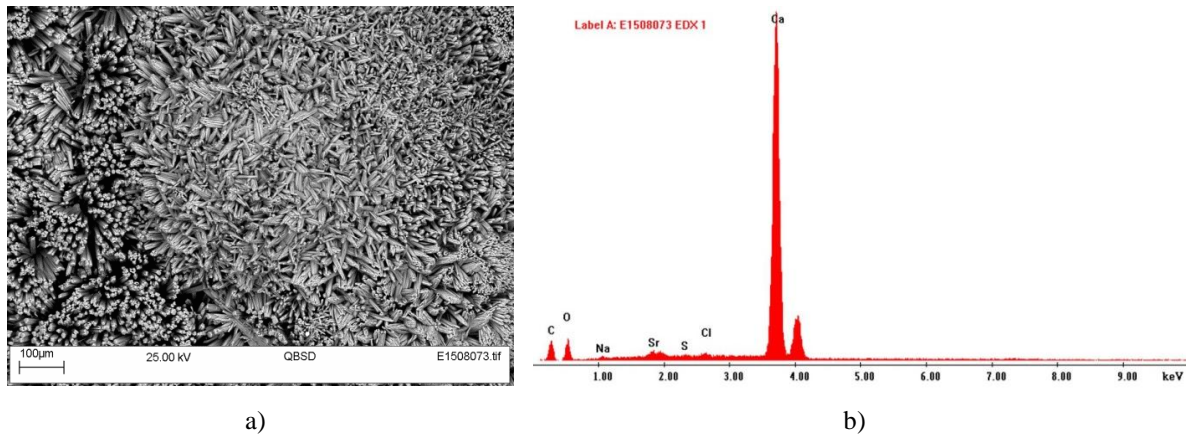
Figure 5.4:    Top view analysis from the deposit from 30 and 60ºC samples: a) SEM image showing needle structure typical from aragonite; b) bulk EDX analysis from (a) showing strong peak of Ca followed by presence of C and O. Sample: Al 20% holiday from 60ºC test.



a)                                b)
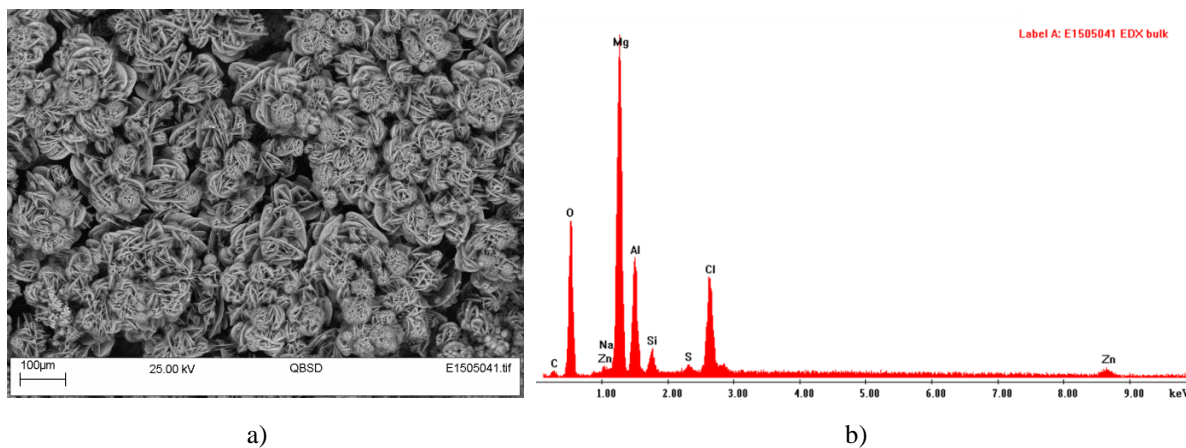
Figure 5.5:    Top view analysis from the deposit from 90ºC samples: a) SEM image showing flower shape structure; b) bulk EDX analysis from (a) showing strong peak of Mg followed by presence of O. Sample: AlMg 10% holiday from 90ºC test.

*Cross Section*

Three regions were analysed in the SEM: holiday area, the interface holiday/TSA coating area and the TSA coating. Images were labelled to be linked with further EDX analysis. As the EDX results were similar among samples, only the result from one sample will represent each label. For full results see APPENDIX B, C and D.

In the holiday area the calcareous deposit was observed along the steel surface and no visual degree of corrosion was noticed (Figure 5.6 to 5.8), suggesting that the layer was protecting the steel since the early stages of the exposure. The deposits from 30 and 60°C samples presented different aspects from 90°C samples. At 30 and 60°C there were two layers composing the deposit: a dark grey in the bottom and a light grey on the top. At 90°C a single dense layer was formed. The EDX (Figure 5.12) was performed in each of the layers as labelled in the images (rectangle and circle). It was found that at 30 and 60°C the inner layer was composed basically by Mg and O and the external layer mainly by Ca, C and O. At 90°C it was only formed the Mg-O layer.

At 60°C the layers appeared also mixed what may have happened probably due to some change in the pH during the test which led to the dissolution of the Ca layer and formation of Mg layer instead and then formation of Ca layer again. This may have ben caused due to failures in the heater along the test. This, however, did not disturb the main characteristics of the layers composed mainly by Mg (inner) and Ca (outer).  The fact that the deposit at 30 and 60°C is not touching the steel surface is due to the detachment that happened at some point during the test or after it during the drying of the sample.

When analysing the interface holiday/TSA (Figure 5.9 to 5.11) it is possible to observe that the calcareous deposit is also formed in the edges of the holiday and grows on the TSA deposit with the same configuration: an inner layer of Mg-O and an outer layer of Ca compound. This growth happens in the whole extension of the coating; however it takes place on the aluminium oxide layer (EDX in Figure 5.13) that first grows in the TSA due to its passive behaviour in seawater as mentioned in item 3.6. This fact leads to the belief that the calcareous deposit is at first formed in the holiday area and later in the TSA coating as hydration reaction happens on aluminium surface before the calcareous deposit formation (LAJEVARDI 2011). This could be observed by Ce and Paul[CE 2016] where TSA samples with holiday (4%) were exposed to seawater at boiling temperature for different periods of time. After 2h exposure, the calcareous deposit in holiday area was formed,

however no presence on TSA could be yet observed. After 355 h exposure the brucite layer was present on aluminium oxide film.

Additionally, presence of rust at the edges of the holiday in samples 5% AlMg and 20% AlMg could be observed. The EDX showing Fe and O peaks are shown in Figure 5.14. It suggests that rust took place previous to the formation of the calcareous deposit on steel. This behaviour will be further discussed in section 5.2.
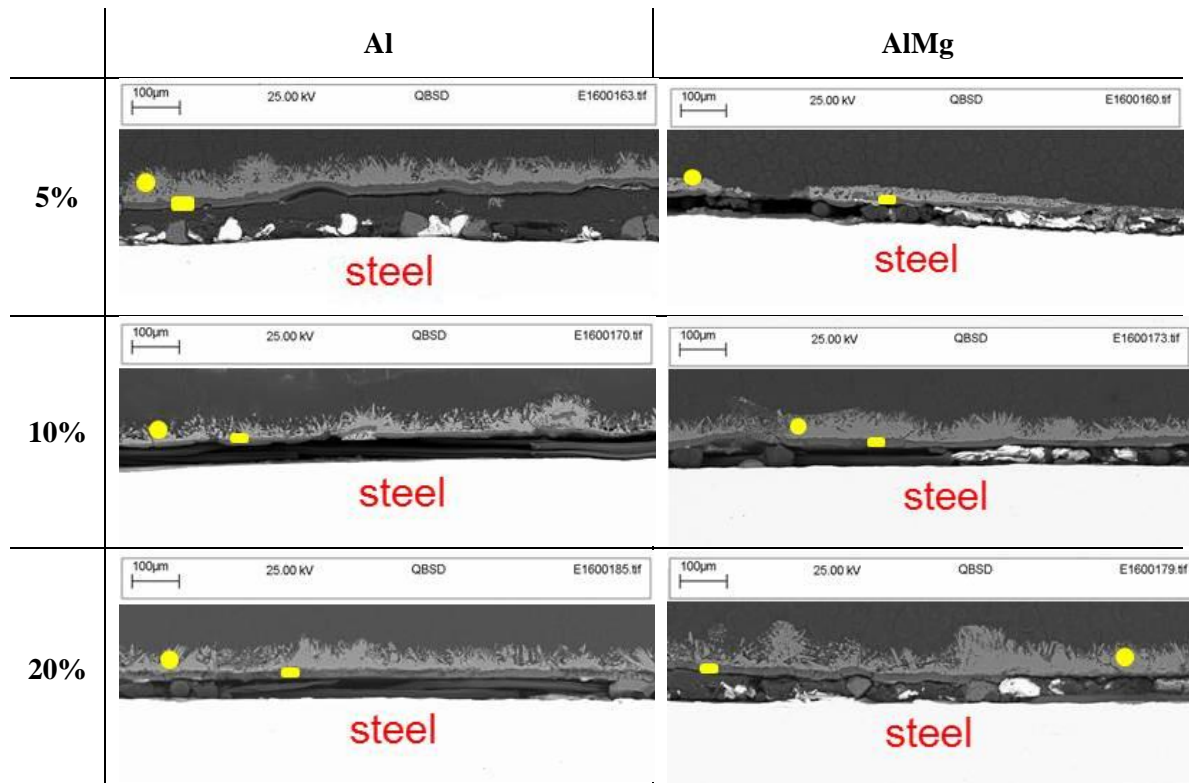


Figure 5.6:   Cross section of the holiday area from samples exposed to 30ºC synthetic seawater under free potential. The two layers observed are marked in yellow.

|  | **Al** | **AlMg** |
|---|---|---|
| **5%** |  |  |
| **10%** |  |  |
| **20%** |  |  |
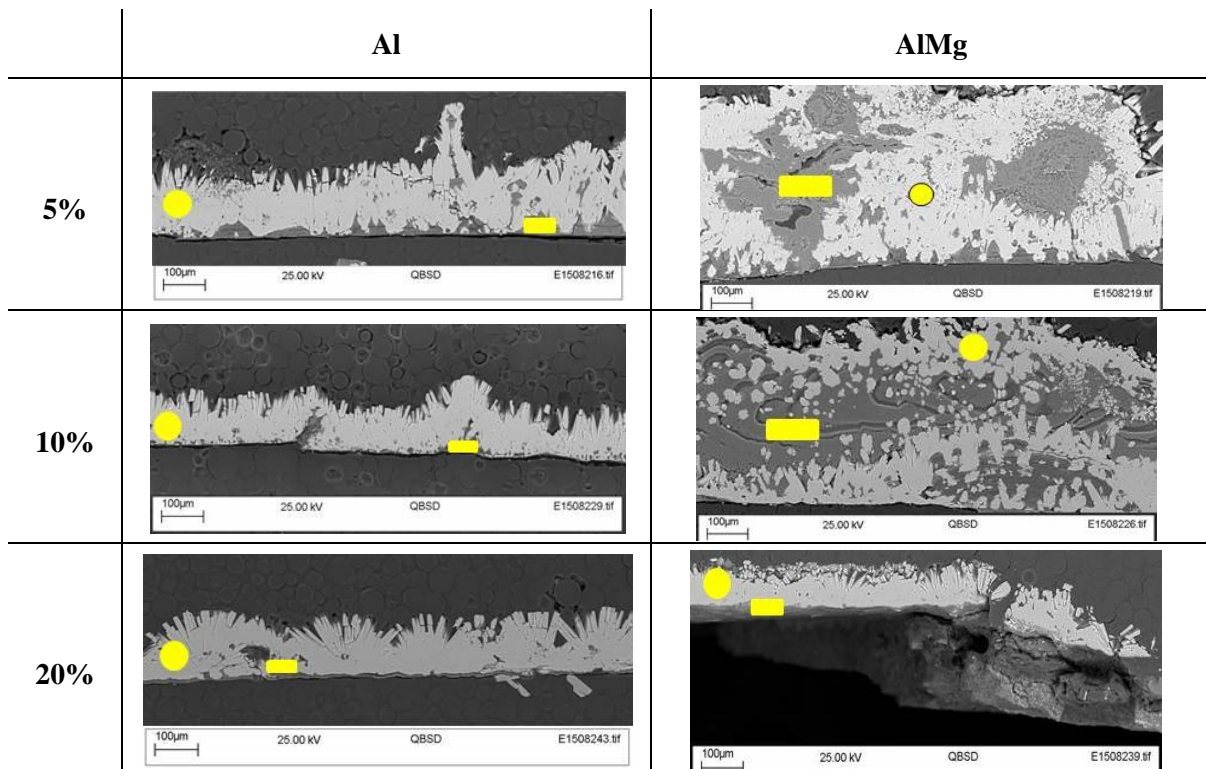
Figure 5.7:   Cross section of the holiday area from samples exposed to 60ºC synthetic seawater under free potential. The two layers observed are marked in yellow.

|  | **Al** | **AlMg** |
|---|---|---|
| **5%** |  |  |
| **10%** |  |  |
| **20%** |  |  |
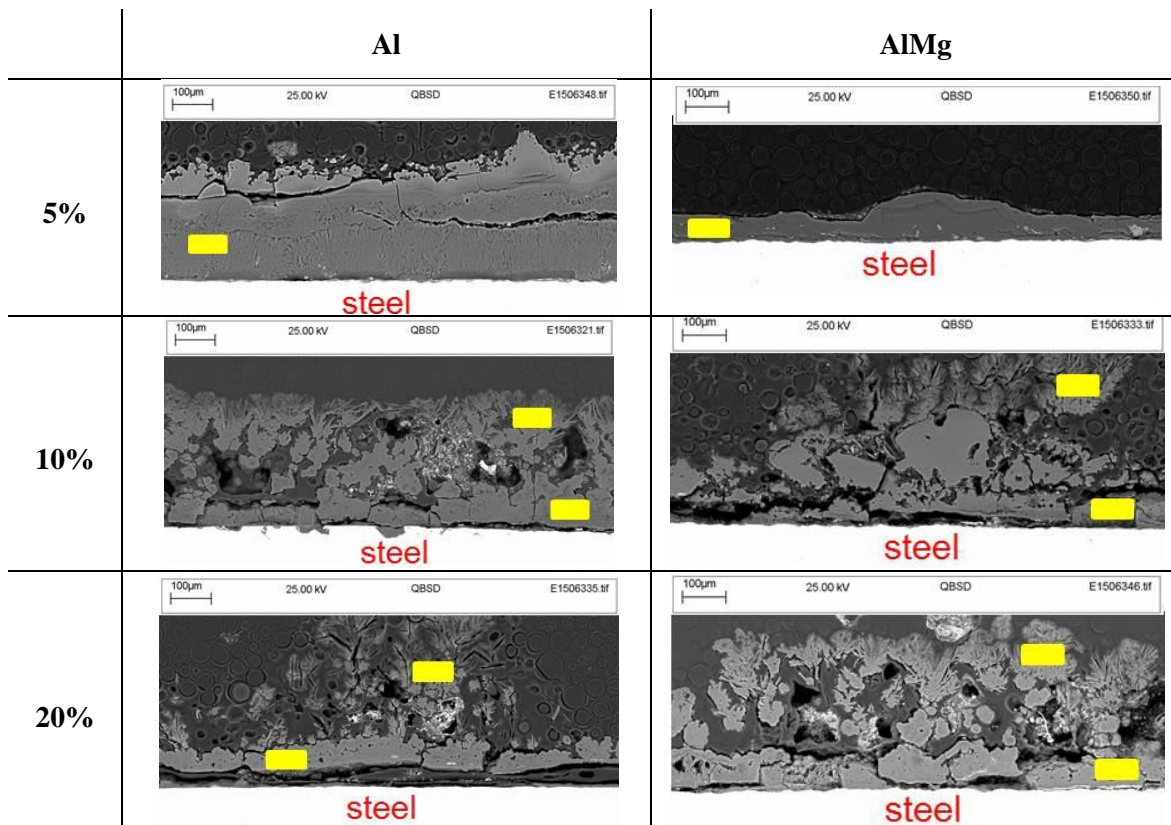
Figure 5.8:   Cross section of the holiday area from samples exposed to 90ºC synthetic seawater under free potential. The layers observed are marked in yellow.
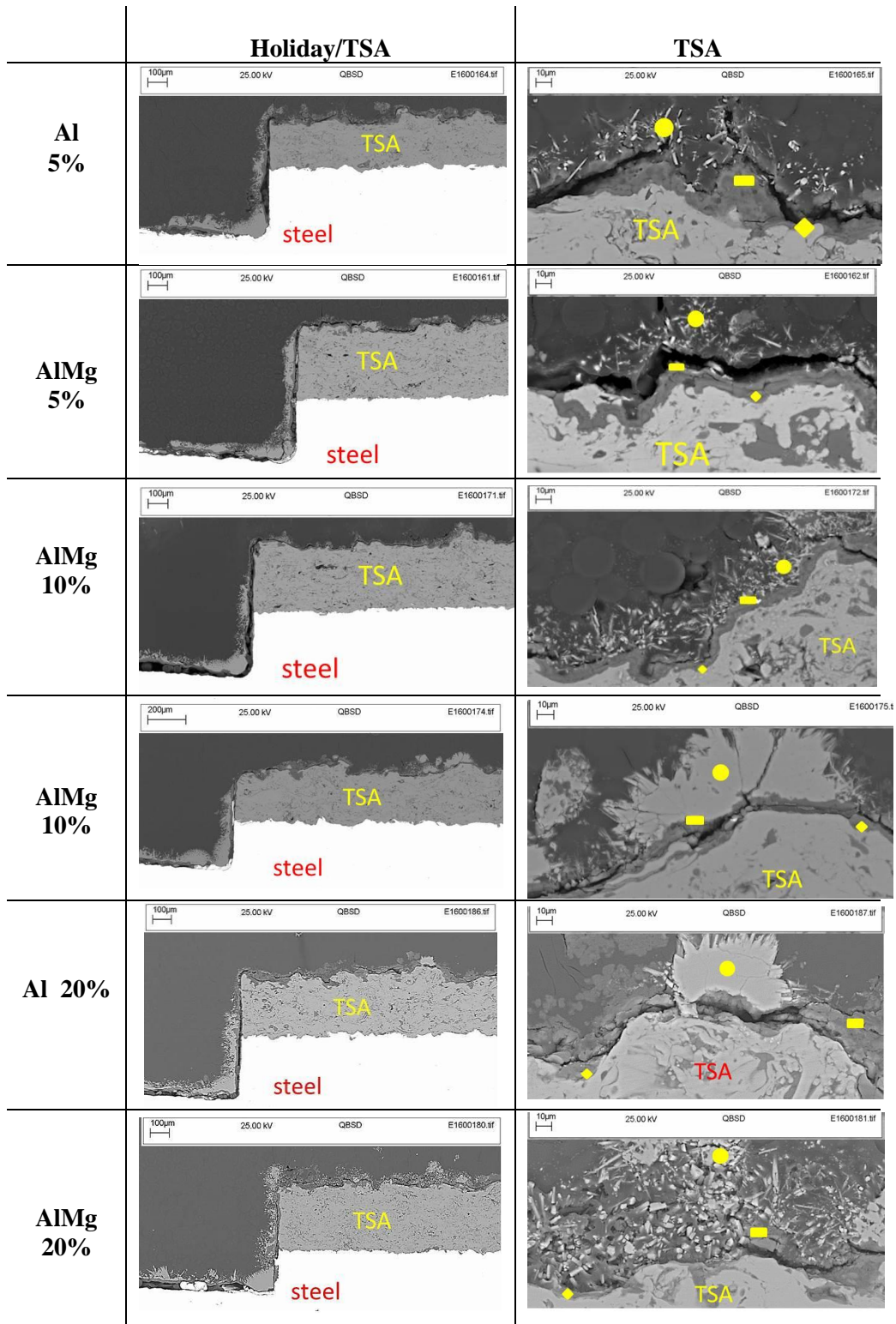
Figure 5.9:   SEM images from the interface holiday/TSA and TSA exposed to synthetic seawater at 30ºC.

|  | **Holiday/TSA** | **TSA** |
|---|---|---|
| **Al 5%** | | |
| **AlMg 5%** | | |
| **Al 10%** | | |
| **AlMg 10%** | | |
| **Al 20%** | | |
| **AlMg 20%** | | |
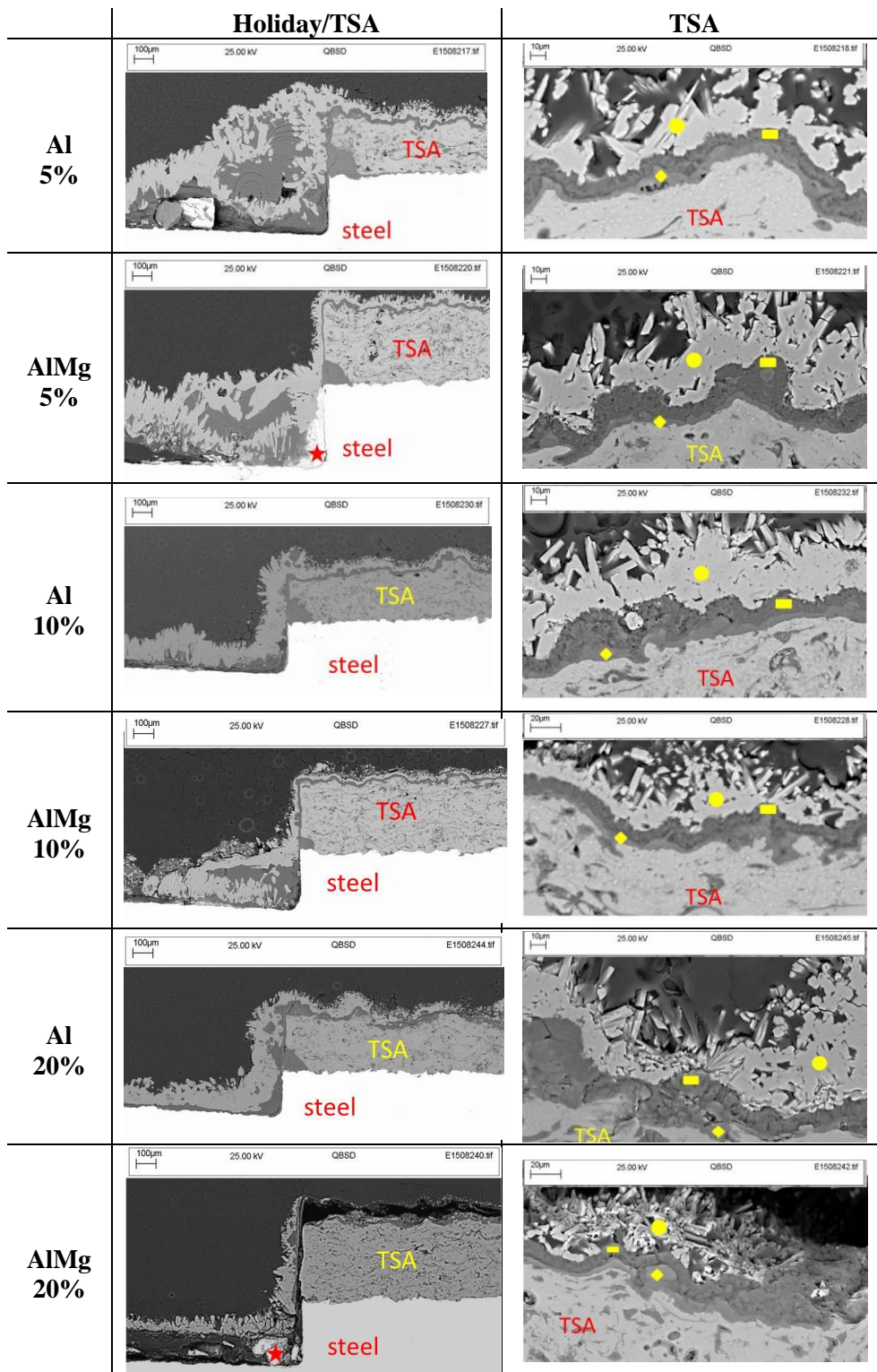
Figure 5.10: SEM images from the edges of the holidays exposed to synthetic seawater at 60ºC.
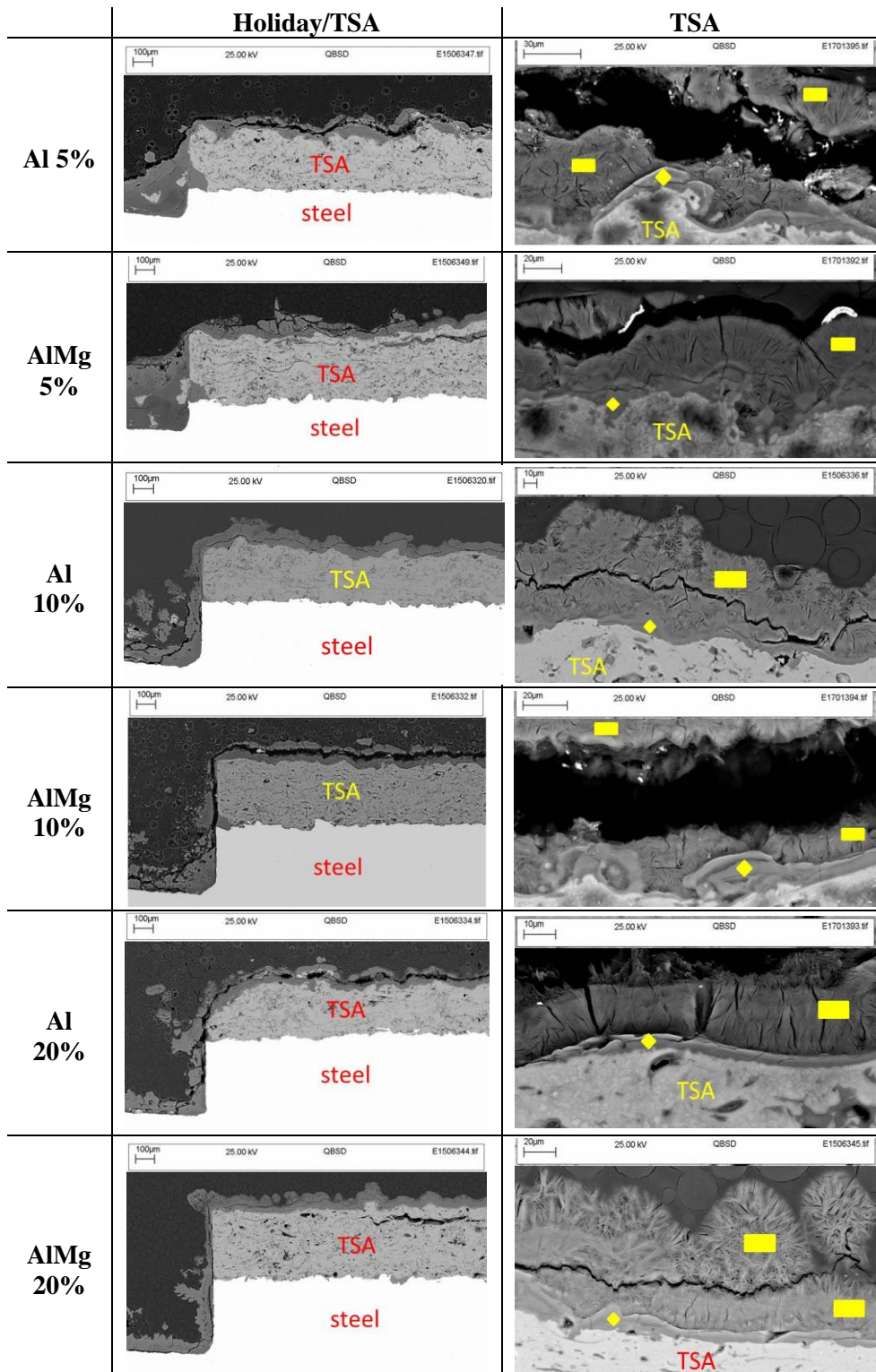
Figure 5.11: SEM images from the edges of the holidays exposed to synthetic seawater at 90ºC.
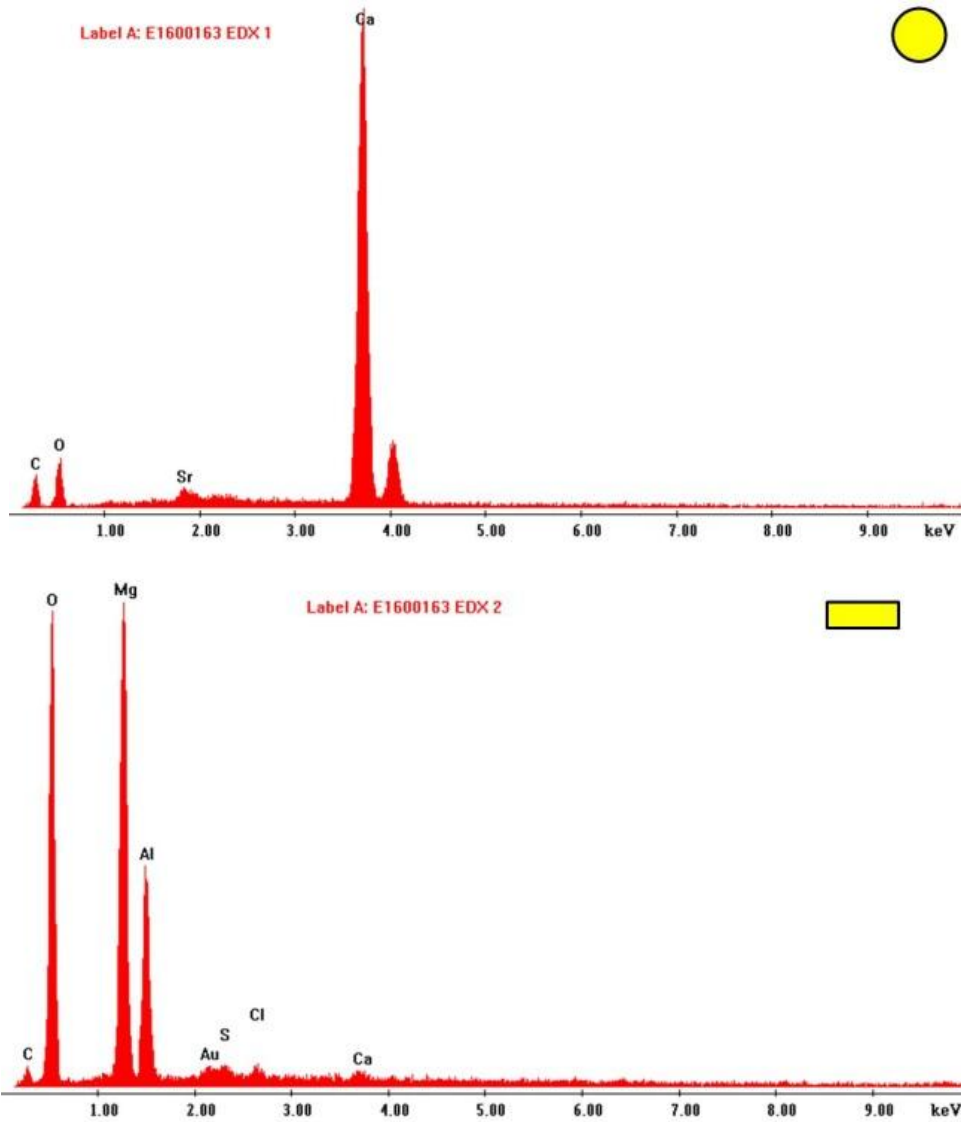
Figure 5.12: EDX of the calcareous deposit layers formed in the holiday area and on TSA coating in samples exposed to 30ºC, 60ºC and 90ºC labelled according Figure 5.6 to Figure 5.11: SEM images from the edges of the holidays exposed to synthetic seawater at 90ºC.
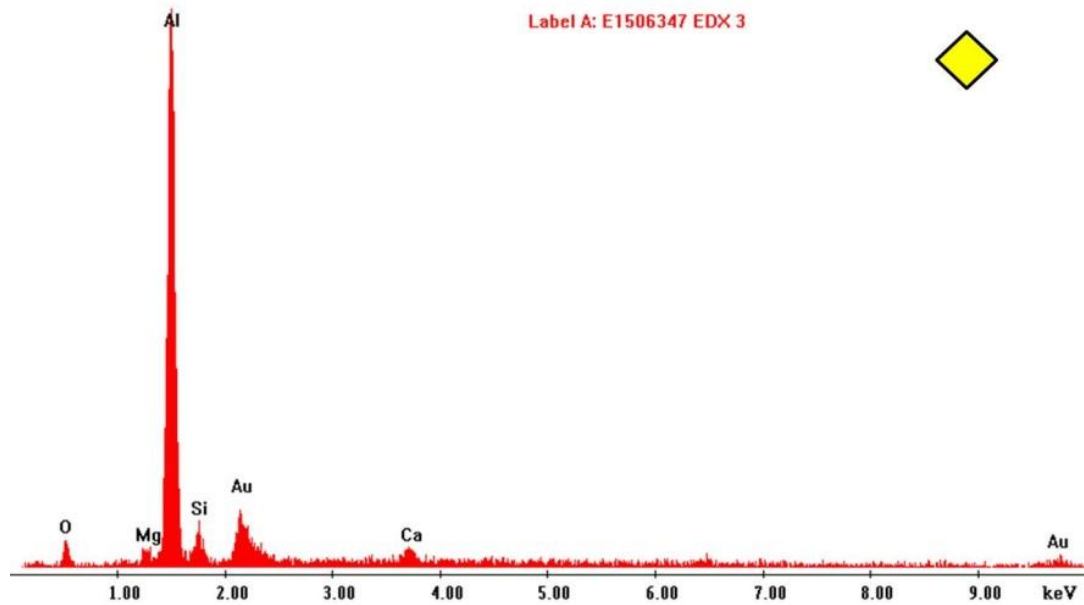
Figure 5.13: EDX of the calcareous deposit layers formed in the holiday area and on TSA coating in samples exposed to 30ºC, 60ºC and 90ºC labelled according Figure 5.9 to 5.11. Sample: Al 5% holiday from 30ºC test.
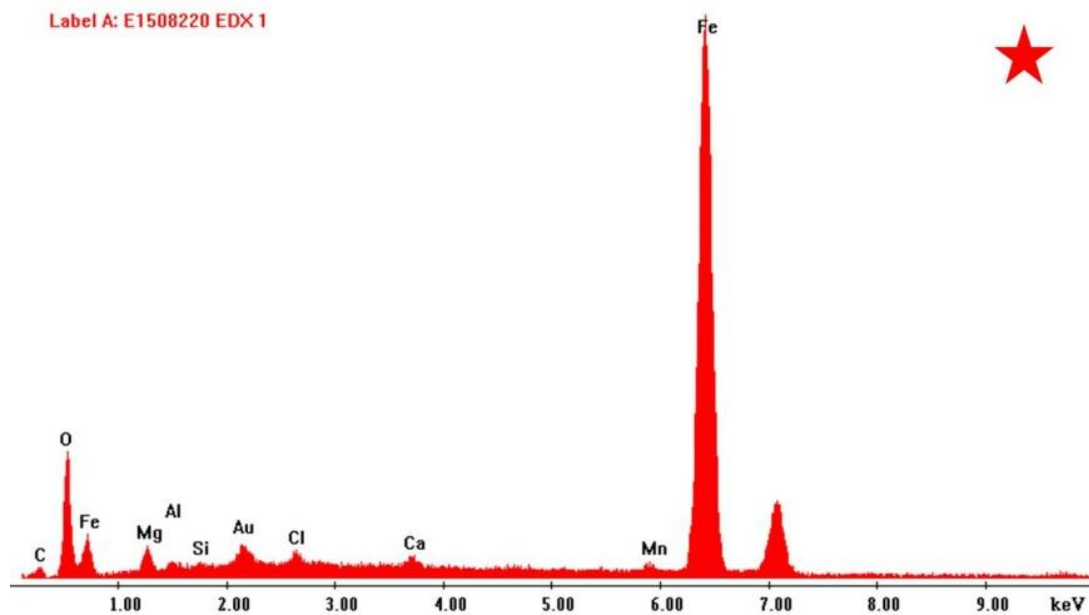


Figure 5.14: SEM spectra showing peaks of Fe and O found in specimens exposed to 60°C as labelled in Figure 5.10. Sample: AlMg 5% holiday from 60ºC test.

Additionally, no detachment or other defect in the TSA was present (Figure 5.9 to 5.11). The TSA thickness was measured as an average of 10 measurements in each sample and the value obtained was approximately $332 \pm 5$, $309 \pm 6$ and $303 \pm 3$ µm for 30, 60 and 90°C respectively what shows that very little of the coating was consumed during exposure considering that the nominal thickness applied of 300 µm. Those values suggest

that aluminium oxide promptly protected the TSA when exposed to the seawater, which was further also protected by the calcareous deposit formed on it, even when only Mg-layer was present, as observed in Figure 5.11. Also, literature reports that accelerated corrosion of aluminium happens in the range of 70 and 80°C (GHALI 2010, DAVIS 1999). Therefore, it is possible that at 90°C the low content of oxygen was beneficial to the TSA coating, providing a low corrosion rate until the calcareous deposit was formed, from where the corrosion was then also prevented by physical barrier. Figure 5.15 shows the solubility profile of oxygen in water versus temperature up to 100°C. It can be observed the tendency of the $O_2$ content to decrease with temperature (SCHÜTZE 2016, GHALI 2010). At the boiling point all the oxygen is expelled from the water and solubility is considered zero (GHALI 2010). Taking into account only the oxygen concentration, the corrosion rate is expected to decrease with temperature; however, there is compensation by the chemical reaction kinetics, increasing the rate of diffusion of ions to the interface metal-water, which can double with a 10°C rise in temperature (GHALI 2010). This can also explain the presence of rust on steel in samples 5% AlMg and 20% AlMg at 60°C (Figure 5.10) which was probably prevented by further formation of the calcareous deposit.
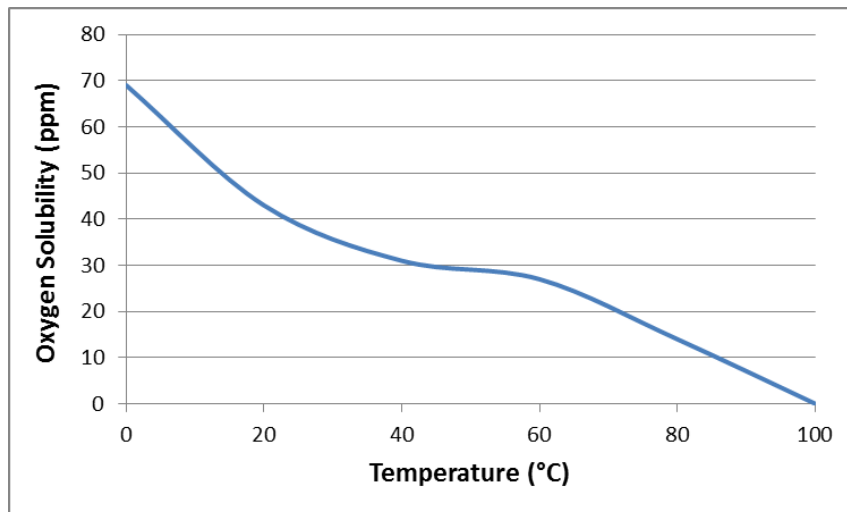


Figure 5.15: Oxygen solubility in water up to 100°C (data from GHALI 2010).

5.1.3    Crystalline Phases Identification

The XRD analysis from deposits from the holiday area could define the phases present in the calcareous deposit as $Mg(OH)_2$ (brucite) and $CaCO_3$ (aragonite). At 30 and 60°C both phases were present, while at 90°C only brucite took place. As results were similar, only one pattern of each case is represented in Figure 5.16 and 5.17. Full results can be found in APPENDIX E.
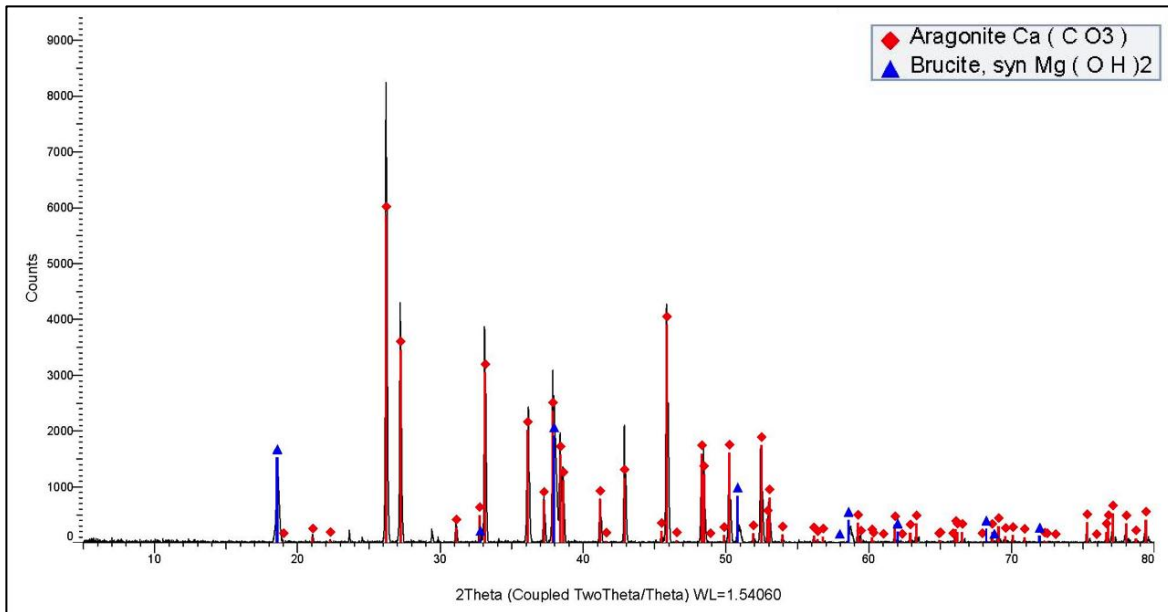
Figure 5.16: XRD patterns of deposit formed in samples exposed to synthetic seawater at 30 and 60°C, showing presence of brucite and aragonite. Sample: AlMg 20% holiday at 60°C.
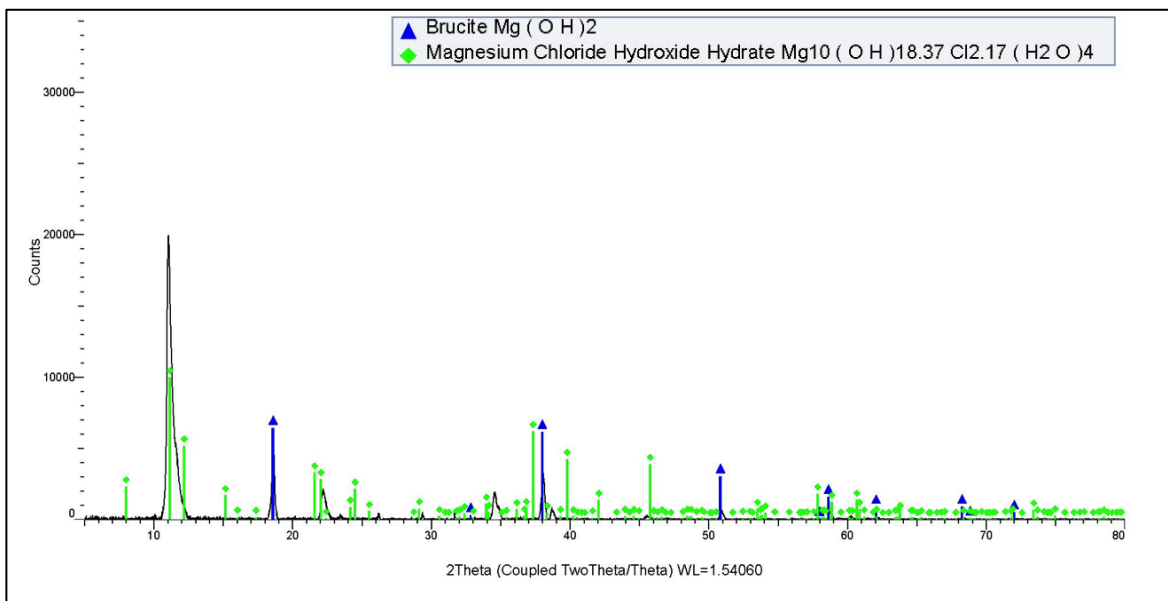


Figure 5.17: XRD patterns of deposit formed in samples exposed to synthetic seawater at 90°C, showing presence of brucite. Sample: AlMg 5% holiday at 90°C.

### 5.1.4    Corrosion Data Analysis

The corrosion data from 30, 60 and 90°C tests were plotted separately for each temperature regarding its potential ($E_{corr}$) and corrosion rate. Apart from the results of the samples with holiday, it will be also presented a comparison with the TSA coat from glass rod samples both Al and AlMg alloy (see item 4.7.2) and the bare carbon steel (see item 4.7.3), represented as black lines in the graphs. Moreover, as the corrosion test in the steel

was run until its potential stabilisation was reached (~5 days) the data was extrapolated up to 145 days allowing a better comparison against the results from the other samples.

*Potential*

The potential data is important as it supplies the information about the protectiveness achieved in the samples. As mentioned before, the recommended cathodic potential for the C-steel is between -800 and -900 $mV_{Ag/AgCl}$ (DNV-RP-B401, ISO 15589-2). The potentials reached at 30, 60 and 90°C tests are shown from Figure 5.18 to 5.20 and the initial data are zoomed in the graphs.

At 30°C (Figure 5.18) it is possible to observe a drop in potential in all samples, but in the TSA ones. Initially, the steel potential was approximately -450 $mV_{Ag/AgCl}$, which rapidly decreased and stabilized around -690 $mV_{Ag/AgCl}$. It is known that generally the free potential for C-steel in water at room temperature is in order of -600 $mV_{Ag/AgCl}$ (JAVAHERDASHTI 2013). The dropping behaviour in steel to more negative potentials in the first two hours of experiment is expected due to its initial severe corrosion. Its stabilisation, on the other hand, can be explained by the formation of γ-FeOOH (lepidocrocite), a brown colour deposit, confirmed by XRD analysis (see APPENDIX F). It was already reported that the low conductivity and the physical barrier of this early stage film formed on steel surface in aqueous media able to reduce the oxidation of of Fe to $Fe^{2+}$ ions and from this point on the diffusion of surrounding water species may be retarded. The formation of the film is highly influenced by $Cl^{-}$ together with high pH, where nucleation is quicker (MONTOYA 2013).

The TSA samples, instead, experienced an initial increase of potential from approximately -1022 $mV_{Ag/AgCl}$ (AlMg) and -1270 $mV_{Ag/AgCl}$ (Al), which difference may be related to different reactiveness property due the addition of Mg in the former, to less negative potentials, followed by values oscillating around -900 $mV_{Ag/AgCl}$. This initial increase is probably related with the loss of the air-formed oxide film in some areas, however the subsequent film restauration due to hydrolyse reactions were able to lead the TSA to potentials between -850 and -1000 $mV_{Ag/AgCl}$ (DAVIS 1999). Traces of $Al_2O_3$ plus brucite and aragonite were found on both Al and AlMg TSA surface through XRD analysis (see APPENDIX G).

The coated samples with holiday also presented a decrease from the initial potential which varied between -700 and -900 $mV_{Ag/AgCl}$ what represents a mix of

behaviour from steel and TSA coating. The steady values were found between -800 and -920 mV, therefore the samples are considered in the cathodic protection zone for C-steel (see Table 3.6), what is a good achievement considering that the coating was damaged. In this case, the potential drop is probably related to the limitation of oxygen in the steel surface (partially consumed by TSA corrosion, partially by the diffusion that was prevented by the calcareous deposit on the steel.

At 60°C (Figure 5.19) most of samples presented different initial behaviour. The bare steel sample showed a slight dropping from approximately -600 to around -676 $mV_{Ag/AgCl}$, stabilising around -656 $mV_{Ag/AgCl}$. Such stability may be related to the different type of iron oxide present on steel surface, which now was composed by mainly the $Fe_3O_4$ (magnetite), a black colour deposit, followed by α-FeOOH (goethite) (see APPENDIX F). The magnetite is due to grow on steel in alkaline conditions when extremely low oxygen content applies and when low flow takes place. This layer can be a resistant film (GÜLICH 2010). The TSA samples potential remained constant probably due to the faster precipitation of brucite and aragonite on its surface, as found by XRD. Also, differently from 30°C samples, the aluminium oxide film formed was $Al(OH)_3$ (gibbsite) (see APPENDIX G).

Samples with holiday generally presented a stable behaviour from the beginning of the test, apart from the AlMg 5% sample which dropped to more negative potentials (around -1240 $mV_{Ag/AgCl}$) however had its potential increased to the initial value in less than five hours of test. The final potentials were kept between -875 and -900 mV. It is known that the seawater temperature influences mainly diffusion, reaction rates and solubility (see Table 3.9) (HARTT 1984, NEVILLE 2002). Therefore, at 60°C a faster precipitation of calcareous deposit is expected what can explain the sooner stability in the potential values at 60°C compared to 30°C.

At 90°C (Figure 5.20) the bare steel sample had an initial increase from -600 $mV_{Ag/AgCl}$ to much less negative potentials around -200 $mV_{Ag/AgCl}$, what represents a much higher anodic activity when compared to 30 and 60°C. The XRD analysis showed the presence of $Fe_3O_4$ (magnetite), and also a significant amount of NaCl in its deposit (APPENDIX F), however two high peaks did not have its match found, but may be related to complex seawater element. Under extreme pHs (too high or too low) this film can be formed, however it is not usually stable (MACHMUDAH 2015). Probably, the lack of

presence of other FeOOH constituent, as found at 30 and 60°C, affected the protectiveness of the steel, keeping its potential much lower than previous tests.

The holiday samples at 90°C showed a drop until ~0.18 h of test what, considering the curves of the TSA samples, may be more related with reactions on the TSA coating rather than the steel surface, as same behaviour is observed in TSA samples. As it can be seen in Figure 5.8, only $Mg(OH)_2$ was present at steel surface and start growing when high pH is achieved (9.5 at room temperature) (NEVILLE 2002, BARCHICHE 2003). This value is expected to be lower at higher temperature, therefore facilitating the compound deposition. However, the aluminium oxide found on TSA surface was $Al(OH)_3$ (gibbsite and bayerite) instead of $Al_2O_3$ previous present at 30 and 60°C (see APPENDIX G). Thus, this ageing process may have played a role in the decreasing of potential of holiday and TSA samples, leading it to more negative therefore more protective values. Steady potentials values were found between -800 and -900 $mV_{Ag/AgCl}$. The hydrogen evolution is expected to happen at more positive values in hot steel when compared to steel at room temperature (FISCHER 1983).



Figure 5.18:  Potential of samples exposed to the synthetic seawater at 30°C for ~135 days in free corrosion potential.

Figure 5.19: Potential of samples exposed to the synthetic seawater at 60°C for ~145 days in free corrosion potential.



Figure 5.20: Potential of samples exposed to the synthetic seawater at 90°C for ~130 days in free corrosion potential.

Table 5.1 summarises the approximate potential ranges obtained from holiday samples in each test.

Table 5.1:   Potentials achieved by the samples with holiday in free potential tests.

| Test | 30°C | 60°C | 90°C |
|---|---|---|---|
| Potential (mV$_{Ag/AgCl}$) | between -800 and -920 | between -875 and -900 | between -800 and -900 |

*Corrosion Rate*

The corrosion rate curves are shown from Figure 5.21 to 5.23 and are given in mm/year. Initial characteristics of the curves are consistent with the potential data previously presented, therefore will not be discussed again.

At 30°C (Figure 5.21) the bare steel presented at first a severe corrosion rate of 0.8 mm/year, stabilising in ~0.2 mm/year what is considered a poor or not satisfactory corrosion rate by literature given in Table 5.2 and 5.3, which provides the corrosion rate classification for carbon steel according to two different authors. The graph also gives an interesting comparison between samples with holiday coated with different coating alloy: Al provided a lower corrosion rate (~0.04 to ~0.02 mm/year) compared to AlMg (~0.01mm/year) which were followed by the curves from the TSA samples where TSA-Al reached better corrosion rate. Similar results were acquired by GARTLAND[GARTLAND 1990] where the TSA composed by Al presented an overall better corrosion performance over the AlMg alloy, however this phenomenon is not well known. Although those differences were observed, all the corrosion rates were kept in a low range of 0.01 to 0.001 mm/year and no influence regarding the size of the holiday was noticed.

Figure 5.22 shows that samples with holiday exposed at 60°C synthetic seawater had the corrosion rate dropped from around 0.01 mm/year (with exception of AlMg 5% which dropped from 0.11 mm/year) to values between 0.06 and 0.001 mm/year. However, here no distinction regarding the coating alloy applied on steel was presented. The glass rod TSA coated samples presented the lowest corrosion rate, which was expected, as no damage is present, with values around 0.0004 mm/year.

At 90°C (Figure 5.23) The TSA-Al and TSA-AlMg samples reached values as low as ~0.0001 mm/year while samples with holiday presented values between 0.0051 and 0.045 mm/year. The holiday size apparently affected the corrosion rate which was defined around 30 days of experiment, having a faster decreasing rate in the corrosion rate when compared to 30 and 60°C test, what suggests that the deposit formation happened much faster than previously and must be directly related with the localised pH on steel surface. However, it seems that for different steel surface areas it took longer for the full width and

thickness of the Mg- layer to be reached, allowing species diffusion through it, until a full cover happens. Comparison with bare steel is not represented at 90°C, due to problem with corrosion data acquisition at this temperature.

Thus, the coated samples with holiday presented very good corrosion rate, what shows the high protectiveness of the coating even when damage up 20% of the area surface is taking place. The corrosion rate dropping happened smoothly. An important observation is that, although a $CaCO_3$ was not present at 90°C samples (Figure 5.8 and 5.11), the $Mg(OH)_2$ layer formed was not porous and kept corrosion rate below 0.1 mm/year. Although this is higher value than the achieved when $CaCO_3$ was present, it is still satisfactory according Table 5.2 and 5.3. Therefore, previous statements from literature (item 3.7.1) mentioning that brucite shall be less protective than aragonite (PALMER 2008, CHENGJIE 2014) does not seem to be totally true as it seems to be dependent on the steel surface area: the 5% holiday size, for example, reached values around 0.01 mm/year, comparable to corrosion rates obtained at 30 and 60°C where $CaCO_3$ was also present. Therefore, the proportion cathode-anode in the samples may play a role in the as the corrosion on anode is affected.



Figure 5.21: Corrosion rate of samples exposed to the synthetic seawater at 30°C for ~135 days in free corrosion potential.

Figure 5.22: Corrosion rate of samples exposed to the synthetic seawater at 60°C for ~145 days in free corrosion potential.



Figure 5.23: Corrosion rate of samples exposed to the synthetic seawater at 90°C for ~130 days in free corrosion potential.

Table 5.2:    Qualitative classification of corrosion rates for carbon steel (BABOIAN 2005).

| Corrosion rate (mm/year) | Description |
|---|---|
| < 0.03 | negligible or excellent |
| 0.03 to 0.08 | mild or very good |
| 0.08 to 0.13 | good |
| 0.13 to 0.20 | moderate to fair |
| 0.20 to 0.25 | poor |
| > 0.25 | very poor to severe |

Table 5.3:    Classification for steel corrosion rate (REVIE 2008).

| Corrosion rate (mm/year) | Description |
|---|---|
| < 0.15 | Good corrosion resistance, suitable for critical parts |
| 0.15 to 1.5 | Satisfactory if a higher rate of corrosion can be tolerated |
| > 0.15 | Usually not satisfactory |

In order to assure the values obtained by the software, the corrosion data were also calculated following Equation 3.1 to 3.4 and the last day of each test was considered. The corroding specie was taken to be Al and therefore the B value used was 18 mV. General values used in the equations are specified in Table 5.4. The last day of test was considered for the calculations and intermediate data used along the calculations can be found in APPENDIX K. The obtained and calculated corrosion rates are compared in Table 5.5. No considerable difference between obtained and calculated values was observed as the rates were kept in the same range than those presented in Figure 5.21 to 5.23.

Table 5.4:    General values used for the corrosion rate calculation (BABOIAN 2002, SANKARA 2013).

| $\Delta E$ (V) | $B_{Al}$ (mV) | K | $\dfrac{EW}{\rho}$ |
|---|---|---|---|
| 0.02 | 18 | $3.27 \times 10^{-3}$ | 3.33 |

Table 5.5: Obtained and calculated corrosion rate values for samples with holiday exposed to 30, 60 and 90°C in synthetic seawater after ~145 days in free corrosion potential.

| Sample | Corrosion Rates (mm/year) | | | | | |
| | 30°C | | 60°C | | 90°C | |
| | obtained | calculated | obtained | calculated | obtained | calculated |
|---|---|---|---|---|---|---|
| Al 5% | 0.0009 | 0.0012 | 0.0007 | 0.0006 | 0.0051 | 0.0059 |
| Al 10% | 0.0013 | 0.0015 | 0.0014 | 0.0016 | 0.013 | 0.013 |
| Al 20% | 0.0015 | 0.0021 | 0.0011 | 0.0019 | 0.045 | 0.032 |
| AlMg 5% | 0.010 | 0.016 | 0.0007 | 0.001 | 0.010 | 0.008 |
| AlMg 10% | 0.009 | 0.006 | 0.0008 | 0.012 | 0.019 | 0.014 |
| AlMg 20% | 0.010 | 0.009 | 0.0017 | 0.011 | 0.033 | 0.024 |

Figure 5.24 shows the plot of the calculated corrosion rates of samples with holidays. Generally, the highest CR comprises samples exposed to 90°C test with largest holiday size. At 60°C highest CR are from 10 and 20% holiday AlMg and at 30°C all AlMg samples presented worse CR.
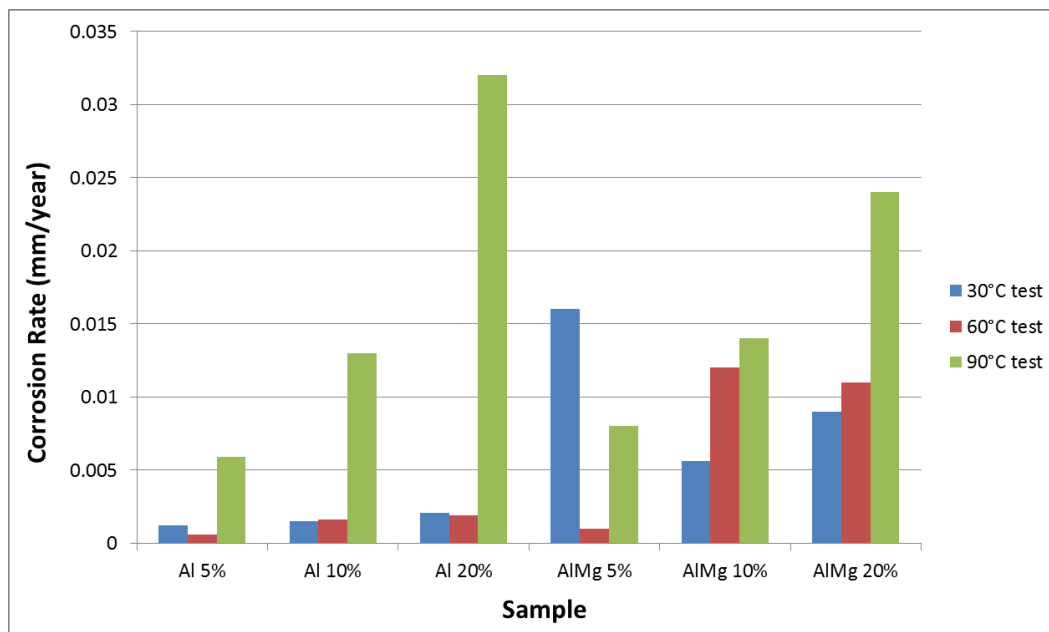


Figure 5.24: Calculated corrosion rate values of samples with holidays, considering the last day of test.

## 5.2 Local pH test

Although a test at 90°C could not be performed due to the temperature range of the pH probe (up to 60°C), this temperature will also be considered further in the discussion when it can be applied. The local pH was monitored up to 350 h and samples after exposure can be seen in Figure 5.25. The dark circle within the holiday is the area touched by the pH probe. The SEM and XRD analyses, where presence of brucite and aragonite were confirmed, can be found in APPENDIX J. The fact that the pH probe was

touching the steel surface may open a discussion regarding a possible obstruction of the oxygen diffusion to the steel surface, what could lead to a wrong pH data. However, the results obtained at 30°C test were already expected, since it should be similar to those at 25°C available in literature. Moreover, although past experiments applied potential, this present study uses TSA coating, which polarises the steel even without external potential applied. Therefore, the results at 30°C in this study were comparable with modelling and experimental past researches, which were not touching the steel surface. It should also be highlighted that even with a careful pH calibration previous to each experiment, the results are expected to be approximate values.

The graph pH versus time graph can be seen in Figure 5.26. The initial pH of ~7.2 increased to 9.87 and from that point it slightly decreased to ~9.6 and later reached a maximum of 10.19 in 20 h. This maximum peak was followed by a smooth drop of pH until stabilization occurred at pH ~8.8. At 60°C the pH increased from 7.51 to a peak of 9.54 in approximately 4h, from where a sharper drop happened until a steady pH of ~7.9 after ~220 h of test.

During the test some events were photographed. At 30°C it is possible to see the rust-colour corrosion product formed on the edges of the holiday after 18h of exposure (Figure 5.27a), which means that at first the steel suffers corrosion. This could explain the rust found in the samples AlMg 5% and AlMg 20% in Figure 5.10, from 60°C steady temperature test. Although those were the samples at 60°C, it is likely to have happened in all samples, however the chance to visualise it depends on the sectioning of the sample to be done right at the place where the rust is present, what may not always have happened. This initial corrosion process could also be a crevice corrosion due to the sharp edges in the holiday, however a previous rust formation was also mentioned by Fischer[Fischer 1983] where roughness was present in hot bare steel samples exposed to seawater. The rust was prevented to grow further as the rust area did not expanded from that showed in Figure 5.27a, what can be seen also in Figure 5.27b. It is possible to identify a thin layer that was being formed within the holiday area in 82 h of experiment. At this point the calcareous deposit was making itself visible. The time the events were registered do not represent the time that it started, but the time it was observed.

At 60°C, the only event observed was in 17 h of test where a thick calcareous deposit layer was already formed (Figure 5.28). This is due to the fact that faster kinetics applies at higher temperatures and will be further discussed in item 5.2.1.
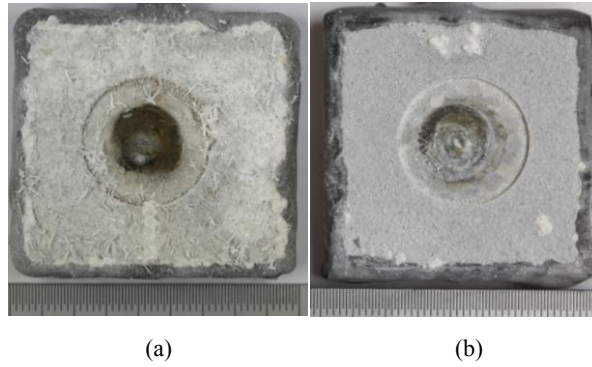
(a)                                    (b)

Figure 5.25: Local pH test samples after exposure up to 350 h at 30°C (a) and 60°C (b).
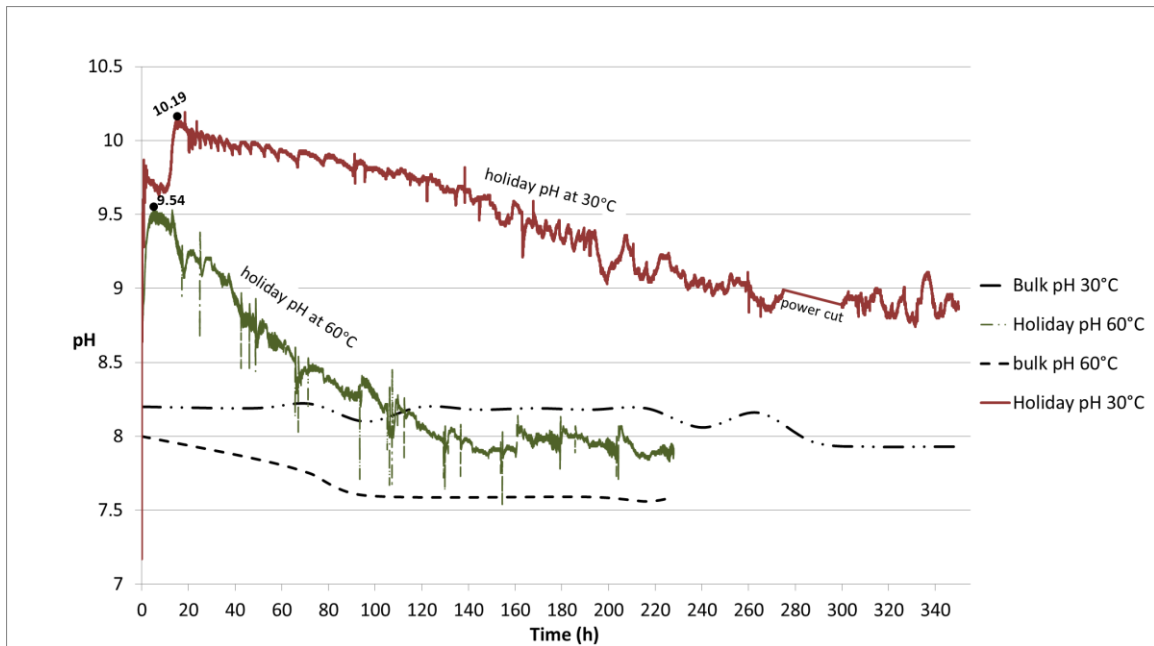


Figure 5.26: pH profiles obtained from the holiday area at 30°C and 60°C synthetic seawater. The pH of the respective bulk seawater is also presented.



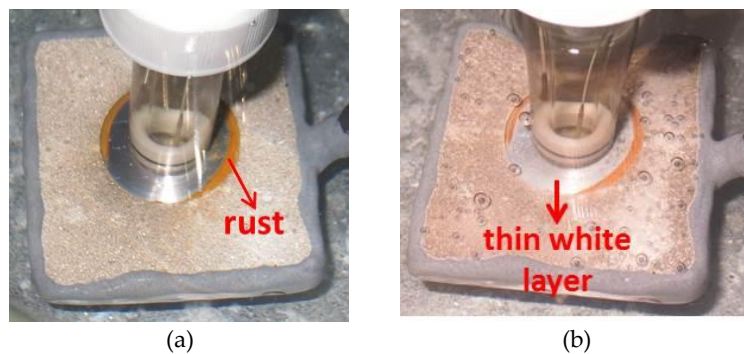(a)                                    (b)

Figure 5.27: Photographs showing the specimen (with holiday) exposed to 30°C seawater; (a) after 18h showing formation of rust on the edges of the holiday at pH 10.08, and (b) after 82 h showing a thin white layer in the holiday at pH 9.84.

Figure 5.28: Photographs showing the specimen (with holiday) exposed to 60°C seawater after 17h showing the holiday covered by a visible deposit of calcareous matter, pH 9.2.

5.2.1    Effect of Temperature on Solubility

The main events that lead to the formation of calcareous deposit such as i) higher local pH at the steel surface (Equation 2.6) and its effect in calco-carbonate system (Equation 2.16 and 2.17), ii) ionic products of the compound ions exceeding the solubility product of Mg and Ca, and iv) solubility effect in the compounds presented in Table 3.9. However, the presence of $CO_2$ in the seawater plays an important role in the formation of $CaCO_3$ as it will affect the calco-carbonate equilibrium in water which species are interrelated following the Equations 4.1 and 4.2 (FAUST 1998).

$$CO_{2(aq)} + H_2O \rightleftharpoons H_2CO_3 \rightleftharpoons H^+ + HCO_3^- \tag{4.1}$$

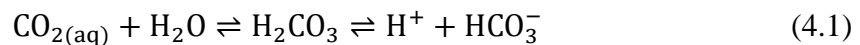$$HCO_3^- \rightleftharpoons H^+ + CO_3^{2-} \tag{4.2}$$

Figure 5.29 shows the solubility of $CO_2$ in water up to 60°C, expressed in amount of substance that is soluble in 100 g of water. It is noticeable that the curve decreases as the temperature increases. At 30°C its solubility is 0.1257g/100g, while at 60°C it is 0.0576g/100g (PERRY 1997). At higher temperatures data is scarce, but according Perry and Green[PERRY 1997] data, the solubility of $CO_2$ in seawater at 90°C is zero. Also, a modelling study at a pressure of 0.06 MPa (0.6 bar) at 80°C reports that the solubility of $CO_2$ is only 0.003 mol% (CARROL 1991). Although the data mentioned is for $CO_2$ at 1 atm and the partial pressure of $CO_2$ ($P_{CO_2}$) in air is ~400 ppmv, the profile given in Figure 5.26 is still valid since same logic is applied.  Those data suggests that the increase in temperature with consequent reduction of $CO_2$ in seawater will diminish the probability of the $CaCO_3$ formation and thus at 90°C the deposition of $CaCO_3$ is unlikely, what matches with the observed in Figure 5.8 and 5.11. Another factor to be considered is that the concentration of $Ca^{2+}$ ions in seawater is only 0.04% compared to 0.13% of $Mg^{2+}$ ions (see

Table 3.4). Brucite is a very thin layer but is able to diminish the oxygen diffusion to the steel surface where it starts to form.
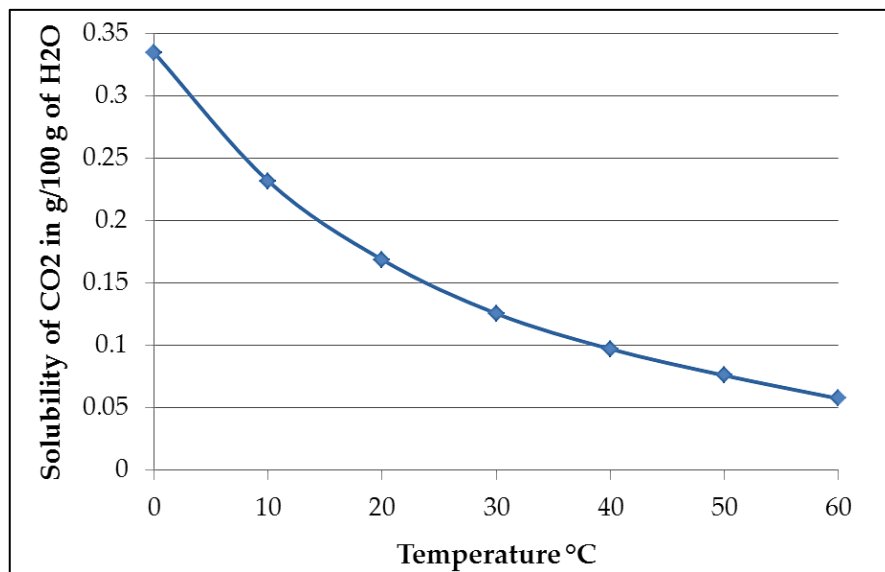


Figure 5.29: Solubility of pure $CO_2$ in water up to 60°C. Data taken from Perry and Green (PERRY 1997).

In summary, only brucite is expected to form at high temperature mainly due to i) higher amount of $Mg^{2+}$ available in solution than $Ca^{2+}$, ii) reduced solubility of $CO_2$ leading to less availability of carbonate species preventing $CaCO_3$ to be formed.

Bearing the observations and discussions in item 4.2 in mind, the following mechanism can be assumed: as seen in Figure 5.26, a maximum point was reached followed by a drop in both 30 and 60ºC. Primarily, the cathodic reaction increases the local [OH⁻] right at the steel surface, what results in the pH increase. Such increasing is prevented after the maximum values of 10.19 at 30°C and 9.54 at 60°C, values which are favourable for the $Mg(OH)_2$ precipitation, what will be further proved in section 4.2.2 [YAN 1993]. This is a very thin base layer (see APPENDIX J) that is able to hinder the diffusion of oxygen towards the steel surface in some areas, where it starts to form. This layer serves as a base layer for the further growth of $CaCO_3$, which is dependent of $CO_2$ diffusion as mentioned earlier and therefore on the calco-carbonate equilibrium (Equations 4.1 and 4.2. Thus, the $CO_2$ is also being consumed to form $CaCO_3$, delaying the pH stabilization as the $CaCO_3$ is still being formed. Once both layers are fully formed, it acts as a organic barrier against further steel corrosion (BARCHICHE 2004, NEVILLE 2002, AKAMINE 2002). In summary, two events are happening even after the maximum peak at 30°C - (i) local formation of OH⁻ and (ii) consumption of $CO_2$ for the formation of $CaCO_3$.

At 60°C, the calcareous deposit was already formed in 17h (Figure 5.26), straight after the maximum peak was reached. This faster limitation of oxygen towards the steel surface, whose content is already less than at 30°C (LEE 1988), rapidly blocked further cathodic reaction and therefore the generation of OH⁻, decreasing the pH faster than at 30°C. Considering less availability of $CO_2$ in solution at 60°C; it seems that the pH was more dependent on the local [OH⁻] at this temperature. The stabilisation also may be related with the hydrogen evolution (Equation 2.3): as the calcareous scale deposited, oxygen reduction reaction rate is diminished while and hydrogen evolution becomes the mainly cathodic reaction, decreasing the pH (OKSTAD 2007).

### 5.2.2 Calculation of minimum pH

In order to obtain more details about the environment that leads to the calcareous deposit formation on steel surface, it is important to know the favourable pH at specific temperature for the deposit precipitation to occur. Those values are reported in literature at 25°C (see item 2.7), but information at the temperature used in this study is lacking.

The minimum pH for precipitation of brucite and aragonite were calculated from the thermodynamic data (Table 5.6) of the species related to its precipitation (Equations 2.15 and 2.17). The value was also calculated at 90°C, even though the local pH experiment was not conducted at this temperature.

Table 5.6: Thermodynamic properties of different species in aqueous solution at 25°C (LIDE 2005, ANDERSON 2009).

| Element | $\Delta H°_f$ (kJ/mol) | S° (J/molK) |
|---|---|---|
| $CO_3^{2-}$ | -677.1 | -56.9 |
| $Ca^{2+}$ | -542.8 | -53.1 |
| $CaCO_3$ (aragonite) | -1207 | 88.7 |
| $Mg^{2+}$ | -466.85 | -138.07 |
| $OH^-$ | -230 | -10.8 |
| $Mg(OH)_2$ | -924.53 | 63.18 |

Firstly, the ΔG° of the reactions where then calculated at 30, 60 and 90°C through Equation 4.3:

$$\Delta G^° = \Delta H - T\Delta S \qquad (4.3)$$

The results were further used to calculate the solubility product ($K_{sp}$) of brucite and aragonite at the different temperatures using Equation 4.4, where R is the ideal gas constant with value 8.314 J.mol$^{-1}$.

$$K_{sp} = \exp^{\frac{-\Delta G°}{RT}}$$ (4.4)

Table 5.7: Calculated values of ΔG° and Ksp of brucite and aragonite at 30 and 60°C.

| Compound | Temperature (°C) | ΔG° [ J.mol$^{-1}$] | $K_{sp}$ [mol$^3$L$^{-3}$] |
|---|---|---|---|
| Mg(OH)$_2$ | 30 | 65024.77 | 6.24 x 10$^{-12}$ |
| | 60 | 71922.47 | 5.28 x 10$^{-12}$ |
| | 90 | 78607.97 | 4.93 x 10$^{-12}$ |
| CaCO$_3$ | 30 | 47335.90 | 6.97 x 10$^{-9}$ |
| | 60 | 53296.90 | 4.39 x 10$^{-9}$ |
| | 90 | 59257.90 | 2.99 x 10$^{-9}$ |

The $K_{sp}$ (Equation 4.5) can be built from brucite formation reaction already specified in Equation 2.15.

$$K_{sp}^{Mg(OH)_2} = [Mg^{2+}][OH^-]^2$$ (4.5)

what leads to Equation 4.6:

$$[OH^-] = \sqrt{\frac{K_{sp}^{Mg(OH)_2}}{[Mg^{2+}]}}$$ (4.6)

The ionic product of water (Kw) is expressed in Equation 4.7 and the values are specified in Table 5.8 (MARSDEN 2006, WHITTEN 2013, DELYANNIS 1978).

$$K_w = [H^+][OH^-] \text{ or } [H^+] = \frac{K_w}{[OH^-]}$$ (4.7)

which could be used for the calculation of the minimum pH required for the precipitation of Mg(OH)$_2$ (Equation 4.8. The concentration of Mg$^{2+}$ was calculated from data in Table 4.4 as 0.054 M. The $K_{sp}$ was taken from Table 5.7.

$$pH_{Mg(OH)_2} = -\log[H^+] = -\log\frac{K_w}{\sqrt{\frac{K_{sp}^{Mg(OH)_2}}{[Mg^{2+}]}}}$$ (4.8)

The same logic can be used for the calculation of the minimum pH necessary for the formation of CaCO$_3$, however now the Equation 2.16 which relates the [OH⁻] with the

$[CO_3^{2-}]$ (equal concentrations) must be considered. Then, the Equation 4.9 can be derived, furthering resulting in Equation 4.10. The concentration of $Ca^{2+}$ in synthetic seawater was calculated from the data in Table 4.4 as 0.010 M.

$$[CO_3^{2-}]=\frac{K_{sp}^{CaCO_3}}{[Ca^{2+}]} \quad \text{or} \quad [OH^-]=\frac{K_{sp}^{CaCO_3}}{[Ca^{2+}]} \tag{4.9}$$

$$pH_{CaCO_3}=-\log[H^+]= -\log \frac{K_w}{\frac{K_{sp}^{CaCO_3}}{[Ca^{2+}]}} \tag{4.10}$$

Having the data and expressions needed, it was possible to calculate the minimum pH for the precipitation of both brucite and aragonite. A summary of the data and results can be found in Table 5.8.

Table 5.8: Data and results of the minimum pH required for precipitation of brucite and aragonite (ASTM D1141, MARSDEN 2006, WHITTEN 2013, DELYANNIS 1978).

| Temperature | Concentration (M) in synthetic seawater | | Ionic Product of Water $(mol^2L^{-2})$ | Minimum pH for precipitation | |
|---|---|---|---|---|---|
| (°C) | $[Mg^{2+}]$ | $[Ca^{2+}]$ | $K_w$ | $pH_{Mg(OH)_2}$ | $pH_{CaCO_3}$ |
| 30 | 0.054 | 0.010 | $1.47 \times 10^{-14}$ | **8.86** | **7.61** |
| 60 | 0.054 | 0.010 | $9.60 \times 10^{-14}$ | **8.01** | **6.66** |
| 90 | 0.054 | 0.010 | $38.02 \times 10^{-14}$ | **7.40** | **5.89** |

The results above achieved at 30 and 60°C show that the conditions required for the compounds deposition were generated in the local pH experiment from section 5.2, as the pH right at the steel surface reached values higher (as 10.19 at 30°C and 9.54 at 60°C) than the minimum required. The exact pH where the deposit started to be formed is difficult to predict as it depends on complex interactions involving various seawater species. Same logic is to be applied at 90ºC.

The presence of $Mg^{2+}$ present in seawater, for example, was reported to hinder the nucleation of $CaCO_3$ (BARCHICHE 2003). Neville and Morizot[NEVILLE 2002] considered that the main function of $Mg^{2+}$ is to form the Mg layer which will make the conditions favourable for the further formation of $CaCO_3$. Both considerations are important to understand that prior to the formation of the brucite layer (which consumes the $Mg^{2+}$ ions from the solution by forming a precipitate) no aragonite should be formed. In addition, Barchiche et. al[BARCHICHE 2004, BARCHICHE 2009] mentioned that the presence of $SO_2^{4-}$ ions can prevent the deposition of $CaCO_3$ and allow the precipitation of a magnesium hydroxide

although the mechanism is not entirely clear. These previous experimental data may help to understand the reasons for the delay in the deposition of $CaCO_3$ and why it is only formed at higher pH than the calculated values in Table 5.8.

The decreasing in pH with temperature was already reported by Lee and Ambrose[LEE 1988], who reported that although the amount of dissolved oxygen content in water increases with a decrease in temperature, the diffusion coefficient of oxygen is diminished as well as the hydrogen evolution reaction.

### 5.2.3 Neutral Point of Water at Higher Temperatures

A wrong assumption can arise as at first it seems that $CaCO_3$ is ready to precipitate in acidic media at 60°C, as its favourable pH was found to be 6.6. However, it must be considered that the neutral point of water changes with temperature. It is known that at 25ºC its value is 7.0. At higher temperatures this value is expected to decrease. At 30 and 60ºC this value can be easily calculated through the $K_w$ value from Table 5.8. It is known that the neutrality happens when the relation in Equation 4.11 takes place.

$$[OH^-] = [H^+] \tag{4.11}$$

which, according Equation 4.7, can be rewritten as Equation 4.12:

$$K_w = [H^+]^2 \tag{4.12}$$

Using above equation, the neutral point of water was calculated as 6.92 at 30°C, 6.51 at 60°C and 6.21 at 90ºC. It can be observed that at the latter temperature, the $CaCO_3$ is ready to be formed at slightly acid media however the delay effect of the other species present in the seawater, already discussed, would probably push this value to alkaline pH.

### 5.2.4 Mechanism of the Calcareous Deposit Formation

From the exposure tests at 30, 60 and 90°C and the local pH experiment, the main mechanisms involved in the growth of calcareous deposit on the steel surface could be built, and the following can be suggested:

i)      The availability of oxygen leads to the steel corrosion, which starts to happen on the edge of the exposed steel surface, where anodic reactions take place, releasing electrons to cathodic areas;

ii)      Oxidation also happens on the TSA, where aluminium oxide is formed on the surface, releasing electrons and polarising the steel;

iii)      The cathodic reaction produces $OH^-$, increasing the pH right at the steel surface;

iv)     As soon as the local pH reaches the required value at certain temperature, brucite is allowed to precipitate. Its growth starts to decrease the local pH due to prevention of further anodic reactions, as it restricts oxygen diffusion to the steel surface;

v)     In parallel, the diffusion of $CO_2$ into the seawater is happening, acting in the calco-carbonate equilibrium and forming carbonate $(CO_3^{2-})$. The formation of $OH^-$ also facilitates its production and further formation of $CaCO_3$;

vi)     The $CaCO_3$ will precipitate as long as the pH is favourable and the $Mg(OH)_2$ have already been formed, however at 90°C, its precipitation will not happen due to lack of $CO_2$.

A schematic of a cross section view is given in Figure 5.30, where $P_{O2}$ and $P_{CO2}$ are the partial pressures of the respective elements.
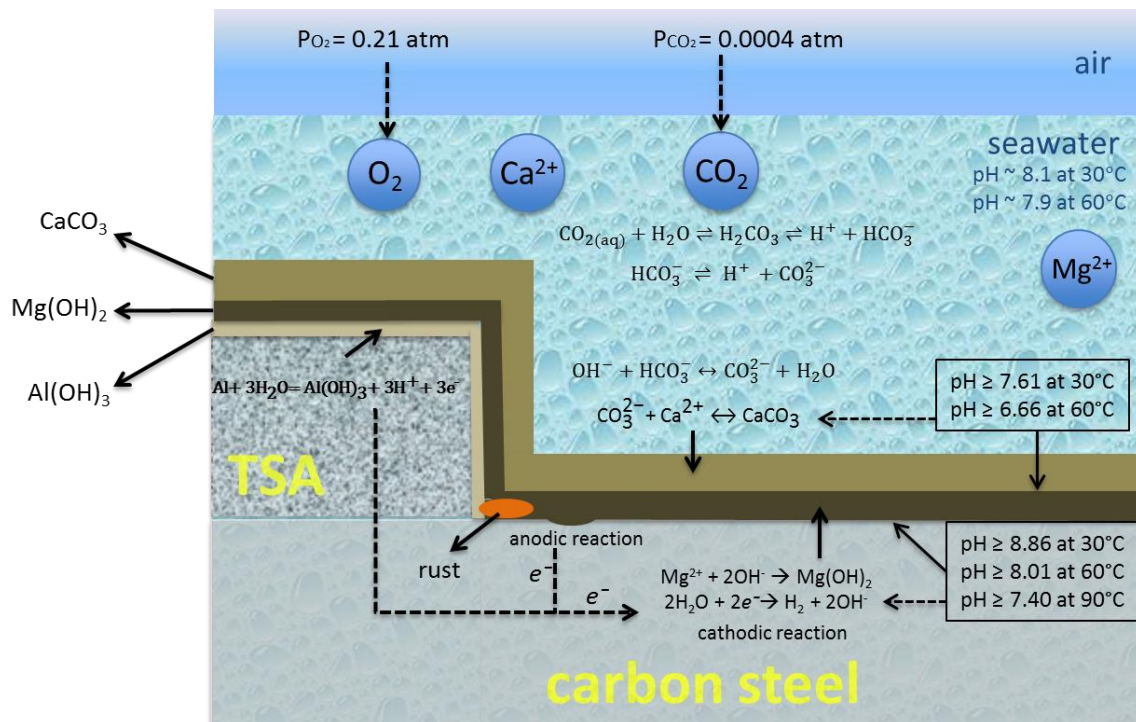


Figure 5.30:  Schematic of the mechanism of the calcareous deposit formation when steady temperature is applied.

5.3        Thermal Gradient Test

The thermal gradient test results will be presented in items 5.3.1 to 5.3.4.

5.3.1      Visual Inspection

Samples after the exposure to the thermal gradient test are showed in Figure 5.31. Buried samples presented a dark brown aspect due to the sand that remained attached to its surface. It was not removed in order to keep the calcareous deposit that was believed to have precipitated. Samples CP6 (unburied, unsealed) and CP7 (unburied, sealed) were lost before the end of the test due to the fully corrosion that happened by an unclear reason, but must be related to the oil leaking that happened in the final moments of the test, mixing the seawater with oil and heating the same. Although those samples were lost for the characterisation test, its corrosion data were kept. Also, it is possible to observe a green deposit on some samples, what happened to be Zn and Cu, probably provided by contamination from the connection wires at some point of the test.  As those events happened after the formation of the protective deposits on the specimens, which is supposed to have formed in the early stages of the experiment, it did not influence the main results.
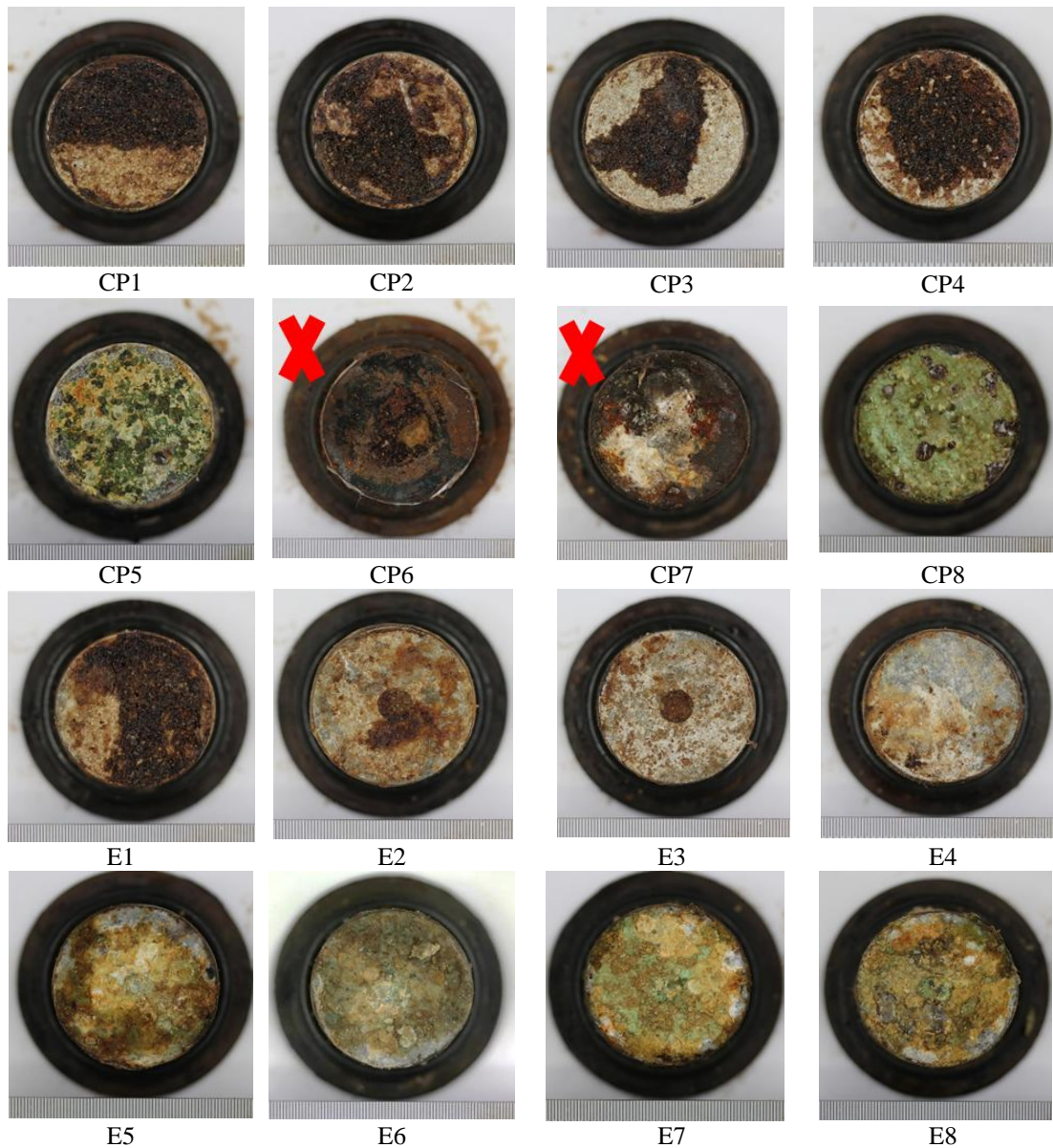
Figure 5.31: Samples after to the thermal gradient exposure.

## 5.3.2   Microstructural Characterization

Due to the contamination and the sand attached to the samples' surfaces, only cross section view analysis will be showed as the top view did not give relevant information.

### *Free Potential Specimens*

Generally, same deposits were found in the holiday area of the buried and unburied samples, however samples exposed to the sand presented high amount of Si-grains mixed with the deposit. Figure 5.32 shows the buried samples tested under free potential where the image at the right represents a zoom in of the holiday area. Although some amount of the deposit was lost, the analyses were carried out in the remaining

deposit. Basically, Ca and Mg (Figure 5.35a and b) compound were identified as expected, but now also Ca-S-O compound took place as labelled and showed in EDX spectra in Figure 5.35c. The unburied samples presented a homogeneous layer along the holiday due to lack of sand. The layer was a mix of Ca and Mg compound as labelled in Figure 5.33 and showed in the EDX in Figure 5.35a and b. This mixing may have happened due to the temperatures changes and adjustments in the beginning of the test, providing successive solubility and precipitation of Mg and Ca. Again zinc and copper also appeared (Figure 5.35e), probably from some contamination from the surroundings during the test. The EDX results from each sample can be found in APPENDIX H.
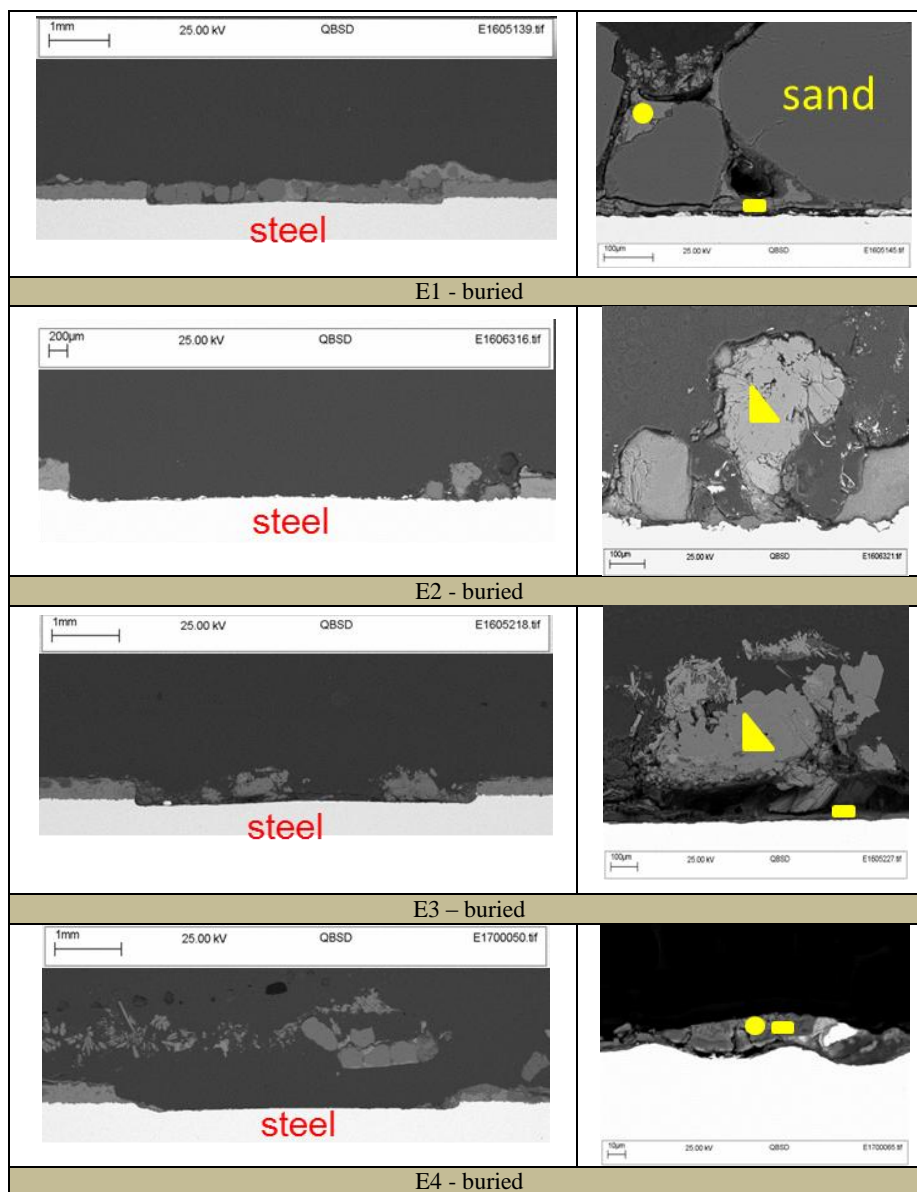


Figure 5.32: Cross-section of the buried samples exposed to the thermal gradient test under free-potential.

| | |
|---|---|
| | E5 - unburied |
| | E6 - unburied |
| | E7 –unburied |
| | E8 - unburied |
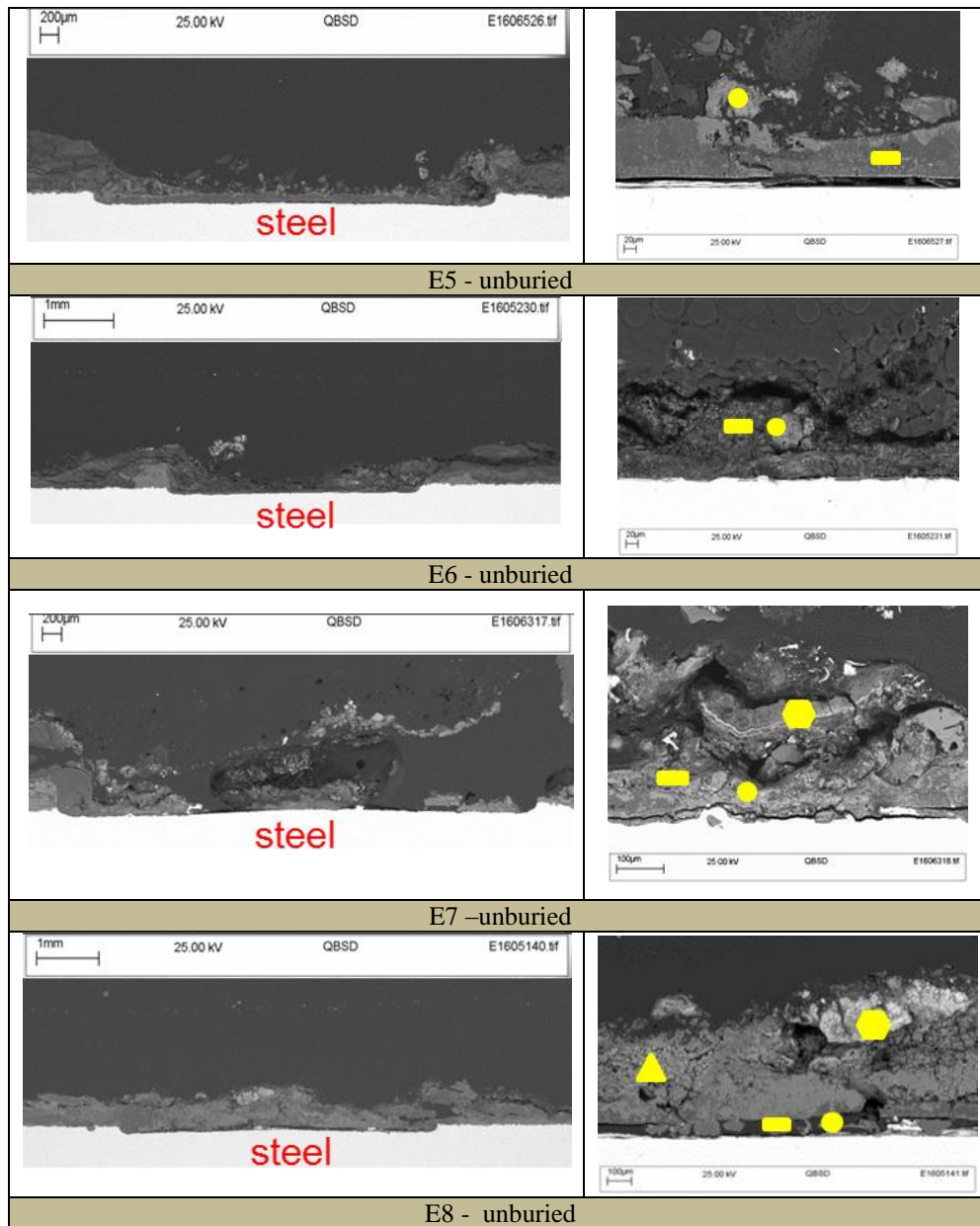
Figure 5.33: Cross-section of the unburied samples exposed to the thermal gradient test under free-potential.

When sealed and unsealed samples are compared (Figure 5.34) it is possible to observe that no sealing remained on the TSA, which was sometimes highly consumed into aluminium-oxide as labelled and analysed by EDX in Figure 5.35f (full results in APPENDIX I). Although the remaining TSA was very irregular, an average of ten measurements of TSA thickness in each sample was taken in order to obtain a general range of thickness remained after exposure from all samples. It was found that thicknesses varied between $154 \pm 4$ and $272 \pm 3$ µm, showing that sometimes the loss of coating was high compared to the nominal thickness of 300 µm.
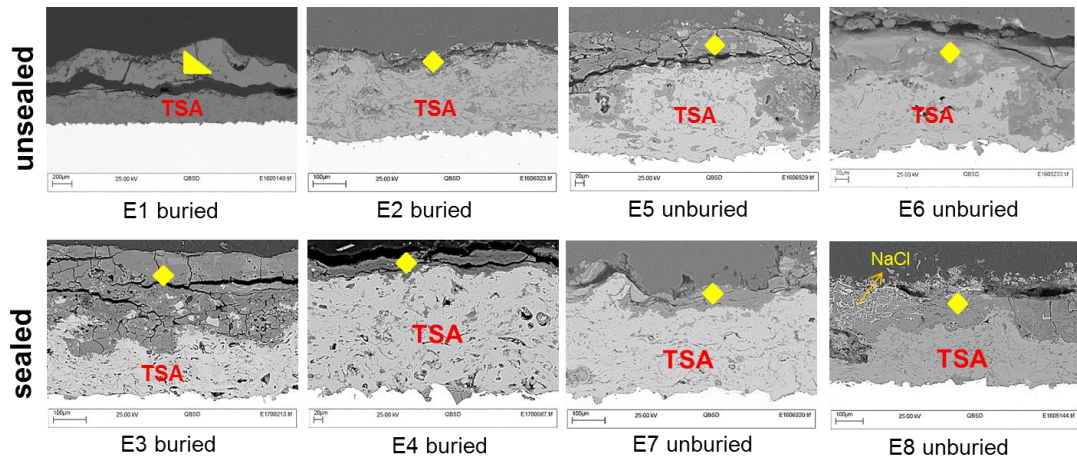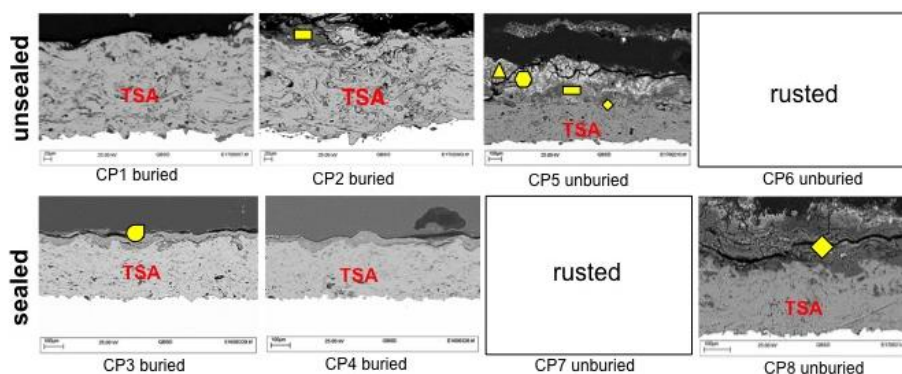
Figure 5.34: Analysis in the TSA coating, comparing sealed and unsealed $E_{corr}$ samples.
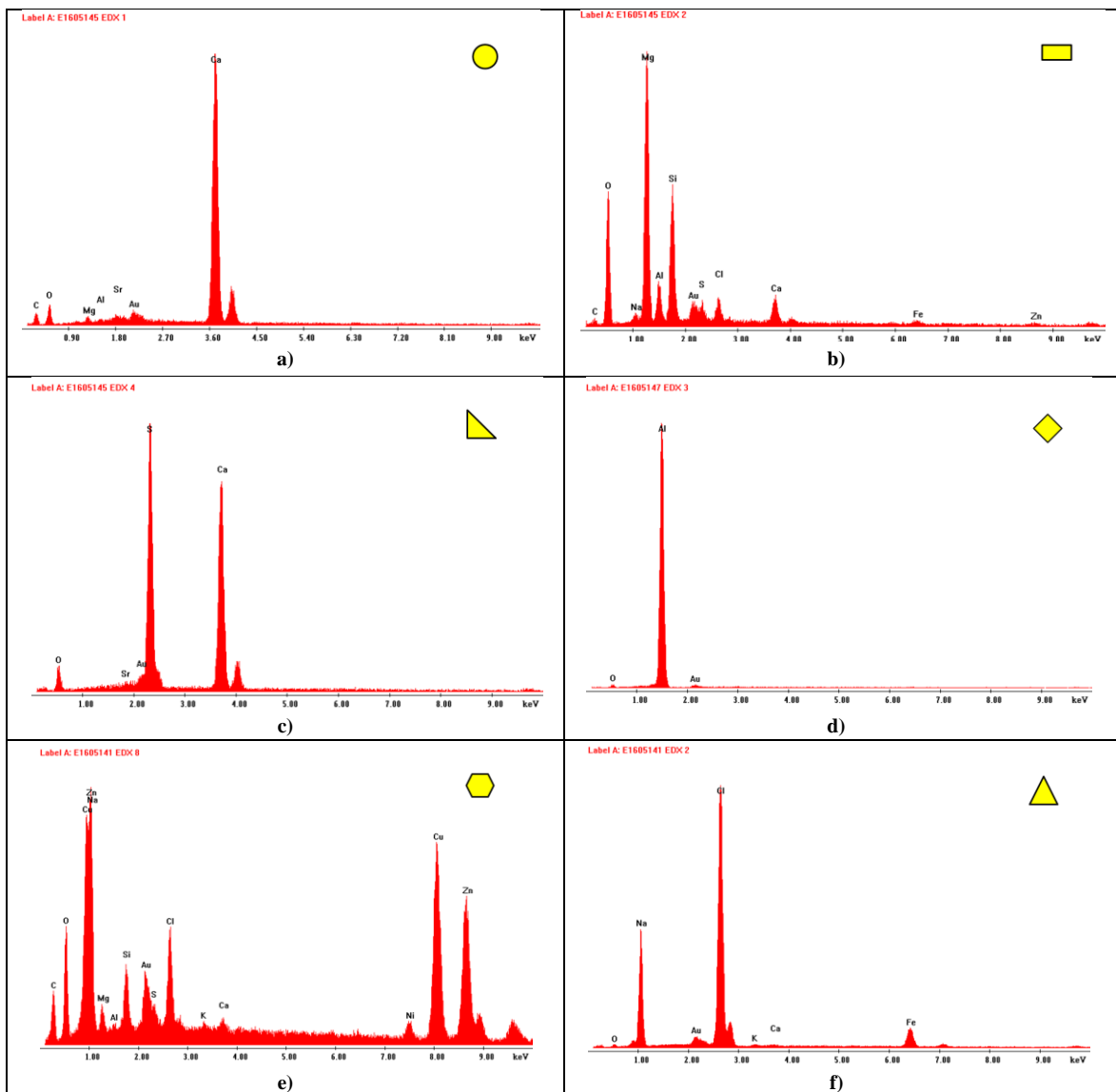


Figure 5.35: EDX results as labelled in Figure 5.32 to Figure 5.34. Results from samples E1 and E8 where the following mean peaks were detected, a) Ca, C and O; b) Mg and O; c) Ca, S and O; d) Al and O; e) Cu and Zn; f) Na and Cl.

Regarding the holiday area, the polarised samples presented same characteristics as the free potential samples, showed in Figure 5.36(buried condition) and Figure 5.37(unburied condition), which comprises only two of the samples due to the loss of CP6 and CP8 as mentioned earlier. The EDX identified the main deposits as Ca-C-O (Figure 5.39a), Mg-O (Figure 5.39b), Ca-S-O (Figure 5.39c) and compounds and also Zn, Cu, and NaCl (Figure 5.39d and e) were present (full results can be seen in APPENDIX H).
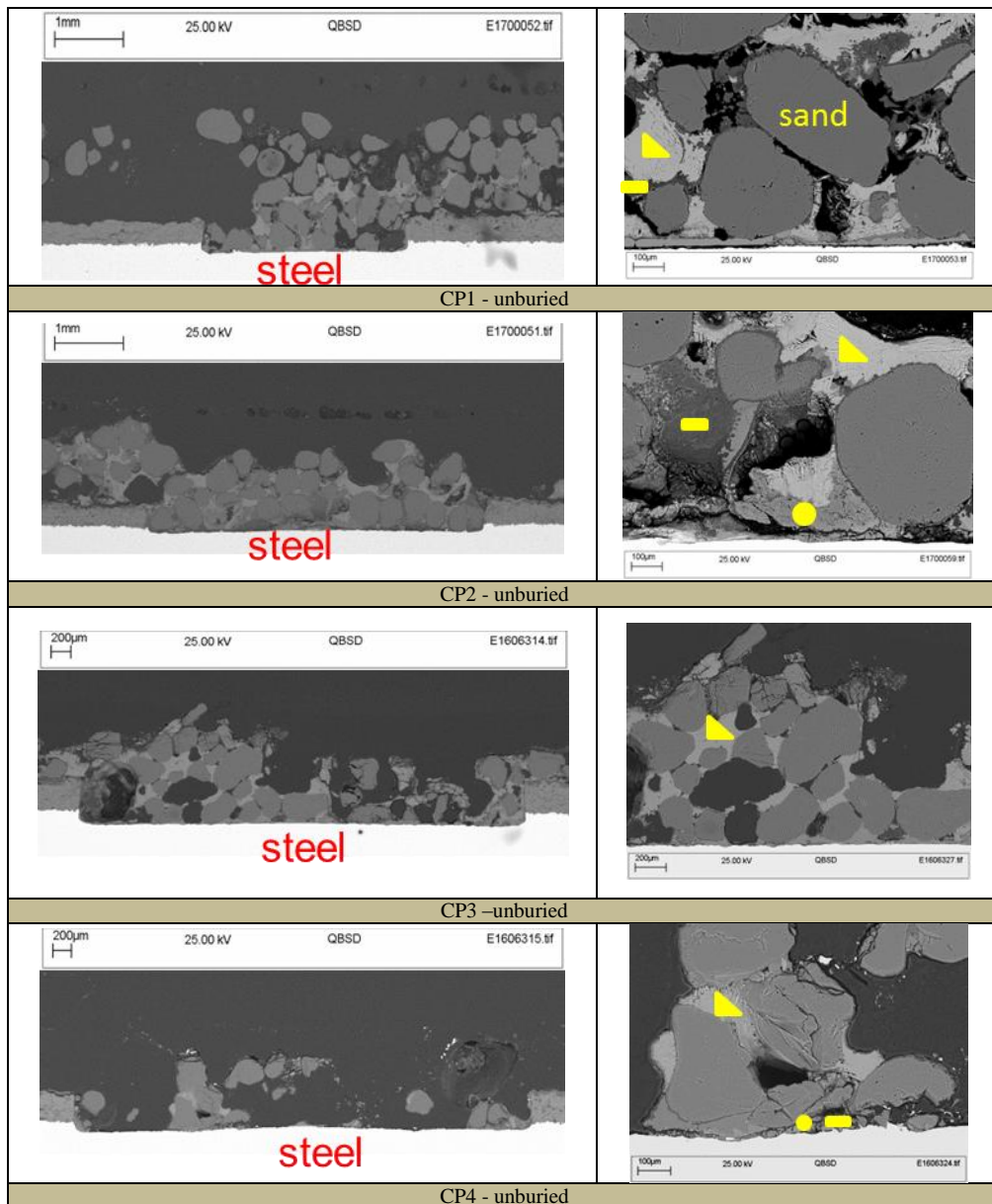


Figure 5.36: Cross-section of the buried samples exposed to the thermal gradient test under -950 mV$_{Ag/AgCl}$.
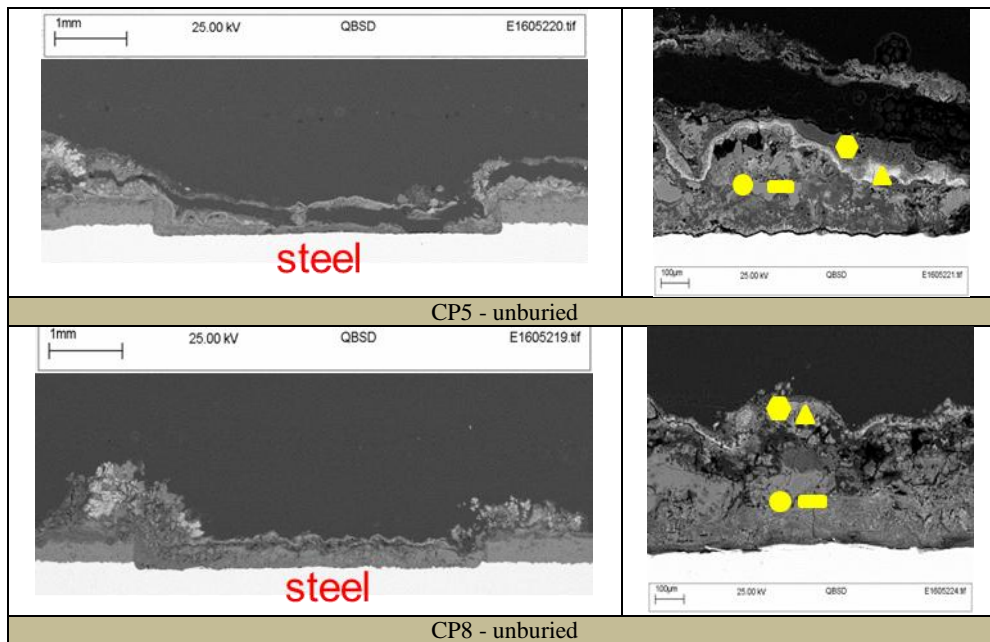
Figure 5.37: Cross-section of the unburied samples exposed to the thermal gradient test under -950 mV$_{Ag/AgCl}$.

By Figure 5.38 it could be observed that the coating was less consumed into aluminium oxide (Figure 5.39f – full results in APPENDIX I) compared to the E$_{corr}$ samples. Also, some traces of aragonite and brucite could be seen in samples CP2 and CP5, providing some protection against the consumption of the TSA coating. Probably, the polarisation increased the local pH on TSA, making it favourable for the deposition of those constituents. Moreover, it could be observed that the sealing was still present in samples CP3 and CP4, both unburied samples, which was not consumed as previously. The polarisation acting together with the physical protection of the sand barring some of the oxygen diffusion towards the samples' surface was beneficial as the consumption of the sealing was prevented. Thicknesses after exposure were kept between ~250 to 302 μm, higher range compared to samples at free potential.



Figure 5.38: Analysis in the TSA coating, comparing sealed and unsealed polarised samples.
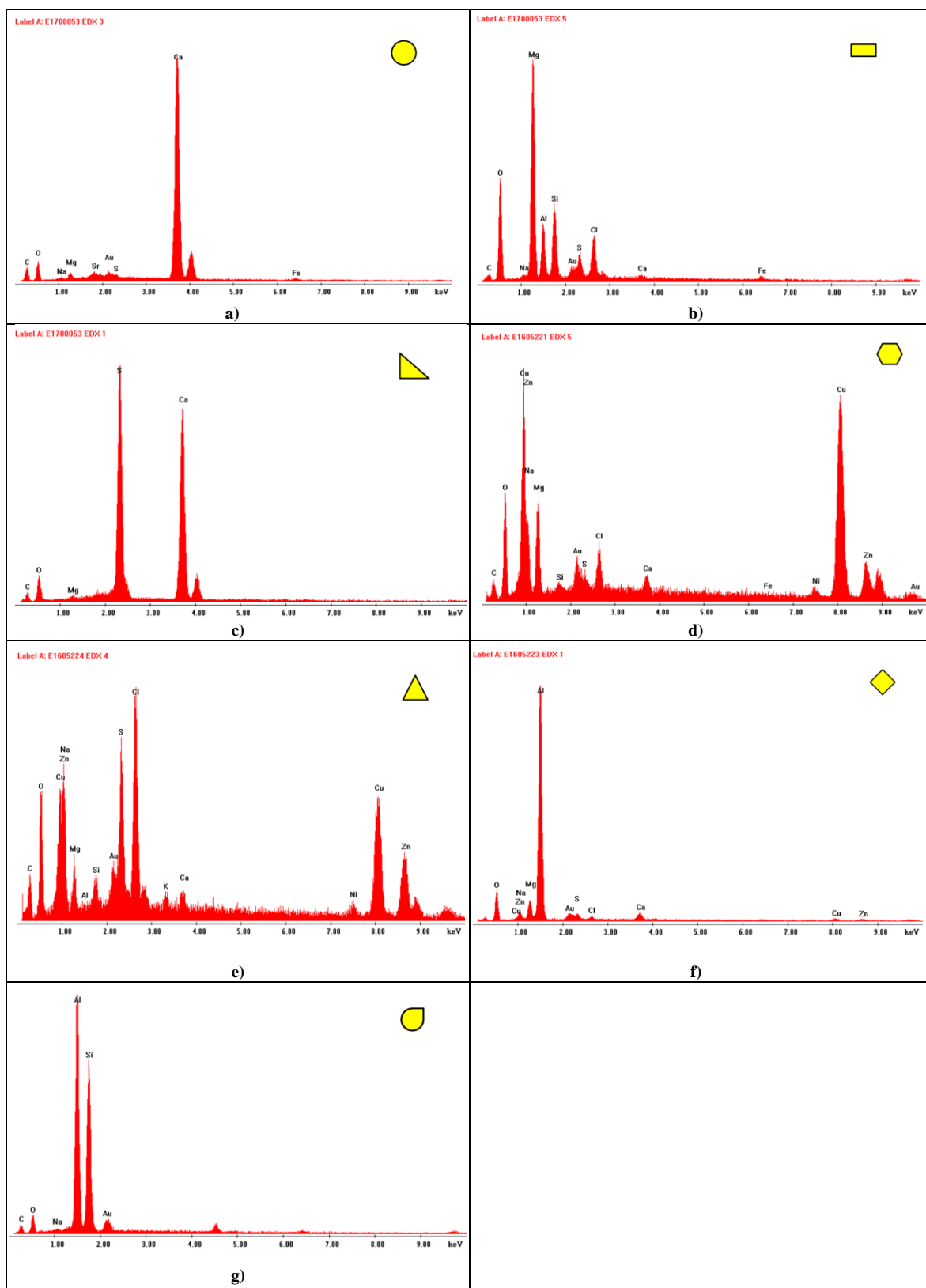
Figure 5.39: EDX results as labelled in Figure 5.36 to Figure 5.38. Results from samples CP3 and CP5 where the following main peaks were observed: a) Ca, C and O; b) Mg and O; c) Ca, S and O; d) Al and O; e) Zn and Cu ; f) Na and Cl; g) Al and Si.

### 5.3.3    X-Ray Diffraction

Due to difficulty to extract the deposit from some of the samples for the XRD analysis, it could only be performed in deposits from samples E2 and E7 (Figure 5.40), as well as CP5 and CP8 (Figure 5.41). The deposits were extracted from holiday area and TSA surface. The Al-Si sealing was not detected in sample E7. Traces of aragonite and brucite were observed in all samples apart from sample E2 probably due to very few amount formed and high loss of the deposit in the holiday as can be seen in Figure 5.42. In samples CP5 and CP8 only traces of brucite were observed. However, mainly NaCl, Cu and Zn took place. The Ca-S-O element observed in buried samples (Figure 5.32 and 5.36) could be identified as Gypsum ($CaSO_4.2H_2O$).



E2 – free potential, buried, unsealed

E7 – free potential, unburied, sealed
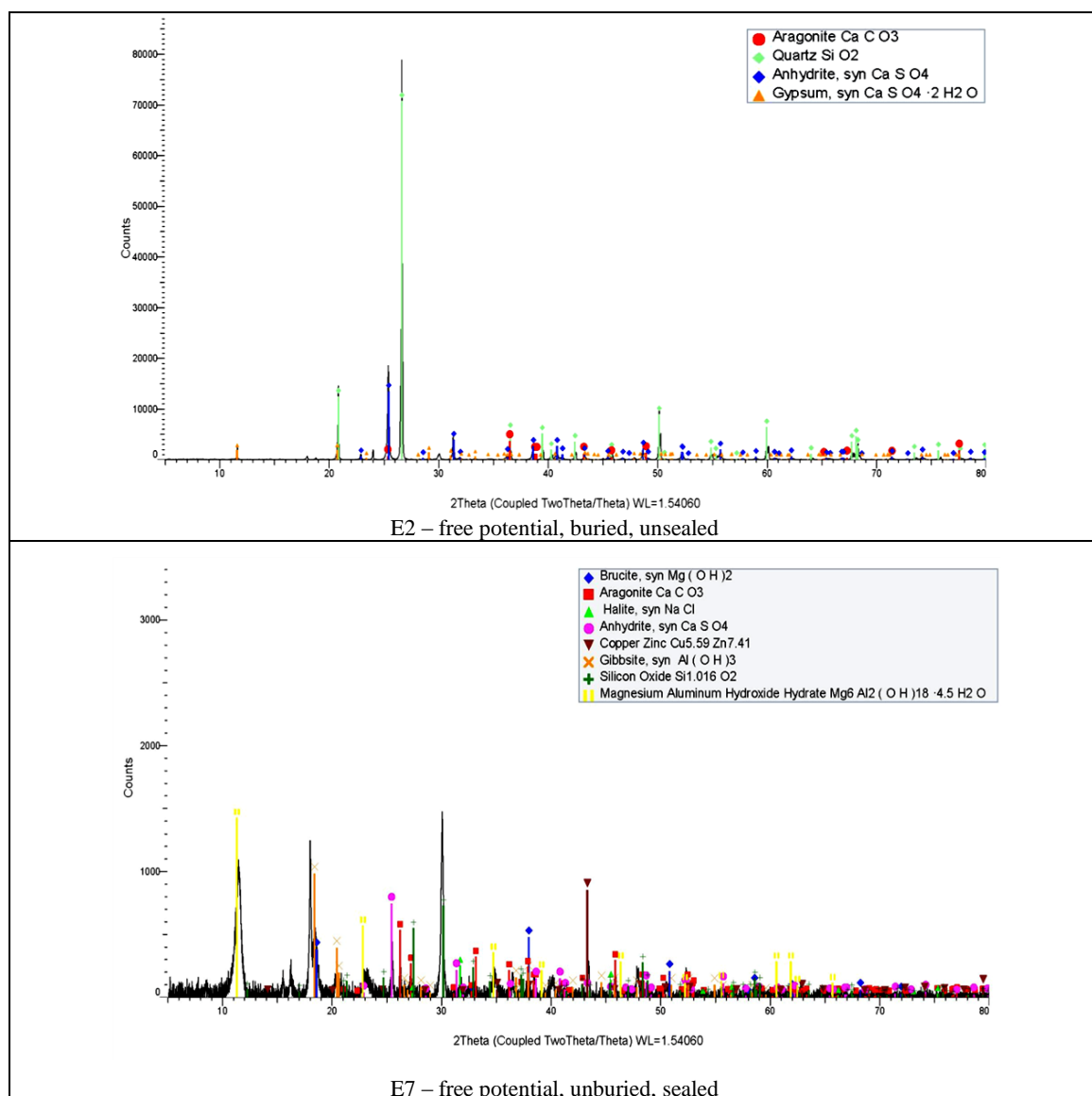
Figure 5.40: XRD patterns from deposits formed in samples E2 (above) and E7 (below). Presence of brucite and aragonite were detected.
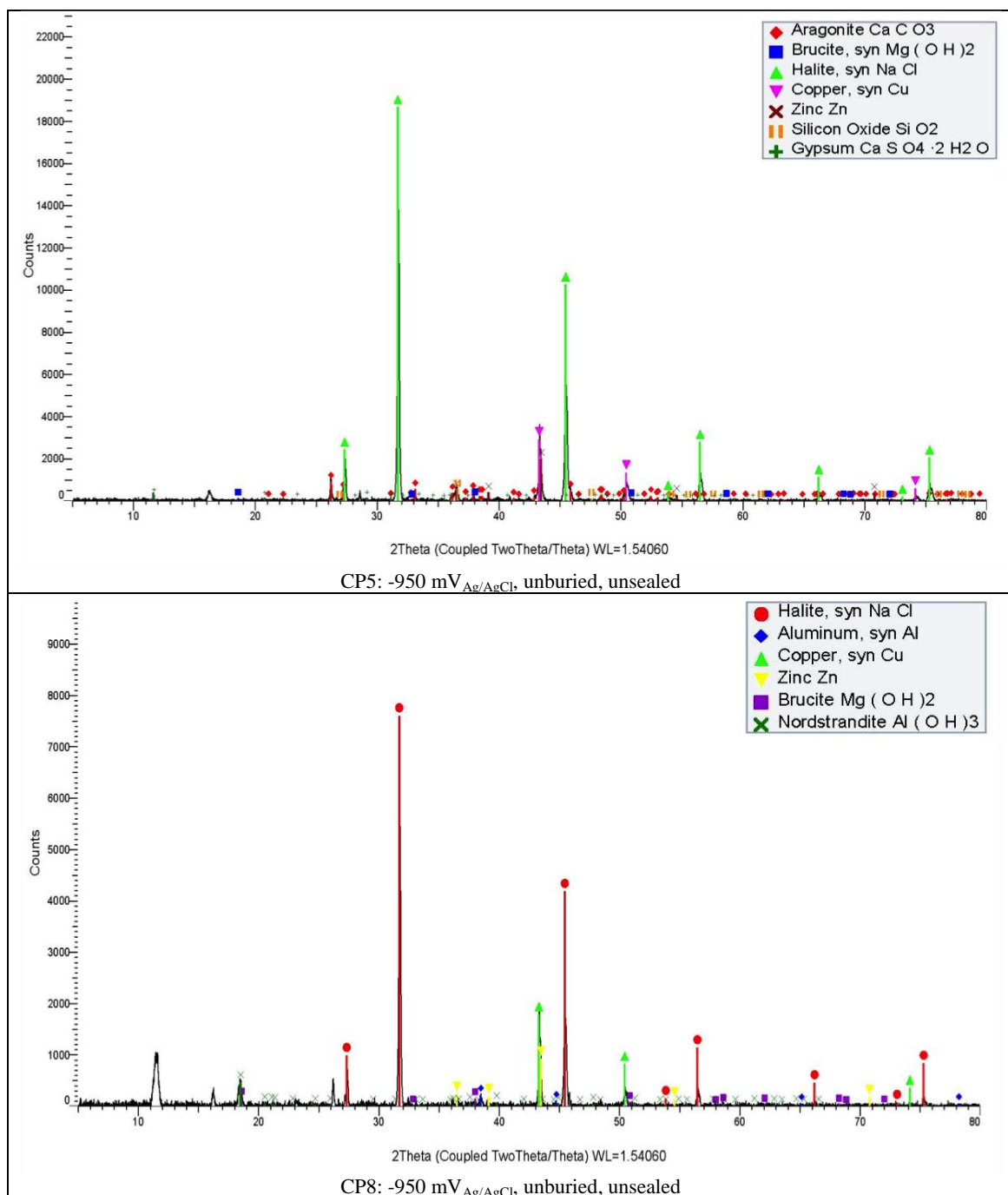
Figure 5.41: XRD patterns from deposits formed in samples CP5 (above) and CP8 (below). Presence of brucite and aragonite were detected.

Gypsum is a well kwon element to precipitate from the seawater, which leads to a saturation/supersaturation of some elements and their precipitation. The first constituent to be expected is a small amount of $CaCO_3$ due to the low concentration of bicarbonate and carbonate ions in seawater (0.014% by weight). When the volume of seawater is reduced to 19% of its original volume, calcium sulphate is precipitated either as an anhydrite ($CaSO_4$) or as gypsum ($CaSO_4.2H_2O$). The sodium chloride in the form of halite (NaCl) is formed in higher amount when the volume is reduced to 9.5% of the original one. The

final volume (4%) will contain the highly chlorides of potassium and magnesium (WRIGHT 1995). The pH of the bulk seawater will change as the compounds precipitate from seawater.

The formation of gypsum in thermal gradient test can be explained by its solubility data. It can be observed in Figure 5.42 that the solubility reaches a maximum between 30-40°C from where the values starts to fall until 100°C (in temperature range 0 to 100°C). Therefore, precipitation of $CaSO_4$ is expected to occur in higher amounts at low and high temperatures. Figure 5.43 gives the temperature monitored by the thermocouples (as specified in Figure 4.4) along the test. Buried samples stabilised at ~100°C, where the solubility value reaches its minimum and precipitation is favourable.
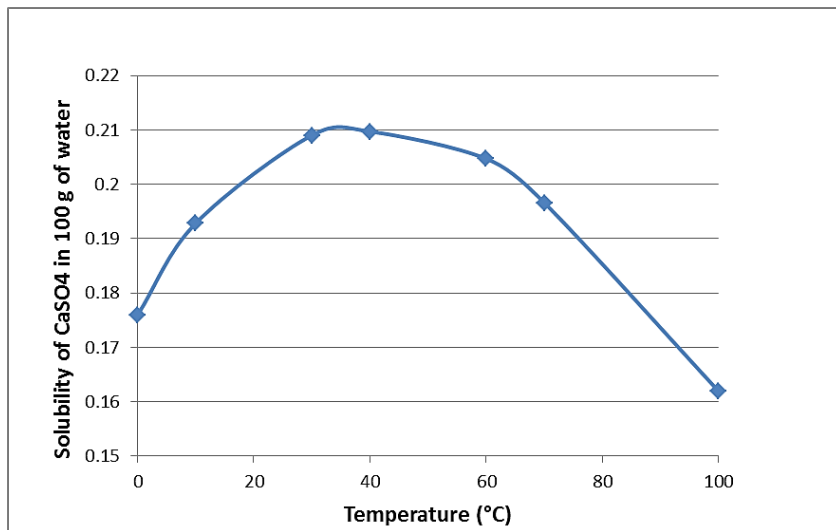


Figure 5.42: Calcium sulphate solubility profile (PERRY 1997).
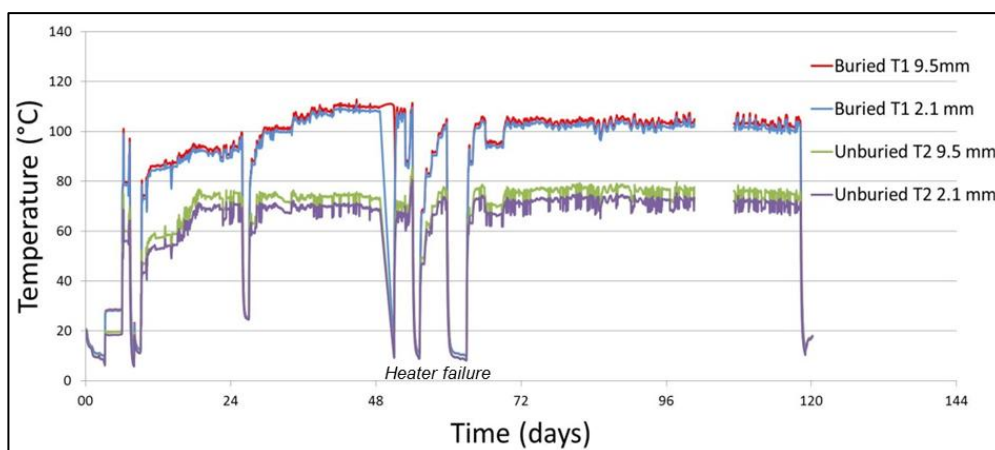


Figure 5.43: Temperature from thermal gradient test acquired from thermocouples at different distance from surface.

The unburied samples were maintained in temperatures where some $CaSO_4$ would be expected, however no presence was observed (Figure 5.33 and 5.37), having only traces detected by the XRD from sample CP5 (Figure 5.40). That may have happened because in buried condition the sand works as an interfacial barrier for the seawater. It can be seen in Figure 5.32 and 5.36 that the gypsum was found trapped among the sand grains, while probably the seawater has washed the gypsum formed in unburied samples away. Same must have happened with samples in steady temperature test, where buried condition was not applied.

5.3.4    Corrosion Data

Potential, corrosion rate and current demand of the samples from thermal gradient test are showed below.

*Potential and Corrosion Rate (free potential samples)*

Samples under free potential (E1 to E8) had their potential x time and corrosion rate x time plotted.

The potential (Figure 5.44) presented instability in the initial days, which may have happened due to the temperature adjustments in the beginning of the test as observed in Figure 5.43. Samples E1 and E2 which are duplication of the same condition achieved potential as negative as -1064 in the 4$^{th}$ day of test, but later achieving approximate -700 mV$_{Ag/AgCl}$ after 8 days. No proper discernment between sealed and unsealed samples can be estimated. However, in the first day of test, it is possible to see in the zoomed in image of the graph that a dropping to more negative potentials happens in the buried samples achieving more negative potentials from the 2$^{nd}$ day of test, while unburied samples keep in potentials around 670 mV$_{Ag/AgCl}$. Buried and unburied potentials follow instability until the 10$^{th}$ days in potentials between -745 and -835 mV$_{Ag/AgCl}$ until 115 days of test. Those values are below the ones reached previously at steady temperatures and it is lower than the protective potential specified in standards (which is -800 and -900 mV), however, it must be considered that it represents the TSA acting as the only polarisation source, in a more severe environment. No clear relationship regarding the different conditions applied on the samples could be noticed.

Figure 5.44: Potential obtained from $E_{corr}$ samples exposed to thermal gradient.

Figure 5.45 shows the corrosion rate curve at free potential. In the zoomed in image inset in the graph it is possible to see that initially (in the first 10 days of test) a slightly better CR were achieved by sealed samples E3 and E4, which were buried, what suggests that the sand barrier plus the sealing were acting effectively against corrosion. Same behaviour was not followed by sealed unburied samples (E7 and E8), suggesting that when heating is applied and another physical barrier (as sand) is not present, the sealing is not effective. Between 10 and 30 days of test, the best performance was given by the buried samples (E1, E2, E3 and E4), what was expected once the sand promotes a physical barrier against the oxygen diffusion due to the more restrictive drainage of the seawater (REVIE 2000, REVIE 2011).

After ~70 days of test, the stabilisation of the corrosion rate was being shaped, which was kept between 0.35 and 0.01 mm/year. Surprisingly, most of the samples (E2, E3, E4) that presented the best performance in the beginning of the test (i.e. buried condition), presented the poorest corrosion rate values as high as ~0.35 to ~0.1 mm/year in ~115 days of test. Sample E1, on the other hand, finished the test with the lowest corrosion rate among all samples, with value ~0.01 mm/year. Sample E4 presented a very poor CR (around 0.35 mm/year) what may have happened by loss of deposit around the 45th day as

it can be seen in Figure 5.32, where a wide area not covered by corrosion products can be seen, compared to the other samples.

The corrosion rate results suggest that the sand may have worked against the corrosion in the beginning of the samples exposure; however, after the oxygen happened to have reached the samples surface through the seawater, it seems that corrosion was facilitated by the lack of flow. When sealing was present in buried samples, even lower initial CR could be achieved. It can be observed in Figure 5.32 and 5.33 that the exposed steel did not suffer severe corrosion and therefore the final corrosion rate represents mainly the consumption of TSA into aluminium oxide (Figure 5.34). Literature reports that in most soils the corrosion occurs in form of deep pitting, being more damaging for the metal than a uniform corrosion rate (REVIE 2008, DAVIS 1999). Moreover, the soil characteristics can compromise the performance of the cathodic protection if, for example, the conductivity of the soil is not appropriated considered (REVIE 2011).



Figure 5.45: Corrosion rate obtained from $E_{corr}$ samples exposed to thermal gradient.

Corrosion rates were confirmed by calculation using Equation from 3.1 to 3.4 and a point near to the end of the test (~115th day) was considered for each sample. The general values used in equations are in Table 5.4 and the full data can be found in APPENDIX K. The obtained and calculated corrosion rates are compared in Table 5.9 and although calculated values were a bit higher, no large discrepancy was observed.

Table 5.9: Obtained and calculated corrosion rate values for samples exposed to thermal gradient under free potential.

| Sample | Corrosion Rate (mm/year) | |
| --- | --- | --- |
| | Obtained | Calculated |
| E1 | 0.0018 | 0.0028 |
| E2 | 0.109 | 0.112 |
| E3 | 0.056 | 0.074 |
| E4 | 0.363 | 0.422 |
| E5 | 0.039 | 0.045 |
| E6 | 0.023 | 0.032 |
| E7 | 0.038 | 0.048 |
| E8 | 0.064 | 0.079 |

Figure 5.46 compares the corrosion rates in the end of the test. Sample E4 presents a much higher corrosion rate, followed by sample E2. Other samples had the values below 0.1 mm/year. According Tale 5.2 and 5.3, sample E4 (buried and sealed) provided a poor corrosion rate, however it should be considered that no external CP was being applied.
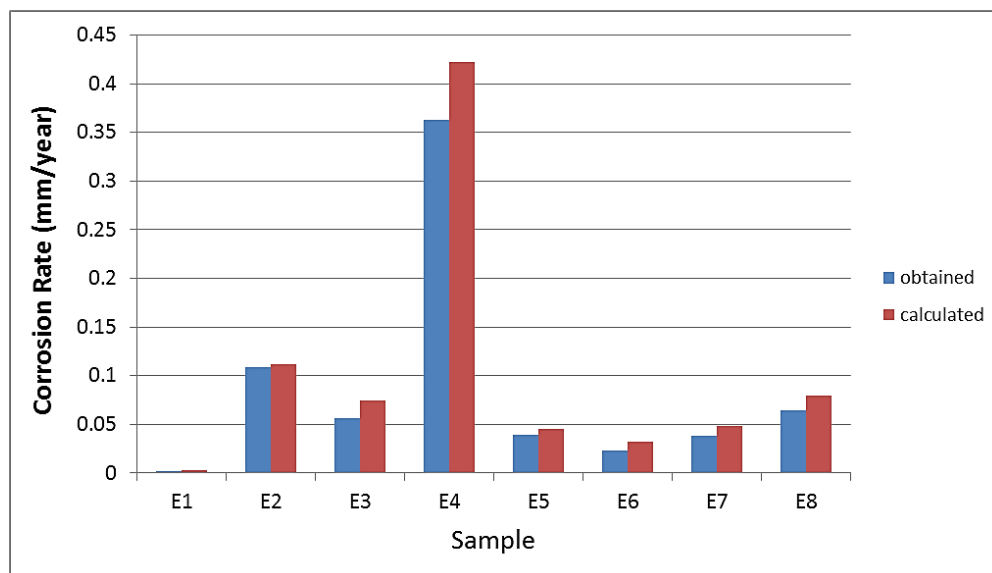


Figure 5.46: Obtained and calculated corrosion rates at the end of the test comparison of samples exposed to thermal gradient test under free potential.

*Current Demand (polarized samples)*

Samples polarised at -950 mV$_{Ag/AgCl}$ (CP1 to CP8) had their current density x time plotted (Figure 5.47). The tendency of the values to stabilize around zero is clear. Connection failures happened during the test, what most affected sample CP4, having its data acquired only between 25 and 70 days of test. Values were kept in the range 0.02 to 0.05 mA/cm$^2$ after ~120 days of test. The sign of the values will not be considered as it only specifies the direction of current accordingly to the equipment convention of positive direction.

Samples CP1, CP3 and CP6 presented more stable current densities, which stabilised from day 50$^{th}$ near zero. Samples CP3 and CP4 were the buried samples where the sealing could be seen in cross-section in Figure 5.38. Initial instable behaviour of sample CP8 could be attributed to the formation of a relatively thick layer of aluminium oxide as observed in Figure 5.38 identified as Al(OH)$_3$ by XRD analysis (Figure 5.41).



Figure 5.47: Average current density from samples CP1 to CP8 exposed to thermal gradient at -950 mV/$_{Ag/AgCl}$.

The standard DNV-RP-B401 mentions that current density (initial, final and mean) for components coated with Al is 0.001 mA/cm$^2$. For components internally heated an increase of 0.00002 mA/cm$^2$ should be considered for each °C above 25°C. As observed in Figure 5.43 the temperatures were kept around 100°C in buried condition and 70°C in unburied condition. Therefore, respective current demand applied for the samples

in this study would be approximately 0.0025 and 0.0019 mA/cm$^2$. Table 5.10 shows the current demand obtained in the end of the test of each sample. Samples achieved approximate values with the specified or lower, apart from samples CP5 and CP7, which presented values above to the recommended by the standard.  It must be pointed out this sample was the one where high level of rust was observed (see Figure 5.31). Sample CP5 did not present evidence of corrosion and, although it can be seen by Figure 5.31 that some consumption of the coating happened, it was further avoided by aluminium oxide and magnesium layer that was formed. Somehow sample CP6 presented reasonable current demand and CR, although was highly consumed into rusting as well. It is possible that different iron oxide formed in both samples was different, and worked as a film barrier at some point in sample CP6 as it is possible to see that until approximately the day 7 its current demand was high as 0.059 mA/cm$^2$, from where it started to decrease until it stabilised around zero after day 50. The same did not happen with sample CP7 where poor values were kept until the end of the test.

Table 5.10:   Approximated current demand obtained by polarised samples in thermal gradient test.

| Sample | Condition | Current Demand (mA/cm$^2$) |
|--------|-----------|----------------------------|
| CP1 | buried | 0.0014 |
| CP2 | buried | 0.0012 |
| CP3 | buried | 0.0016 |
| CP4 | buried | 0.007 |
| CP5 | unburied | 0.006 |
| CP6 | unburied | 0.002 |
| CP7 | unburied | 0.050 |
| CP8 | unburied | 0.0013 |

As comparison, the corrosion rate was calculated following Equation 3.6. The results are showed in Figure 5.48. Apart from sample CP7, which presented non-satisfactory CR, all other samples had their values maintained lower than 0.076 mm/year. Those results show good CR when compared to Table 5.2 and 5.3.
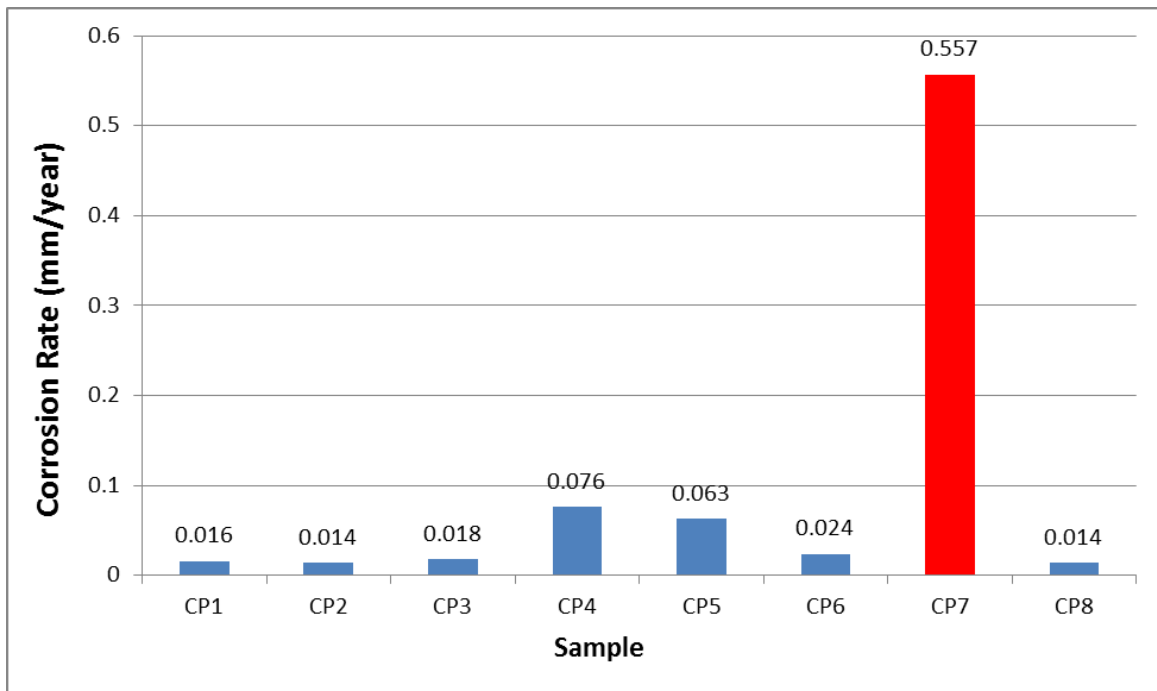
Figure 5.48: Calculated corrosion rate of polarised samples exposed to thermal gradient test.

## 5.4    Adhesion Tests

Figure 5.49 and 5.50 show both plate and dollies after the adhesion test. It is possible to see that both adhesive and cohesive (red arrows) failure happened in TWAS-Al and TWAS-AlMg.

The total average of the coatings adhesion was 24.72 MPa, where the average from the TWAS - Al samples was 23.22 MPa and the TWAS - AlMg was 26.22 (Figure 5.51). Both values are above than the minimum value of 7 MPa required by industry (NACE NO. 12/AWS C2.23M/SSPC CS-23). The lower bond strength related to the TSA-Al is not clear but could be attributed to the different wire thickness used for this alloy.

The values obtained are comparable with the values obtained by Shrestha and Sturgeon[SHRESTHA 2005] who compared the adhesion of different thermal spray processes for aluminium coating – among  it flame spray, purecoat and high velocity – and found the highest bond strength in the arc spray, with a value of 20 MPa although presenting mainly cohesive failure (the test method used was not specified).
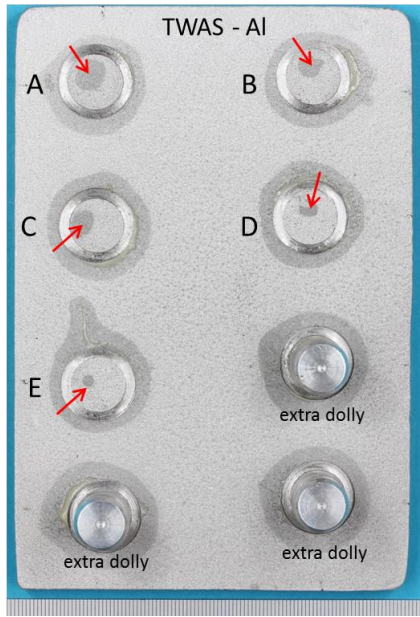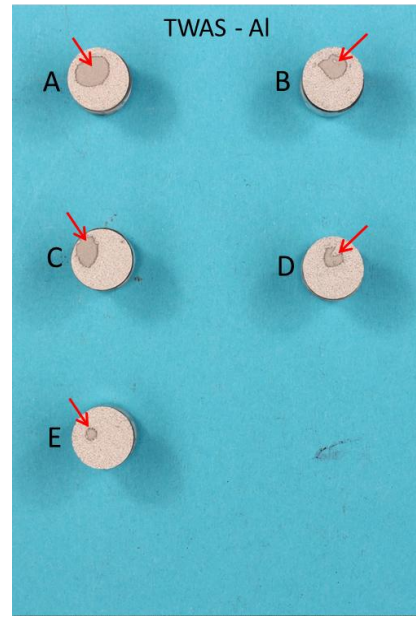
Figure 5.49: Adhesion test of TWAS - Al: a) steel plate after the test; b) test dollies from (a) after adhesion test.
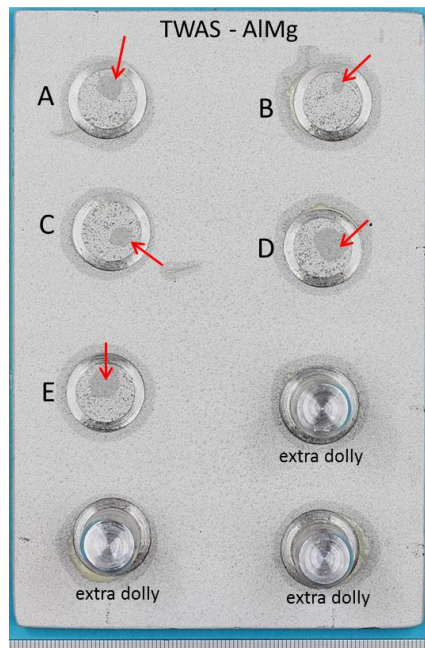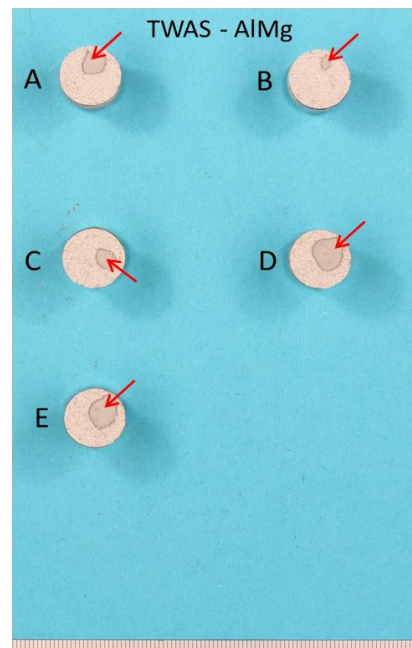


Figure 5.50: Adhesion test of TWAS - AlMg: a) steel plate after the test; b) test dollies from (a) after adhesion test.
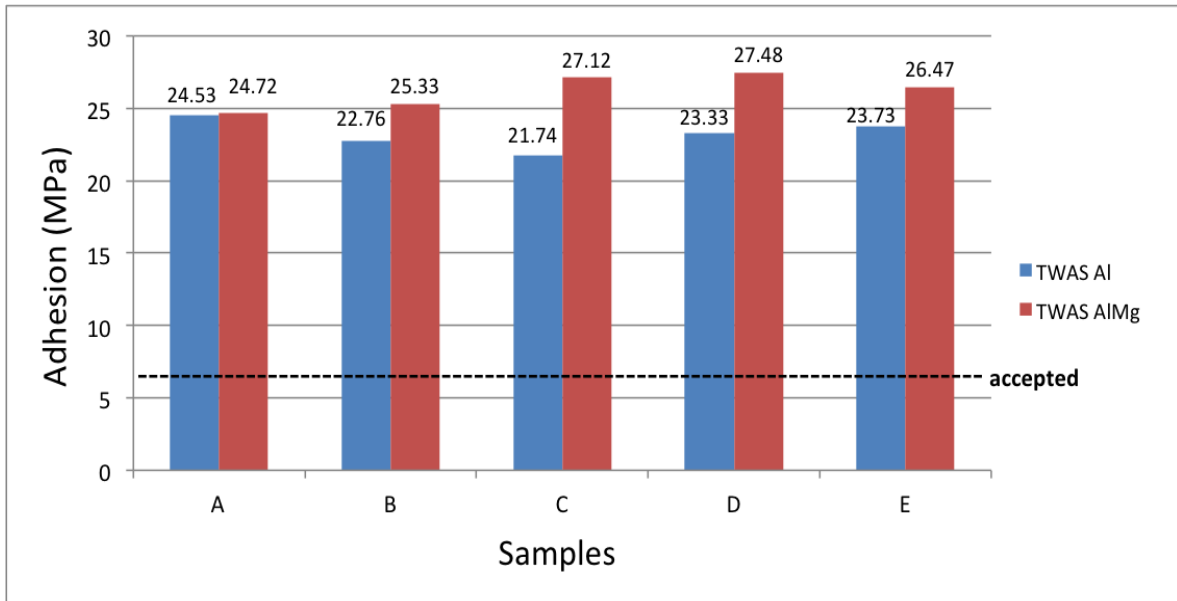
Figure 5.51: Adhesion results obtained for TWAS - Al and TWAS - AlMg coating.

# 6    CONCLUSIONS

The study gathered information for better understanding the formation of the calcareous deposit on cathodically polarised steel. The TSA polarised the steel surface facilitating the local generation of OH$^-$ by cathodic reactions. In the first set of tests, where constant temperatures (30, 60 and 90°C) were applied, the TSA coating did not present any damage like blister or cracks after exposure. Moreover, it was covered by aluminium oxide and calcareous deposit and very little of the TSA was consumed. The TSA − without external CP − was able to polarise the steel between -800 and -900mV$_{Ag/AgCl}$, while corrosion rate stabilized between 0.02 and 0.01 mm/year. The temperature affected the type of the deposit formed within the holiday and on the TSA: at 90°C only Mg(OH)$_2$ was formed. At 30 and 60°C a dense protective brucite film was formed previous to aragonite layer. The TSA composition (Al and AlMg) had little effect on corrosion rate as well as the holiday size applied (5, 10 and 20% of the surface area). Adhesion values acquired were between 22 and 28 MPa, much higher than the 7 MPa specified by industrial standards.

Maximum local pH within the holiday was found in 10.19 and 9.54 at 30 and 60°C respectively. A layer of Mg-containing is expected to be formed before the Ca-containing layer and, although other species present in the seawater may also influence (delay) the CaCO$_3$ formation. Calculations showed that the minimum pH necessary for the precipitation of Mg(OH)$_2$ (brucite) in synthetic seawater is 8.86 at 30°C, 8.01 at 60°C and 7.40 at 90°C while for the CaCO$_3$ the values are 7.61, 6.66 and 5.89 for the respective temperatures. However, presence of some species in synthetic seawater (inhibitors) pushes the deposition to higher pH values. The dissolved CO$_2$ in the synthetic seawater plays an important role in the precipitation of CaCO$_3$ by acting in the calco-carbonate equilibrium. The mechanism of calcareous deposit formation was built considering the parameters used in the study.

When thermal gradient was applied the calcareous deposit (sometimes appearing as a mixed layer) was also formed within the holidays preventing further corrosion of the

steel, however in buried conditions a layer of $CaSO_4.2H_2O$ (gypsum) could also be observed due to its solubility behaviour at the temperatures reached. Samples left at free potential showed potentials between -745 and -835 $mV_{Ag/AgCl}$ and corrosion rate were between ~0.4 and 0.002 mm/year. When external polarisation was applied, the corrosion rate was found below 0.076 mm/year. The sealant was effective only in the early stages of the test (first ten days) on buried samples under polarisation where corrosion rates were lower compared to other samples. Thickness of the coating after exposure of samples under external polarisation was between 250 to 302 µm, higher than the thickness of ~154 to 172 µm obtained by samples left under free potential.

Finally, the presence of the calcareous deposit (Mg and Ca-compounds) on the exposed steel surface, if damage in the TSA takes place, is extremely important to guarantee the pipeline's shelf-life extension. The TSA itself presented good performance when simulating service in hot seawater.

# 7 FUTURE WORKS

Other than the tests presented could be explored to complement the calcareous deposit and TSA performance study:

- Application of pressure (simulating minimum of 2000 m depth) and low to high temperature in order to study the combined behaviour of oxygen and $CO_2$ solubility in seawater to observe how it affects the formation of calcareous deposit. Data regarding this matter is still scarce in literature;

- Monitor the local pH on bare steel surface with external CP providing protective potential between -800 and $-900mV/_{AgAgCl}$ at high temperature in order to compare with the local pH values obtained by TSA polarisation to obtain the effect purely from the TSA coating on polarisation;

- Other electrochemical techniques such as cyclic voltammetry and electrochemical noise technique could be applied to monitor the corrosion products nucleation on steel surface in order to acquire more details on the evolution of the corrosion process;

- Deeper study regarding the growth of the calcareous deposit on the TSA coating to better understand the kinetics and pH change involved;

- Deeper study about hydrogen evolution in hot steel exposed to seawater would be beneficial to complement the present results;

- Adhesion tests considering high temperatures;

- Long term tests could be applied (2 years tests);

- Tests under insulation could also be explored.

# 8        REFERENCES

**ACM Instruments**. Linear Polarisation Resistance. Available in <http://www.acminstruments.com/media/ACM/ApplicationNotes/apn-LPR-v1.0.pdf>. Accessed: December 2016.

**AGSCO** Corporation. Technical Data. Available in: <http://catalog.agsco.com/Asset/Silica%20Testing%20Sand%20TDS.pdf>. Accessed: March 2016.

AKAMINE, K.; KASHIKI, I. Corrosion Protection of Steel by Calcareous Electrodeposition in Seawater (Part 1), **Zairyo-to-Kankyo**, v.51, p. 496-501; 2002.

AKAMINE, K.; KASHIKI, I. Corrosion Protection of Steel by Calcareous Electrodeposition in Seawater (Part 2), **Zairyo-to-Kankyo**, v. 52, p. 401-407; 2003.

AMERICAN SOCIETY FOR TESTING AND MATERIALS. **ASTM C778-06**: Standard Specification for Standard Sand, 2006.

AMERICAN SOCIETY FOR TESTING AND MATERIALS. **ASTM D1141**: Standard Practice for the Preparation of Substitute Ocean Water, 2013.

AMERICAN SOCIETY FOR TESTING AND MATERIALS. **ASTM D4541**: Standard Test Method for Pull-Off Strength of Coatings Using Portable Adhesion Testers, 2009.

AMERICAN SOCIETY FOR TESTING AND MATERIALS. **ASTM G82-98**: Standard Guide for Development and Use of a Galvanic Series for Predicting Galvanic Corrosion Performance, 2014.

AMERICAN WELDING SOCIETY. **AWS C2.18-93**: Guide for the Protection of Steel with Thermal Sprayed Coatings of Aluminum and Zinc and their Alloys and Composites;1993.

ANDERSON, G. M. **Thermodynamics of Natural Systems**, 2nd ed., Cambridge, UK: Cambridge Press, p. 162; 2009.

AWWA MANUAL M27. **External Corrosion – Introducation to Chemistry and Control**, 2nd ed., Denver, USA: American Water Works Association, p. 41-55; 2004.

BABOIAN, R. **Corrosion Tests and Standards - Application and Interpretation**, 2nd ed., West Conshohocken, PA: ASTM International, p. 828; 1995.

BABOIAN, R. **Corrosion Tests and Standards: Application and Interpretation**, 2nd ed., Pennsylvania, USA: ASTM International, p. 239; 2005.

BABOIAN, R; TRESEDER, R. S. **NACE Corrosion Engineer's Reference Book**. 3rd ed, Houston, USA: NACE International, p. 88-89; 2002.

BAI, Y.; BAI, Q. **Subsea Engineering Handbook**. 2nd ed., Gulf Professional Publishing, Oxford, UK, p. 3-4,229-239; 2012.

BARCHICHE C., DESLOUIS C., FESTY, D.; GIL, O., REFAIT P.; TOUZAIN, S. and TRIBOLLET B. Characterization of Calcareous Deposits by impedance Techniques 3 – Deposit of $CaCO_3$ in the Presence of Mg(II). **Eletrochimica Acta,** v. 48, p. 1645-1654; 2003.

BARCHICHE C., DESLOUIS C., GIL O., REFAIT P. *et al*. Characterization of Calcareous Deposits by Eletrochemical Method Role of Sulphates, Calcium Concentration and Temperature. **Eletrochimica Acta**, v. 49, p. 2833-2839; 2004.

BERNER, R. A. The Role of Magnesium in the Crystal Growth of Calcite and Aragonite from Sea Water. **Geochimica Acta**, v. 39, p. 489-494; 1975.

BHATIA, A. **Thermal Spraying Technology and Applications**. Department of the Army, United States, p. 16, 17, 41, 43; 1999.

BREZONIK, P. L. **Chemical Kinetics and Process Dynamics in Aquatic Systems**, Boca Raton, Florida, USA: Lewis Publishers, p. 300; 2002.

BRITISH STANDARDS INSTITUTION. **BS EN ISO 14919**: Thermal Spraying – Wires, Rods and Cords for flame and Arc Spraying – Classification – Technical Supply Conditions, BSI Standard Publication; 2015.

CARROL, J. J.; SLUPSKY, J. D.; MATHER, A. E. The Solubility of Carbon Dioxide in Water at Low Pressure. **J. Phys. Chem.**, v. 20, p. 1201-1209; 1991.

CHANDLER, K. A. **Marine and Offshore Corrosion.** Thetford, UK: Butterworth-Heinemann Ltd, p. 100; 1985.

CHENGJIE, L.; MIN, D.; JING, Q., *et al*. Influence of Temperature on the Protectiveness and Morphological Characteristics of Calcareous Deposits Polarized by Galvanostatic Mode, **Acta Metallurgica Sinica**, v. 27, p. 131-139; 2014.

CE, N.; PAUL, S. Thermally Sprayed Aluminum Coatings for the Protection of Subsea Risers and Pipelines Carrying Hot Fluids. **Coatings**, v. 6, p. 1-11; 2016.

CRAWNER, D**. Thermal Spray Processes**. Ohio, USA: ASM Handbook, p. 33-53; 2013.

DAVIS, J. R. **Corrosion of Aluminum and Aluminum Alloys**. Ohio, USA: ASM International, p. 25-38; 1999.

DELYANNIS, A.; DELYANNIS, E. Proceedings of the Sixth International **Symposium on Fresh Water from the Sea**. European Federation of Chemical Engineering, Gran Canaria, Spain, p. 183-192; 17-22 Sep.1978.

DESLOUIS, C.; FESTY, D.; GIL, O. *et al*. Characterization of Calcareous Deposits in Artificial Seawater by Impedance Techniques – I. Deposit of $CaCO_3$ without $Mg(OH)_2$, **Electrochimica Acta**, v. 43, p. 1891-1901; 1997.

DET NORSKE VERITAS. **DNV-RP-B401**: Cathodic Protection Design, Recommended Practice; 2010.

DET NORSKE VERITAS. **DNV-OS-F101**: Offshore Standard. Submarine Pipeline Systems; Recommended Practice;2013.

DET NORSKE VERITAS. **DNV RP-F103:** Recommended Practice. Cathodic Protection Pipelines by Galvanic Anodes, Recommended Practice; 2010.

DEXTER, S. C; LIN, S. H. Calculation of Seawater pH at Polarized Metal Surfaces in the Presence of Surface Films. **Corrosion**, v. 48, p. 50-60; 1992.

DODD, J. R; STANTON R. J. Paleoecology: Concepts and Applications, 2$^{nd}$ ed, John Wiley & Sons, p. 347; 1990.

FAUCHAIS, P.; VARDELLE, A. **Thermal Sprayed Coatings Used Against Corrosion and Corrosive Wear**. Advanced Plasma Spray Applications; Dr. Hamid Jazi, Intech, p. 1-38; 2012.

FAUST, S.D.; Aly, O. M. **Chemistry of Water Treatment**. 2$^{nd}$ ed., Boca Raton, Florida: CRC Press, p. 200; 1998.

FEDERAL HIGHWAY ADMINISTRATION. **FHWA:** Corrosion Costs and Preventive Strategies in the United States. U.S. Publication No. FHWA-RD-01-156, 2002.

FISCHER, K. P. Hot Risers in the North Sea: A Parametric Study of CP and Corrosion Characteristics of Hot Steel in Cold Water. **Annual OTC** (Houston-USA), p. 451-457; 1983.

GARTLAND, P.O.; EGGEN, T. G. Cathodic and Anodic Properties of Thermally Sprayed Al- and Zn-based Coatings in Seawater. **Corrosion**, Paper No. 367, Las Vegas, United States, 1990.

GARVERICK, L. **Corrosion in the Petrochemical Industry**, 1$^{st}$ ed., Ohio, USA: ASM International, p. 315, 371; 1994.

GHALI, E. **Corrosion Resistance of Aluminium and Aluminium Alloys**, New Jersey, USA: John Wiley & Sons, p. 49-76; 2010.

GOLDBERG, E. D.  **Global Coastal Ocean Marine Chemistry**, vol. 5, Harvard University Press, p. 140; 2003.

GÜLICH, J. F. **Centrifugal Pumps**. 2$^{nd}$ ed., Heidelberg, Germany: Springer, p. 835; 2010.

HARTT, W. H.; CULBERSON, C.H.; SMITH, W. S. Calcareous Deposits on Metal Surfaces in Seawater – A Critical review. **National Association of Corrosion Engineers**, v. 40, p.609-618; 1984.

HEIDERSBACH, R.  **Metallurgy and Corrosion Control in Oil and Gas Production**, New Jersey, United States:  John Wiley & Sons, p. 16-18, 2011.

ILIESCU, M, TURDEANU E. Thermal Sprayed Coatings Adhrence – Influencing Parameters. **WSEAS Transactions on Systems And Control**, v. 3, p. 1014 – 1023; 2008.

INTERNATIONAL ORGANIZATION FOR STANDARDIZATION. **ISO 15589-2**. (Modified) Petroleum and Natural Gas industries – Cathodic Protection of Pipeline Transportation Systems. Part 2: Offshore Pipelines; 2004.

JAVAHERDASHTI, R.; NWAOHA, C.; TAN, H. **Corrosion and Materials in the Oil and Gas Industries**. Boca Raton, FL, USA: CRC Press, p. 492,536; 2013.

KUIPER G. L. Stability of Offshore Risers Conveying Fluid. Delf, The Netherlands: Eburon, p. 1-4; 2008.

LAJEVARDI, S. A.; TAFRESHI, H.; SHAHRABI, T. Investigation of Calcareous deposit Formation on 5052 Aluminium Alloy under Cathodic Polarisation in Natural and Artificial Sea Water. **Corros. Eng. Sci. Technol**., v. 46, p. 249-255; 2011.

LEE, R. U.; AMBROSE, J. R. Influence of Cathodic Protection Parameters on Calcareous Deposit Formation. **Corrosion**, v. 44, p. 887-891; 1988.

LEWANDOWSKI, Z.; LEE, W. C.; Characklis, W. G.; Little, B. Dissolved Oxygen and pH Microelectrode Measurements at Water-Immersed Metal Surfaces. **Corrosion**, v. 45, p. 92-98; 1989.

LIBES, S. M. **Introduction to Marine Biogeochemistry**, 2nd ed., London, UK: Elsevier, p. 382; 2009.

LIDE, R. D. **CRC Handbook of Chemistry and Physics**, 86th ed.; Boca Raton, FL, USA: CRC Press, p. 5:3-42, 5:66-69; 2005.

LORKING, K.F.; Mayne, J. E. O. The Corrosion of Aluminium. In Journal of Applied Chemistry, **Journal of Applied Chemistry**, v. 11, p. 170-180, 1961.

MANAHAN, S. E. **Environmental Chemistry**, 8th ed., Boca Raton: CRC PRESS, p. 55; 2005.

MARCUS, P.; MANSFELD, F. **Analytical Methods in Corrosion Science and Engineering**, 1st ed., Boca Raton, USA: CRC Press, p. 444-449; 2006.

MACHMUDAH, S.; ZULHIJAH, R.; WAHYUDIONO; SETYAWAN H.; KANDA, H; GOTO M. Magnetite Thin Film on Mild Steel Formed by Hydrothermal Electrolysis for Corrosion Prevention. **Chemical Engineering Journal**, v. 268, p. 76-85; 2015.

MARSDEN, J. O., HOUSE, C. I. **The Chemistry of Gold Extraction**, 2nd ed., Littleton, Colorado, USA: Society for Mining Metallurgy & Exploration, p. 122; 2006.

MOLLER, H. The Influence of $Mg^{2+}$ on the Formation of Calcareous Deposits on a Freely Corroding Low Carbon Steel in Seawater. **Corrosion Science**, v. 49, p. 1992-2001; 2006.

MONTOYA, P; MARIN, T; ECHAVARRIA, A; CALDERON, J. A. Influence of Anion and pH on the Electrochemical C-Deposition and Transformation of Iron Oxy-Hydroxide. **Int. J. Electrochem. Sci.**, v. 8, p. 12566-12579; 2013.

MYERSON A. S. **Handbook of Industrial Crystallization,** 2nd ed., Massachusetts, USA Butterworth-Heinemann, p. 2-10; 2001.

NEVILLE, A.; MORIZOT, A. P. Calcareous Scales Formed by Cathodic Protection - an Assessment of Characteristics and Kinectics, **Journal of Crystal Growth**, 243, p. 490-502; 2002.

NICHOLS, G. **Sedimentology and Stratigraphy**, 2nd ed., Wiley-Blackwell, chapter 16.4; 2009.

NORSOK STANDARD. **M-001**: Materials Selection; 2002.

NORSOK STANDARD. **M-501**: Surface Preparation and Protective Coating.; 2012.

OKSTAD, T.; RANNESTAD, Ø.; JOHSEN, R.; NISANCIOGLU, K. Significance of Hydrogen Evolution during Cathodic Protection of Carbon Steel in Seawater. **Corrosion**, v. 63, p. 857-865; 2007.

PACKTER, A.; DERBY, A. Co-precipitation of magnesium iron III hydroxide powders from aqueous solutions. **Cryst. Res. Technol.**, v. 21, 1391–1400; 1986.

PALMER, A. C. **Subsea Pipeline Engineering**. 2nd ed., Tulsa, USA: PennWell Books, p. 264-282; 2008.

PAREDES, R. S. C; AMICO, S. C.; OLIVEIRA, A. S. C. M. The Effect of roughness and pre-heating of the substrate on the morphology of aluminium coatings deposited by thermal spraying, **Surface and Coatings Technology**, v. 200, p. 3049-3055; 2006.

PAUL, S. **Corrosion Control for Marine - and Land-Based Infrastructure Applications**, ASM Handbook, United States, v. 5A, p. 248-252; 2013.

PERRY, R. H.; GREEN, D. W. **Perry's Chemical Engineers' Handbook.** 7th ed, New York, USA: McGraw-Hill Education, p. 2-122; 1997.

REINHART, F. M. **Corrosion of Metal and Alloys in the Deep Ocean**. Technical Report, U. S. Naval Engineering Laboratory, p. 185-190; 1976.

REVIE, R. W. Uhlig's Corrosion Handbook, 2nd ed., New York: Wiley-Interscience, p. 329-348; 2000.

REVIE, R.W. **Uhlig's Corrosion Handbook**. 3rd ed., USA: John Wiley & Sons, p. 103-104, 151-154, 333-347, 720-732; 2011.

REVIE. W. H.; UHLIG, H. H. **Corrosion and Corrosion Control**, 4th ed., Hoboken, New Jersey: John Willey & Sons, p. 16; 2008.

ROBERGE, P. R. **Corrosion Inspection and Monitoring**, 1st ed., Hoboken, New Jersey: John Wiley & Sons, p. 235; 2007.

ROUSSEAU, C.; BARAUD, F.; LELEYTER, L. *et al*. Calcareous Deposit Formed under Cathodic Protection in the Presence of Natural Marine Sediments: A 12 Month Experiment, **Corrosion Science**, v. 52, p. 2206-2218; 2010.

SALGAVO, G.; MAFFI, S.; MAGAGNIN, L. et al.  Calcareous Deposits, Hydrogen Evolution and pH on Structures under Cathodic Polarization in Seawater, **International Offshore and Polar Engineering Conference/13**, (Honolulu, USA), p. 353; 2003.

SANKARA, P. **Corrosion Control in the Oil and Gas Industry**. Saint Louis, US: Gulf Professional Publishing, p. 454-465; 2013.

SCHÜTZE, M.; ROCHE, M.; BENDER, R. **Corrosion Resistance of Steels, Nickel Alloys, and Zinc in Aqueous Media**, 1st ed. Frankfurt, Germany: Wiley VCH, p.6; 2016.

SCHWEITZER, P. A. **Corrosion and Corrosion Protection Handbook**. New York, USA: Chem-Pro Corporation, v. 19, p. 23-24; 1983.

SHIFLER, D.A. Understanding Material Interactions in Marine Environments to Promote Extended Structural Life. **Corrosion Science**, v. 47, p. 2335-2352; 2005.

SHREIR, L. L.; JARMAN, R. A.; BURSTEIN, G. T**. Corrosion. Metal/Environment Reactions**. 3rd ed., Oxford, UK: Butterworth-Heinemann Ltd, v. 1, p. 10:3-10:10, 13:1-13:2; 1994.

SHREIR, L. L.; JARMAN, R. A.; BURSTEIN, G. T**. Corrosion. Corrosion Control,** 3rd ed., Oxford, UK: Butterworth-Heinemann Ltd, v. 2, p.10:40-41, 14:29; 1994.

SHRESTHA, S; STURGEON, A. Characteristics and electrochemical corrosion behaviour of thermal sprayed aluminium (TSA) coatings prepared by various wire thermal spray processes. EUROCORR, Lisbon, Portugal, 4-8 September, p. 1-7; 2005.

SUKIMAN, N. L.; ZHOU, X.; BIRBILIS, N. et al. **Durability and Corrosion of Aluminium and its Alloys: Overview, Property Space, Techniques and Developments.** Aluminium Alloys - New Trends in Fabrication and Applications, Intech, Chapter 2, p. 48-53; 2012.

TALBOT, D.; TALBOT, J. **Corrosion Science and Techonology**. 2nd ed, Boca Raton, FL, United States: CRC Press, p. 453-454; 2007.

TAN, J; CHAN, K. S. Understanding Advanced Physical Inorganic Chemistry: The Learner's Approach. Singapore: World Scientific Publishing Co Pte Ltd, 1$^{st}$ ed, p. 295, 2011.

THE SOCIETY FOR PROTECTIVE COATINGS, AMERICAN WELDING SOCIETY, AND NACE INTERNATIONAL. **SSP-CS 23.00/AWS C2.23M/NACE No12**. Specification for the Application of Thermal Spray Coatings (Metallizing) of Aluminum, Zinc and their Alloys and Composites for the Corrosion Protection of Steel, Joint Standard, 2003.

THE SOCIETY FOR PROTECTIVE COATINGS, AMERICAN WELDING SOCIETY, AND NACE INTERNATIONAL. **NACE NO. 12/AWS C2.23M/SSPC CS-23 Standard Practice Item No. 21100**: Specification for the Application of Thermal Spray Coatings (Metallizing) of Aluminum, Zinc and their Alloys and Composites for the Corrosion Protection of Steel, 2016.

THOMASON ,W.H.; STEIN, O.; TROND, H.; KARL, P.F. Deterioration of Thermal Sprayed Aluminum Coatings on Hot Risers Due to Thermal Cycling. **Corrosion**, N°. 04021, p. 1-16; 2004.

UNITED STATES NAVY. **Procedure Handbook for Shipboard Thermal Sprayed Coatings Applications**. San Diego, California, p. 17-18, 81-83; 1992.

U.S. ARMY CORPS OF ENGINEERS. Thermal Spraying: New Construction and Maintenance. Washington, DC, Engineer Manual No. 1110-2-3401, p. 6-1 ; 1999.

WEST, R. C.; LIDE, D. R. **CRC Handbook of Chemistry and Physics**, 70$^{th}$ ed.; Boca Raton, FL, USA: CRC Press, p. B-79; 1995.

WHITTEN, K. W.; DAVIS, R. E.; PECK, L; STANLEY, G. G. **Chemistry**, 10$^{th}$ ed., Belmont, USA: Cengage Learning:, p. 711; 2013.

WRIGHT, J. M.; COLLING, A. **Seawater: Its Composition, Properties and Behaviour**, 2nd ed.; Milton Keynes, England: Butterworth-Heinemann, p. 32; 1995.

YAN, J. F.; NGUYEN, T. V.; WHITE, R. E.; GRIFFIN, R. B. Mathematical Modeling of the Formation of Calcareous Deposits on Cathodically Protected Steel in Seawater. **Journal of the Electrochemical Society**, v. 140, p. 733-744; 1993.

YAN, L. **Techniques for Corrosion Monitoring**. Cambridge, UK: Woodhead Publisher, p. 166; 2008.

YANG, Y.; SCANTLEBURY, J. D.; KOROLEVA E. V. A. Study of Calcareous Deposits on Cathodically Protected Mild Steel in Artificial Seawater. **Metals**, v. 5, p. 439-456; 2015.

APPENDIX A – Top View SEM Images



| 5% holiday 99.5%Al (100x) | 10% holiday 99.5%Al (100x) | 20% holiday 99.5%Al (100x) |
| --- | --- | --- |
| 5% holiday Al-5%Mg (100x) | 10% holiday Al-5%Mg (100x) | 20% holiday Al-5%Mg (100x) |
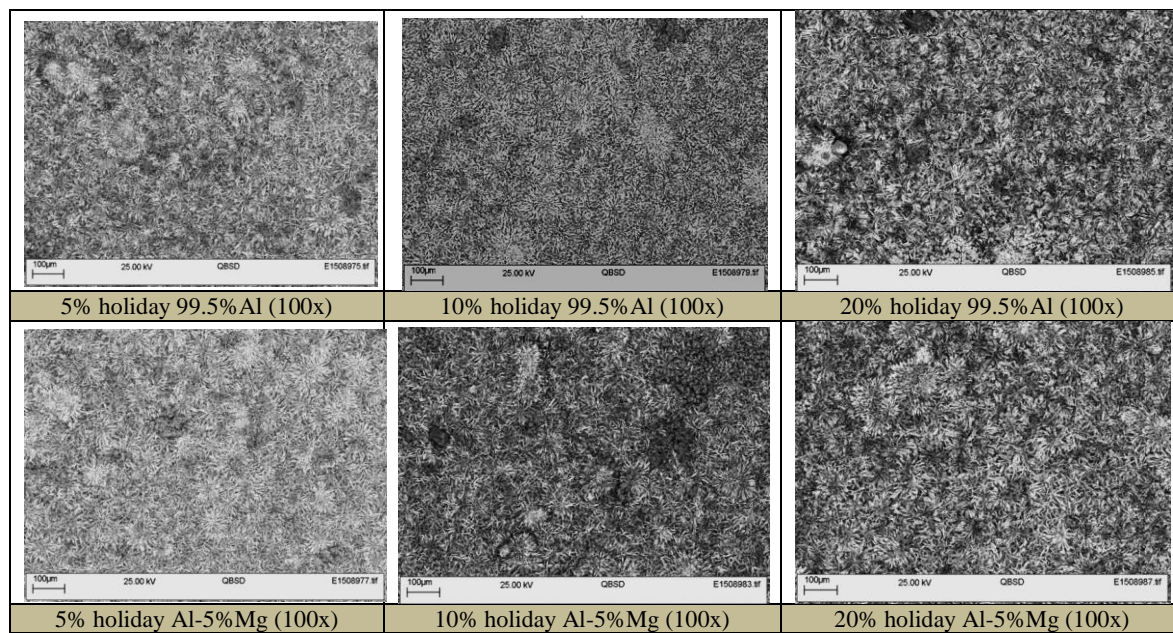
Figure A.1: Top view SEM images of calcareous deposit formed at 30ºC test. Calcium carbonate can be observed.

| 5% holiday 99.5%Al (38x) | 10% holiday 99.5%Al (100x) | 20% holiday 99.5%Al (100x) |
| 5% holiday Al-5%Mg (100x) | 10% holiday Al-5%Mg (100x) | 20% holiday Al-5%Mg (100x) |
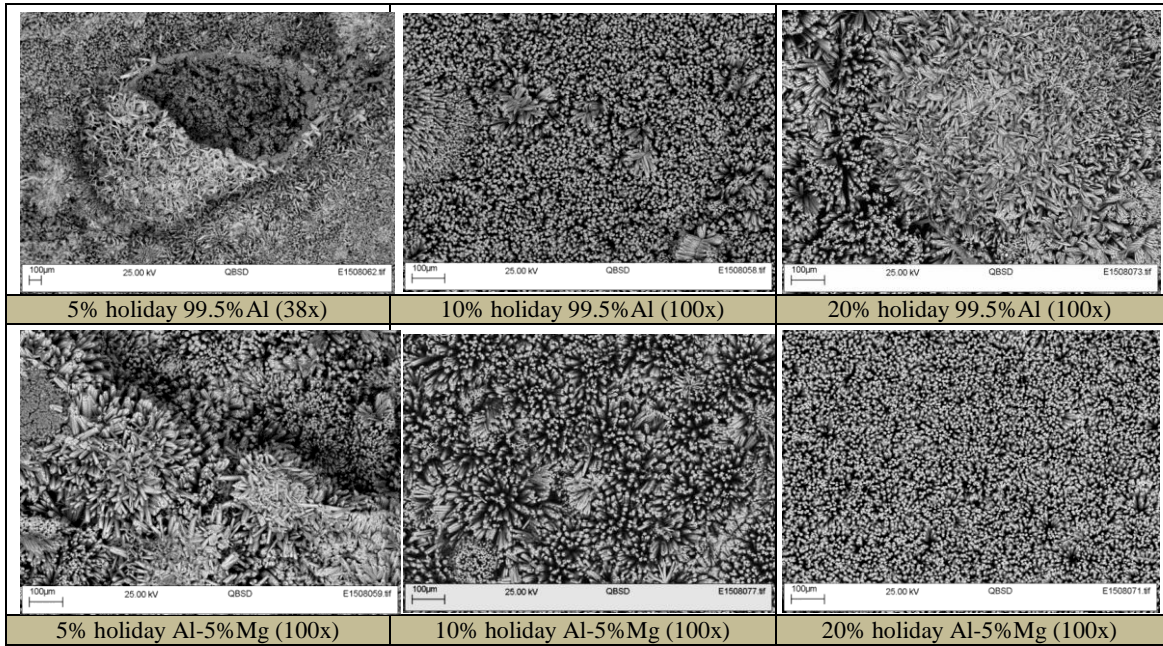
Figure A.2: Top view SEM images of calcareous deposit formed at 60ºC test. Calcium carbonate can be observed.



| 5% holiday 99.5%Al (100x) | 10% holiday 99.5%Al (100x) | 20% holiday 99.5%Al (100x) |
| 5% holiday Al-5%Mg (100x) | 10% holiday Al-5%Mg (100x) | 20% holiday Al-5%Mg (100x) |
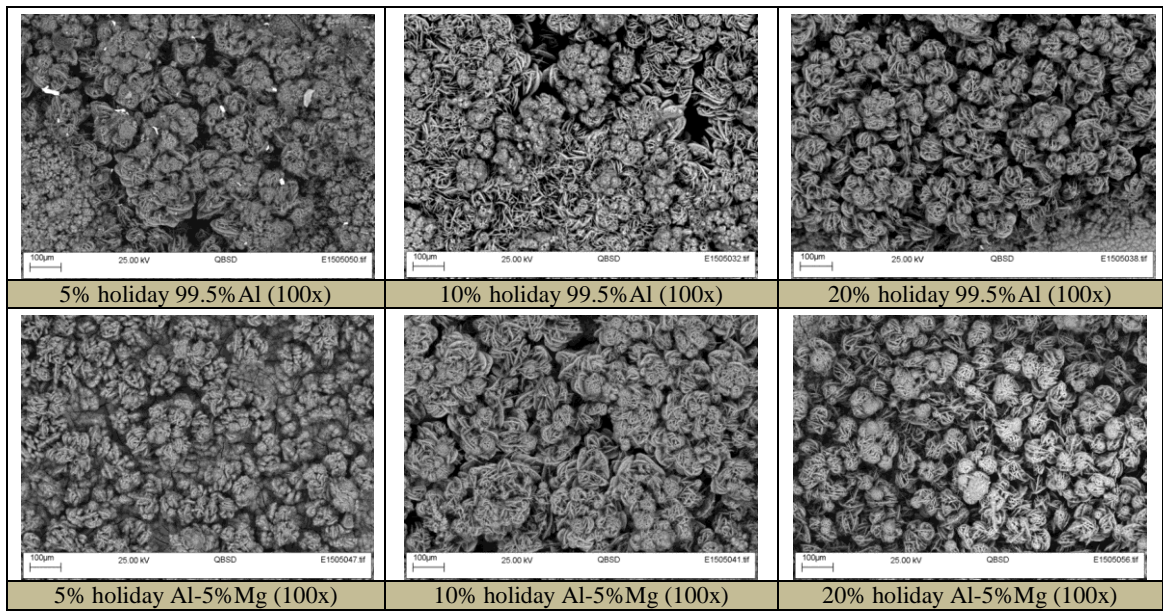
Figure A.3: Top view SEM images of calcareous deposit formed at 90ºC test. Brucite can be observed.

APPENDIX B – EDX of Samples Exposed at 30 ºC
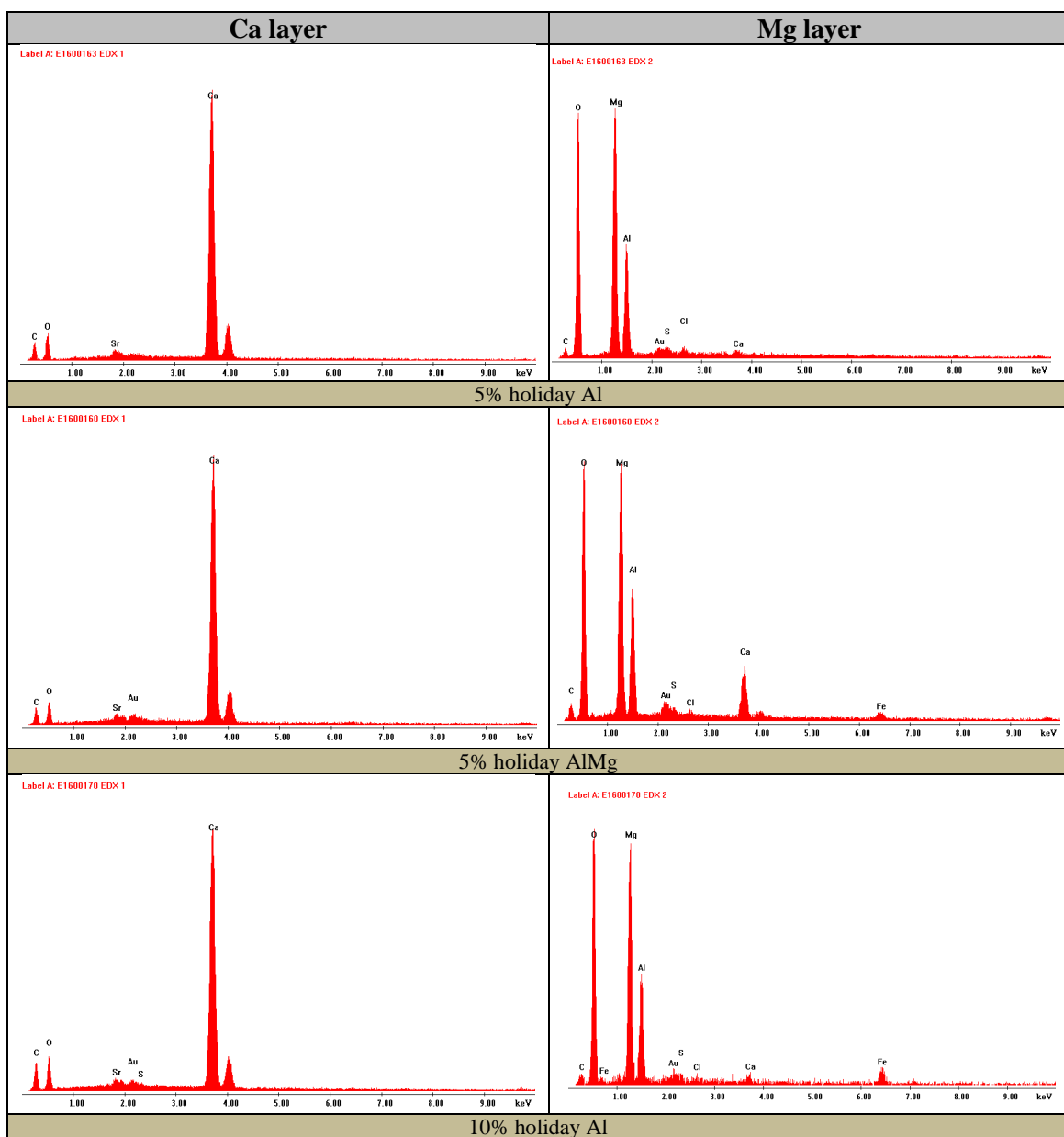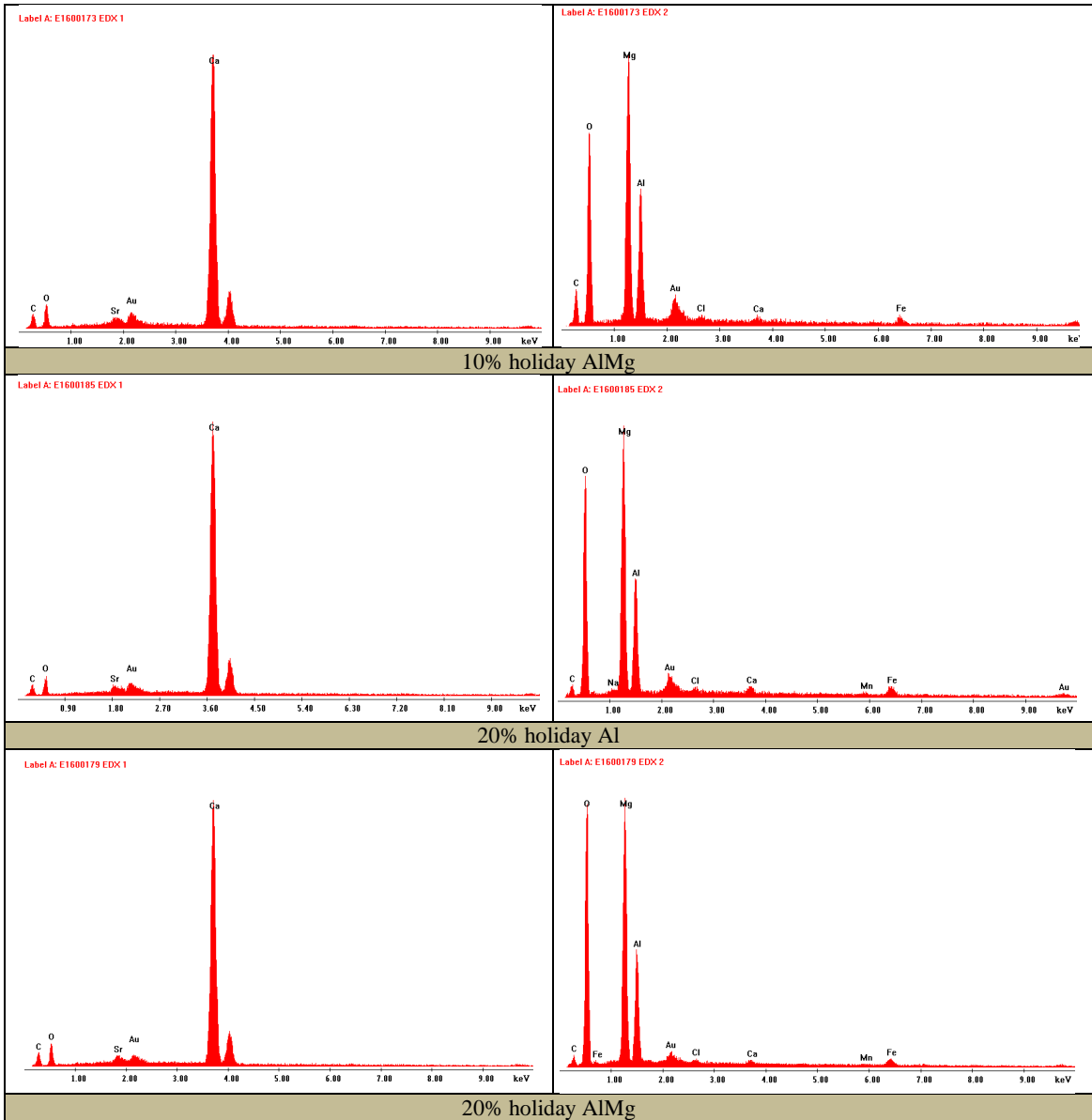
Figure B.1:   EDX in the holiday in cross-section – 30ºC test.
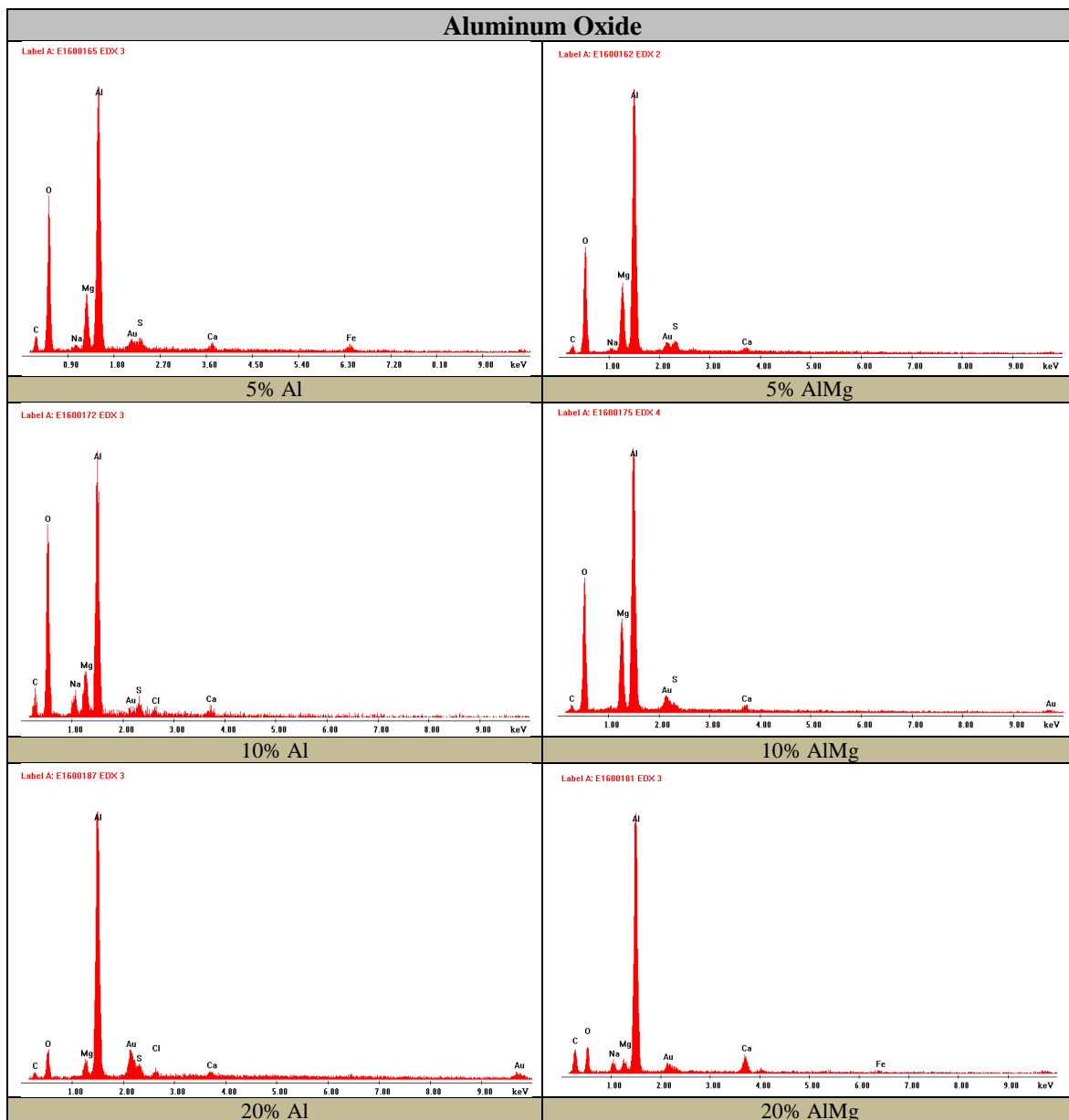
Figure B.2:   EDX on the TSA - 30ºC test.

APPENDIX C – EDX of Samples Exposed at 60 ℃
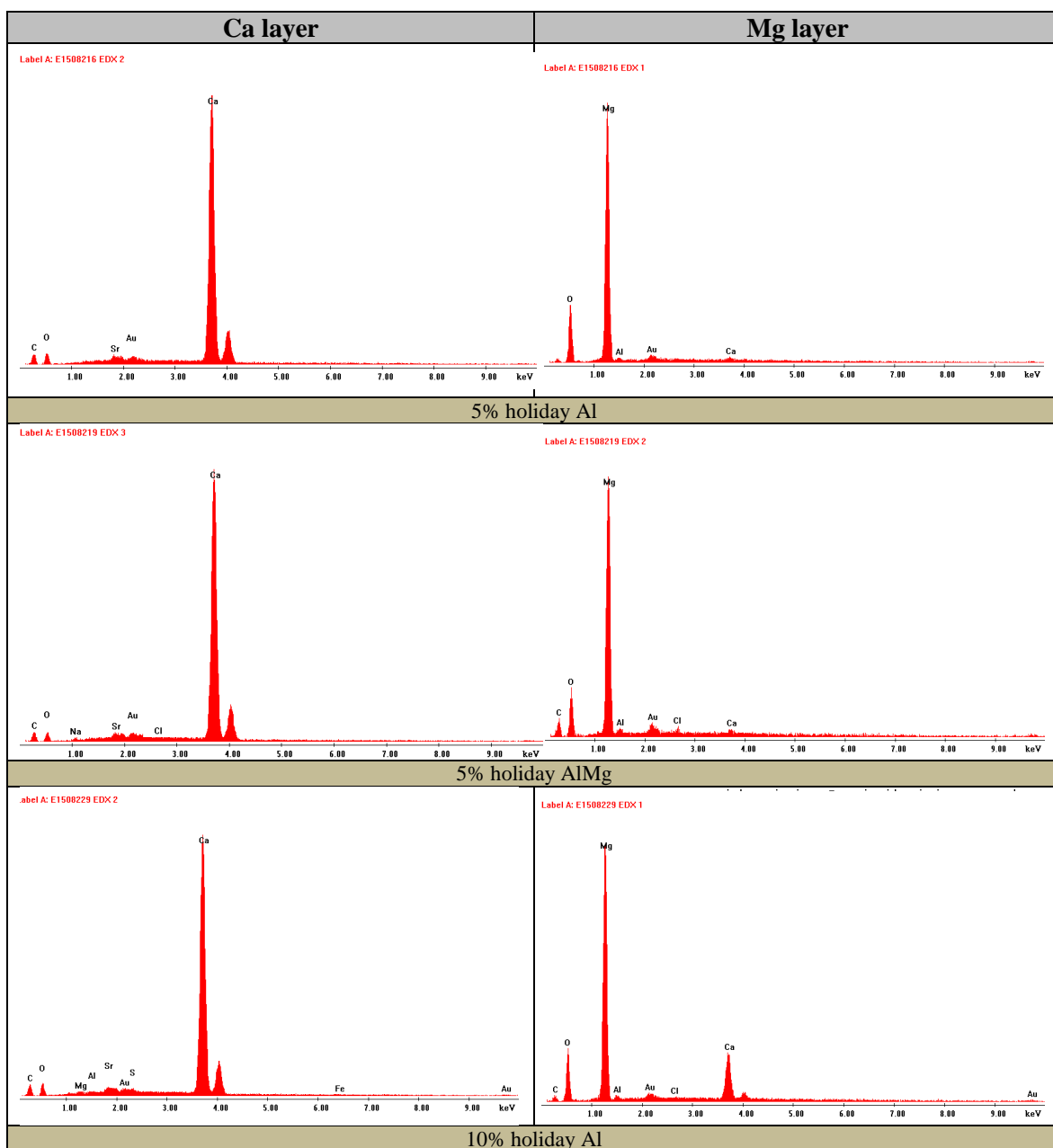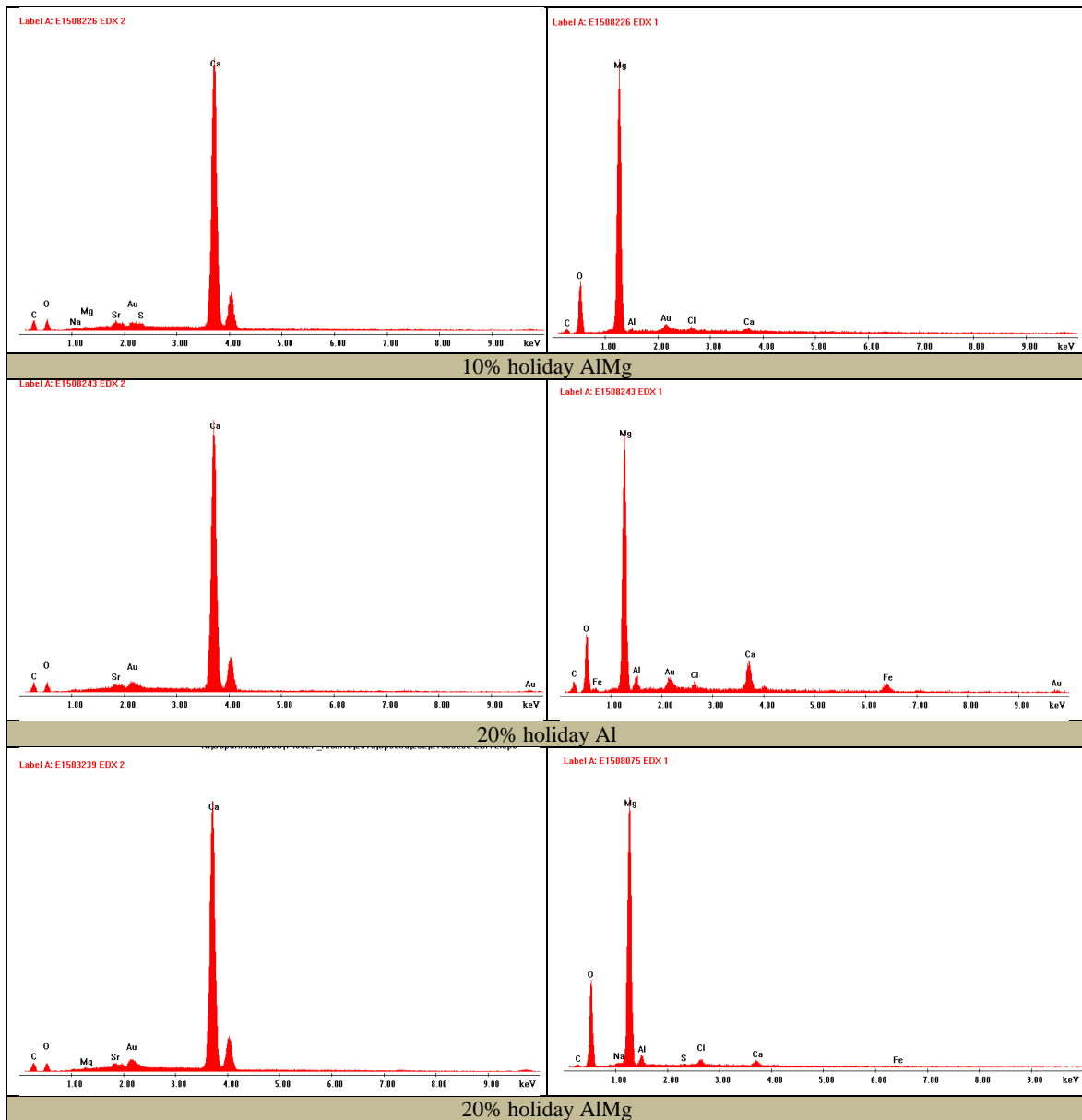
Figure C.1:   EDX from the holiday in cross-section – 60ºC test.
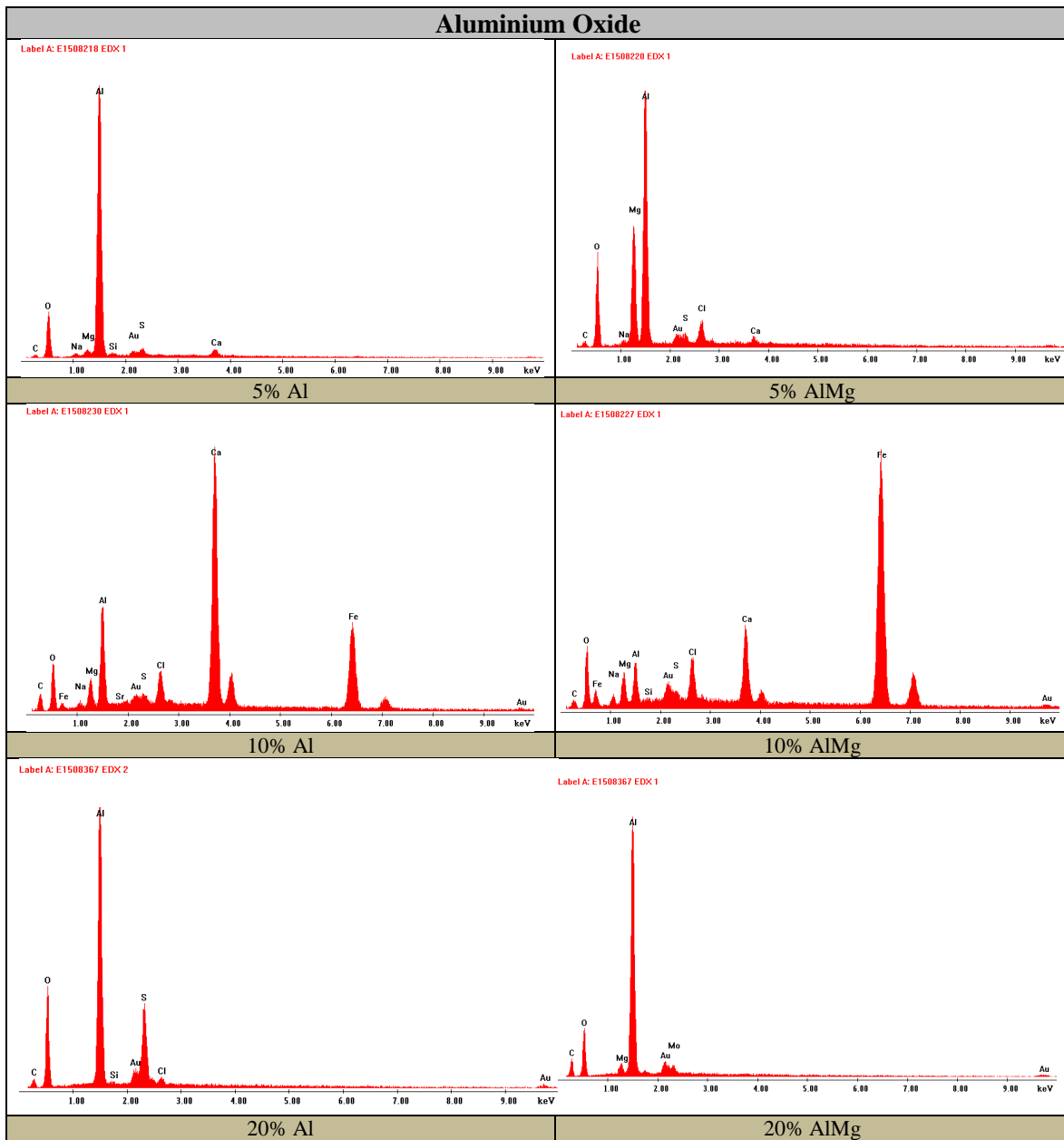
Figure C.2: EDX on the TSA - 60ºC test.
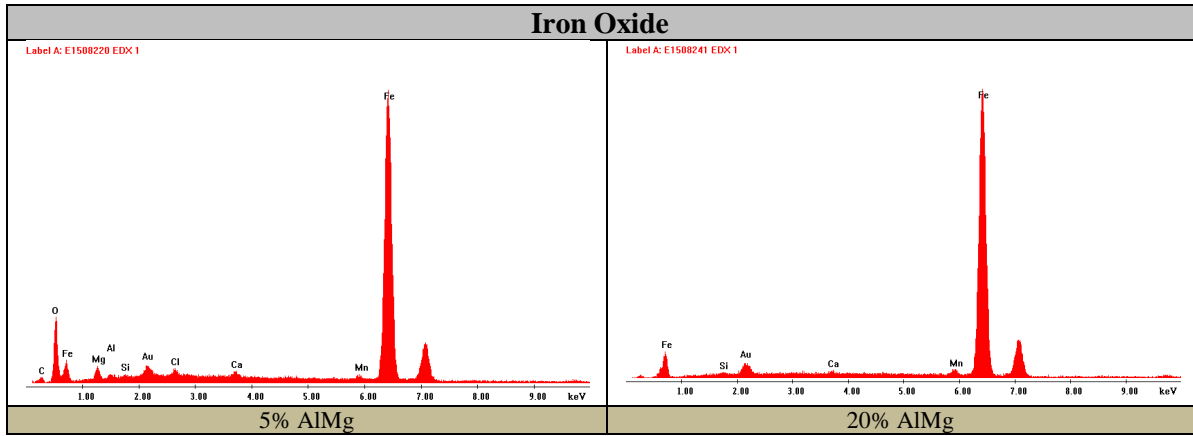
Figure C.3:   EDX in the interface holiday/TSA - 60ºC test.
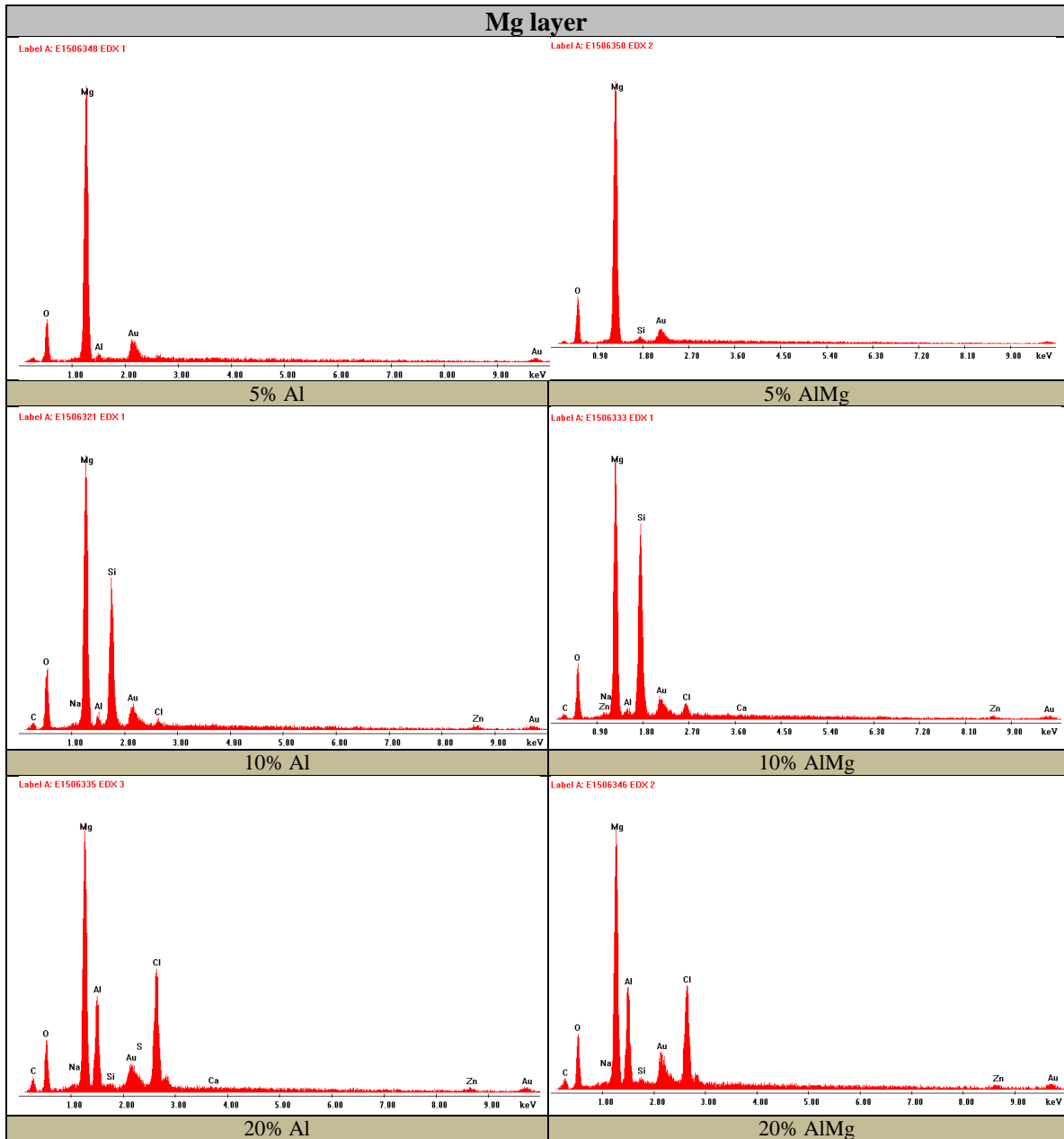
Figure D.1:   EDX from the holiday area in cross-section – 90ºC test.
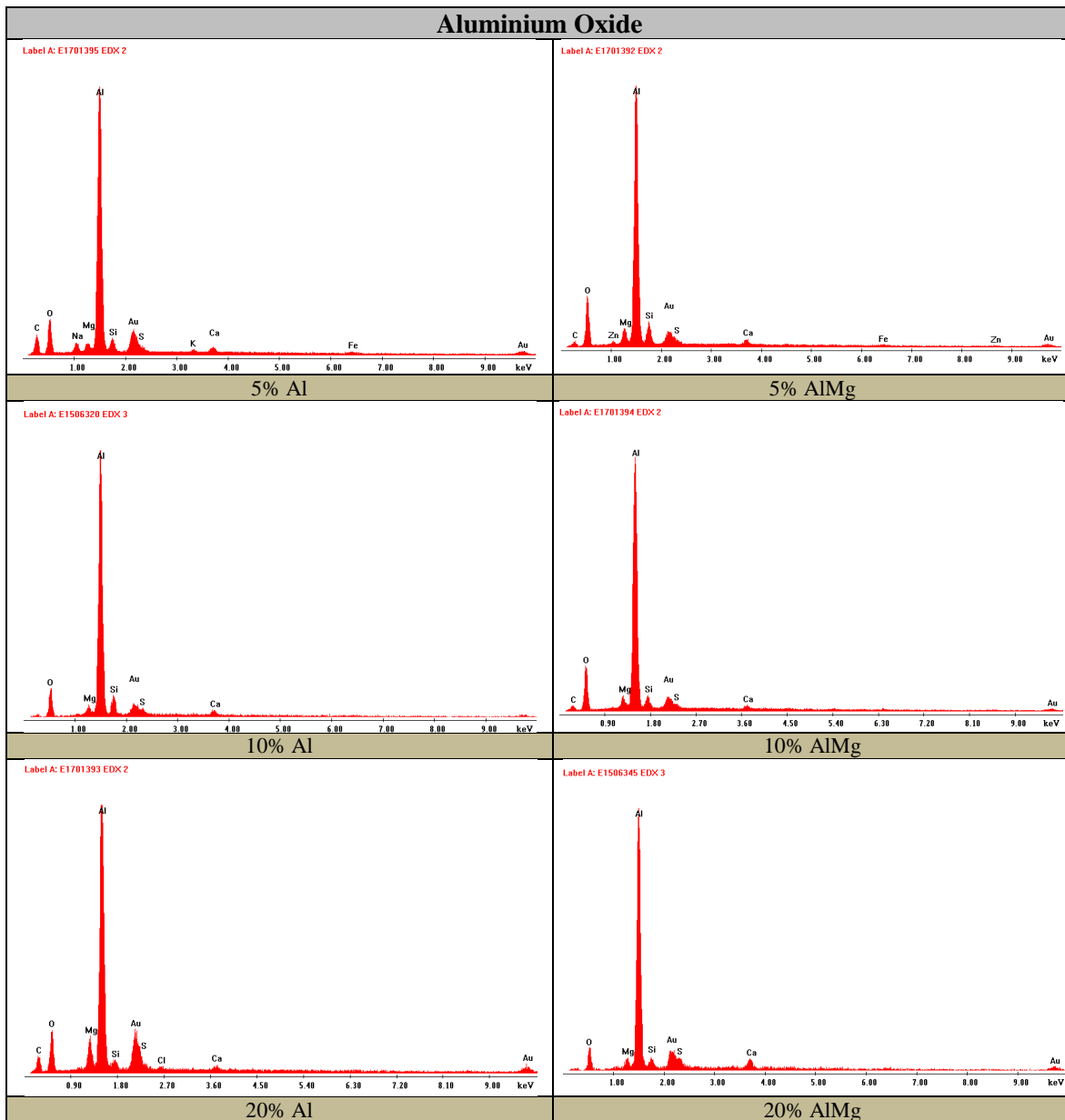
Figure D.2: EDX on the TSA - 90ºC test.

APPENDIX E – XRD from Holidays' Deposits - 30, 60 and 90ºC Tests.



| 5% holiday Al | 5% holiday AlMg |
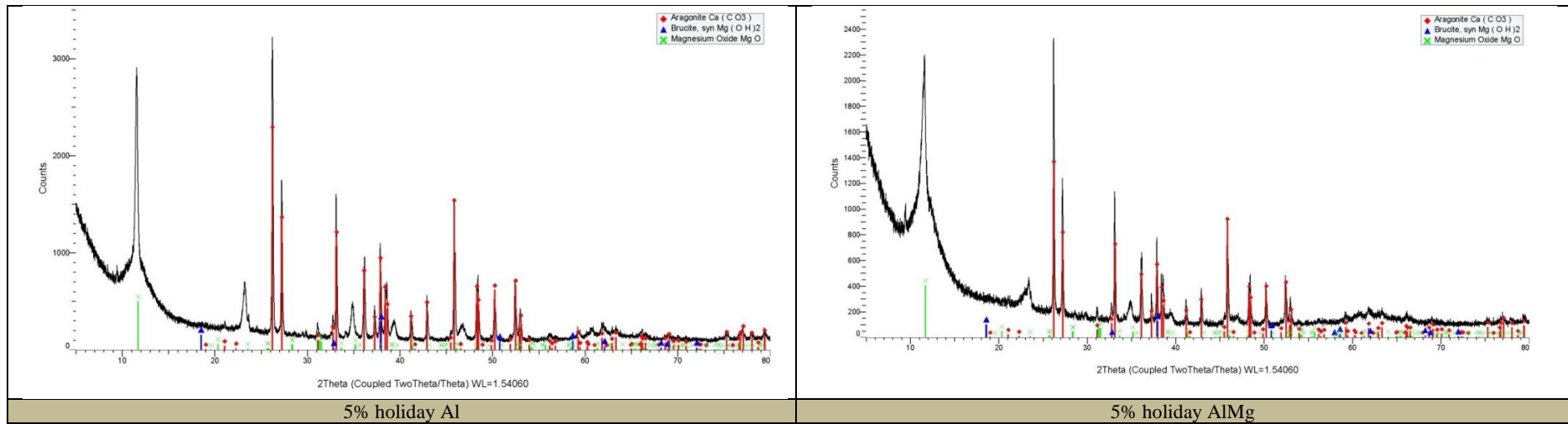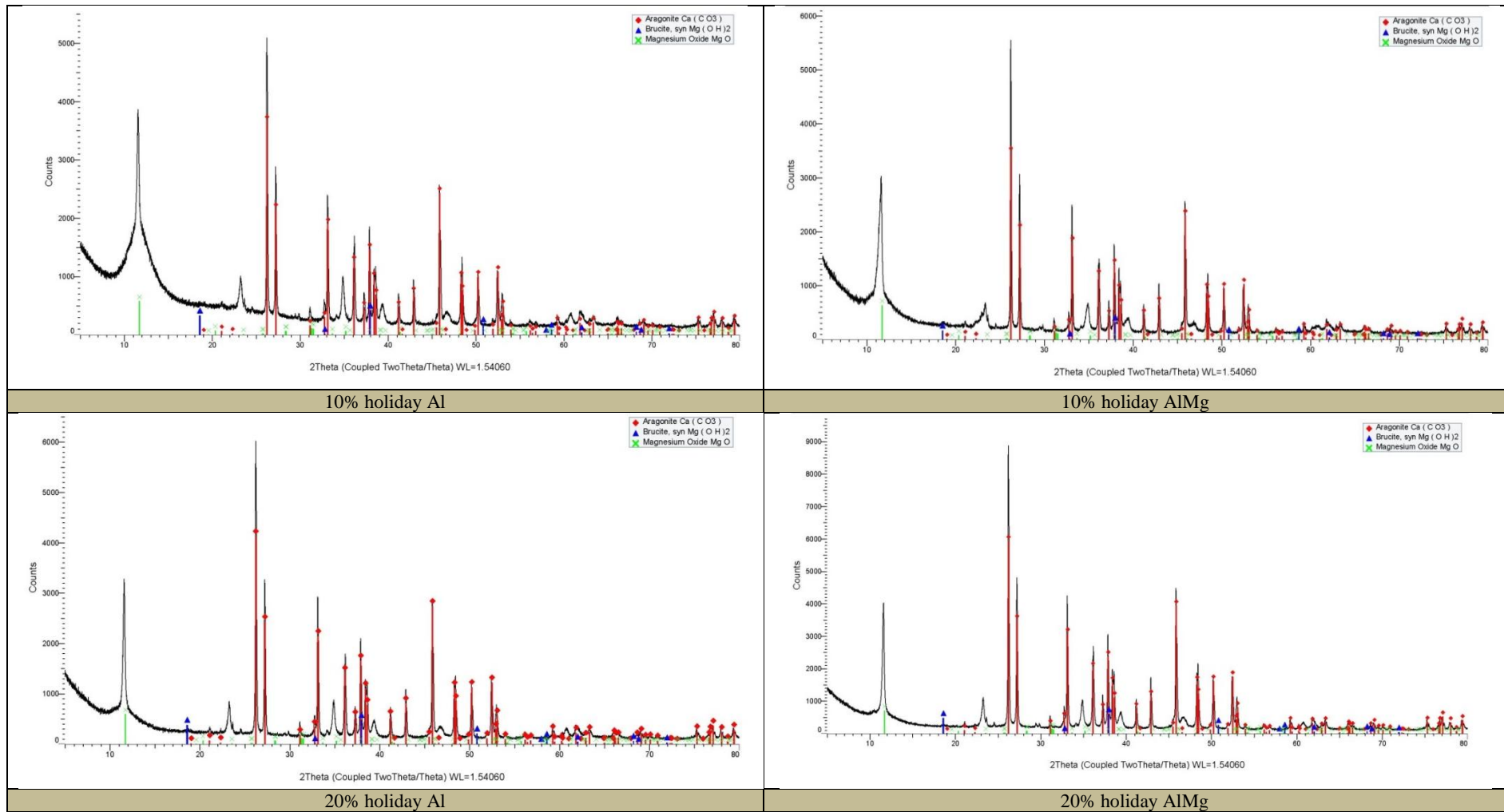
Figure E.1:   XRD from holiday deposits formed in 30ºC test.
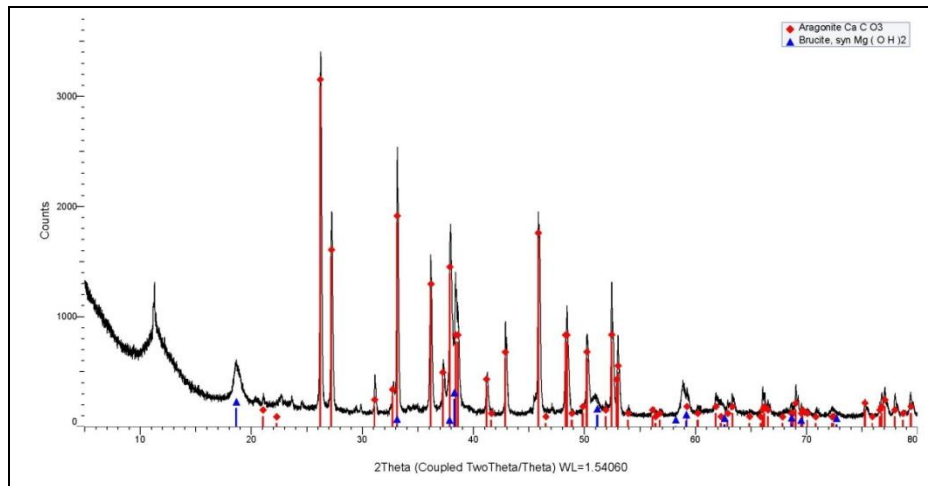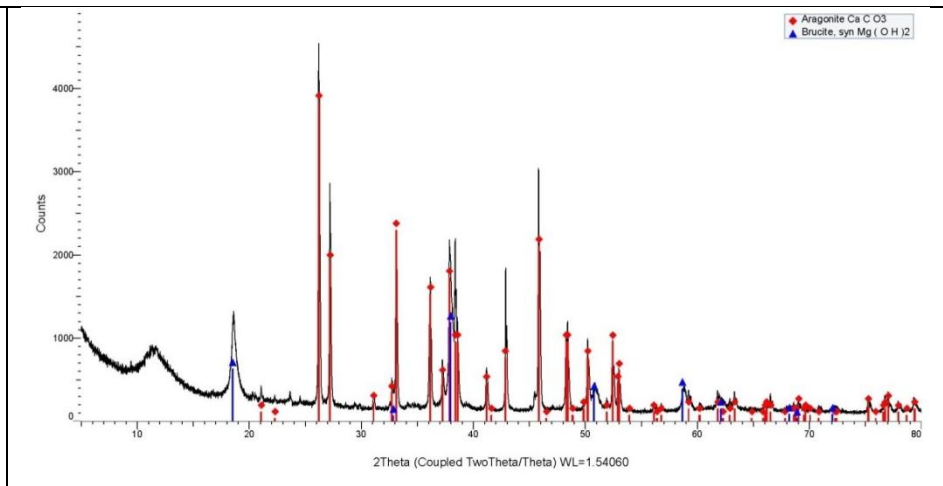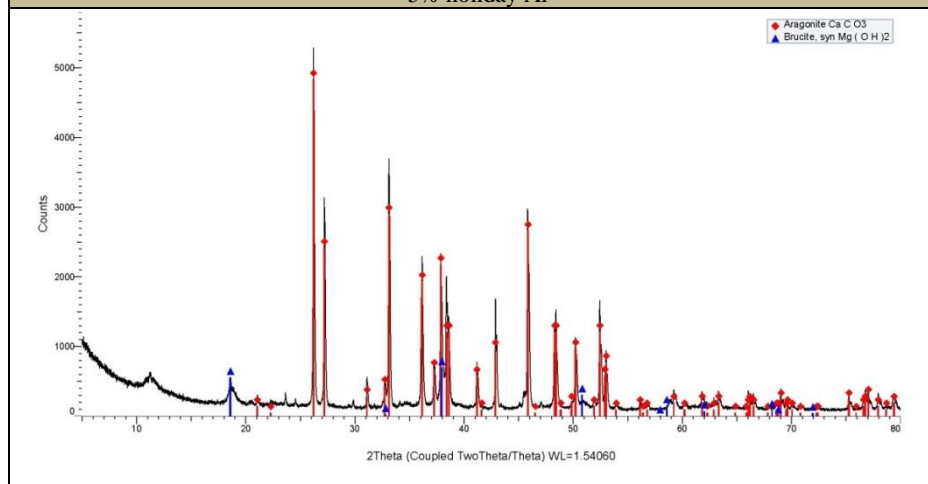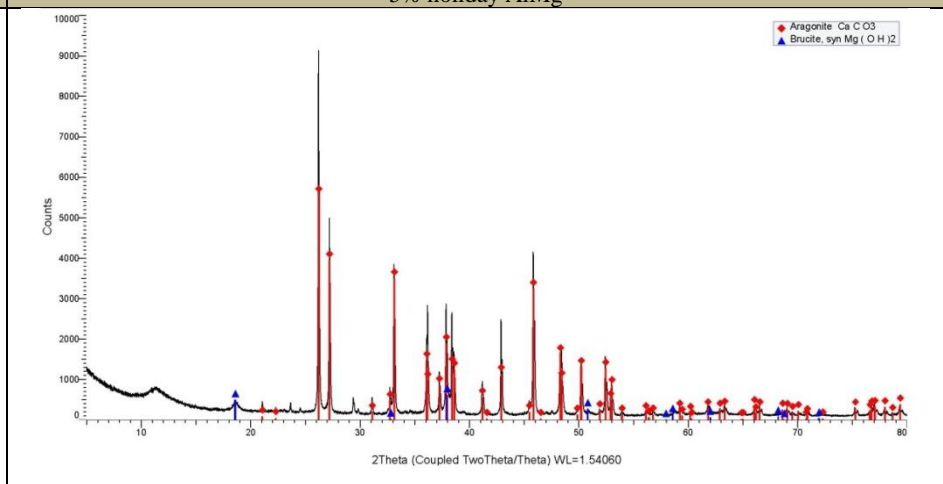
| 5% holiday Al | 5% holiday AlMg |
|---|---|
| 10% holiday Al | 10% holiday AlMg |

| 20% holiday Al | 20% holiday AlMg |
|---|---|
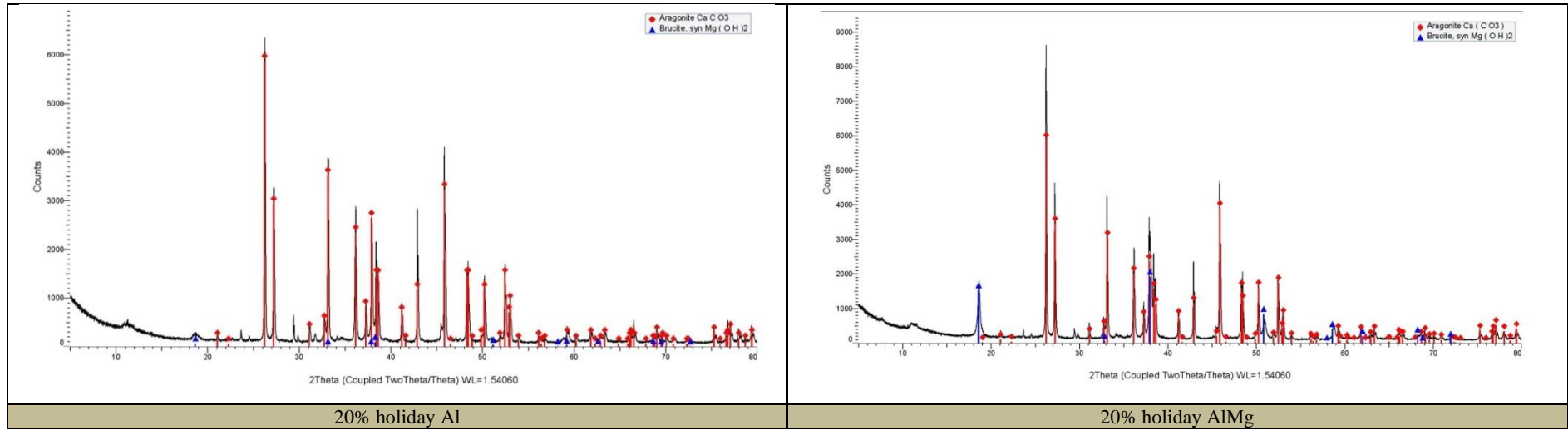
Figure E.2:   XRD from holiday deposits formed in 60ºC test.
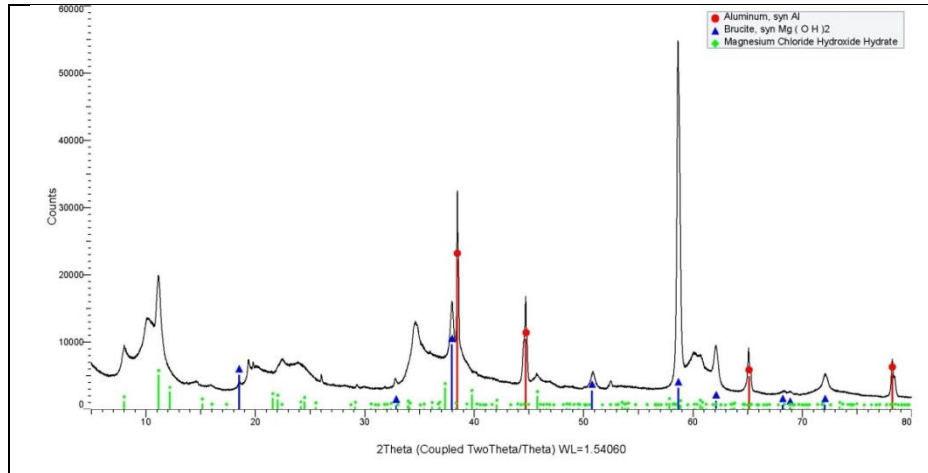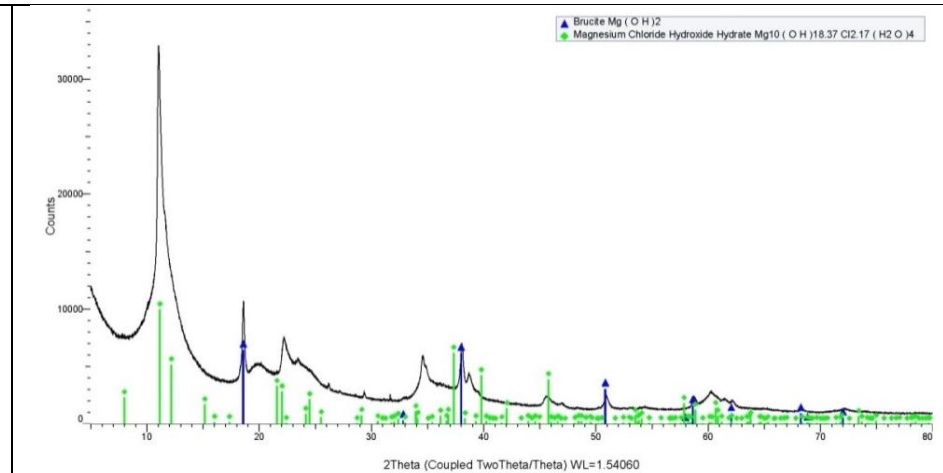
5% holiday Al
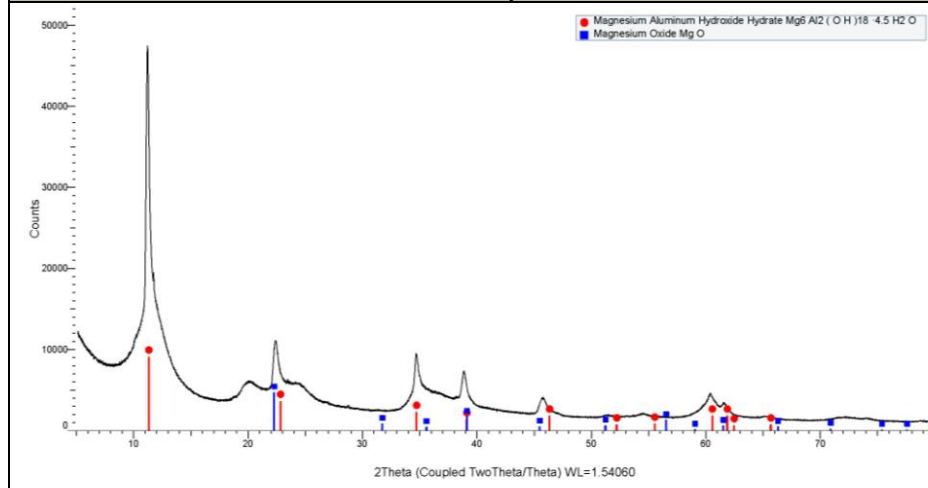

5% holiday AlMg
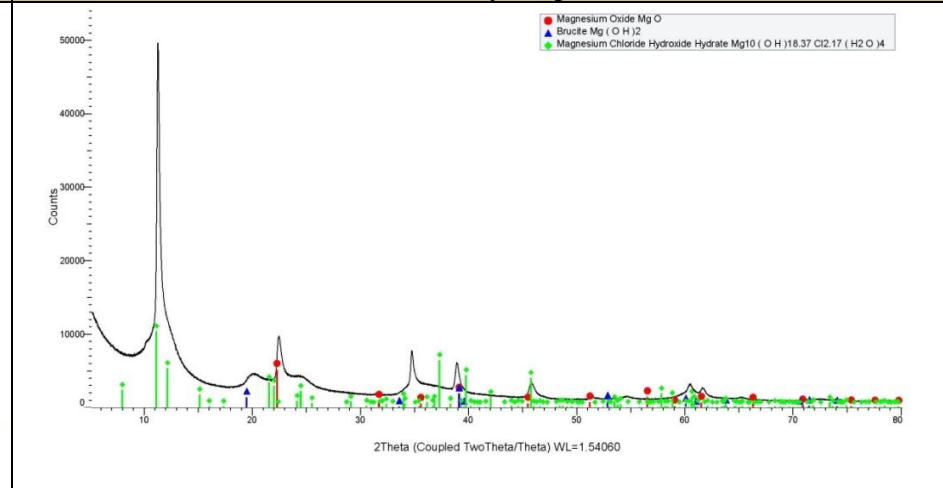

10% holiday Al


10% holiday AlMg
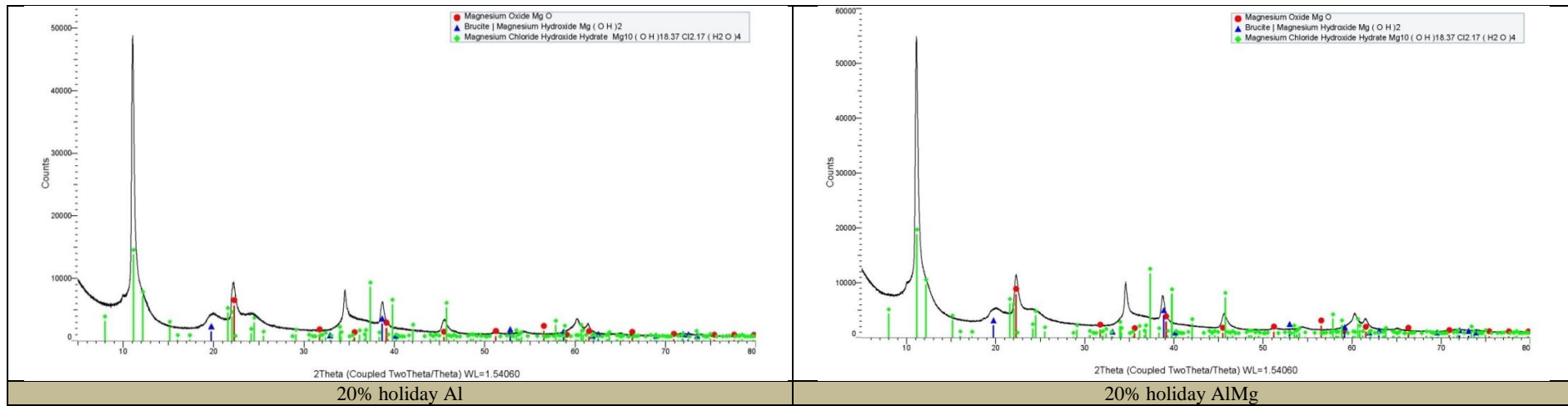
Figure E.3:   XRD from holiday formed in 90ºC test.

APPENDIX F – XRD from Deposit from Carbon Steel Corrosion Test
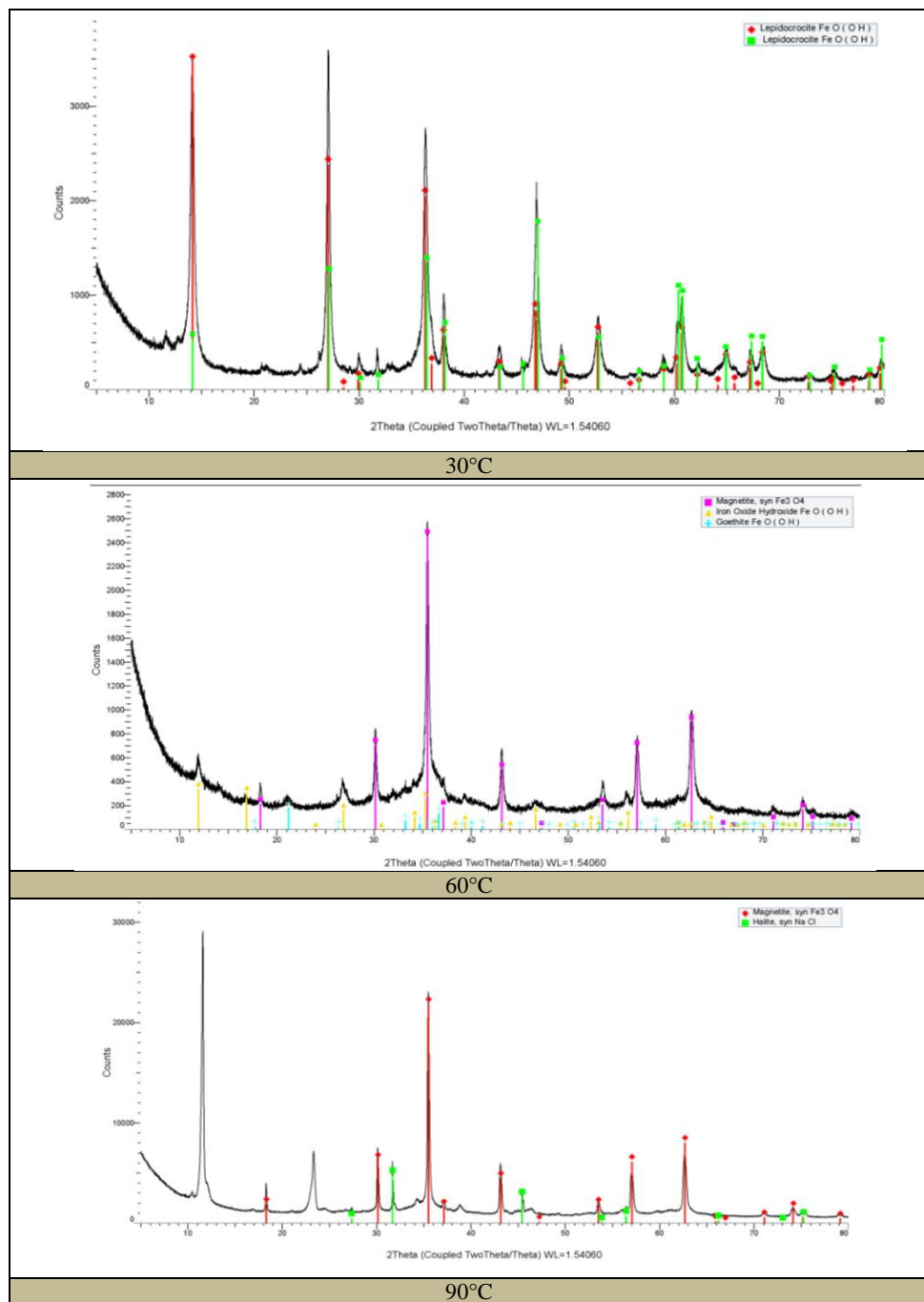


Figure F.1:   XRD from carbon steel corrosion deposit

APPENDIX G – XRD of Deposit from Glass Rods
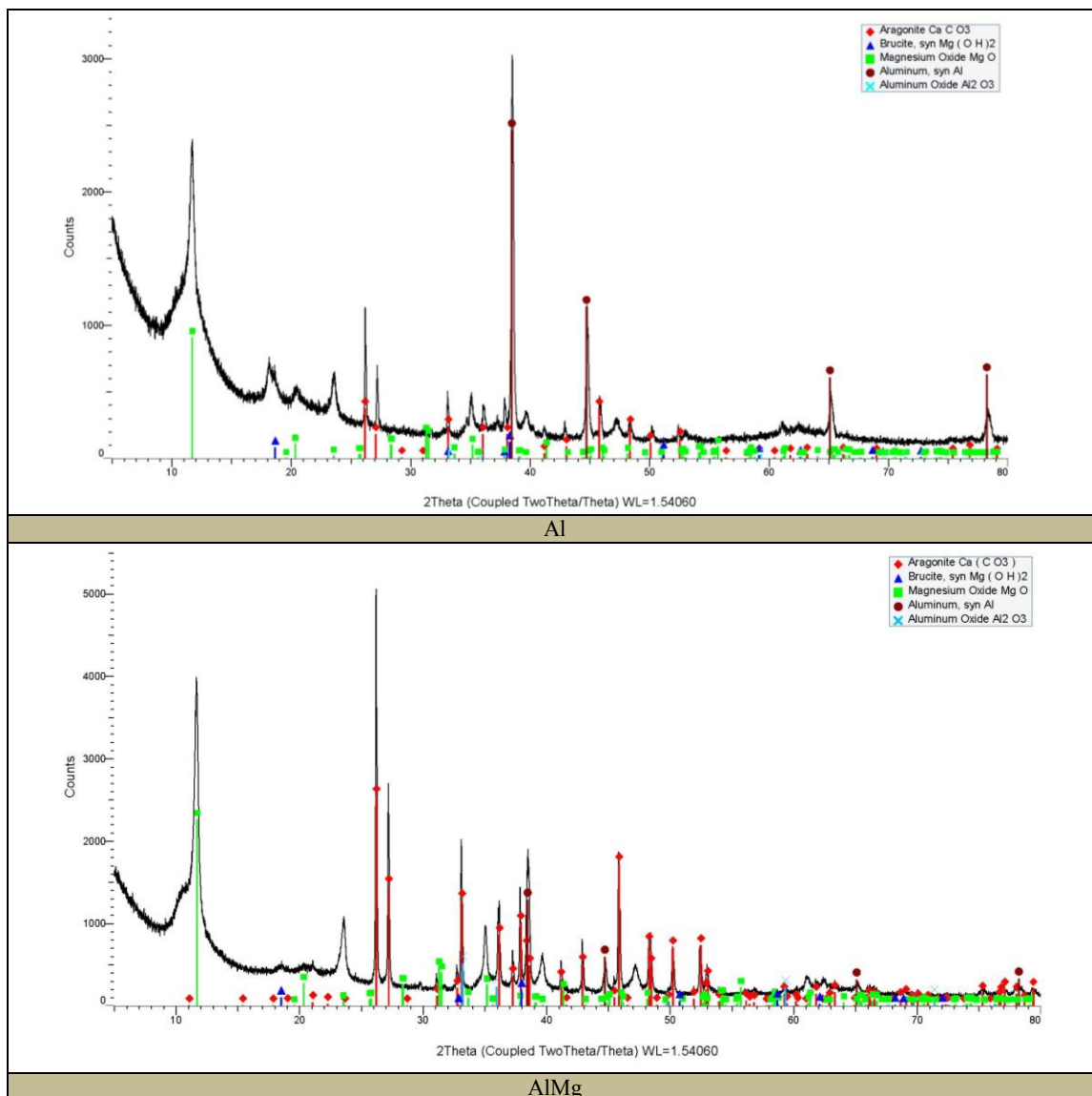


Figure G.1:   XRD from glass rods deposits formed in 30°C test.
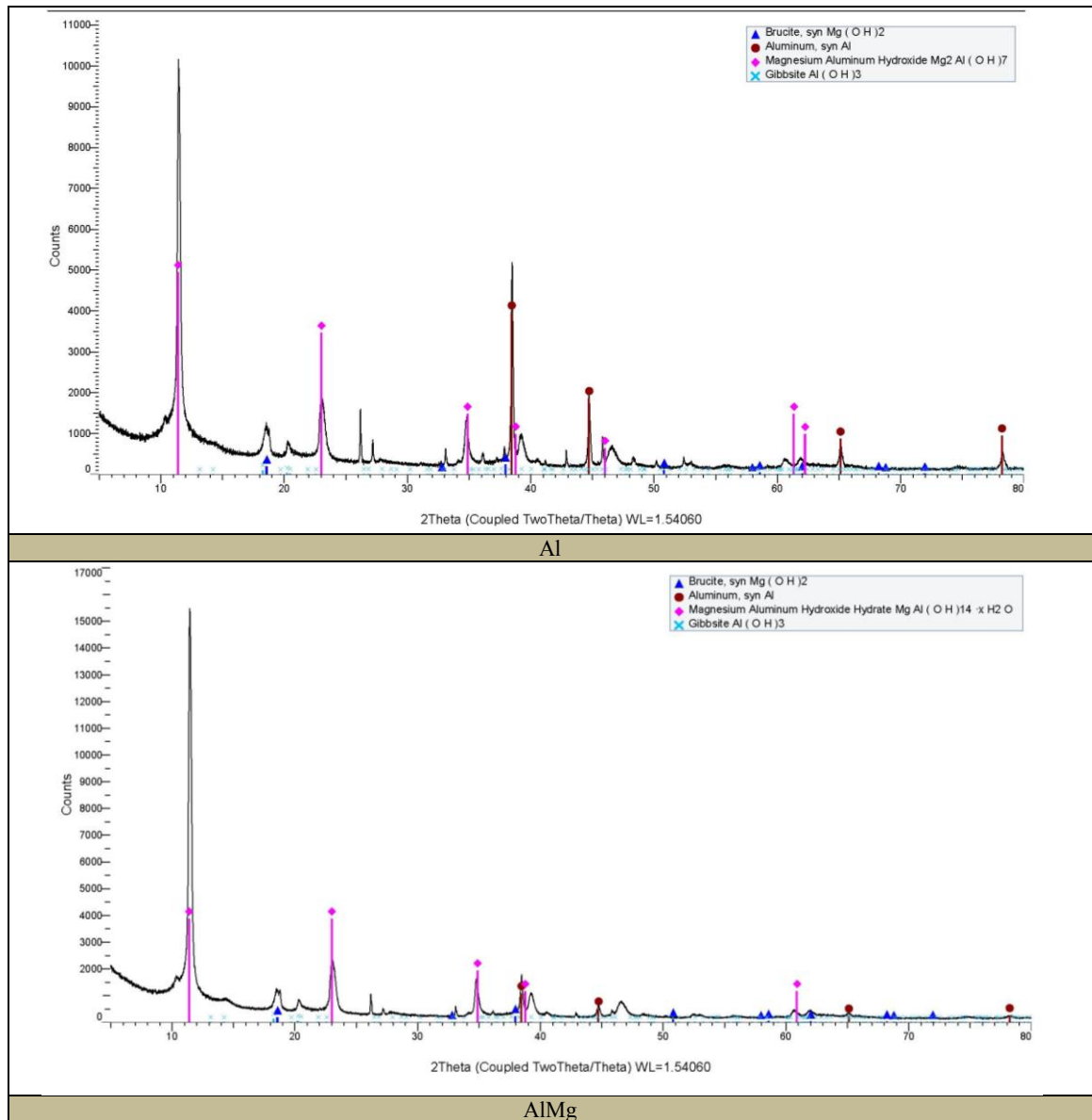
Figure G.2: XRD from glass rods deposits formed in 60°C test.
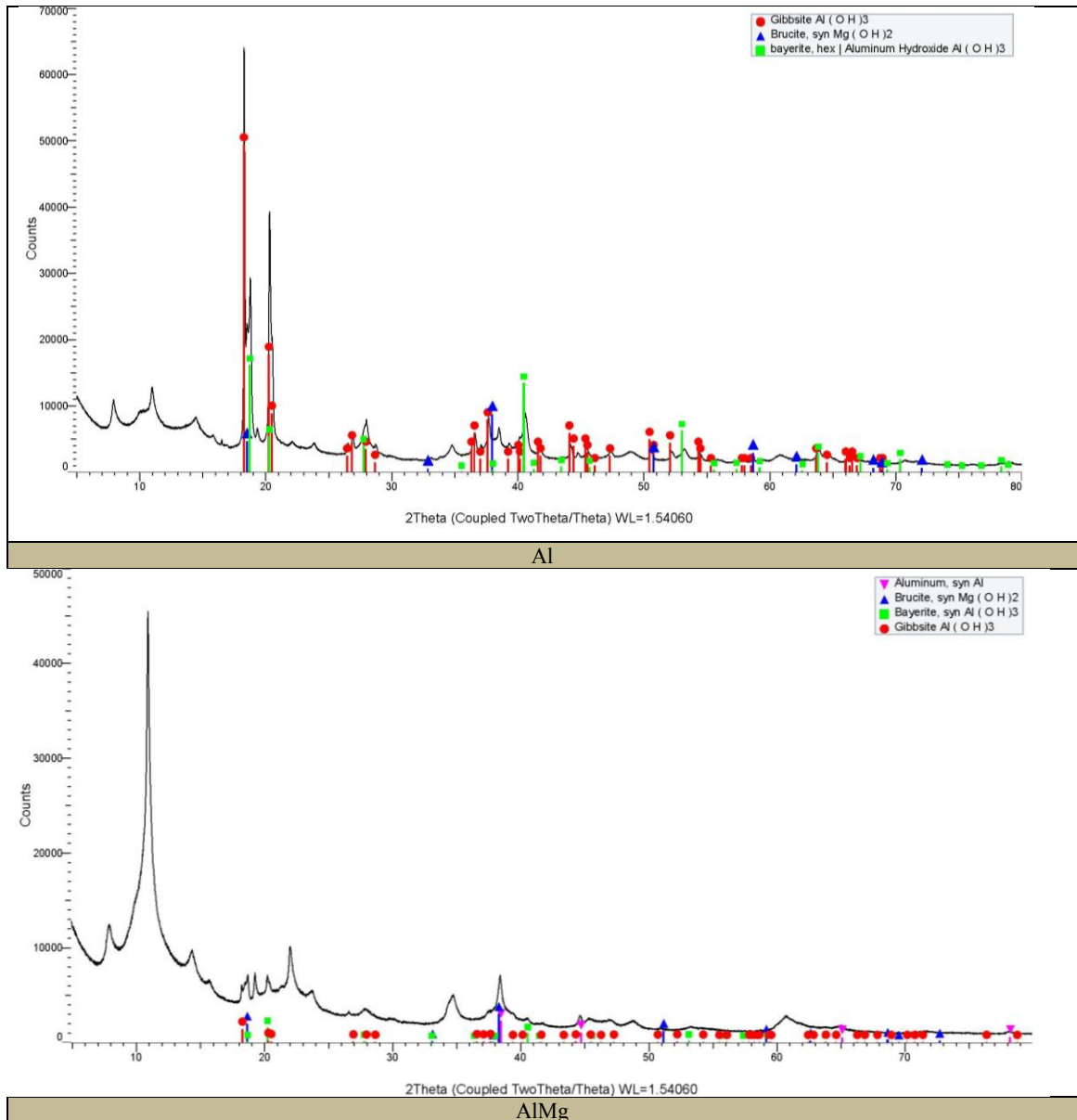
Figure G.3:   XRD from glass rods deposits formed in 90°C test.

# APPENDIX H – EDX in Holiday Area of Samples from Thermal Gradient Test
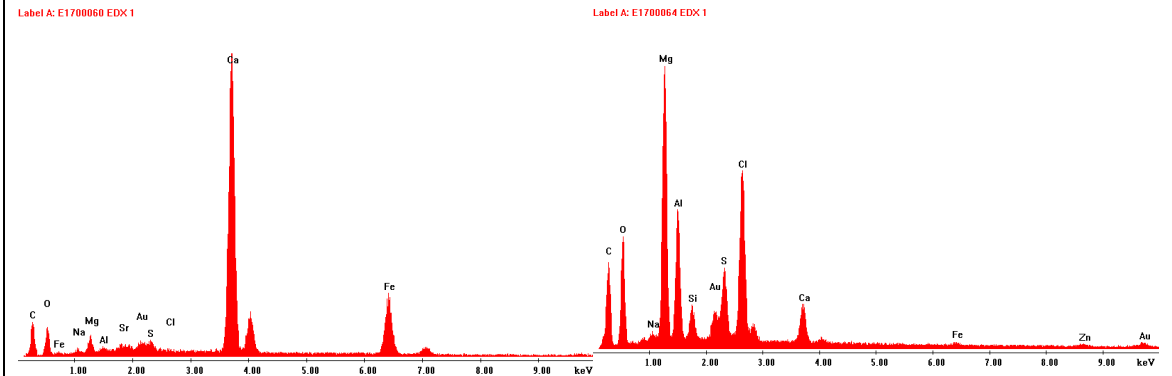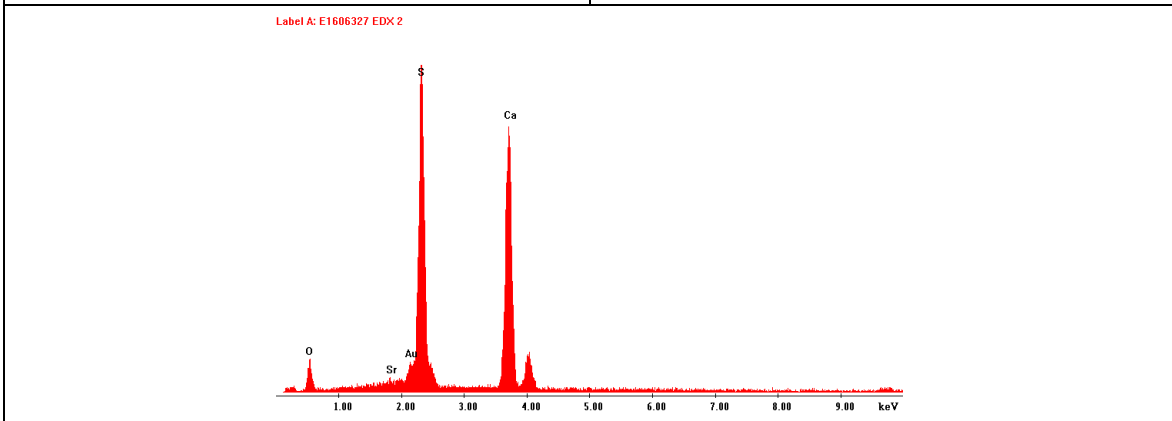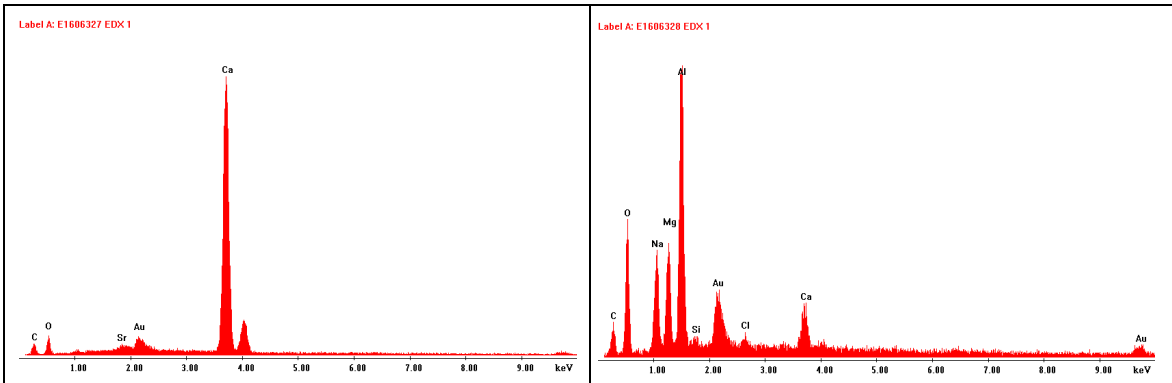


E1



E2
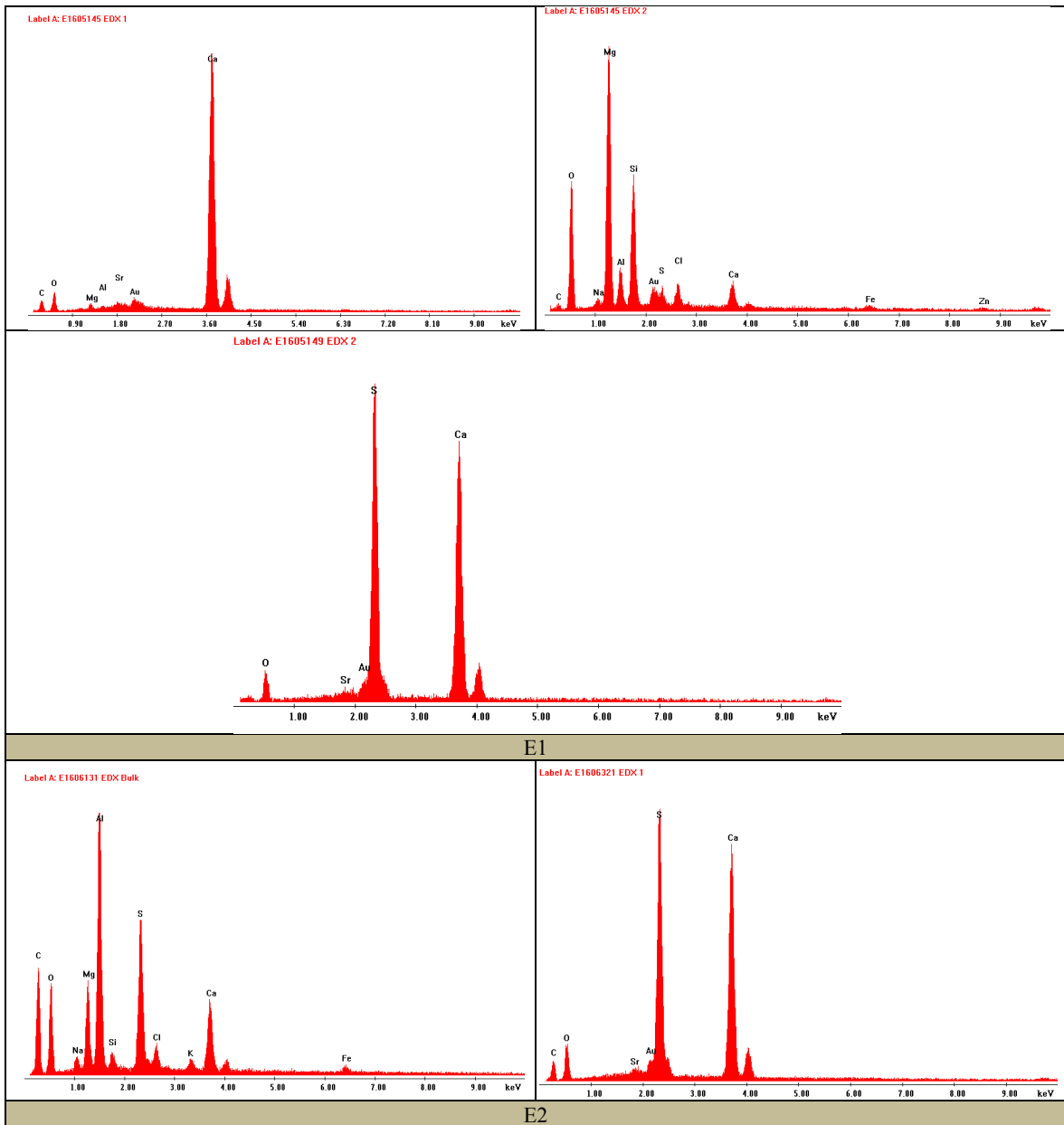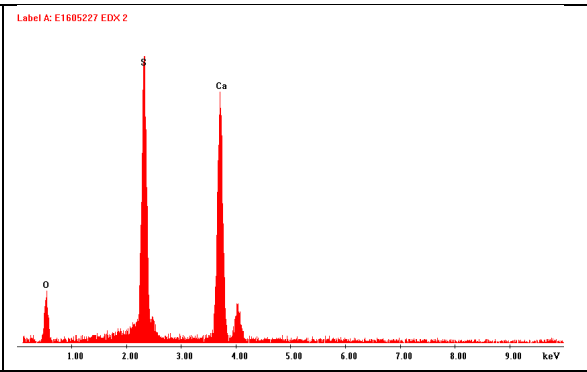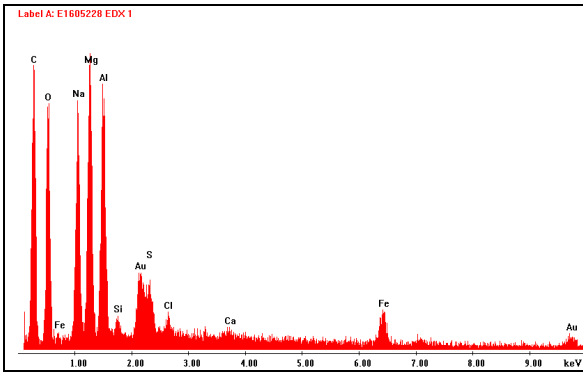
E3
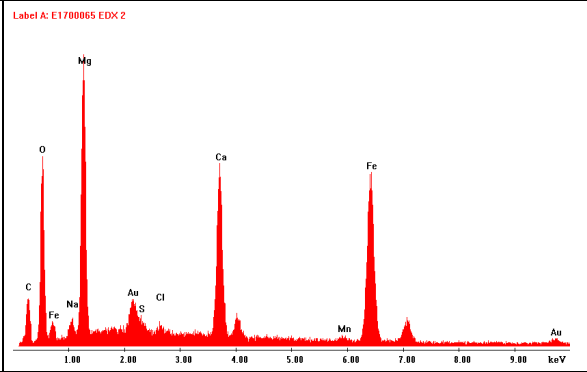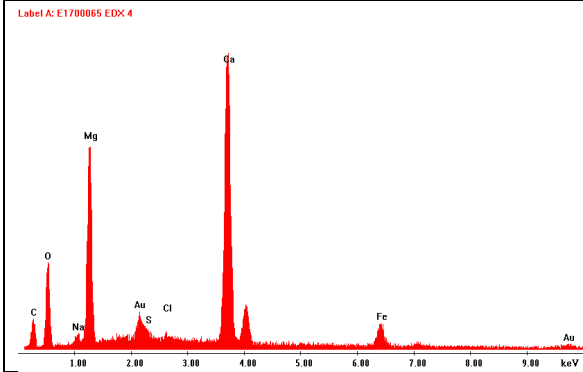
E4
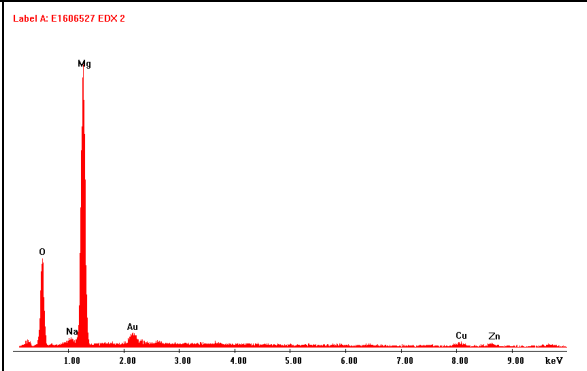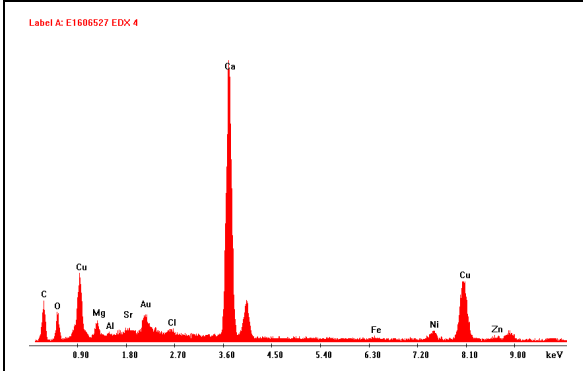
E5
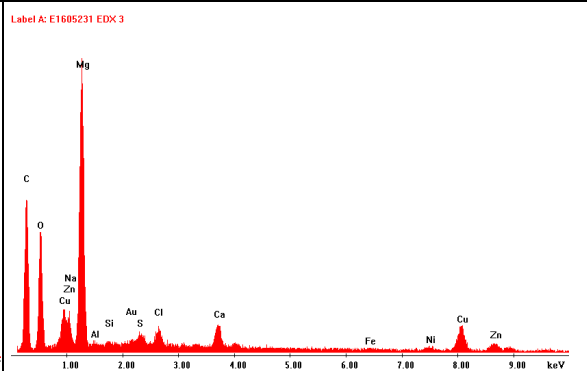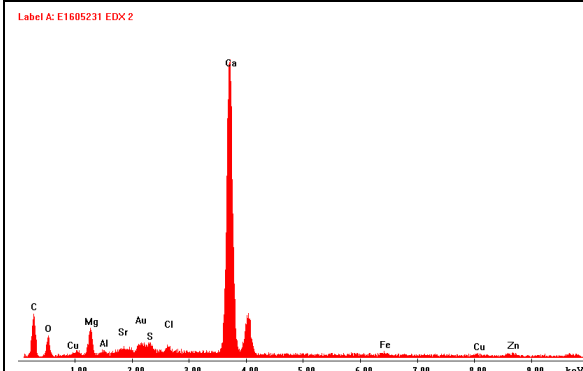
E6
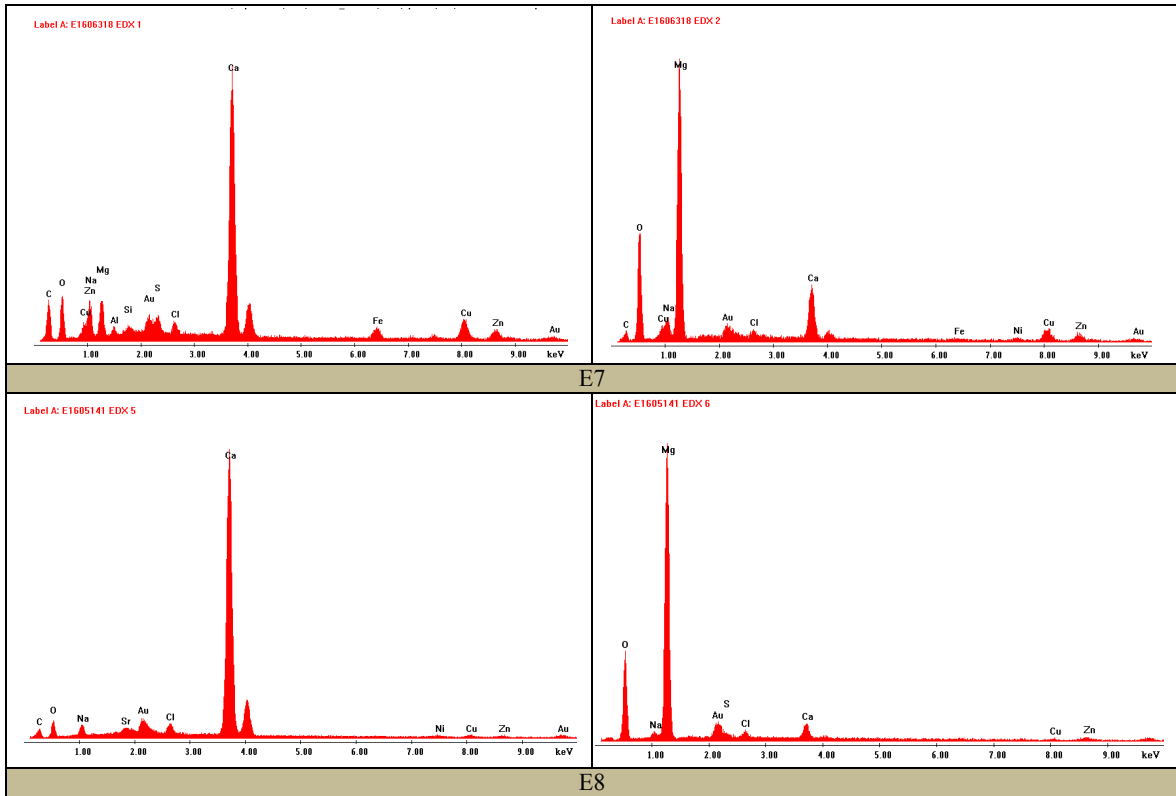
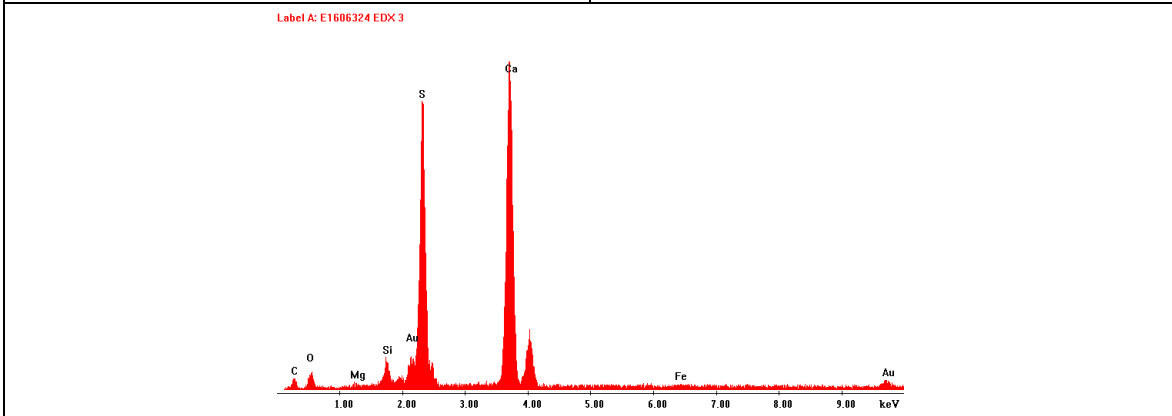Figure H.1: EDX from the holiday of buried and unburied samples exposed to thermal gradient test under free potential.
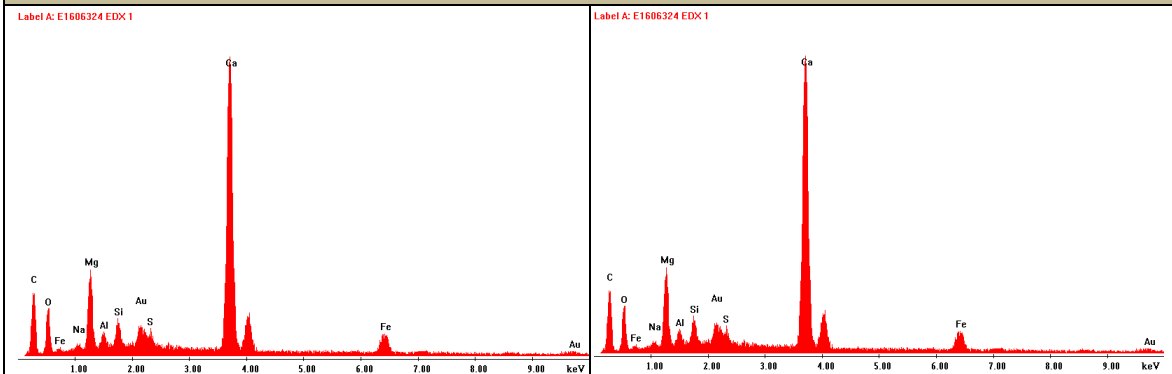
CP1



CP2

133
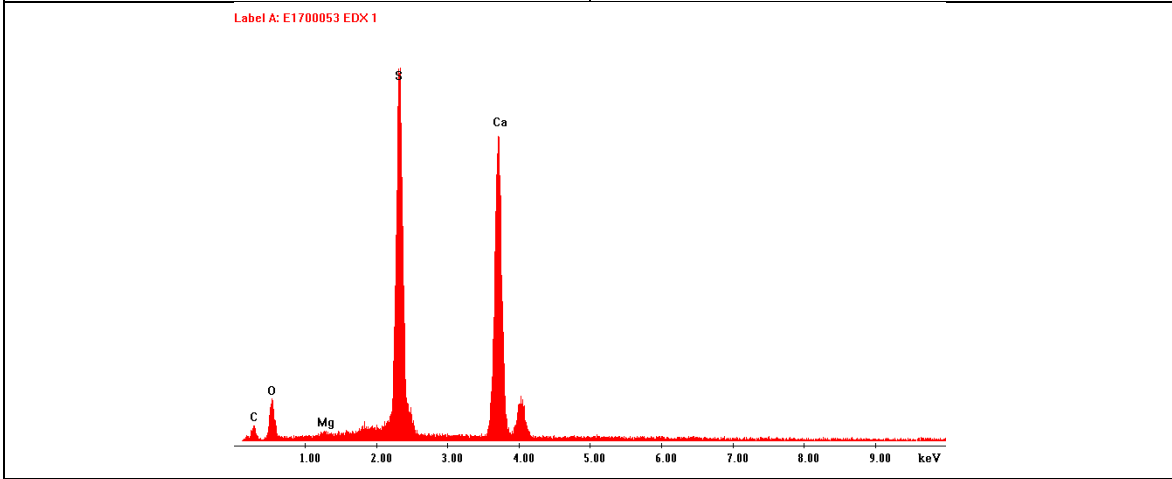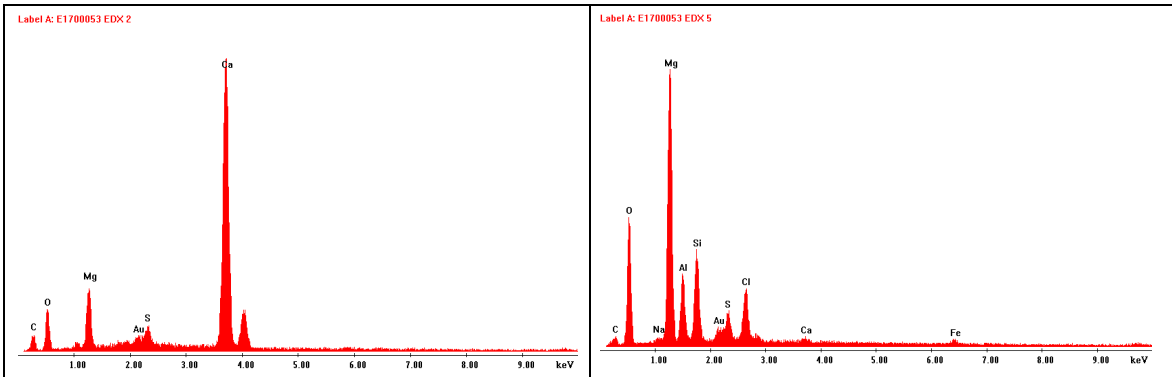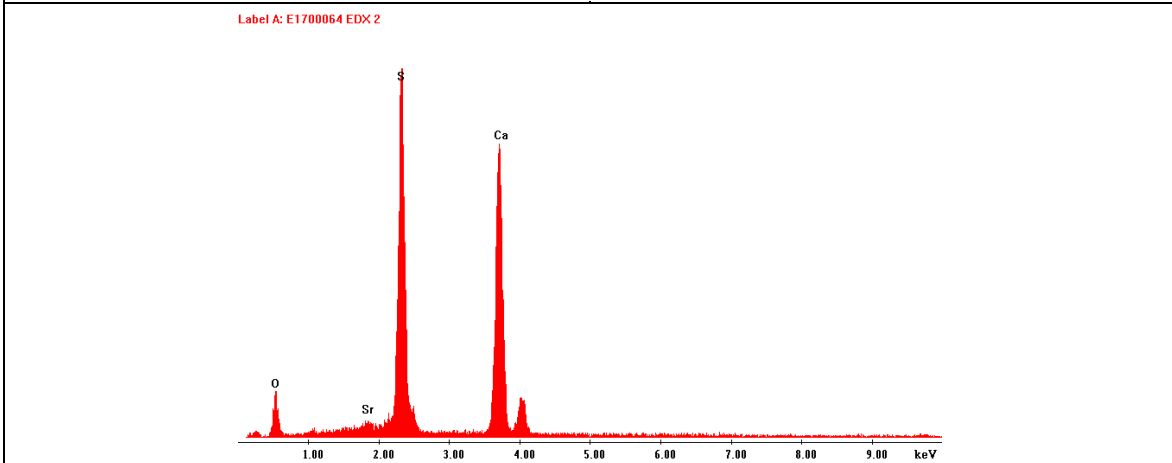
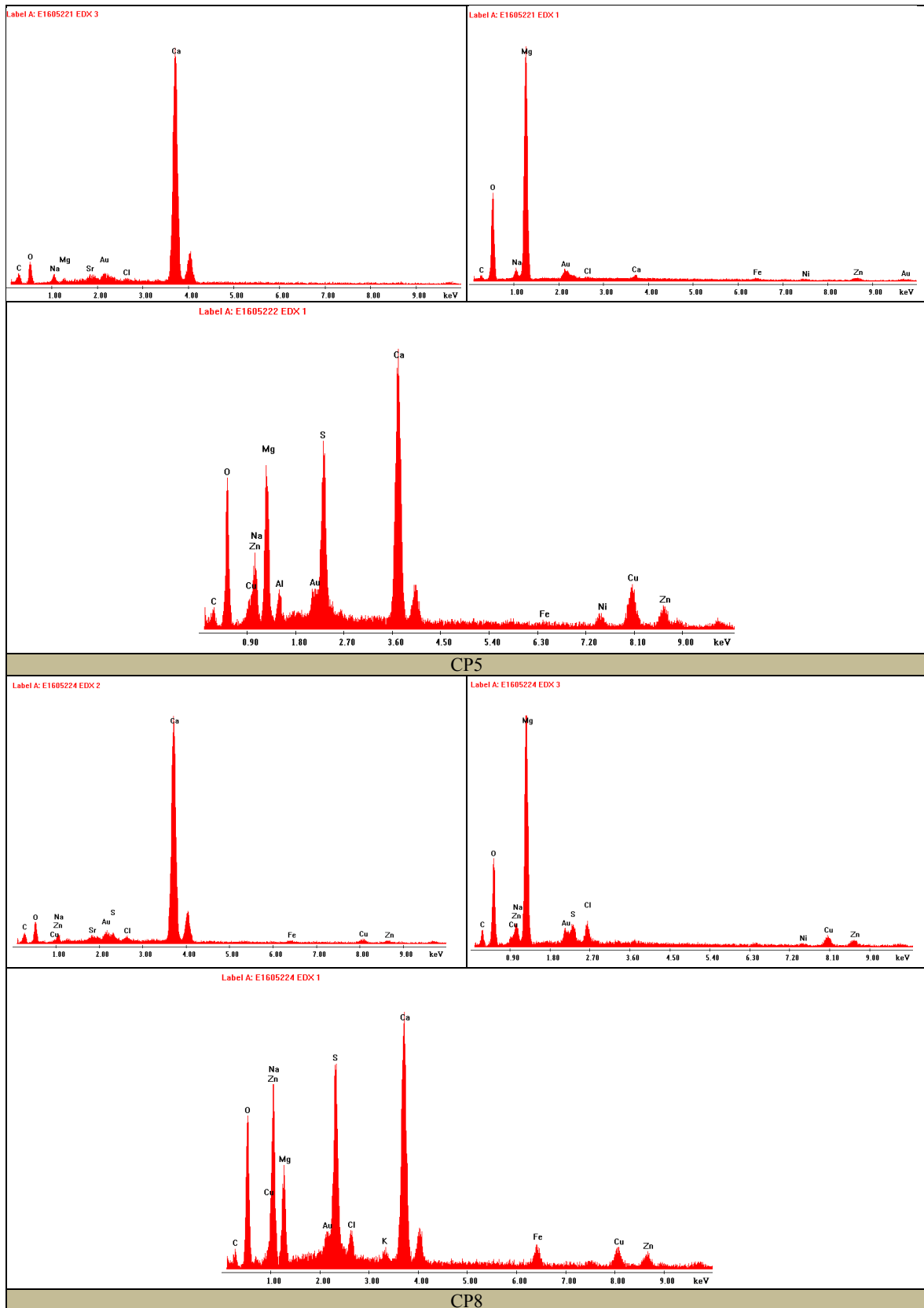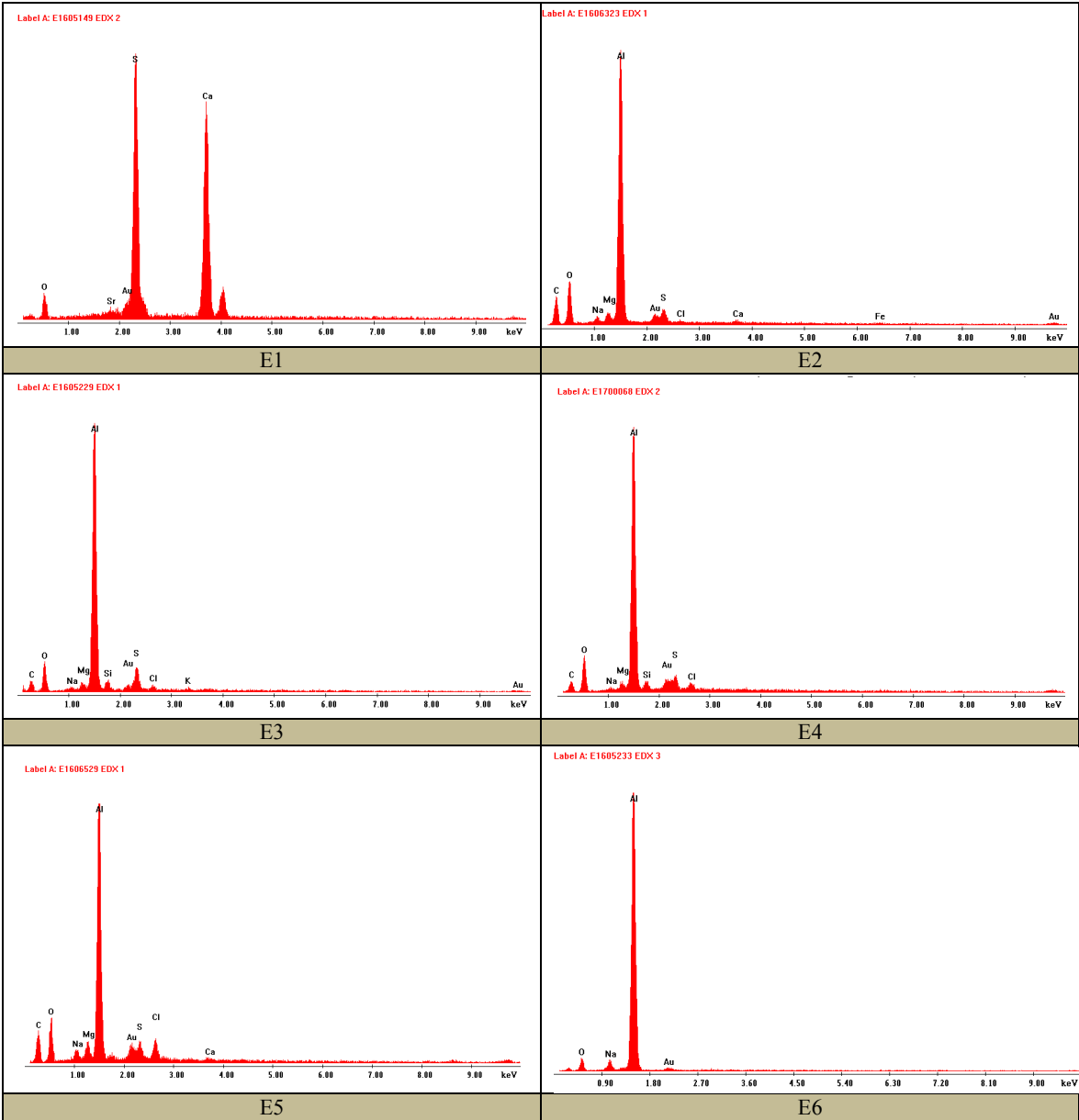CP3

CP4

Figure H.2:  EDX from the holiday of buried and unburied samples exposed to thermal gradient test under -950 mV/$_{\text{Ag/AgCl}}$.

APPENDIX I –  EDX  on TSA Deposits of Samples from Thermal Gradient Test


E1


E2


E3


E4


E5


E6

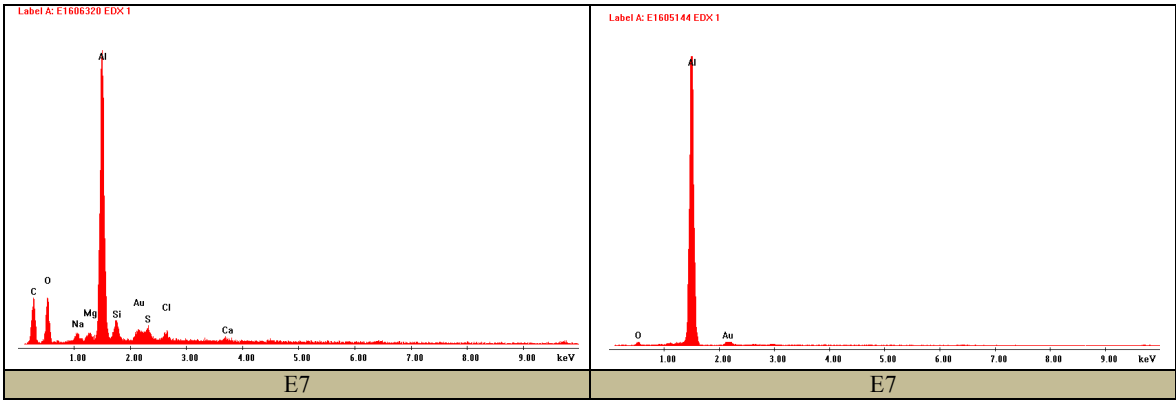Figure I.1: EDX on the TSA of samples exposed to the thermal gradient under free potential.
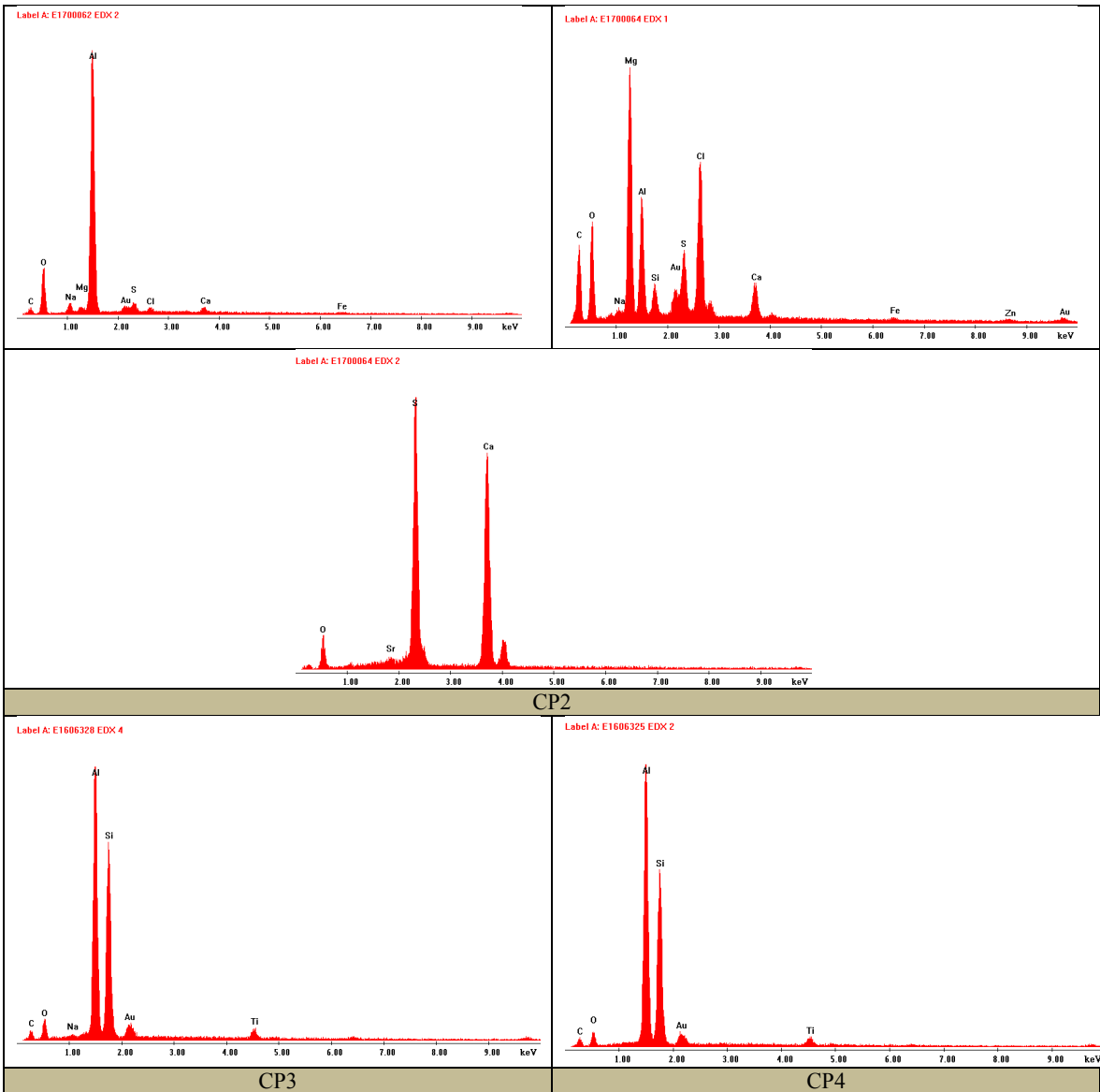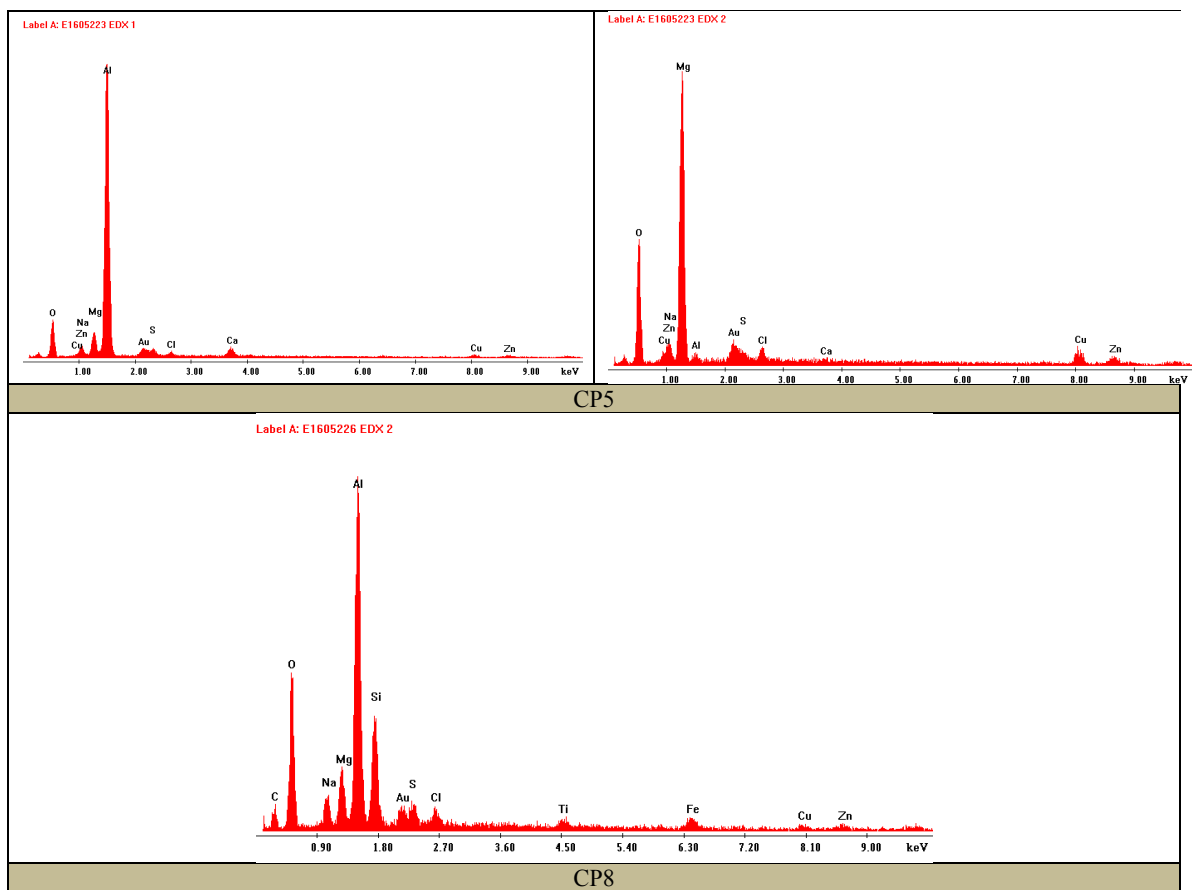
Figure I.2: EDX from holiday of sealed and unsealed samples exposed to the thermal gradient under -950 mV/$_{Ag/AgCl}$.

APPENDIX J – Local PH Test: Microstucture, EDX and XRD



| Top view | Holiday | TSA |
|----------|---------|-----|
| 30°C | | |
| 60°C | | |

Figure J.1:    Microstructure of local pH test at 30 and 60°C.

Figure J.2:    EDX cross-section from sample exposed to 30°C test.


Figure J.3:    EDX cross-section from sample exposed to 60°C test.

Figure J.4:    XRD from sample exposed to 30°C test.

Figure J.5:    XRD from sample exposed to 60°C test.

APPENDIX K – Calculated Corrosion Data

Table K.1: Values used for the corrosion rate calculation of samples exposed to different temperatures.

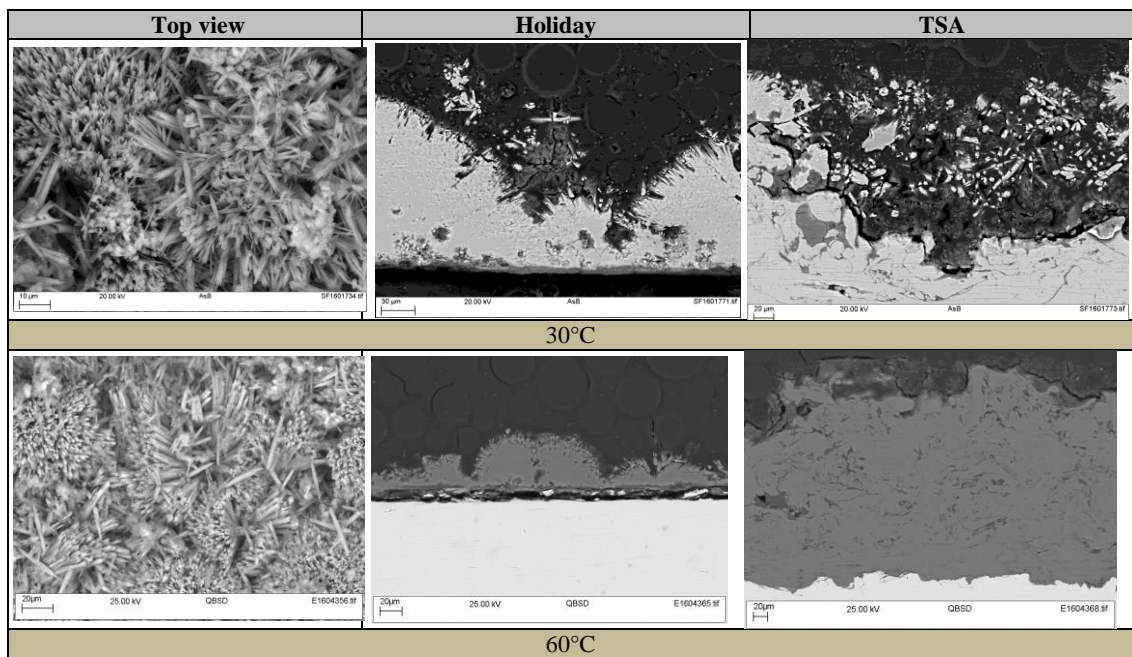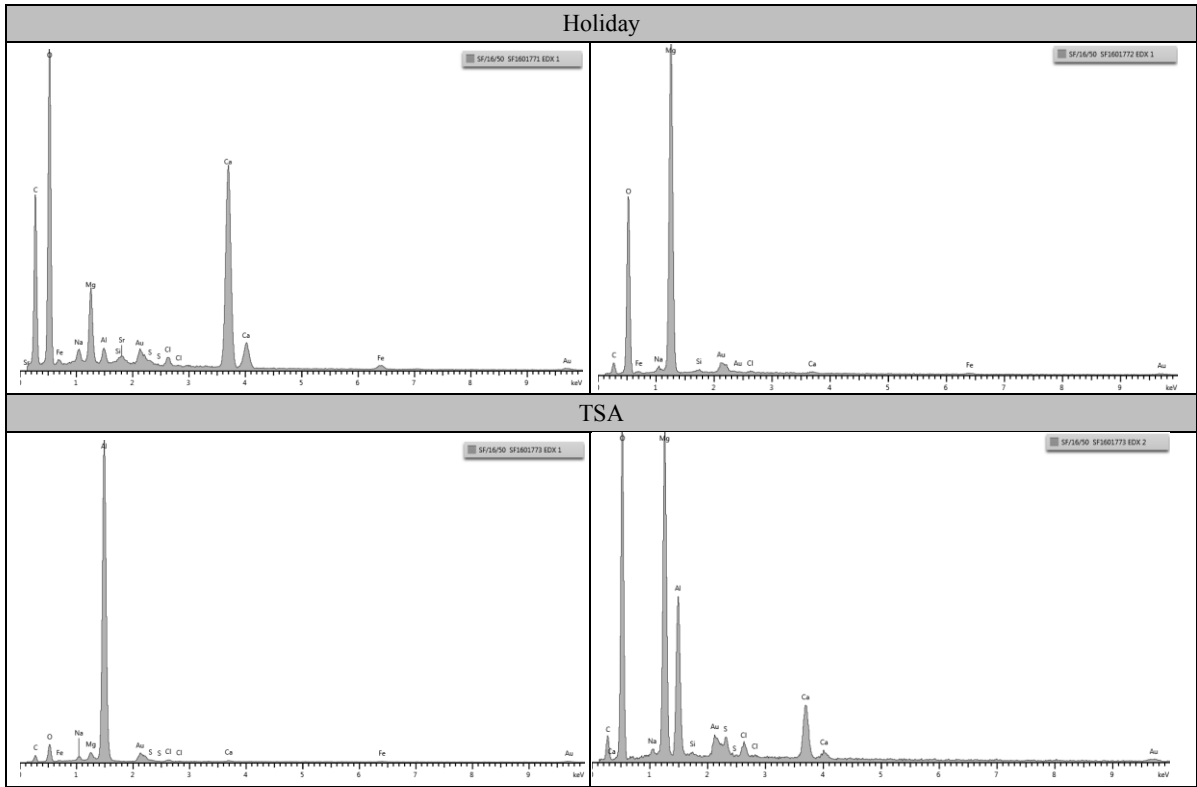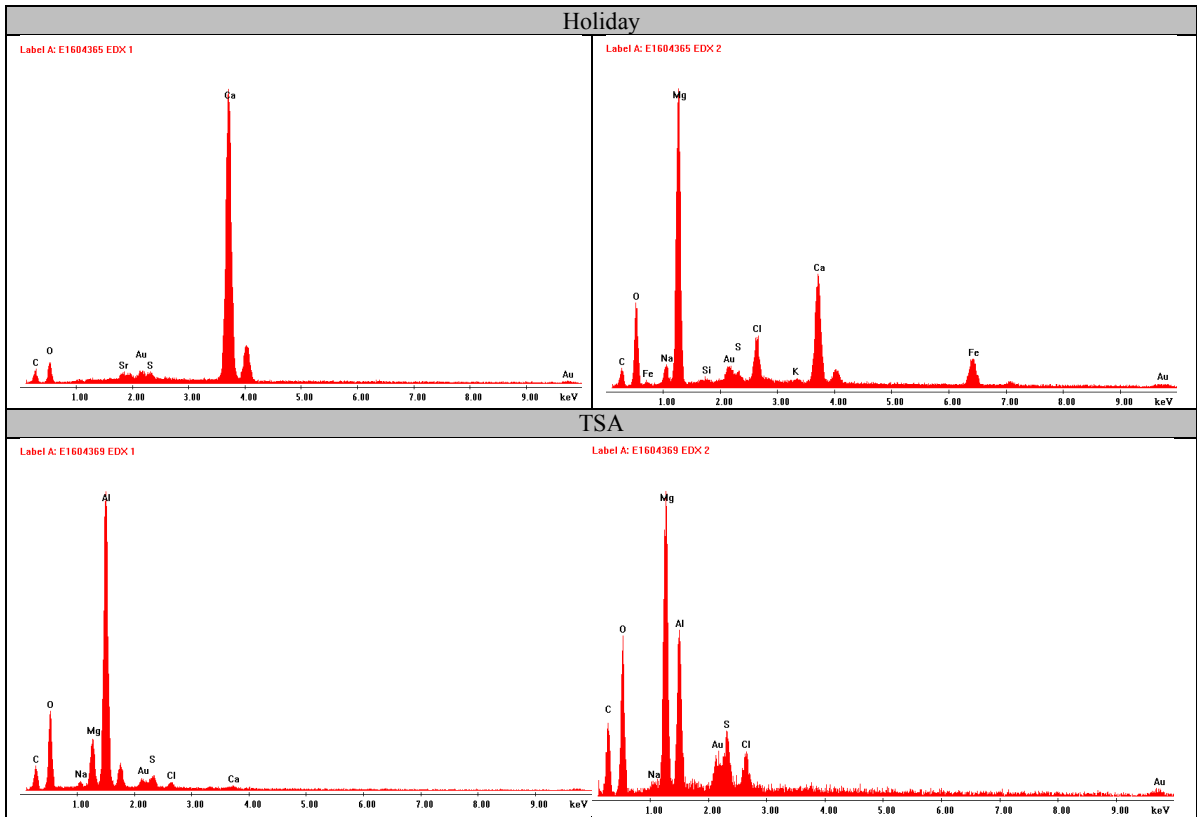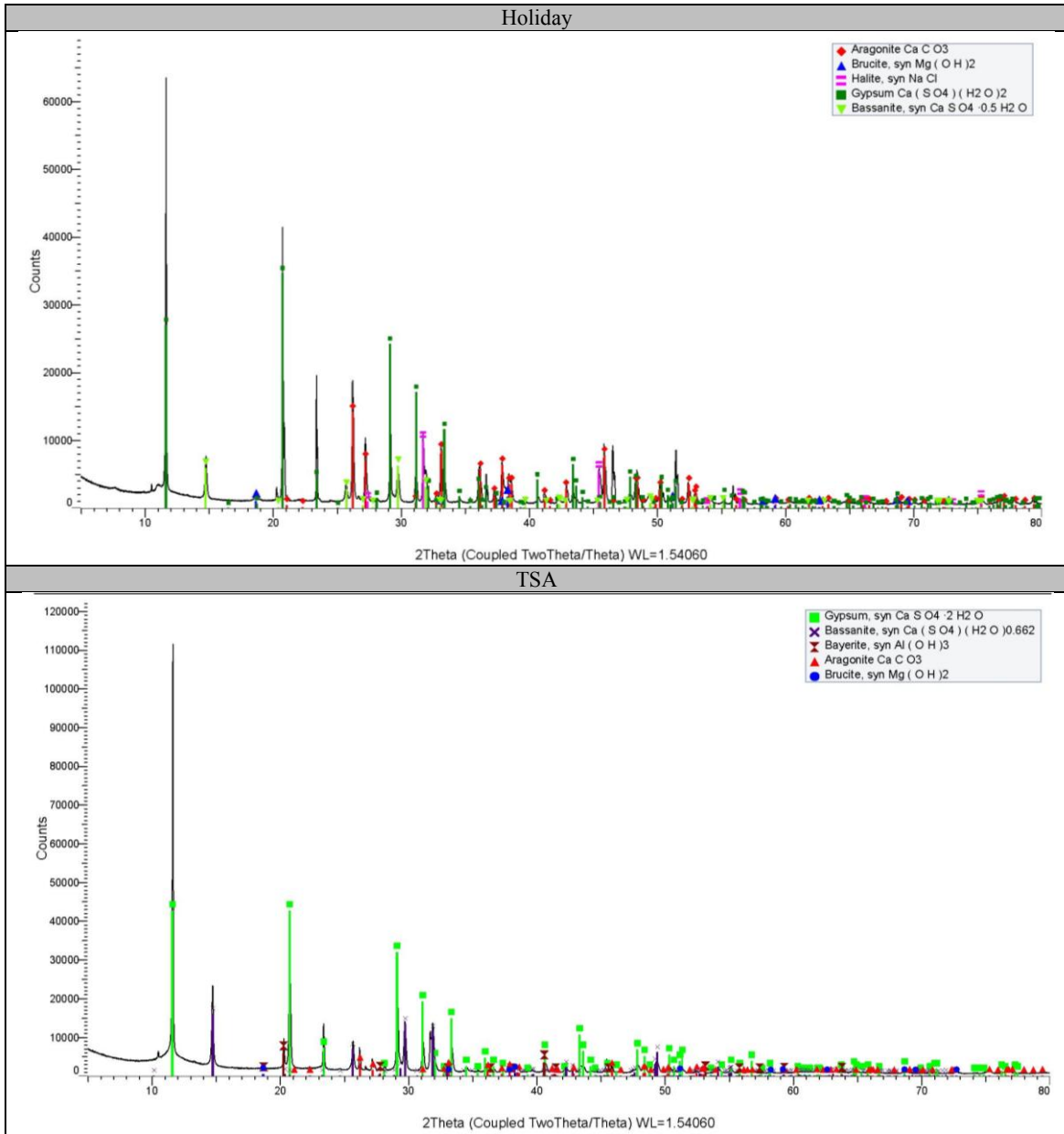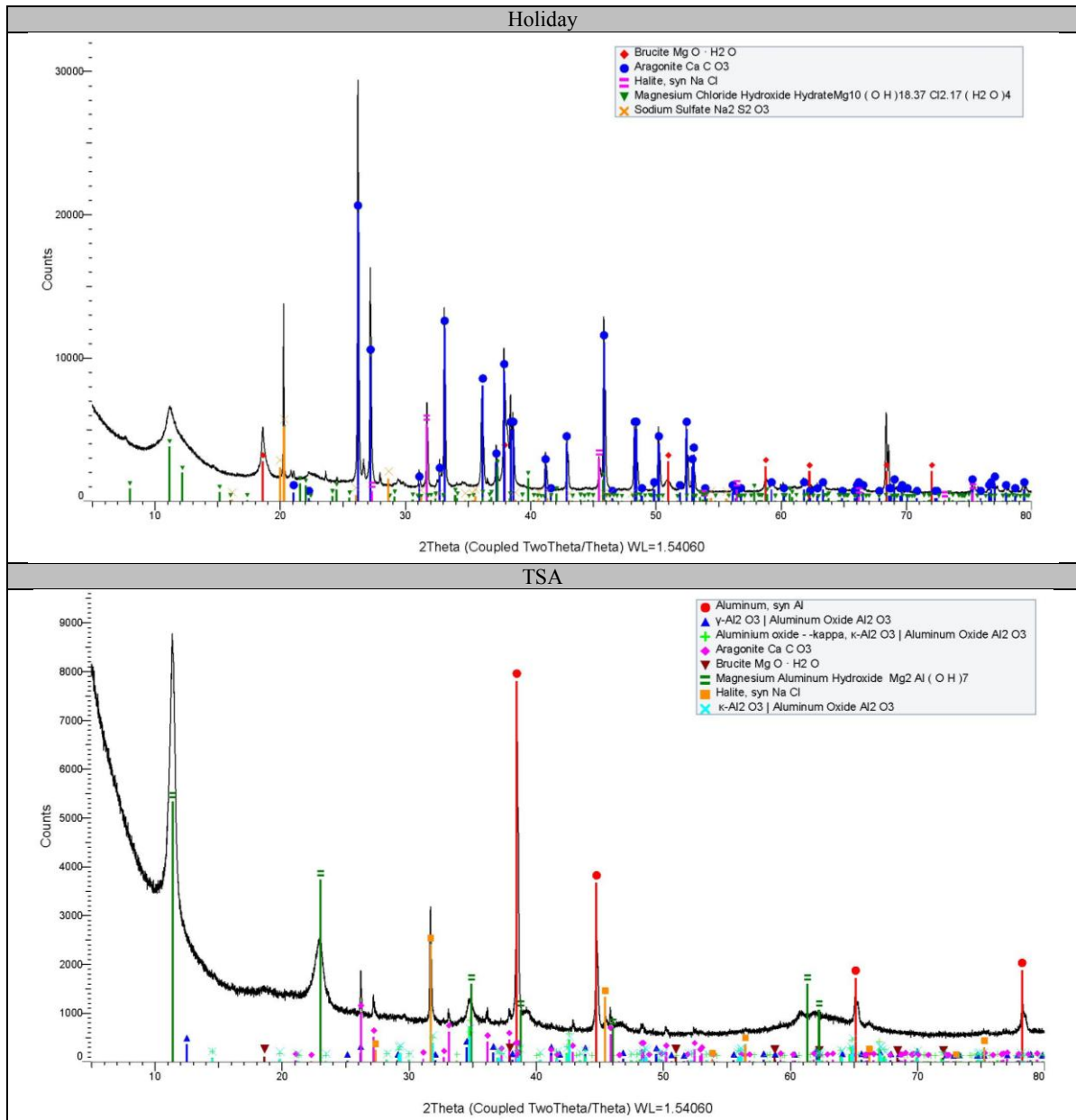| Temperature (°C) | Sample | $i$A (mA/cm$^2$) | $i\beta$ (mA/cm$^2$) | $\Delta i$ (A/cm$^2$) | $R_p$ ($\Omega.cm^2$) | $i_{corr}$ ($\mu A/cm^2$) |
|---|---|---|---|---|---|---|
| 30°C | Al 5% | $5.36 \times 10^{-5}$ | $1.76 \times 10^{-4}$ | $1.227 \times 10^{-7}$ | 162999.18 | 0.110 |
| | Al 10% | $4.57 \times 10^{-5}$ | $1.959 \times 10^{-4}$ | $1.5 \times 10^{-7}$ | 133155.79 | 0.135 |
| | Al 20% | $4.45 \times 10^{-4}$ | $2.30 \times 10^{-4}$ | $2.15 \times 10^{-7}$ | 93023.25 | 0.193 |
| | AlMg 5% | $-9.32 \times 10^{-4}$ | $6.76 \times 10^{-4}$ | $1.6 \times 10^{-6}$ | 12438.58 | 1.45 |
| | AlMg 10% | $-1.669 \times 10^{-4}$ | $4.029 \times 10^{-4}$ | $5.698 \times 10^{-7}$ | 35100.03 | 0.512 |
| | AlMg 20% | $-6.091 \times 10^{-4}$ | $4.008 \times 10^{-4}$ | $1.009 \times 10^{-6}$ | 19803.94 | 0.909 |
| 60°C | Al 5% | $1.438 \times 10^{-4}$ | $2.107 \times 10^{-4}$ | $6.69 \times 10^{-8}$ | 298953.66 | 0.060 |
| | Al 10% | $-1.845 \times 10^{-4}$ | $2.16 \times 10^{-5}$ | $1.629 \times 10^{-7}$ | 122774.70 | 0.146 |
| | Al 20% | $-1.55 \times 10^{-4}$ | $4.29 \times 10^{-5}$ | $1.979 \times 10^{-7}$ | 101061 | 0.178 |
| | AlMg 5% | $7.31 \times 10^{-5}$ | $1.79 \times 10^{-4}$ | $1.068 \times 10^{-7}$ | 187265.91 | 0.096 |
| | AlMg 10% | $3.87 \times 10^{-5}$ | $1.66 \times 10^{-4}$ | $1.278 \times 10^{-7}$ | 156494.52 | 1.15 |
| | AlMg 20% | $-9.8 \times 10^{-5}$ | $2.04 \times 10^{-5}$ | $1.18 \times 10^{-4}$ | 168918.92 | 1.06 |
| 90°C | Al 5% | $-3.777 \times 10^{-4}$ | $2.329 \times 10^{-4}$ | $6.106 \times 10^{-7}$ | 32754.67 | 0.549 |
| | Al 10% | $-6.913 \times 10^{-4}$ | $6.657 \times 10^{-4}$ | $1.357 \times 10^{-6}$ | 14738.00 | 1.221 |
| | Al 20% | $-1.648 \times 10^{-3}$ | $1.674 \times 10^{-3}$ | $3.322 \times 10^{-6}$ | 6020.47 | 2.989 |
| | AlMg 5% | $- 3.862 \times 10^{-4}$ | $4.16 \times 10^{-4}$ | $8.022\ 10^{-7}$ | 24931.43 | 0.721 |
| | AlMg 10% | $-7.4 \times 10^{-4}$ | $7.1 \times 10^{-4}$ | $1.45 \times 10^{-6}$ | 13793.10 | 1.300 |
| | AlMg 20% | $-1.282 \times 10^{-3}$ | $1.238 \times 10^{-3}$ | $2.52 \times 10^{-6}$ | 7936.50 | 2.268 |

Table K.2: Values used for the corrosion rate calculation of samples exposed to thermal gradient.

| Sample | $i$A (mA/cm$^2$) | $i$β (mA/cm$^2$) | Δi (A/cm$^2$) | $R_p$ (Ω.cm$^2$) | $i_{corr}$ (μA/cm$^2$) |
|--------|------------------|------------------|---------------|------------------|------------------------|
| E1 | -1.85 x 10$^{-4}$ | 1.02 x 10$^{-4}$ | 2.87 x 10$^{-4}$ | 69565.22 | 0.258 |
| E2 | -5.786 x 10$^{-3}$ | 5.692 x 10$^{-3}$ | 1.147 x 10$^{-2}$ | 1742.36 | 0.112 |
| E3 | 4.654 x 10$^{-3}$ | 2.899 x 10$^{-3}$ | 7.554 x 10$^{-3}$ | 2647.63 | 6.79 |
| E4 | -2.481 x 10$^{-2}$ | 1.827 x 10$^{-2}$ | 4.309 x 10$^{-5}$ | 464.15 | 38.78 |
| E5 | -3.059 x 10$^{-3}$ | 1.585 x 10$^{-3}$ | 4.645 x 10$^{-6}$ | 4305.7 | 4.18 |
| E6 | -2.069 x 10$^{-3}$ | 1.189 x 10$^{-3}$ | 3.258 x 10$^{-6}$ | 6137.23 | 2.933 |
| E7 | -3.198 x 10$^{-3}$ | 1.712 x 10$^{-3}$ | 4.91 x 10$^{-6}$ | 4072.9 | 4.419 |
| E8 | -5.3036 x 10$^{-3}$ | 2.849 x 10$^{-3}$ | 8.152 x 10$^{-6}$ | 2453.17 | 7.337 |